Doctorate Dissertation
博士論文

Exploring Molecular-Cloud Formation Using the Intensity Anomalies of the OH 18 cm Transition

(OH 18 cm 線の強度異常を用いた分子雲形成の研究)

A Dissertation Submitted for Degree of Doctor of Philosophy
December 2018
平成30年12月博士（理学）申請

Department of Physics, Graduate School of Science,
The University of Tokyo
東京大学大学院理学系研究科
物理学専攻

Yuji Ebisawa
海老澤 勇治

Abstract

Stars are born through gravitational contraction of the gas in the densest parts of interstellar clouds, which are called molecular-cloud cores. Since molecular-cloud cores are formed from rather diffuse atomic clouds, exploring formation and evolution of molecular clouds is a key to understanding a vast diversity of stars and their planetary systems. Large-scale structures of molecular clouds have extensively been studied mainly by observing the rotational transitions of carbon monoxide (CO). The hyperfine-structure transition of the hydrogen atom (H), so-called 21 cm transition, has also been observed to trace atomic clouds. Evolution from atomic clouds to molecular clouds is thus studied by comparing the spatial distributions of the spectral lines of CO and H. However, the evolution is not well understood, since there remains a gap between structures traced by these lines. This gap corresponds to a diffuse part of molecular clouds that is not well traced by CO, and hence, it is called the CO-dark molecular gas. In this thesis, we develop a new tool to fill this gap for full understanding the molecular-cloud formation, based on the observations of the OH 18 cm transition in the radio wavelength region.

The OH 18 cm transition, consisting of the four hyperfine structure (hfs) components at frequencies of 1612 MHz, 1665 MHz, 1667 MHz, and 1720 MHz, have been observed toward a few representative nearby molecular clouds with the Effelsberg 100-m telescope, the GBT 100-m telescope and Very Large Array (VLA); a diffuse cloud HCL2E, a well-known photodissociation region ρ-Ophiuchi, cold dark clouds L183 and L169, filamentary dark clouds Lupus-1 and Pipe nebula, a starless core TMC-1(CP), and a filamentary structure in the north part of TMC-1 (TMC-1FN). From these observations, the three types of the hyperfine intensity anomalies have been identified: (1) the 1612 MHz line absorption, (2) the 1665 and 1667 MHz line absorption, and (3) the 1720 MHz line absorption. Since no strong radio continuum background source is associated with the observed sources, these absorptions appear against the cosmic microwave background (CMB). In order to explore the origin of each hyperfine anomaly, a statistical equilibrium calculation code is developed. In particular, the effect of the far-infrared (FIR) pumping and the line overlaps are found to be essential for

understanding the anomaly (3) found in TMC-1FN and TMC-1(CP). As a result, the above three hyperfine intensity anomalies including the absorption features are successfully reproduced. The physical conditions necessary to cause each anomaly are constrained to be: (1) a diffuse warm gas ($T_k > 40$ K), (2) a gas kinetic temperature warmer than 90 K, and (3) a cold ($T_k < 30$ K) and dense ($N(\mathrm{OH}) > 10^{15}$ cm^{-2}) gas illuminated by the strong FIR radiation.

It is demonstrated that the gas kinetic temperature can be determined accurately from the intensities of the four hfs lines, for the (1) and (2) cases. This is a novel aspect of the OH 18 cm transition as a good thermometer of molecular clouds. A temperature distribution in a molecular cloud provides us with information on the heating effect by UV field and/or dynamical interactions between molecular clouds. This information is closely related to a molecular-cloud formation, since the UV controls chemical reactions in molecular clouds, and the cloud-cloud collisions lead to core formation there. We then apply this technique to the molecular clouds in HCL2E, L183, ρ-Ophiuchi, Lupus-1, and Pipe nebula. As a result, the possible heating effects by the interstellar UV radiation (HCL2E and L183), the UV radiation from nearby OB stars (ρ-Oph and Lupus-1), and the filament-filament collisions (Pipe nebula) are revealed.

In addition, the interferometric observations of the OH 18 cm transition have been conducted toward TMC-1FN with VLA. The hyperfine anomaly is not observed with VLA, which is contrary to the (1) 1612 MHz and (3) 1720 MHz absorptions observed with the Effelsberg telescope toward this source. We present that a cold and dense core embedded in TMC-1FN is revealed by VLA, where the 1612 MHz and 1720 MHz absorptions are resolved out.

These results suggest that the OH 18 cm transition is a powerful tracer of a molecular-cloud formation in a wide range of H_2 density from diffuse clouds to dense cores, by combining the single-dish and interferometric observations.

Contents

CHAPTER 1. Introduction

In this thesis, a new tool to study molecular-cloud formation, that is the 18 cm transition of hydroxyl radical (OH), is presented. Since stars are formed in dense parts of molecular clouds, the formation process of molecular clouds is thought to largely affect the subsequent star-formation. Recent radio observations, particularly those with ALMA (Atacama Large Millimeter/submillimeter Array), have revealed the vast diversity of newly born stars and their disk/envelope systems in physical structures and chemical compositions (e.g. Sakai et al. 2014; Oya et al. 2016). Their origins should be related to the formation history of each star. In this context, understanding of formation and evolution processes of molecular clouds is of fundamental importance.

For a long time, molecular clouds have extensively been studied mainly by the rotational transitions of carbon monoxide (CO) (Dame et al. 1987; Mizuno et al. 1995; Fukui et al. 2008). On the other hand, diffuse atomic clouds have been traced by the 21 cm transition of the hydrogen atom ([H I]) (Kalberla et al. 2005; Peek et al. 2011). However, the distributions of CO and [H I] are much different, and hence, it is very difficult to investigate the transition zone from atomic clouds to molecular clouds. Indeed, a diffuse part of molecular clouds, where CO molecules are photodissociated by strong interstellar UV radiations, cannot fully traced by CO. Since such a diffuse gas (the so-called CO-dark molecular gas) plays an important role in the transition from atomic clouds to molecular clouds (Smith et al. 2014; Glover & Smith 2016), a new observational method to trace this region has been awaited.

In order to solve this long-standing problem, we conducted observations of the OH 18 cm transition and analyzed them by the non-LTE (local thermodynamic equilibrium) modeling. This transition is considered to be a good tracer of the CO-dark gas (Ebisawa et al. 2015; Allen et al. 2015; Xu et al. 2016; Tang et al. 2017), since the OH molecules are easily formed in diffuse molecular clouds as an intermediate species in the formation of CO. It has the Λ-type doubling transition at the wavelength of 18 cm, which can be observed even in a diffuse condition due to its low critical density. Interestingly, the OH 18 cm transition is known to exhibit intensity anomalies toward molecular clouds according

to previous observations (Mattila et al. 1979; Harju et al. 2000; Xu et al. 2016). However, its origin is not well understood due to the complex excitation and de-excitation mechanisms. Solving the origin of the anomalies is essential to make full use of the OH 18 cm transition as a tracer of the transition zone from atomic clouds to molecular clouds.

With this in mind, we observed the four hyperfine structure (hfs) components of the OH 18 cm transition toward several molecular clouds in order to explore the origin of the anomalies. As a result, three types of the intensity anomalies are found: (1) the 1612 MHz line absorption, (2) the 1665 and 1667 MHz lines absorption, and (3) the 1720 MHz line absorption. A statistical equilibrium calculation code is developed, which successfully reproduces the anomalies (1), (2) and (3) with gas kinetic temperatures of > 40 K, > 90 K, and < 30 K, respectively. From these calculations, the pumping mechanism of OH producing each anomaly are systematically understood. In particular, the intensities of the four hfs lines of the OH 18 cm transition are found to be sensitive to the gas kinetic temperature. Therefore, the gas kinetic temperature can be determined accurately from the intensities of the four hfs lines of the OH 18 cm transition. The temperatures determined for the observed sources range from about 30 K to 100 K, which are generally higher than the typical temperature of molecular clouds traced by CO ($\sim$ 10 K). This result suggests that the OH 18 cm transition indeed traces a diffuse warm part of molecular clouds.

The observation of the OH 18 cm transition with an interferometer was also conducted. In this observation, the intensity anomaly was not found. This suggests that a cold dense core embedded in a diffuse warm gas is picked up by the interferometer, while the emission (and absorption) from the warmer extended gas surrounding the core is totally resolved out. Thus, the OH 18 cm transition can be used to study a wide range of molecular clouds, from diffuse clouds to dense cores, by combined analyses of data obtained by the single-dish telescopes and interferometers. Further observations of the OH 18 cm transition would improve our understandings of molecular-cloud formation.

In Section 2.1, we present a brief review on current understandings of molecular clouds, which have extensively been studied by observations and numerical calculations. In Section 2.2, we introduce the hydroxyl radical (OH) as well as the intensity anomalies of its 18 cm transition observed to-

ward molecular clouds. Chapter 3 describes a basic scheme of observations how the spectral data are obtained by radio single-dish telescopes. The performances of the telescopes employed in our observations, the Effelsberg 100-m telescope, the Green Bank 100-m telescope, and the Very Large Array, are also summarized in Chapter 3. Observational results, analyses and discussions on the three types of the intensity anomalies (1)–(3) of the OH 18 cm transition are presented in Chapters 4–6, respectively. Finally, conclusions and future prospects are presented in Chapter 7.

CHAPTER 2. Background

2.1 Molecular cloud

A molecular cloud is a relatively dense part of an interstellar medium (ISM). It is mainly composed of molecular hydrogen (H_2) (∼90%), followed by helium (∼10%) and carbon monoxide (CO) (∼0.01 %). It also contains small dust particles (silicate and carbonaceous compounds) whose mass is about 1% of the gas mass. Since molecular clouds are birth places of stars, understanding their formation process is related to a vast diversity of newly born stars and planetary systems associated with them. A typical H_2 density ($n(H_2)$) of molecular clouds ranges from 10^2 to 10^6 cm^{-3}, where a diffuse part ($n(H_2) = 10^2$–10^3 cm^{-3}) is called a diffuse cloud, while a dense part ($n(H_2) = 10^4$–10^6 cm^{-3}) is called a dense core or a molecular cloud core (Figure 1).

Molecular clouds are formed from atomic clouds ($n(H_2) = 1$–10 cm^{-3}), which are mainly composed of hydrogen atoms (H) (Figure 1). Shielding of the interstellar UV radiation is responsible for the formation of molecular gas from atomic gas, because it controls the photodissociation of molecules.

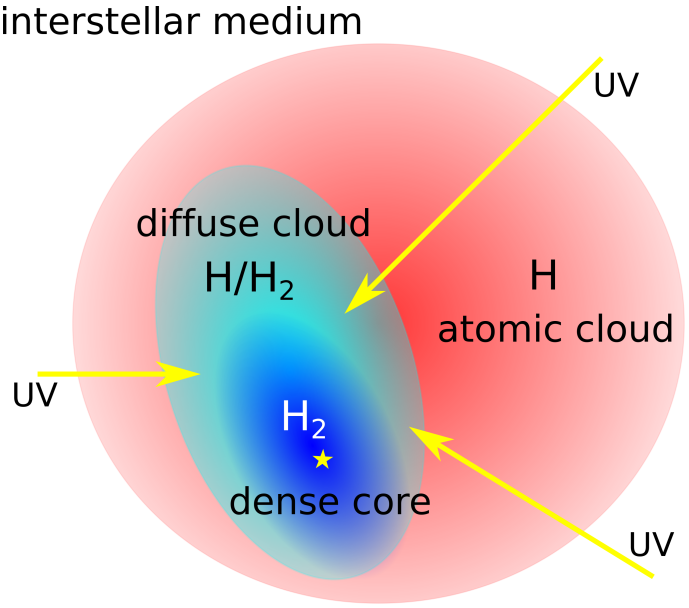

Figure 1. A schematic illustration of an atomic cloud (red), a diffuse cloud (cyan) and a dense core (blue). H_2 molecule is formed in the relatively dense region where the interstellar UV radiation is shielded. Stars are formed in much denser region (dense core) by the gravitational collapse.

Since atomic clouds are almost transparent to the UV radiation due to their low density, H_2 molecules, if even formed, are quickly photodissociated in atomic clouds. On the other hand, H_2 molecules can survive in molecular clouds, where the UV radiation is shielded. Dense cores in molecular clouds are subject to gravitational contraction toward star formation. During this process, various molecular species, such as radicals (OH, CH, NH), carbon-chain molecules (C_2H, C_4H, c-C_3H_2), organic molecules (CH_3OH, CH_3CONH_2, HCOOH), and ions (HCO^+, $H_3{}^+$) are formed through chemical reactions in the gas phase and/or on surfaces of dust grains.

A gas kinetic temperature (T_k) of molecular clouds is determined by a balance between the heating and cooling. Main heating sources are interstellar UV radiations and cosmic rays, whereas the cooling is dominated by spectral emission of gaseous species (mainly CO and C^+) and thermal continuum emission of dust grains. Since diffuse clouds are exposed to interstellar UV radiation to some extent, their gas kinetic temperature depends on the strength of the UV radiation. The temperature tends to be higher for lower H_2 density conditions due to less shielding of the UV radiation, and it typically ranges from 30 to 100 K. In contrast, the UV heating effect is negligible in a denser part ($n(H_2)$ $> 10^3$–10^4 cm^{-3}), where the major heating sources are energy introduced by cosmic rays and that released by gravitational collapse. In such a dense gas, a cooling by the rotational transitions of CO and dust thermal radiation is so efficient due to frequent molecule-molecule and molecule-dust collisions that the gas kinetic temperature is generally as low as $\sim$10 K. Because of a low gas kinetic temperature, molecular clouds are difficult to be observed directly in the optical or near-infrared emissions, although they have recognized as dark patches obscuring the visible light of background stars. Instead, they have been studied by observations of the thermal continuum emission from cold dust grains in the mid- and far-infrared region as well as the rotational transitions of molecules in the radio region.

In this study, we develop a new method to explore the molecular-cloud formation by radio astronomical observations with single-dish telescopes and interferometers. So far, distributions of molecular clouds have been studied mainly by observing the rotational transitions of CO. Although its abundance is four orders of magnitude lower than H_2, it generally gives a bright emission in molecular

clouds. It should be noted that the most abundant molecule in molecular clouds, H_2, is difficult to be observed. Since H_2 is a homonuclear molecule and has no electric dipole moment, the electronic dipole transition does not occur between the rotational levels of H_2. Although the weak electronic quadrupole transition is allowed, it is too faint to be observed in cold molecular clouds. Thus CO, which is the second abundant molecule next to H_2, has extensively been observed as a tracer of molecular clouds.

Dame et al. (1987, 2001) conducted large-scale mapping observations of the CO ($J = 1$–0) line in the entire of the Galactic plane (Figure 2). They found that molecular clouds are concentrated on the Galactic spiral arms and the ring-like region around the Galactic center (so-called molecular ring). Zuckerman & Palmer (1974) estimated a star-formation rate (R_{SF}) in the Galaxy from a molecular mass determined by CO observations ($M_{mol} \sim 10^9$ $M_\odot$), assuming that stars are formed within a free-fall time:

$$t_{ff} = \left(\frac{3\pi}{32G\rho}\right)^{1/2} \sim 4 \times \left(\frac{10^2}{n}\right)^{1/2} \mathrm{Myr}. \quad (1)$$

They concluded that R_{SF} ($\sim M_{mol}/t_{ff} \sim 10^3$ $M_\odot \mathrm{yr}^{-1}$) is about two order of magnitude lower than the observed value inferred from statistical observations of O and B stars ($\sim$1 $M_\odot$ yr^{-1}) (Biermann & Tinsley 1974). The low star-formation rate requires a mechanism that suppresses star formation in molecular clouds, such as turbulence and/or magnetic field, although it is still controversial.

Structures and kinematics of molecular clouds have extensively been studied by observing the rotational transitions of CO and its isotopologues (^{13}CO and C^{18}O). In particular, nearby molecular clouds such as Taurus ($d = 137$ pc; Sunada & Kitamura 1999; Narayanan et al. 2008; Goldsmith et al. 2008), Lupus ($d = 155$ pc; Tachihara et al. 1996, 2001; Tothill et al. 2009), Ophiuchi ($d =$119 pc; Loren 1989a,b) and Orion ($d = 400$ pc; Castets et al. 1990; Heyer et al. 1992; Plume et al. 2000) are good targets for such studies. The total mass of each molecular cloud ranges from 10^3 to 10^6 $M_\odot$. The observed velocity dispersions of the spectral lines of CO (and other molecules as well) are generally larger than the thermal Doppler broadening:

$$\Delta V_{\mathrm{FWHM}} = \sqrt{\frac{8k_bT\ln 2}{m}}, \quad (2)$$

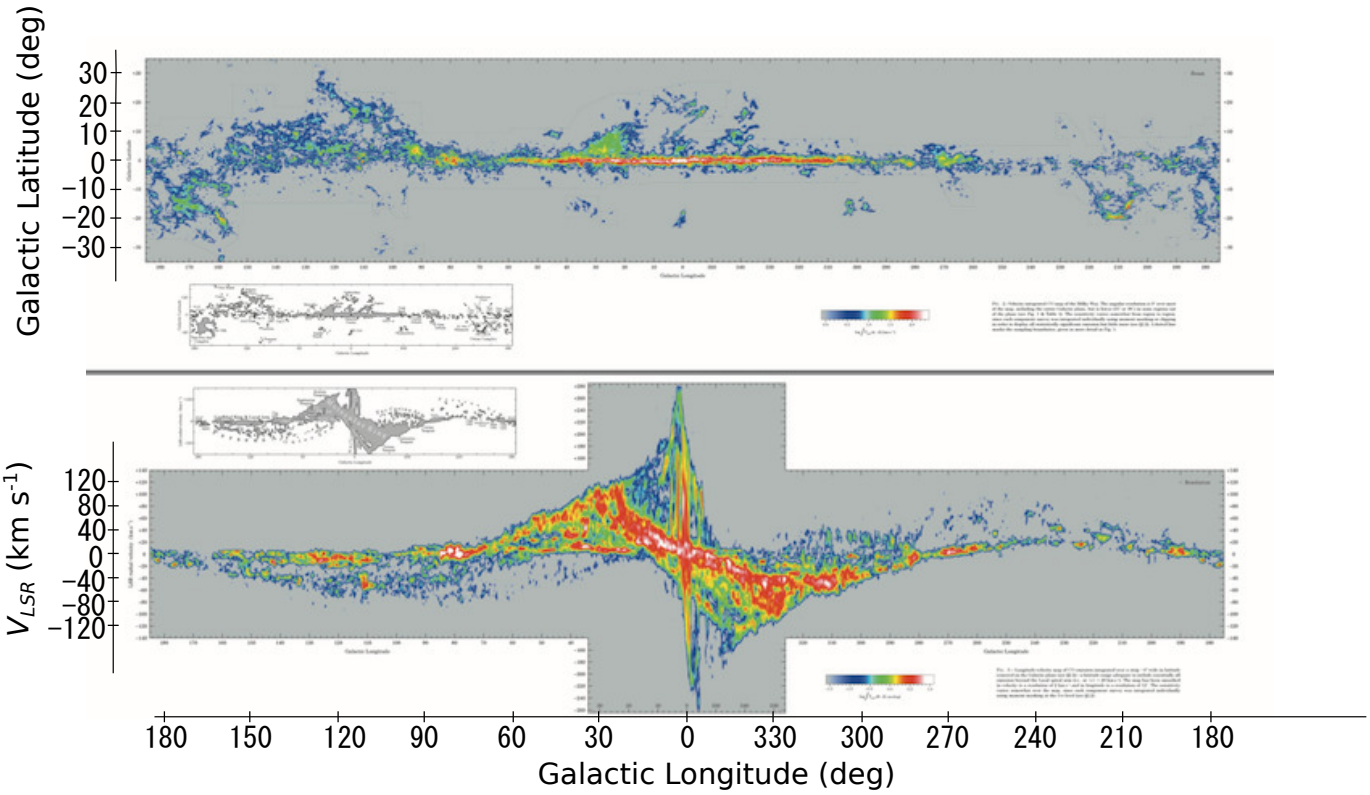

Figure 2. Top and bottom panels show the integrated intensity map and the position-velocity diagram of the CO emission, respectively, along the galactic longitude (l) observed in the entire of the Galaxy by Dame et al. (2001). As shown in the bottom panel, molecular clouds are concentrated on the so-called molecular ring around the Galactic center, which are observed in high red-shifted and blue-shifted velocities at $l \sim 0°$–$30°$ and $l \sim 330°$–$360°$, respectively. Molecular clouds are also distributed in the galactic spiral arms, such as the Perseus Arm seen in $l \sim 40°$–$160°$ ($V_{LSR} \sim -40$ – -100 km s^{-1}) and $l \sim 200°$–$270°$ (V_{LSR} $\sim$ 40–100 km s^{-1}), and the Carina Arm seen in $l \sim 290°$–$320°$ ($V_{LSR} \sim 40$ km s^{-1}). Note that the low velocity components observed in the entire of the galactic longitude originate from nearby molecular clouds associated with the Gould's Belt such as Aquila, Taurus, Lupus, Ophiuchi and Orion.

which equals to $\sim$0.1 km s^{-1} at 10 K. The broader linewidth suggests that molecular clouds are generally turbulent.

Molecular clouds are birth places of new stars. Figure 3 shows the positions of the pre-main-sequence stars observed toward the Taurus molecular cloud, overlaid on the H_2 column density map derived from the CO integrated intensity map observed toward the same region (Goldsmith et al. 2008). Most of the young stars, which are represented by diamonds and squares, are located in the

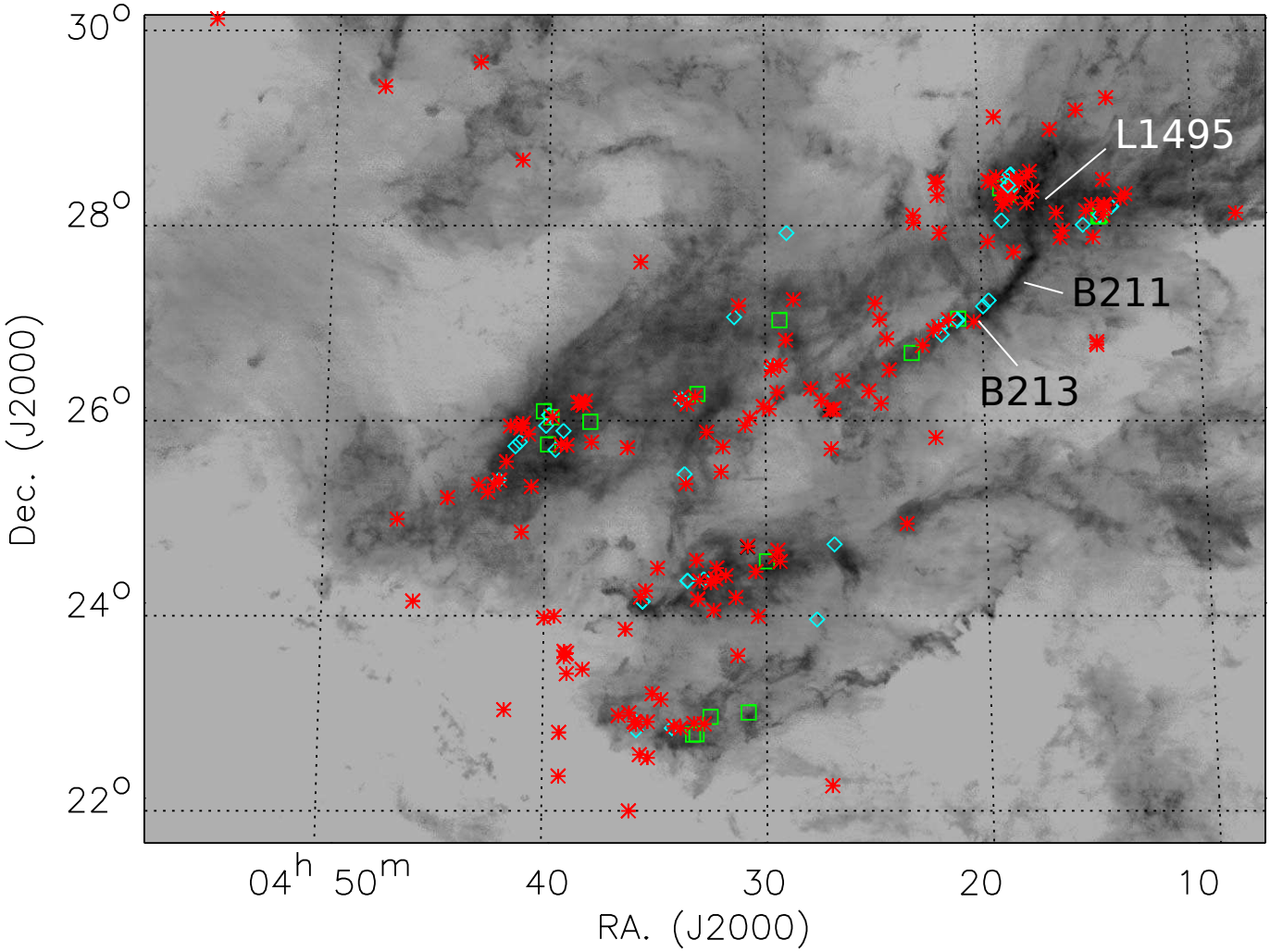

Figure 3. The H_2 column density map of the Taurus molecular cloud derived from the CO integrated intensity map observed with FCRAO (Five College Radio Astronomical Observatory) telescope (Goldsmith et al. 2008). The cyan diamonds, the green squares and red asterisks represent the positions of pre-main-sequence stars in the stage of extended/nebulous protostars, Class I or younger stars, and T Tauri stars, respectively, according to Goldsmith et al. (2008).

regions with a relatively high H_2 column density, suggesting that a star formation indeed occurs in dense parts of molecular clouds. In addition, stars are remarkably aligned along the straight structure in the B213 region ($(\alpha,\ \delta) \sim (4^h22^m0^s,\ 27°0'0'')$), whereas no star is found in the nearby filament in the B211 region $(\alpha,\ \delta) \sim (4^h18^m0^s,\ 27°30'0'')$). It is explained by different evolutionary stages of these regions: B213 is more evolved than B211, and star-formation has already started. Hacar et al. (2013) confirmed this picture on the basis of the mapping observations of the $C^{18}O$ and N_2H^+ lines

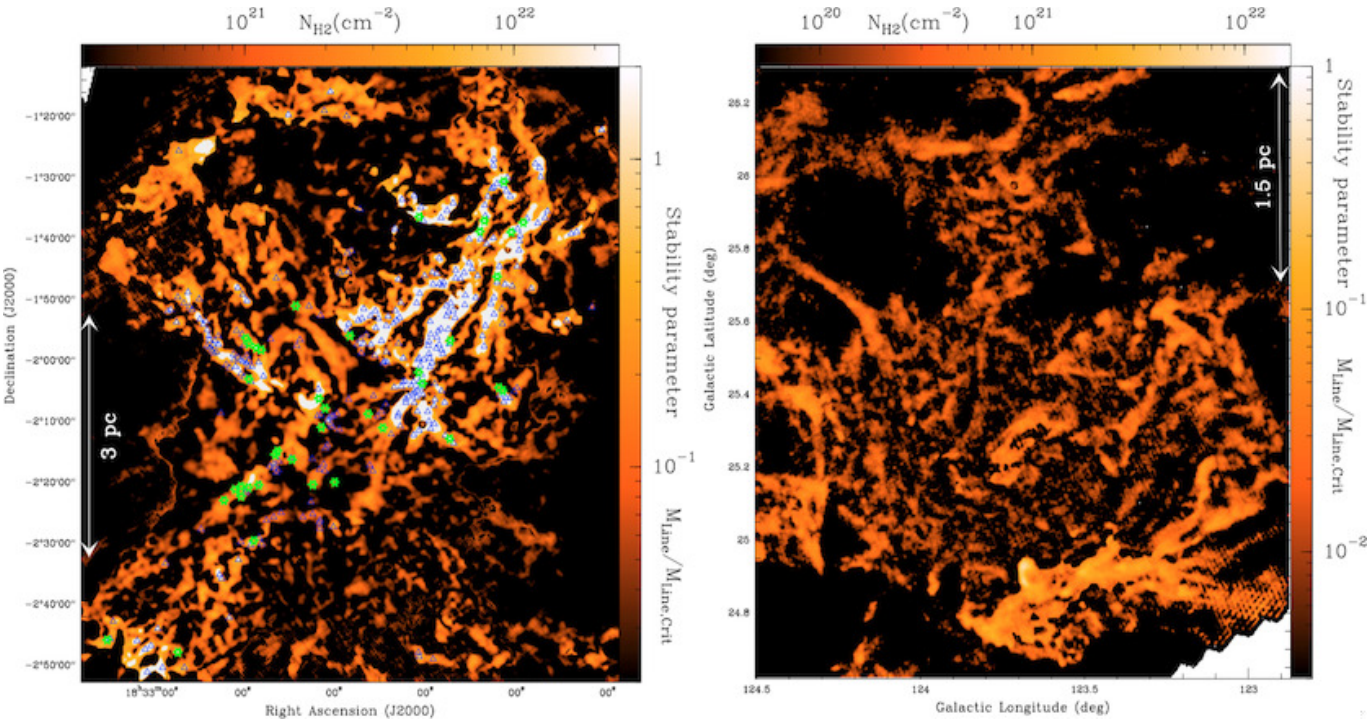

Figure 4. The H_2 column density map of (left) the Aquila cloud ($d = 260$ pc) and (right) the Polaris cloud ($d = 150$ pc) derived from the Herschel SPIRE/PACS data obtained in the Gould's belt survey (André et al. 2010). Various filamentary structures and dense cores along the filaments are extensively observed in the both sources.

toward the large-scale filamentary structure elongated from B213 to L1495 (Figure 3). They reported the bright $C^{18}O$ line and the faint N_2H^+ line in the B211 region, which are contrary to the bright N_2H^+ line and the faint $C^{18}O$ line in the B213 region. Since the N_2H^+ line generally traces cold and dense cores, where CO is frozen out onto dust grains, these results suggest that the B213 region is indeed chemically more evolved than B211. They also studied the detailed velocity structure of the B213/B211/L1495 filament, and identified velocity-coherent sub-filaments, which have typically 0.5 pc in length, within large-scale filaments. In addition, they reported that dense cores tend to be clustered in a certain region, rather than uniformly distributed along the filament, suggesting that dense cores are formed by fragmentation of the sub-filaments.

Such a formation scenario of dense cores and stars within a filamentary structure has extensively been studied, particularly after the results of the Herschel Gould's belt survey with Herschel Space Observatory (André et al. 2010). The observed large-scale far-infrared continuum map revealed the

ubiquity of filamentary structures in molecular clouds (Figure 4), as well as dense cores mostly associated with the filaments. Recently, Arzoumanian et al. (2018) studied a filamentary structure in the L1495 region (Figure 3) by using their CO, ^{13}CO and C^{18}O observations with the Nobeyama 45-m radio telescope. They identified several extended structures surrounding the filament by carefully inspecting the line-of-sight velocity structures on the velocity channel maps and the self-absorption features in the spectra. They argued that the filament repeatedly interacts with the sheet-like extended (diffuse) structures, and such interactions might trigger the star formation there. As explained above, the spectral lines of CO have extensively been observed to study a large-scale structure of molecular clouds as well as distributions and formations of dense cores and filaments. Thus, the CO observations play central roles in studies on structure, kinematics, and formation processes of molecular clouds.

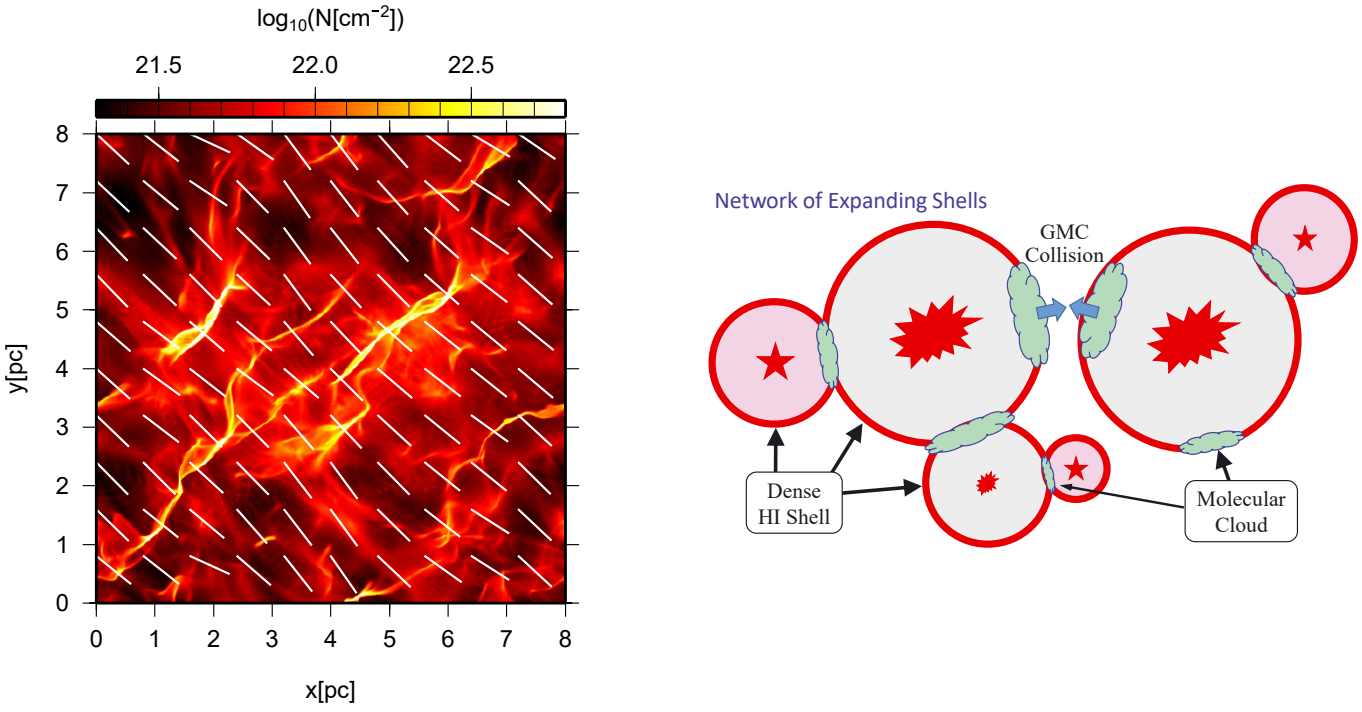

Figure 5. (left) The H column density map determined by MHD (Magnetohydrodynamics) numerical calculations by Inutsuka et al. (2015). The white lines represent the mean magnetic field vector. Filamentary structures are apparently almost perpendicular to the magnetic field direction. (right) A schematic illustration of the molecular-cloud formation caused by multiple compression in the expanding H I shells (Inutsuka et al. 2015).

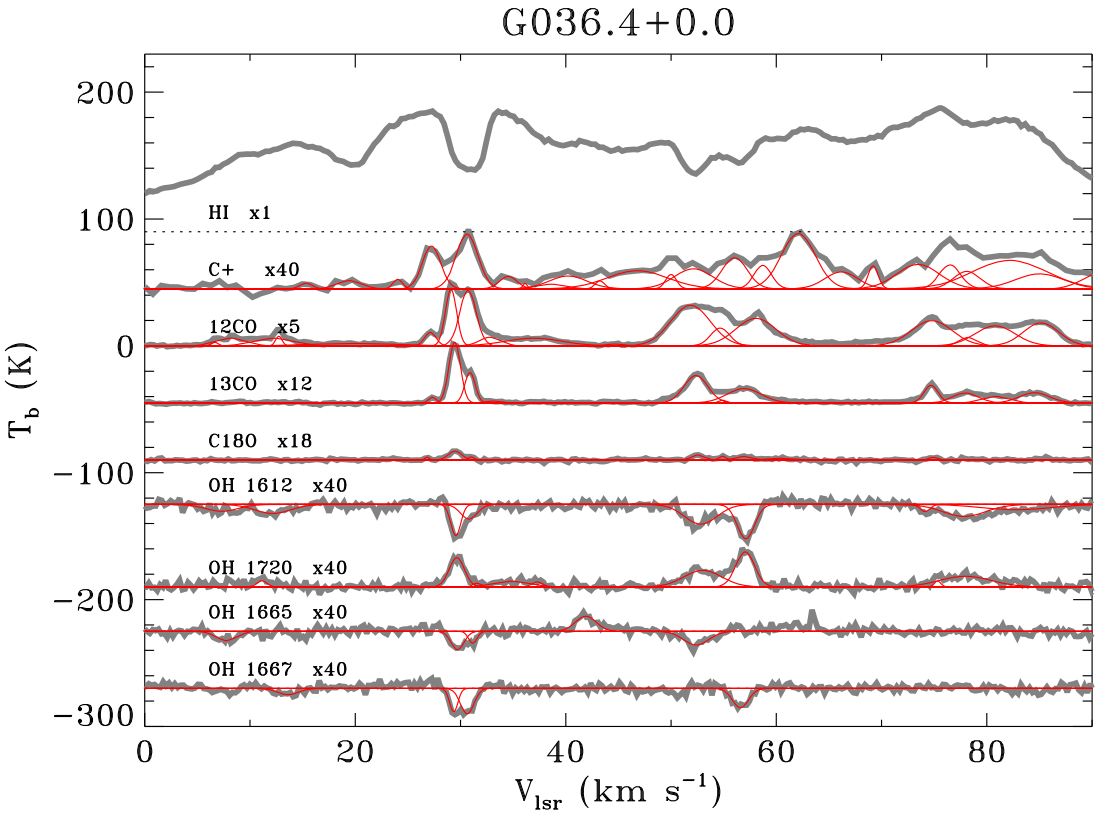

Figure 6. The spectra of the 1667 MHz, 1665 MHz, 1720 MHz and 1612 MHz lines of OH, $C^{18}O$, ^{13}CO, CO, C^+ and [H I] observed toward the Galactic plane cloud G036.4+0.0.

Spatial distributions and spectral lines of CO are often compared with those of the so-called 21 cm transition of the H atom ([H I]). It is the transition between the hyperfine levels due to proton-spin in the ground electronic state of the H atom, and is known as a good tracer of atomic gas (Kalberla et al. 2005; Peek et al. 2011; Winkel et al. 2016). Molecular gas traced by CO is often surrounded by an extended [H I] gas which has larger velocity dispersion than CO, suggesting that molecular clouds are formed by compression of atomic gas (Tachihara et al. 2001; Heiner & Vázquez-Semadeni 2013; Pineda et al. 2013; Duarte-Cabral et al. 2015). Such a scenario is confirmed by numerical calculations simulating molecular-cloud formation from atomic gas by hydrodynamic calculations (Inoue & Inutsuka 2012; Inutsuka et al. 2015). Inutsuka et al. (2015) reported that molecular clouds are formed in the interface of so-called H I shells, which are expanding shell-like dense structures in atomic clouds associated with supernova remnants or H II regions, as schematically illustrated in Figure 5 (right). They presented that a relatively cold ($T_k < 100$ K) and dense atomic gas is

readily formed in H I shells, and molecular clouds can be formed by multiple compression of these cold atomic gas in the interface region. As shown in the left panel of Figure 5, the multi-compression scenario well reproduces the filamentary structures in molecular clouds, according to the numerical simulations by Inutsuka et al. (2015). Hence, understanding the interface of an atomic gas and a molecular gas is closely related to the structure and the formation of molecular clouds as well as subsequent dense-core and star-formation processes.

Nevertheless, it is still controversial how atomic clouds are evolved into molecular clouds, since such transition regions are not well traced by neither CO nor [H I] lines. This is because that most CO molecules are photodissociated by the interstellar UV field in such a diffuse part, whereas hydrogen mostly becomes H_2 there. The diffuse molecular gas which is not well traced by CO emission is called CO-dark molecular gas. About a half of molecular cloud mass comes from the CO-dark region according to recent numerical calculations (Smith et al. 2014; Glover & Smith 2016). This suggestion emphasizes an importance of tracing a CO-dark gas in molecular-cloud formation. Although observational studies of a CO-dark gas are rather difficult, it would be traced by some atoms, ions, or molecules which appear in chemical processes in the formation of CO, such as CH (Sakai et al. 2012; Xu & Li 2016), C (Maezawa 2000; Kamegai et al. 2003; Pineda et al. 2017), C^+ (Tang et al. 2016; Mookerjea et al. 2016) and, OH (Ebisawa et al. 2015; Allen et al. 2015; Xu et al. 2016; Tang et al. 2017). For example, Tang et al. (2017) conducted observations of the [H I], CO, OH and C^+ lines toward many sources near the Galactic plane, and reported that about 18 % of the clouds identified with OH are CO-dark. The C^+ ion also traces a CO-dark gas, whereas its detection rate is generally lower than OH, according to Tang et al. (2017). They presented that a denser part of a CO-dark molecular gas is not well traced by C^+, since C^+ rather traces an atomic gas and a diffuse molecular gas where the UV radiation is not well shielded. On the other hand, OH can trace a diffuse molecular gas as well as much denser parts including dense cores, suggesting that OH is a better tracer of a CO-dark molecular gas. Figure 6 shows representative spectra observed by Tang et al. (2017) exhibiting that OH and C^+ traces the CO-dark gas. For instance, the $\sim$41.9 km s^{-1} component is seen in OH, whereas CO and its isotopologues lines are almost absent. These

studies are essentially important to understand the evolution from atomic gas to molecular gas, that is essential part of molecular-cloud formation. In this study, we tackle this long-standing problem with radio observations of the OH 18 cm transition.

2.2 The OH 18 cm transition

The 18 cm transition of hydroxyl radical (OH) was the first spectral line from interstellar molecules detected in the radio wavelength region (Weinreb et al. 1963). Since OH is easily formed in diffuse clouds via the following oxygen chemistry (Hollenbach et al. 2009), it is relatively abundant in various clouds including diffuse clouds. A neutral O atom, which is a main form of oxygen in diffuse clouds, is ionized by the following reactions with H^+ and ${H_3}^+$:

$$O + H^+ \rightarrow O^+ + H \tag{3}$$

$$O + {H_3}^+ \rightarrow OH^+ + H_2. \tag{4}$$

${OH_3}^+$ is formed from O^+ and OH^+ through successive reactions with H_2:

$$O^+ + H_2 \rightarrow OH^+ + H \tag{5}$$

$$OH^+ + H_2 \rightarrow {OH_2}^+ + H \tag{6}$$

$${OH_2}^+ + H_2 \rightarrow {OH_3}^+ + H. \tag{7}$$

Then, ${OH_3}^+$ forms H_2O and OH by electron recombination reactions:

$${OH_3}^+ + e \rightarrow H_2O + H \tag{8}$$

$$\rightarrow OH + H_2 \tag{9}$$

$$\rightarrow OH + H + H \tag{10}$$

$$\rightarrow O + H_2 + H. \tag{11}$$

An OH molecule returns to an O atom by photodissociation under the UV radiation:

$$OH + h\nu \rightarrow O + H. \tag{12}$$

Numerical calculations incorporating the above oxygen chemistry have been conducted to estimate the abundance of OH relative to hydrogen atom ($X(\mathrm{OH})$) in diffuse clouds. Hollenbach et al. (2012)

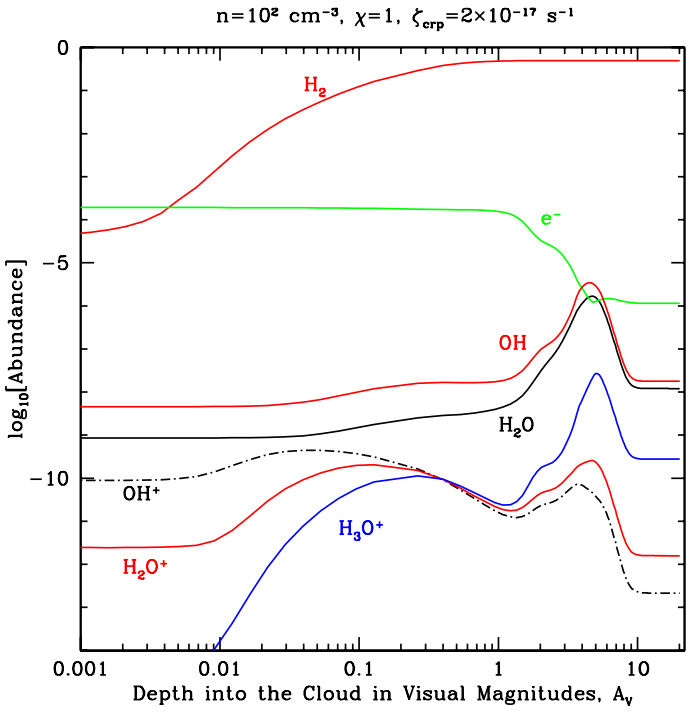

Figure 7. Abundances of molecules as a function of the visual excitation (A_v) equivalent to the depth into the cloud calculated by Hollenbach et al. (2012). The diffuse-cloud condition is assumed for the density.

showed that the OH abundance is almost constant (10^{-7}) over a wide range of the visual extinction (A_v) between 0.001 and 1, and it has a peak ($X(\mathrm{OH}) \sim 10^{-5}$) at $A_v \sim 5$, according to their chemical model calculations assuming a diffuse cloud condition (Figure 7). Draine & Katz (1986) conducted chemical model calculations assuming a gas compressed by a MHD (Magnetohydrodynamics) shock in diffuse clouds, and reported that the OH abundance is enhanced as high as 5×10^{-5} in a shock compressed gas. These studies suggest that OH indeed exists abundantly in diffuse clouds, and it also traces the transition region in which molecular-cloud formation occurs. Since OH is a intermediate molecule in the formation process of CO via following chemical reactions (van Dishoeck & Black 1988),

$$\mathrm{C^+ + OH \rightarrow CO^+ + H} \tag{13}$$

$$\rightarrow \mathrm{CO + H^+} \tag{14}$$

$$\mathrm{CO^+ + H_2 \rightarrow HCO^+ + H} \tag{15}$$

$$\mathrm{HCO^+ + e \rightarrow CO + H,} \tag{16}$$

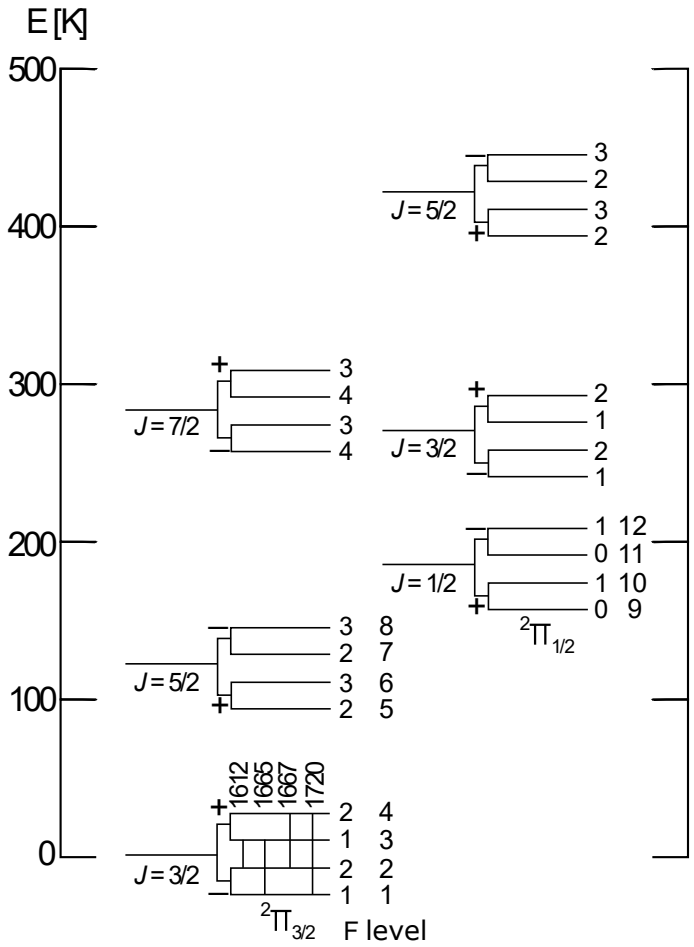

Figure 8. The rotational energy level structure of OH. The display of the fine and hyperfine structure levels is schematic and the separations of the split energy levels are not drawn to scale.

OH is considered to trace a diffuse part of molecular clouds, which cannot be well traced by CO, i.e. CO-dark molecular gas.

In astronomical observations, OH has been observed in its rotational transitions in the far-infrared (FIR) wavelengths region and the Λ-type transitions in the radio wavelengths region. In this study, we observe the one of the latter transitions, the OH 18 cm transition. Figure 8 shows the rotational energy diagram of OH, which consists of the two rotational ladders of the $^2\Pi_{3/2}$ and $^2\Pi_{1/2}$ states, where the state is represented by $^{2\Sigma+1}\Pi_\Omega$ ($\Omega = \Sigma + \Lambda$). Here, Σ and Λ denote the components of the electronic spin angular momentum ($\boldsymbol{S}$, $|\boldsymbol{S}| = 1/2$) and orbital angular momentum ($\boldsymbol{L}$, $|\boldsymbol{L}| = 1$), respectively, projected to the molecular axis (O-H bond). The $^2\Pi_{3/2}$ and $^2\Pi_{1/2}$ ladders are caused by the spin-orbit interaction between $\boldsymbol{S}$ and $\boldsymbol{L}$, where Σ and Λ are parallel ($|\Omega| = 3/2$) and anti-parallel

($|\Omega| = 1/2$) to each other, respectively. It should be noted that $|\boldsymbol{S}| = 1/2$ and $|\boldsymbol{L}| = 1$ originate from a single unpaired electron of the p_π orbital in the OH radical. F and J in Figure 8 represent the total angular momentum and that excluding nuclear spin of proton ($\boldsymbol{I}$), respectively, which can be written as $\boldsymbol{F} = \boldsymbol{R} + \boldsymbol{L} + \boldsymbol{S} + \boldsymbol{I}$, and $\boldsymbol{J} = \boldsymbol{R} + \boldsymbol{L} + \boldsymbol{S}$, respectively, in a vector form. $\boldsymbol{R}$ is the angular momentum of end-over-end molecular rotation.

Since OH is a relatively light molecule, energy separations between the rotational levels are quite large due to its rapid rotation, which fall in the FIR wavelength regime. For example, the rotational transition from $^2\Pi_{3/2}$ $J = 5/2$ to $^2\Pi_{3/2}$ $J = 3/2$ and that from $^2\Pi_{1/2}$ $J = 3/2$ to $^2\Pi_{1/2}$ $J = 1/2$ appear at the wavelengths of 120 μm and 163 μm, respectively. Spectroscopic observations of the rotational transitions of OH were studied by the airborne and space telescopes in the FIR wavelength region, KAO (Kuiper Airborne Observatory) and ISO (Infrared Space Observatory), respectively. However, their spatial resolution and sensitivity were limited. The PACS spectrometer of the Herschel Space Telescope allowed much better spatial resolution ($\sim$10 arcsec) covering a frequency range from 60 to 210 μm, although its velocity resolution is still poor (150–200 km s^{-1}) (Figure 9). The heterodyne spectrometer HIFI of Herschel provided much better velocity resolution of 0.3 km s^{-1}, but its frequency range only covers the 163 μm transition. SOFIA (Stratospheric Observatory for Infrared Astronomy) is now available to observe the rotational transition of OH (119 μm and 163 μm) with maximum velocity resolution lower than 0.01 km s^{-1} (Figure 10). So far, these transitions have mostly been observed toward high-mass star forming regions, since their upper state energies are higher than 100 K from the ground state. On the other hand, they are fairly weak and difficult to be observed in diffuse clouds, although there have been a few studies detecting these transitions in absorption. The OH lines of the Galactic ISM are observed in absorption against the strong background FIR continuum emission from hot cores with SOFIA (Wiesemeyer et al. 2016).

On other hand, each rotational energy level is slightly split into two levels, as indicated by + and - in Figure 8. This is called as Λ-type doubling, that is the energy split caused by the coupling of molecular rotation ($\boldsymbol{R}$) and the orbital angular momentum ($\boldsymbol{L}$), as schematically explained in Figure 11. This split is rather small in comparison with the energy gaps between rotational energy levels.

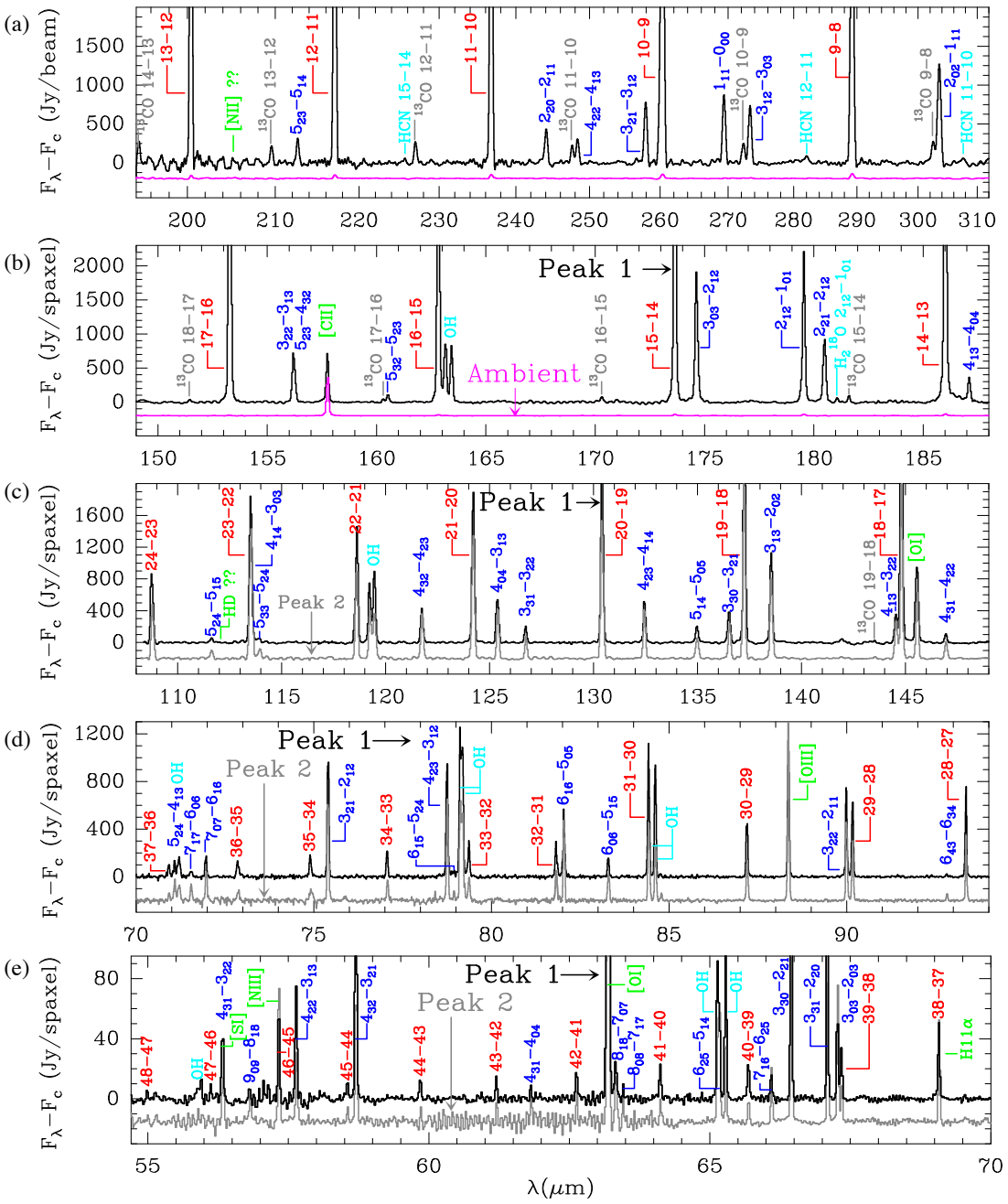

Figure 9. The Herschel SPIRE (a) and PACS ((b)–(e)) spectra observed toward the Orion BN/KL by Goicoechea et al. (2015). The rotational transitions of OH at wavelengths of 163 μm ($^2\Pi_{1/2}$ $J = 3/2$ – $^2\Pi_{1/2}$ $J = 1/2$), 119 μm ($^2\Pi_{3/2}$ $J = 5/2$ – $^2\Pi_{3/2}$ $J = 3/2$), 84 μm ($^2\Pi_{3/2}$ $J = 9/2$ – $^2\Pi_{3/2}$ $J = 5/2$), 79 μm ($^2\Pi_{1/2}$ $J = 1/2$ – $^2\Pi_{3/2}$ $J = 3/2$), 71 μm ($^2\Pi_{1/2}$ $J = 7/2$ – $^2\Pi_{1/2}$ $J = 5/2$), and 65 μm ($^2\Pi_{3/2}$ $J = 9/2$ – $^2\Pi_{3/2}$ $J = 7/2$) are observed.

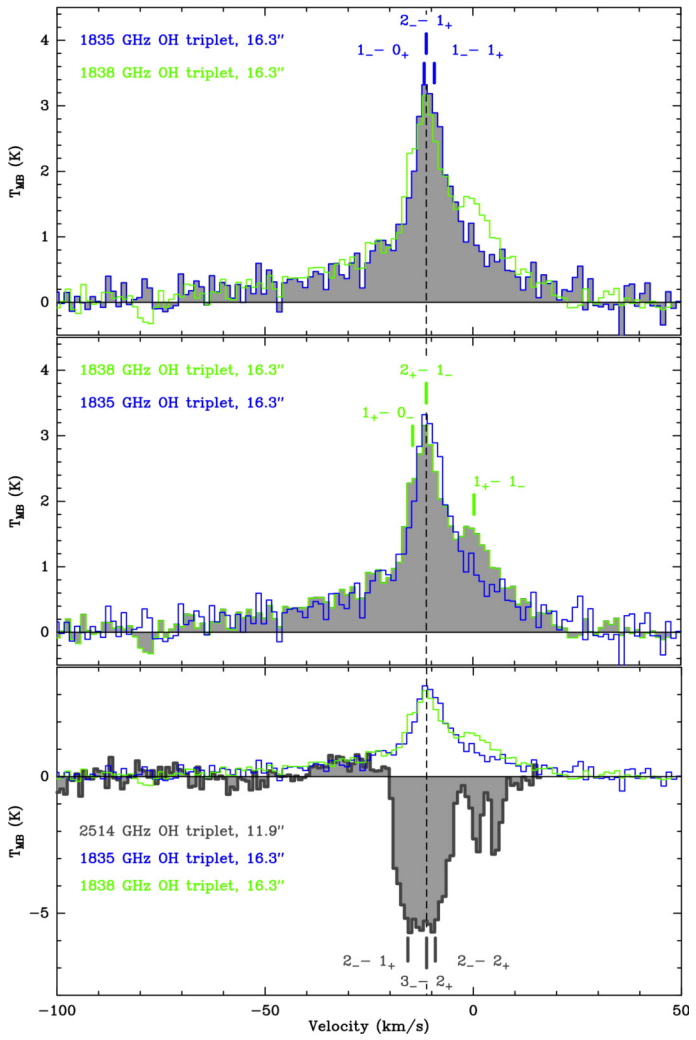

Figure 10. The rotational transitions of OH (163 μm and 119 μm) observed toward the Cepheus A with SOFIA (Gusdorf et al. 2016).

In case of OH, transitions between the Λ-type doubling levels in the same rotational energy state appear in the radio wavelength regime. In particular, the Λ-type doubling transition in the ground rotational state ($^2\Pi_{3/2}$ $J = 3/2$) emits photons at the wavelength of 18 cm. Therefore, this transition is called the OH 18 cm transition. Each Λ-type doubling level is further split into two hyperfine levels through the 'spin-spin' interaction between the nuclear spin ($\boldsymbol{I}$, $|\boldsymbol{I}|$=1/2) of the proton and the electronic spin ($\boldsymbol{S}$). For example, the two Λ-type doubling levels in the $J = 3/2$ $^2\Pi_{3/2}$ ground rotational state have two hyperfine sub-levels with $F = 2$ and 1 each, where $\boldsymbol{S}$ and $\boldsymbol{I}$ are parallel and anti-parallel to each other, respectively. Since the selection rule is $\Delta F = 0, \pm 1$, the OH 18 cm

transition has four hyperfine structure (hfs) components at frequencies near 1612, 1665, 1667 and 1720 MHz (left bottom of Figure 8), as summarized in Table 1. The same feature is seen in the other Λ-type transitions. The 1665 MHz and 1667 MHz lines, where F is unchanged in the transition, are called main lines, while the 1612 MHz and 1720 MHz lines, where F is changed by ± 1, are called satellite lines. Since the upper state energy of the OH 18 cm transition is as low as 0.1 K, OH molecules are easily excited to the upper state by collisions with H_2 even in cold ($\sim$ 10 K) molecular clouds. Furthermore, the critical density of this transition is quite low (< 1 cm^{-3}), suggesting that the OH 18 cm transition can trace diffuse clouds with relatively low H_2 density (10^2 cm^{-3}), as shown later in Chapter 4. Therefore, the OH 18 cm transition has been a unique probe of diffuse and dense interstellar clouds, as well as late-type stars and external galaxies (e.g. Harju et al. 2000; Caswell 2004; Hoffman et al. 2005; Wolak et al. 2012; Darling & Giovanelli 2002).

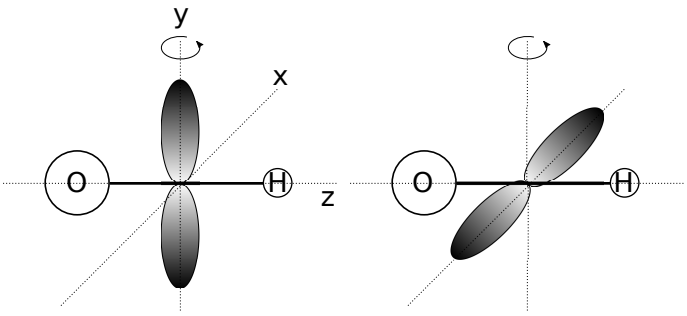

Figure 11. Schematic illustration of the the Λ-type doubling. For OH, the two spatial distribution of the unpaired electron are possible, where they are parallel and perpendicular to the rotation axis (y-axis). These states have slightly different rotation energies of OH.

It is well known that the relative populations of the hyperfine structure (hfs) levels can attain values that deviate from intrinsic values attained in Local Thermodynamic Equilibrium (LTE), i.e., 1612:1665:1667:1720 MHz = 1:5:9:1 (Table 1). This is caused by an interplay of excitation and de-excitation through rotationally excited states ($^2\Pi_{3/2}$ J=5/2 and $^2\Pi_{1/2}$ J=1/2) (Elitzur 1976; van Langevelde et al. 1995). In fact, the 18 cm transition of OH often displays maser emission in star-forming regions (mainly the 1665/1667 lines), supernova remnants (only the 1720 MHz line), and the circumstellar envelopes of mass losing evolved stars (mainly the 1612 MHz line) (Gundermann et al.

Table 1. Frequencies and line strengths of the OH 18 cm transition ($^2\Pi_{3/2}J = 3/2$).

Transition	ν [MHz][a]	$S\mu^2$ [b]	$S\mu^2/S\mu^2{}_{1612}$
$F = 1 - 2$	1612.2310	0.79	1.00
$F = 1 - 1$	1665.4018	4.0	5.06
$F = 2 - 2$	1667.3590	7.1	8.99
$F = 2 - 1$	1720.5300	0.79	1.00

NOTE—[a] Darling (2003). [b] Calculated from the Einstein's A coefficients tabulated in Leiden Atomic and Molecular Database (LAMDA) (Schöier et al. 2005).

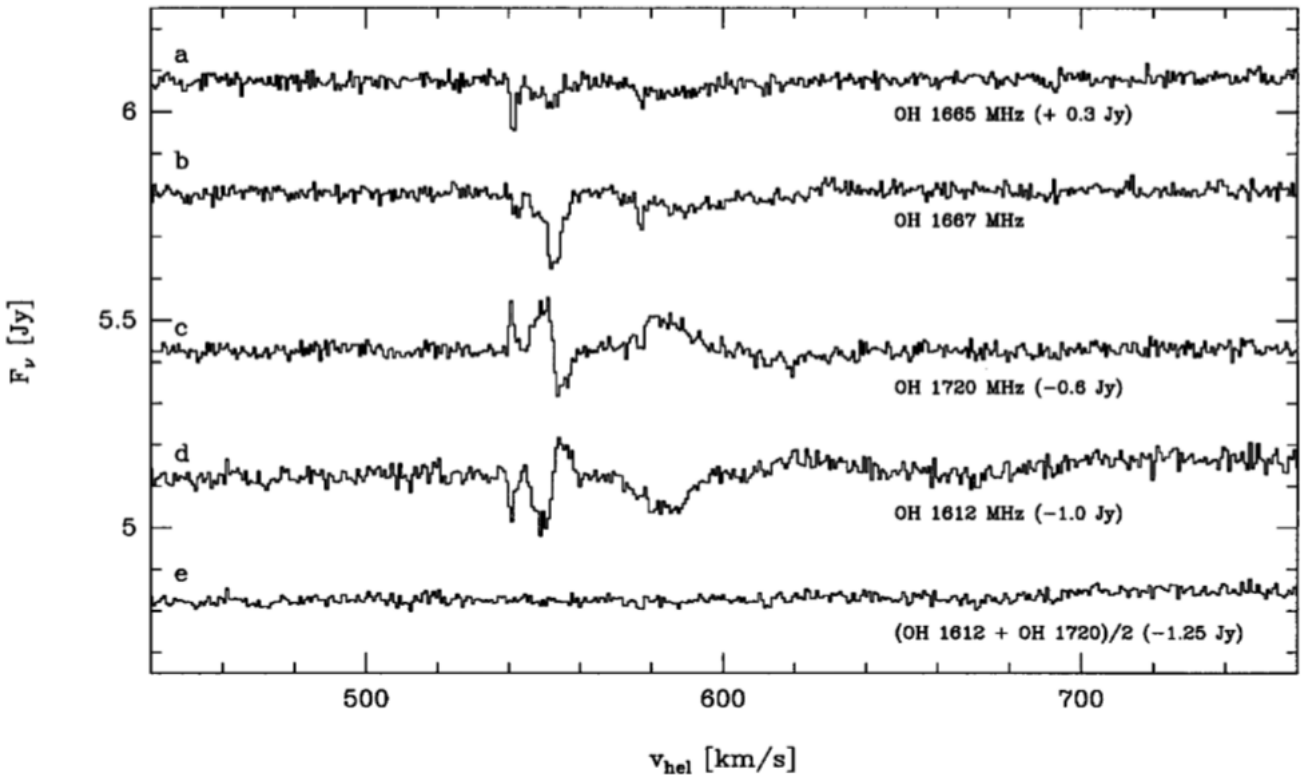

Figure 12. The spectra of the OH 18 cm transition observed toward the Centaurus A (van Langevelde et al. 1995) with ATCA which show clear conjugate features of the satellite lines. Namely, the 1612 and 1720 MHz lines appear in absorption and emission, respectively, in the V_{LSR} of ∼540, 550 and 590 km s^{-1}, whereas they show emission and absorption, respectively, in the V_{LSR} of ∼560 km s^{-1}.

1965; Weaver et al. 1965; Cohen 1995). Furthermore, so-called "conjugate" behavior of the 1612 MHz and 1720 MHz satellite lines, which appear in absorption and emission, respectively, has been

reported for sources with bright background continuum (van Langevelde et al. 1995; Weisberg et al. 2005; Kanekar et al. 2004). Observations of the OH 18 cm transition toward quiescent molecular clouds have also been conducted extensively (e.g. Heiles 1968; Cudaback & Heiles 1969; Crutcher 1973; Myers et al. 1978). Mattila et al. (1979) carried out observations including the satellite lines toward L134, and reported that the 1612 MHz line is fainter than the 1720 MHz line. Even more extreme differences between the two satellite lines were observed toward the HII region W40 by Crutcher (1977). They found that the 1612 MHz line shows absorption at velocities at which the 1720 MHz line shows emission. This "conjugation" of these two lines was also observed toward the diffuse gas in the line of sight toward the active galactic nucleus Centaurus A (van Langevelde et al. 1995), as shown in Figure 12. In addition, the OH 18 cm transition has also been used to measure the magnetic field strength of molecular clouds by using the Zeeman effect (e.g. Crutcher et al. 1993; Troland & Crutcher 2008).

As for astrochemical interest, Turner & Heiles (1974) investigated the relation of the OH abundance to the visual extinction in two regions of the Taurus molecular cloud. Harju et al. (2000) conducted sensitive mapping observations of the OH 18 cm transition toward the filamentary Taurus Molecular Cloud-1 (TMC-1) in Heiles Cloud-2 (HCL2) with the Effelsberg 100 m telescope. This filament is famous for showing significant chemical differentiation: carbon-chain molecules are abundant in the south-eastern part of the filament, whereas NH_3 is abundant in the north-western part (e.g. Little et al. 1979; Hirahara et al. 1992). This chemical differentiation is naturally explained in terms of an chemical evolutionary effect (Hirahara et al. 1992; Suzuki et al. 1992). Harju et al. (2000) investigated the OH/$C^{18}O$ abundance ratio along the ridge from such a chemical point of view, and found that it is almost constant over the ridge. This indicates the almost constant abundance of OH during cloud evolution. At the same time, they reported the intensity anomaly of the hyperfine components. The 1612 MHz and the 1720 MHz lines, both in emission, are slightly brighter and fainter, respectively, than expected for LTE (Figure 13). They argued that this anomaly is due to the contribution of the far IR continuum emission from dust. However, the observed region is limited to the small area of the TMC-1 ridge, and more observations are required to investigate the origin

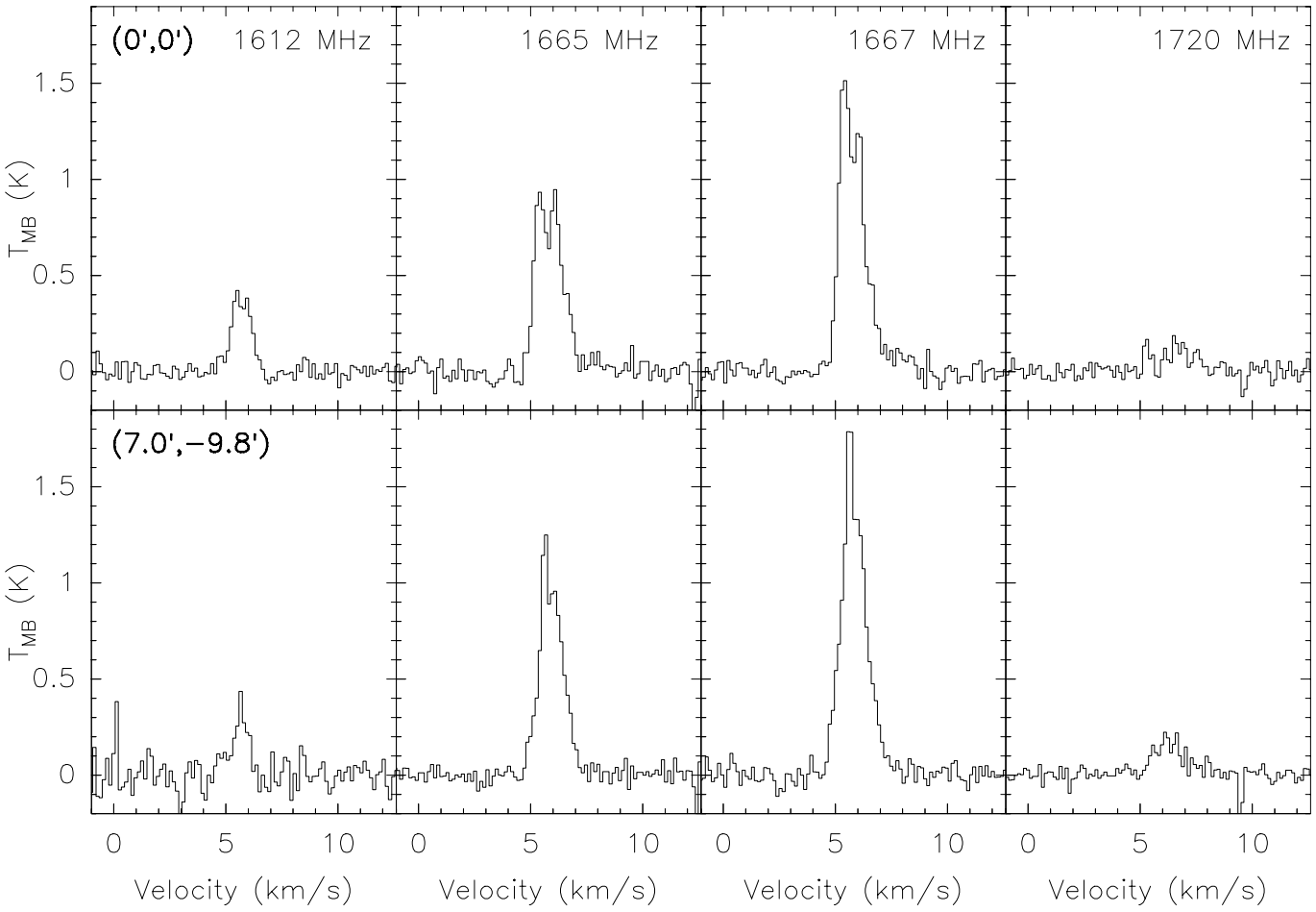

Figure 13. The spectra of the OH 18 cm transition observed toward TMC-1 (Harju et al. 2000). The 1612 MHz line is brighter than the 1720 MHz line.

of the anomaly. A similar hfs anomaly is observed toward a filamentary structure in the north west part of TMC-1 (Xu et al. 2016). They compared spectra of [H I], CO and OH, and suggested that the OH 18 cm transition traces a CO-dark molecular gas.

As mentioned above, there have been vast observational studies of the OH 18 cm transition toward molecular clouds, which revealed the hfs intensity anomaly of this transitions. Nevertheless, its origin has not been understood well due to the quite complex pumping mechanisms of OH. However, this information is necessary to interpret the observed OH spectra quantitatively. In this thesis, we find the three types of hfs anomalies of the OH 18 cm transition in the course of our OH observations toward various molecular clouds, and reveal the origin of each anomaly according to our statistical equilibrium calculations. These anomalies are found to reflect different physical conditions of molecular clouds.

From these results, we present that new aspects of the OH 18 cm transition as a unique tracer of molecular-cloud formation.

CHAPTER 3. INSTRUMENTS

3.1 Radio observations

3.1.1 Radio telescope

In this thesis work, we carried out the observations of the OH 18 cm transition using single-dish radio telescopes and interferometers. In this section, we briefly explain the basic scheme how radio telescopes work to observe the spectral emission of molecules (atoms) from the space. Roughly speaking, single-dish radio telescopes are made up of an antenna, a receiver and a spectrometer (Figure 14). An antenna collects radio signals from space to the focus point using a parabolic reflector. For the prime focus optics, the receiver system is directly placed at the focus. For the Cassegrain optics and the Gregorian optics, convex and concave subreflectors, respectively, are placed in front of the primary focus of the main reflector in order to shift the focal point backward, and a receiver system is placed at the resultant focus. The angular resolution of the telescope is determined by the antenna diameter (D) and the wavelength of the signal (λ) as,

$$\theta_{HPBW} \sim \frac{\lambda}{D} \text{ (radian)}. \tag{17}$$

Namely, the resolution is better for a larger diameter of the main reflector and at a shorter wavelength of observations. Therefore, large single-dish telescopes such as the Effelsberg 100-m, Green Bank

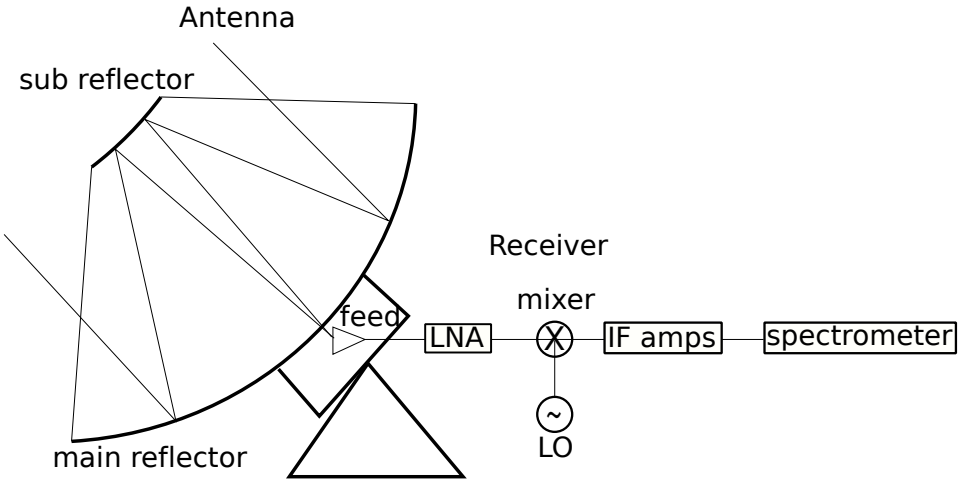

Figure 14. A schematic illustration of the radio telescope.

100-m, Arecibo 300-m and FAST 500-m telescopes have been constructed to obtain a better angular resolution in the centimeter-wave region.

The input signal collected by the antenna is converted to the electronic signal by a feed horn placed on the focus, and is then introduced to the receiver. The main purposes of the receiver are to amplify the input signal to the sufficient level for its analyses and to downconvert its frequency to the intermediate frequency (IF). The former process is necessary, since a radio signal from space is generally as weak as 10^{-19}–10^{-21} W. A cooled low-noise amplifier (LNA) such as HEMT (High Electron Mobility Transistor) operated at 20 K is usually used for this purpose. The downconversion to the IF frequency makes low-noise amplification easier than in the original frequency and also contribute to reducing the energy loss in the transmission cables. The downconversion is done with a non-linear device, called as a mixer. Before the mixing, the input signal has to be coupled to a reference signal generated by a local oscillator, which has a slightly different frequency (f_{LO}) from the input signal (f_{RF}). The mixer outputs the IF signals of the frequencies of $|f_{RF} \pm f_{LO}|$. Only the lower frequency signal ($f_{IF} = |f_{RF} - f_{LO}|$) is usually selected by the low-pass filter in the downconversion process. Low frequency receivers (< 100 GHz) usually perform amplification and downconversion in this order.

On the other hand, the order is reversed in the higher frequencies (> 100 GHz) receiver, since no good LNA is available in the high frequency region. In this case, using a low noise mixer for the downconversion is essential to achieve a good receiver performance, since its conversion loss and noise mainly affects the noise temperatures of the total receiver system. Therefore, low noise superconductor mixers such as SIS (Superconductor-Insulator-Superconductor) and HEB (Hot Electron Bolomerter) are used for this purpose. A cooled low-noise HEMT amplifier is usually employed as the first stage IF amplifier, because its noise also contribute to the receiver noise. Then, the IF signal is further amplified and/or frequency-converted to the other frequency, if necessary, before it is introduced to the spectrometer.

A spectrometer is used to obtain a power spectrum as a function of the frequency ($P(\nu)$) from the input signal ($V(t)$). There are several types of radio spectrometers. First, a filterbank spectrometer

uses a bank of band-pass filters (BPFs) with different passbands to directly obtain the spectrum from $V(t)$. Although the concept is rather simple, the system becomes complex as the increasing number of BPFs. Hence, the number of a channel is limited (e.g. ~ 512) in this case. The second one is an acoust-optical spectrometer (AOS). In AOS, the input electric signal from the receiver is introduced to a piezoelectric device, which generates an acoustic wave within the device. The acoustic wave is then transmitted to a crystal such as TeO_2, by which an irradiated laser beam produces a certain diffraction pattern. The diffraction angle corresponds to the frequency, and the intensity of the diffracted light to the spectral intensity. The spectra of the input signal can thus be obtained by measuring the diffraction pattern using an array detector such as CCD. AOS can be used to obtain a broader band width than the filterbank spectrometer, and was used for a long time in the Nobeyama 45-m radio telescope. The third one is an autocorrelation spectrometer, which is a kind of the digital spectrometer. In this spectrometer, digital autocorrelators are used to calculate the autocorrelation of $V(t)$. The spectrum $P(\nu)$ is obtained by performing Fast Fourier Transform (FFT) to the autocorrelation function. This type of a spectrometer is called the XF spectrometer, where X and F stand for autocorrelation and Fourier transform, respectively. The Fourier transform spectrometer, or FX spectrometer, obtains the spectra by performing FFT and autocorrelation in this order. The performance of the digital spectrometers have been improved as increasing performance of digital devices. Most telescopes including the Effelsberg and GBT employ the digital spectrometer as their backends.

3.1.2 Calibration

The spectrum observed by a radio telescope, which is a power as a function of the frequency $P(\nu)$, is usually represented in terms of an antenna temperature (T_A):

$$P(\nu) = k_b T_A. \tag{18}$$

The antenna temperature is equivalent to a mean brightness temperature of the source weighted by a beam pattern of the antenna. The energy loss by the atmosphere as well as that caused between the aperture and the feed horn must be corrected to obtain the real antenna temperature of the source

($T_A{}^*$), which can be written as,

$$T_A{}^* = T_a \frac{\exp(\tau)}{\eta}, \tag{19}$$

where τ and η are the optical depth of the atmosphere and the antenna efficiency, respectively. In order to estimate τ and η values, a chopper-wheel method (Penzias & Burrus 1973) is employed. In this method, the two reference signals ($P_{\rm sky}$ and $P_{\rm abs}$) are observed in addition to the spectra from the source ($P_{\rm source}$). $P_{\rm sky}$ is measured toward the 'sky' with no radio source, whereas $P_{\rm abs}$ is measured by introducing an absorber, whose temperature is $T_{\rm abs}$, in front of the feed horn. They can be written as,

$$P_{\rm abs} = Gk_b \left(T_{RX} + T_{\rm abs}\right) \tag{20}$$

$$P_{\rm sky} = Gk_b \left[T_{RX} + (1-\eta)T_{\rm gr} + \eta \left(1 - \exp\left(-\tau\right)\right) T_{\rm atm}\right] \tag{21}$$

$$P_{\rm source} = Gk_b T_A + P_{\rm sky}, \tag{22}$$

where G and T_{RX} are the gain and the noise temperature of the receiver, respectively. $T_{\rm atm}$ and $T_{\rm gr}$ represent the atmosphere temperature and the ground temperature, respectively. Assuming that the temperature is the same for the absorber, the ground, and the atmosphere ($T_{\rm abs} \sim T_{\rm gr} \sim T_{\rm atm} \equiv T_{\rm amb}$), the real antenna temperature of the source, $T_A{}^*$, can be determined from $P_{\rm sky}$, $P_{\rm abs}$, $P_{\rm source}$ and $T_{\rm amb}$, as

$$T_A{}^* = T_{\rm amb} \frac{P_{\rm source} - P_{\rm sky}}{P_{\rm abs} - P_{\rm sky}}. \tag{23}$$

The main beam temperature (T_{MB}) is calculated from $T_A{}^*$ by dividing the main beam efficiency (B_{eff}), which is a power received by the main beam of the antenna relative to the total power. If the source has an extended structure comparable to the main beam, the T_{MB} would be the brightness temperature of the source filling the main beam. We employ the main beam temperature as an intensity scale in this thesis, since we study warm diffuse clouds extending in space.

Contributions of the radio sources behind the target are still included in T_{MB}. The position-switch and frequency-switch methods are usually used to subtract the background contribution as well as a receiver response. In the position-switch method, a position with no radio source (OFF position) is observed to measure a background emission of the source position (ON position). The antenna

temperature of the source is calculated by the subtraction ($T_A = T_A$(ON) - T_A(OFF)). This estimate is correct, as long as the receiver gain, the receiver noise and the atmospheric condition are the same for the ON and OFF observations (and the background emission is the same in the ON and OFF positions). Nevertheless, the atmospheric condition varies during the time for moving the antenna between the ON and OFF positions, which result in worse signal-to-noise ratio. This effect can be reduced by using the frequency-switch method, where the frequency of the local oscillator (f_{LO}) is slightly shifted by a certain offset (f_{sw}) instead of switching the position. The antenna temperature is obtained by subtracting the two spectra observed with different f_{LO}. In this case, the time variation of the atmospheric condition is small (or negligible), since switching f_{LO} is much faster than switching a position. The frequency-switch method is also useful when observing molecules tracing a diffuse gas, such as OH, due to a difficulty in finding the OFF position. A drawback is that the spectrum can be affected by the standing waves between the main reflector and the feed horn and/or between the subreflector and the feed horn. However, this effect is not significant for the prime focus receiver in the centimeter-wave region. Therefore, we employed the frequency-switch method in our observations of OH.

Figure 15. The Effelsberg 100-m radio telescope.

Table 2. Basic performance of the Effelsberg 100-m radio telescope[a]

Receiver			Spectrometer	
18 cm/21 cm (1.29–1.73 GHz)			FFTS	
T_{sys}	Beam efficiency	HPBW	Bandwidth	Resolution
18 K (LCP), 19 K (RCP)	0.65	490 arcsec @ 1.66 GHz	100 MHz	3.5 kHz

NOTE—[a] The system noise temperature (T_{sys}), the beam efficiency (B_{eff}), HPBW of the 18 cm/21 cm receiver are listed in the first, second and third columns, respectively. The instantaneous bandwidth and the spectral resolution of the FFTS spectrometer are shown in the fourth and fifth columns, respectively.

3.2 Telescopes

3.2.1 Effelsberg 100-m telescope

The Effelsberg 100-m radio telescope of Max-Planck-Institut für Radioatronomie (MPIfR) in Germany (Figure 15) is one of the two largest fully steerable single-dish telescopes in the world. It can be used to observe a frequency range from 300 MHz to 90 GHz. We observed the four hyperfine structure components of the OH 18 cm transition with the Effelsberg in 2013 and 2016 October. In our observations, the 18 cm/21 cm prime focus receiver was used, whose system noise temperature was about 20 K. The HPBW (half-power beamwidth) beam size was 490 arcsec at 1.66 GHz. The telescope pointing was maintained to be better than 20 arcmin, by observing nearby continuum sources. The facility Fast Fourier Transform Spectrometer (FFTS) was employed as the backend; it has an instantaneous bandwidth of 100 MHz with a frequency resolution of 3.5 kHz. The resolution corresponds to a velocity resolution of 0.56 km s^{-1} at 1667 MHz. The 1612 MHz and 1720 MHz lines of the OH 18 cm transition were separately observed with two frequency settings. The 1665 MHz and 1667 MHz lines were observed in both frequency settings. We used the frequency-switching mode with the frequency offset of 0.1 MHz. We hereafter use main beam brightness temperature (T_{MB}) as the intensity scale, which is calculated from the antenna temperature assuming a main beam efficiency of 0.65. The rms noise levels of the observed spectra are about 8–16 mK. The performance of the receiver and spectrometer are summarized in Table 2.

Figure 16. The 100 meter Green Bank Telescope.

3.2.2 Green Bank Telescope

The 100 meter Green Bank Telescope (GBT) (Figure 16) in the United States is the other largest fully steerable single-dish telescopes besides the Effelsberg 100-m telescope (Section 3.2.1). It is located in the National Radio Quiet Zone (NRQZ) in West Virginia. It has an approximately 175 km × 195 km rectangle shape, in which the use of any instruments emitting radio waves is restricted by law. This minimize radio frequency interferences (RFI) from artificial signals which significantly affect

Table 3. Basic performance of the GBT 100-m radio telescope[a]

Receiver			Spectrometer		
L-Band (1.15–1.73 GHz)			VEGAS		
T_{sys}	Beam efficiency	HPBW	Mode	Bandwidth	Resolution
20 K	0.82	470 arcsec @ 1.66 GHz	11	23.44 MHz	0.4 kHz
			16	11.72 MHz	0.2 kHz

NOTE—[a] The system noise temperature (T_{sys}), the beam efficiency (B_{eff}), HPBW of the L-Band receiver are listed in the first, second and third columns, respectively. The instantaneous bandwidth and the spectral resolution for each mode of the VEGAS spectrometer are shown in the fifth and sixth columns, respectively.

the observation detecting faint signals from space. GBT covers a wide frequency range from 100 MHz to 115 GHz. We used GBT in 2015 and 2017 in order to observe the OH 18 cm transition toward southern sky sources which was difficult to be observed from Effelsberg, although the maximum elevation was as low as 20–30 degree even with the GBT. We employed the L-Band receiver, whose system noise temperature was about 20 K. The HPBW beam size was 470 arcsec at 1.66 GHz. The telescope pointing was maintained to be better than 20 arcmin by observing nearby continuum sources. The VErsatile GBT Astronomical Spectrometer (VEGAS) was employed as a backend. We used the VEGAS mode 11 on 2015, whose instantaneous bandwidth and spectral resolution are 23.44 MHz and 0.4 kHz, respectively. This resolution corresponds to a velocity resolution of 0.07 km s^{-1} at 1667 MHz. Higher resolution mode 16 was used on 2017, whose instantaneous bandwidth and spectral resolution are 11.72 MHz and 0.2 kHz, respectively. The four hfs components of the OH 18 cm transition were simultaneously observed in the same frequency setting. We used the frequency-switching mode with the frequency offset of 3.0 MHz. The performances of the receiver and spectrometer are summarized in Table 3.

Figure 17. The Very Large Array.

Table 4. VLA array configuration

Configuration	B_{max}	B_{min}	θ_{HPBW}@1.5 GHz	θ_{LAS}@1.5 GHz
A	36.4 km	0.68 km	1.3 arcsec	36 arcsec
B	11.1 km	0.21 km	4.3 arcsec	120 arcsec
C	3.4 km	0.035 km	14 arcsec	970 arcsec
D	1.03 km	0.035 km	46 arcsec	970 arcsec

NOTE—The VLA is operated in the four array configurations. Each array configuration properties are shown. The maximum and minimum antenna separations (B_{max} and B_{min}, respectively), the synthesized beam width (θ_{HPBW}) and the largest recoverable angular scale structure (θ_{LAS}) for configurations A–D are represented in each column.

3.2.3 Very Large Array

The Very Large Array (VLA) of National Radio Astronomy Observatory (NRAO) is a large interferometer in the United States. It consists of 27 antennas with 25 m in diameter. They are aligned in a characteristic Y-shape configuration with a radius of about 21 km (Figure 17). The A, B, C and D array configurations are available to trace a wide range of spatial scales from about 1 arcsec to 10 arcmin (Table 4). The most compact D-array configuration was used in our observations. As a frontend, we employed the L-Band receiver to observe the four hfs components of the OH 18 cm transition. The 8-bit sampler was used as a backend, whose instantaneous bandwidth and the spectral resolution were set to be 250 kHz and 0.651 kHz, respectively. The resolution of 0.651 kHz corresponds to the velocity resolution of 0.117 km s^{-1} at 1667 MHz. The field-of-view (FOV) was $\sim$27 arcmin at 1.66 GHz. The typical rms noise temperature was $\sim$ 1.6 mJy/beam, which corresponds to 0.19 K at 1612 MHz, for the resolution of 0.5 km s^{-1} after the integration time of 10 hours.

CHAPTER 4. Absorption feature in the 1612 MHz line of OH

4.1 Introduction

In 2009, the project of our group observing the OH emission in various nearby clouds was conducted with the MPIfR 100-m telescope at Effelsberg. The initial purpose is to compare the OH emission with the CH emission to discuss the chemical evolution of molecular clouds. In the course of this OH 18 cm transition observation, we fortuitously found the conjugate behavior, where the 1612 MHz line is observed in absorption and the 1720 MHz line shows enhanced emission toward the whole Heiles Cloud-2 (HCL2) region. This anomaly is different from that found by Harju et al. (2000), and is similar to that found toward L134 (Mattila et al. 1979) and other molecular clouds mentioned in Section 2.2. Although such anomalies have been discussed in terms of non-LTE effect (Elitzur 1976; Mattila et al. 1979), detailed analyses have not been reported because of a lack of high-quality observational data of the satellite lines. In this Chapter, we demonstrate that this hyperfine anomaly can be used as a good thermometer of molecular clouds over a relatively wide range of the H_2 density. The results obtained by the observations of the OH 18 cm transition toward the translucent cloud at the eastern side of HCL2 (Figure 18), the cold dark cloud L183 (Figure 20), the ρ-Ophiuchi molecular cloud (Figure 22), and the Lupus-1A molecular cloud (Figure 24), as listed in Table 5, are described.

Table 5. Observed sources

Source	R.A. (J2000)	Dec. (J2000)	Distance	Telescope (year)
HCL2E	$04^h48^m15^s.1$	$25°35'15''$	137 pc[a]	Effelsberg (2009, 2013)
L183	$15^h54^m00^s.5$	$-2°51'49''$	110 pc[b]	Effelsberg (2013)
ρ-Ophiuchi	$16^h26^m31^s.4$	$-24°21'44''$	119 pc[c]	Effelsberg (2013)
Lupus-1A	$15^h42^m52^s.4$	$-34°07'53''.5$	155 pc[c]	GBT (2015)

References— [a] Torres et al. (2007), [b] Franco (1989), [c] Lombardi et al. (2008)

4.2 Observation

Observations were carried out with the MPIfR 100 m telescope at Effelsberg in 2013 October, and the 100-m telescope at Green Bank in 2015 March. We observed the four hfs components of the ground-state Λ-type doubling transition of OH (Table 1).

4.3 Data reduction

4.3.1 Effelsberg 100-m telescope

The CLASS (Continuum and Line Analysis Single-dish Software) software was used for the reduction of the Effelsberg data. For the data observed in 2013, we first folded the spectra using the "FOLD" command, which is necessary to reduce the data obtained by the frequency-switching method. In the frequency-switch observations, two slightly different frequencies of the local oscillator (f_{LO}) are used, as explained in Section 3.1.2. The folding process calculates the average of the spectra observed toward the same position with different f_{LO}. Contributions of the background as well as the system response are subtracted by this process, as explained in Section 3.1.2. As for the data observed in 2016, the folding process was automatically performed in the pipeline of the Effelsberg. Then, we flagged the bad data, in which strong RFI (Radio Frequency Interference) signals interfere the real signal from the source. The baseline was subtracted from each spectra by fitting the third order polynomial function using the "BASE" command. We averaged the spectra observed toward each source, where the rms noise of each spectrum is employed as the relative weight. Finally, the intensity scale was converted from the antenna temperature (T_a*) to the main beam temperature (T_{MB}), assuming the main beam efficiency of 0.65 provided by the observatory.

4.3.2 GBT 100-m telescope

The GBTIDL, which is an IDL (Interface Description Language) package developed by the National Radio Astronomy Observatory (NRAO), was used for the reduction of the GBT data. As in the case of the reduction of the Effelsberg data, we first folded the spectra using the "getfs" command. Then, we flagged the bad data which suffer strong RFI signals. The baseline was subtracted from each spectra by fitting the fifth order polynomial function using the "baseline" command. We averaged

the spectra observed toward each source, where the rms noise of each spectrum is employed as the relative weight. Finally, the intensity scale was converted from the antenna temperature (T_a*) to the main beam temperature (T_{MB}), assuming the main beam efficiency of 0.92 provided by the observatory.

4.4 Result

4.4.1 HCL2E

HCL2E (Heiles Cloud-2 East) is a translucent cloud located at 1.5° east of HCL2 in Taurus molecular cloud complex (referred hereafter as HCL2E) (Figure 18). The distance from the Sun is 137 pc (Torres et al. 2007). HCL2E has an apparent size of about 30′, and is connected to HCL2 in the ^{13}CO (J=1-0) emission (Narayanan et al. 2008; Mizuno et al. 1995) (Figure 18) and the [C I] emission (Maezawa 2000). A relatively high C/CO ratio confirms the translucent nature of this cloud, where

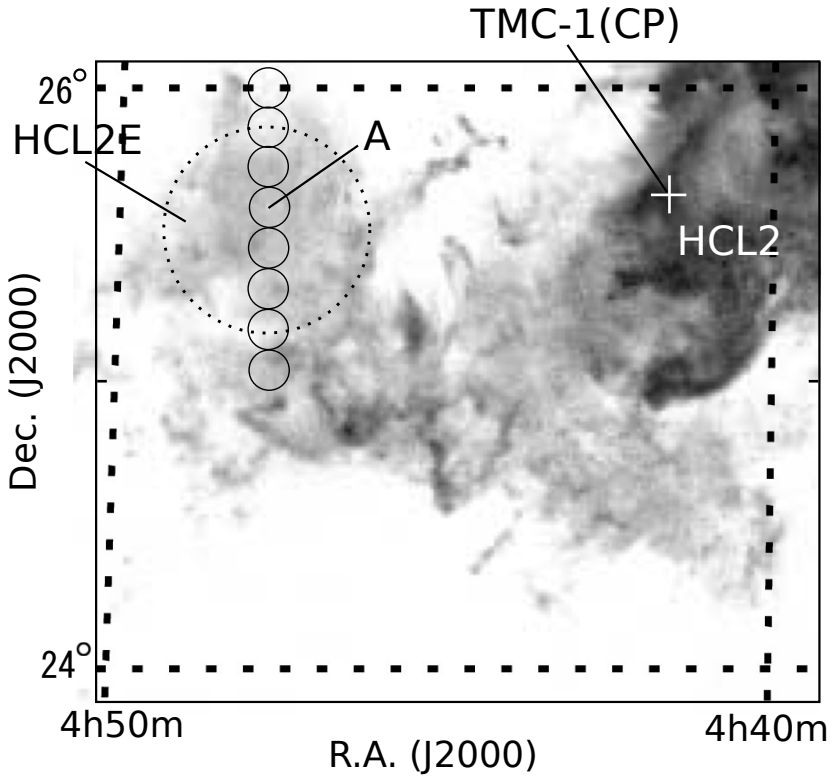

Figure 18. Peak intensity image of the ^{13}CO (J=1–0) line (Narayanan et al. 2008). Solid circles represent the observed positions in HCL2E. "A"is the "central" position, which is a peak of the [C I] intensity (Maezawa 2000). A cross mark represents the position of TMC-1 cyanopolyyne peak (CP).

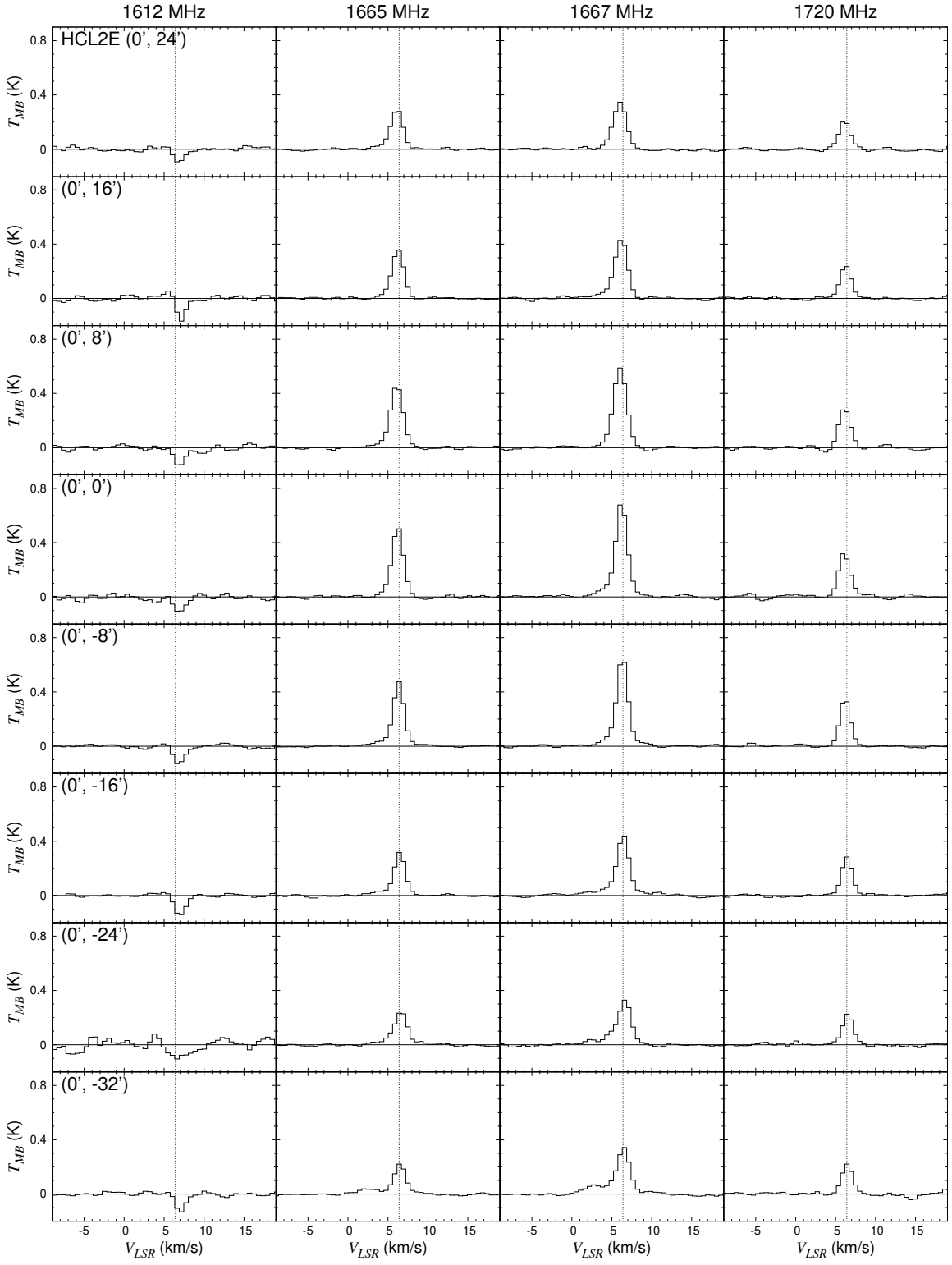

Figure 19. Observed spectra of the OH 18 cm transition toward HCL2E. Vertical dashed lines represent the typical LSR velocity of 6.4 km s^{-1}.

Table 6. Observed line parameters toward HCL2E, L183, ρ-Ophiuchi, and Lupus-1A.

Source (offset)	V_{LSR} (km s^{-1})	FWHM (km s^{-1})	T_{MB}(1612) (K)	T_{MB}(1665) (K)	T_{MB}(1667) (K)	T_{MB}(1720) (K)
HCL2E (0′, 24′)	6.06(2)	1.92(6)	-0.045(9)	0.25(1)	0.30(1)	0.165(9)
HCL2E (0′, 16′)	6.21(3)	1.87(7)	-0.04(1)	0.30(1)	0.38(1)	0.19(1)
HCL2E (0′, 8′)	6.07(2)	1.93(4)	-0.07(1)	0.39(1)	0.51(1)	0.23(1)
HCL2E (0′, 0′)	6.20(1)	1.81(4)	-0.07(1)	0.43(1)	0.58(1)	0.27(1)
HCL2E (0′, -8′)	6.31(1)	1.70(4)	-0.09(1)	0.40(1)	0.56(1)	0.28(1)
HCL2E (0′, -16′)	6.44(2)	1.80(6)	-0.10(1)	0.26(1)	0.38(1)	0.23(1)
HCL2E (0′, -24′)	6.55(3)	2.08(9)	-0.09(1)	0.20(1)	0.28(1)	0.17(1)
HCL2E (0′, -32′)	6.47(4)	1.91(9)	-0.08(1)	0.18(1)	0.29(1)	0.17(1)
L183 (0′, 0′)	2.47(1)	1.37(1)	0.101(7)	0.357(7)	0.586(8)	0.063(7)
L183 (0′, -8′)	2.52(1)	1.71(2)	0.062(5)	0.273(5)	0.483(6)	0.084(5)
L183 (0′, -16′)	2.56(3)	2.15(7)	-0.011(6)	0.086(6)	0.205(7)	0.037(5)
ρ-Oph (-3′, 0′)	3.30(3)	2.02(7)	-0.06(1)	0.21(1)	0.47(1)	0.25(1)
ρ-Oph (4′, -12′)	3.84(1)	1.81(3)	-0.05(1)	0.54(1)	1.00(2)	0.33(1)
ρ-Oph (12′, -15′)	3.74(1)	1.80(2)	0.00(1)	0.63(1)	1.10(1)	0.27(1)
ρ-Oph (20′, -18′)	3.72(1)	1.71(2)	0.11(1)	0.48(1)	0.85(1)	0.15(1)
Lupus-1A (#1)[a] (16′, 16′)/$\sqrt{2}$	4.42(6)	1.92(4)	0.004(2)	0.018(2)	0.047(3)	0.004(2)
Lupus-1A (#2)[a] (8′, 8′) / $\sqrt{2}$	4.80(1)	1.57(2)	-0.013(2)	0.107(2)	0.244(3)	0.084(2)
Lupus-1A (#3)[a] (0′, 0′)	5.23(1)	1.06(0)	-0.015(4)	0.285(5)	0.583(7)	0.168(4)
	5.03(1)	0.28(1)	0.037(9)	0.141(9)	0.22(1)	0.051(9)
Lupus-1A (#4)[a] (-8′, -8′)/$\sqrt{2}$	5.37(1)	1.13(1)	0.023(3)	0.137(5)	0.293(8)	0.056(4)
	5.59(1)	0.42(2)	0.005(6)	0.060(7)	0.130(9)	0.037(6)
Lupus-1A (#5)[a] (-16′, -16′)/$\sqrt{2}$	4.66(8)	2.52(0)	0.007(3)	0.021(3)	0.053(3)	0.001(3)
Lupus-1A (#2a)[a] (-8′, 24′)/$\sqrt{2}$	4.78(1)	1.55(3)	0.009(4)	0.102(6)	0.24(1)	0.057(5)
	4.59(1)	0.55(3)	-0.009(7)	0.104(8)	0.16(1)	0.056(7)
Lupus-1A (#2b)[a] (-16′, 32′)/$\sqrt{2}$	4.82(1)	1.20(2)	0.006(3)	0.074(3)	0.171(3)	0.037(3)
Lupus-1A (#3a)[a] (-16′, 16′)/$\sqrt{2}$	5.06(1)	1.42(3)	-0.005(3)	0.080(3)	0.195(4)	0.037(3)

NOTE—[a] Position numbers are shown in Figure 24. The numbers in the parentheses represent the standard deviation of the Gaussian fit in units of the last significant digits.

the visual extinction is estimated to be about 4 visual magnitudes (Maezawa 2000). We observed the four hfs components of the OH 18 cm transition with the Effelsberg 100-m telescope along the strip line from south to north indicated in Figure 18; 8 positions with 8′ spacing, which corresponds to the HPBW beam size of the telescope. The result is shown in Figure 19. The absorption feature in the 1612 MHz transition is evident for all the positions. Since no radio continuum source is known toward HCL2E, this feature represents absorption against the cosmic microwave background (CMB). Furthermore, the 1720 MHz line is observed in emission with an intensity much stronger than expected from LTE. The intensity of the 1720 MHz line relative to that of the 1667 MHz line is about a half in HCL2E, which is 4.5 times higher than the expected value under the LTE condition (1/9).

The absorption in the 1612 MHz component and the enhanced emission in the 1720 MHz component have been reported for a few other sources as mentioned in Section 2.2 (e.g. Crutcher 1977; van Langevelde et al. 1995; Weisberg et al. 2005; Kanekar et al. 2004). It is known that this anomaly occurs by collisional excitation to rotationally excited states and subsequent radiative relaxation to the ground rotational state. Our observations further confirm that such conjugation occurs in quiescent clouds without bright background continuum emission. The observed line parameters are summarized in Table 12.

4.4.2 L183

L183 is an isolated cold dark cloud without any associated stars, whose distance from the Sun is 110 pc (Franco 1989). A dense core traced by NH_3 exists in the northern part of the cloud, which has been subject to extensive astrochemical studies (e.g. Swade 1989; Dickens et al. 2000). A rather diffuse molecular cloud traced by ^{13}CO is extended toward the southern direction (Laureijs et al. 1995; Lehtinen et al. 2003). We observed the OH 18 cm transition toward three positions with a spacing of 8′ from south to north, as shown in Figure 20. The observation was conducted with the Effelsberg 100-m telescope in 2013. Although the absorption feature of the 1612 MHz line is not clearly seen, the intensity of the 1612 MHz line becomes weaker toward the southern positions, whereas the intensity of the 1720 MHz line relative to the main lines increases (Figure 21). The relative intensities of the four hyperfine components significantly deviate from the intrinsic line strengths, *i.e.*, 1612:1665:1667:1720

MHz = 1:5:9:1 (Table 1), and hence, they are clearly anomalous. This trend can also be seen in the spectra observed toward the L134 cloud (1.5° south of L183) by Mattila et al. (1979), although the signal-to-noise ratio of their spectra is rather poor. As shown in the bottom panel of Figure 21, a marginal absorption feature of the 1612 MHz line may be seen at the southernmost position. The observed line parameters are summarized in Table 12.

4.4.3 ρ-Ophiuchi molecular cloud

The ρ-Ophiuchi molecular cloud is an active star-forming cloud, whose distance from the Sun is 119 pc (Lombardi et al. 2008). It is illuminated by the nearby B2 V star HD147889 (Figure 22), and a part of it constitutes a representative photodissociation region (PDR) (Yui et al. 1993; Liseau et al. 1999; Kamegai et al. 2003). We observed four positions at different distances from HD147889 with the Effelsberg 100-m telescope in 2013. Three of them are aligned on a straight line connecting

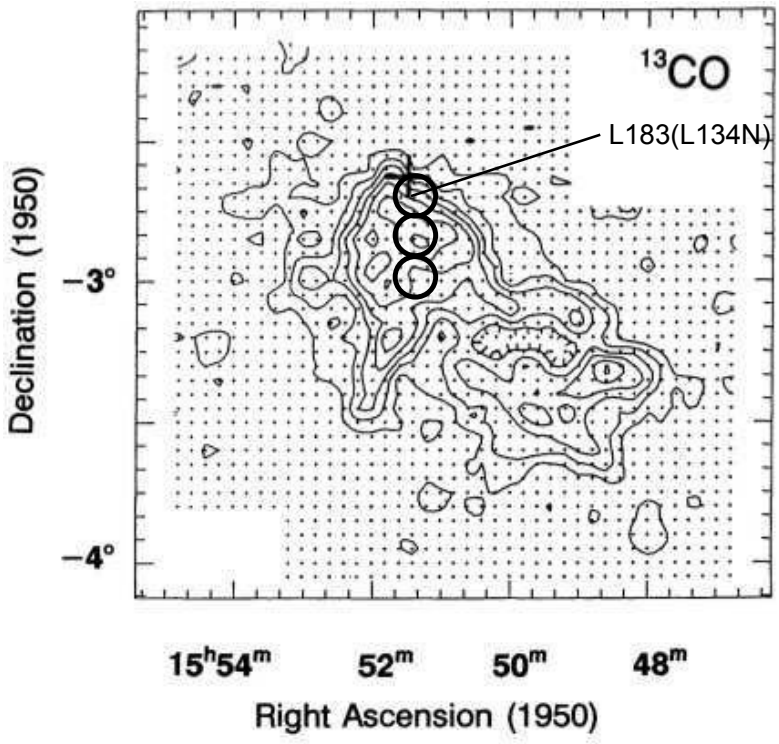

Figure 20. Contours show the integrated intensity map of ^{13}CO (J=1-0) toward L183 reported by Laureijs et al. (1995). The three circles represent the observed position in OH. The cross marks the position of the NH_3 core of L183 (L134N) indicated by Laureijs et al. (1995).

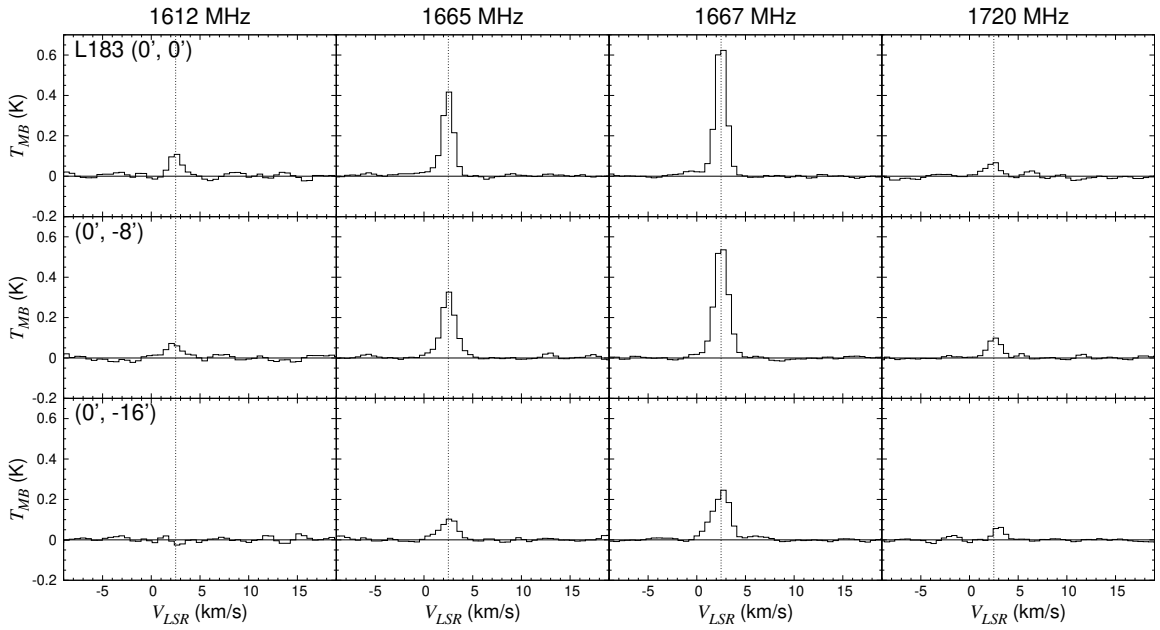

Figure 21. Observed spectra of the OH 18 cm transition toward L183. Vertical dashed lines represent the typical LSR velocity of 2.5 km s^{-1}.

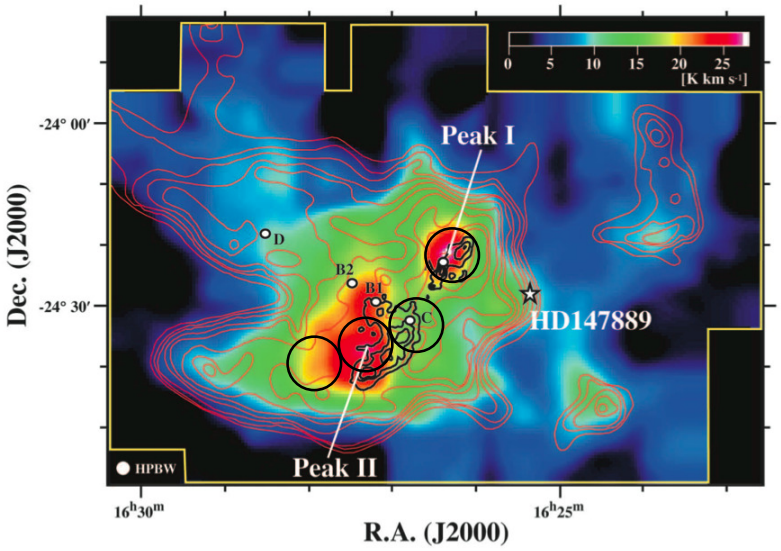

Figure 22. The ρ-Oph region: Black and red contours show the integrated intensity maps of $C^{18}O$ (J=1-0) and ^{13}CO (J=1-0) lines, respectively, overlaid on color image of the integrated intensity map of the [C I] ($^3P_1 - {}^3P_0$) emission (Kamegai et al. 2003). Large black circles represent the positions observed in the OH 18 cm transition. The position of the heating and ionizing star HD147889 is indicated by a star.

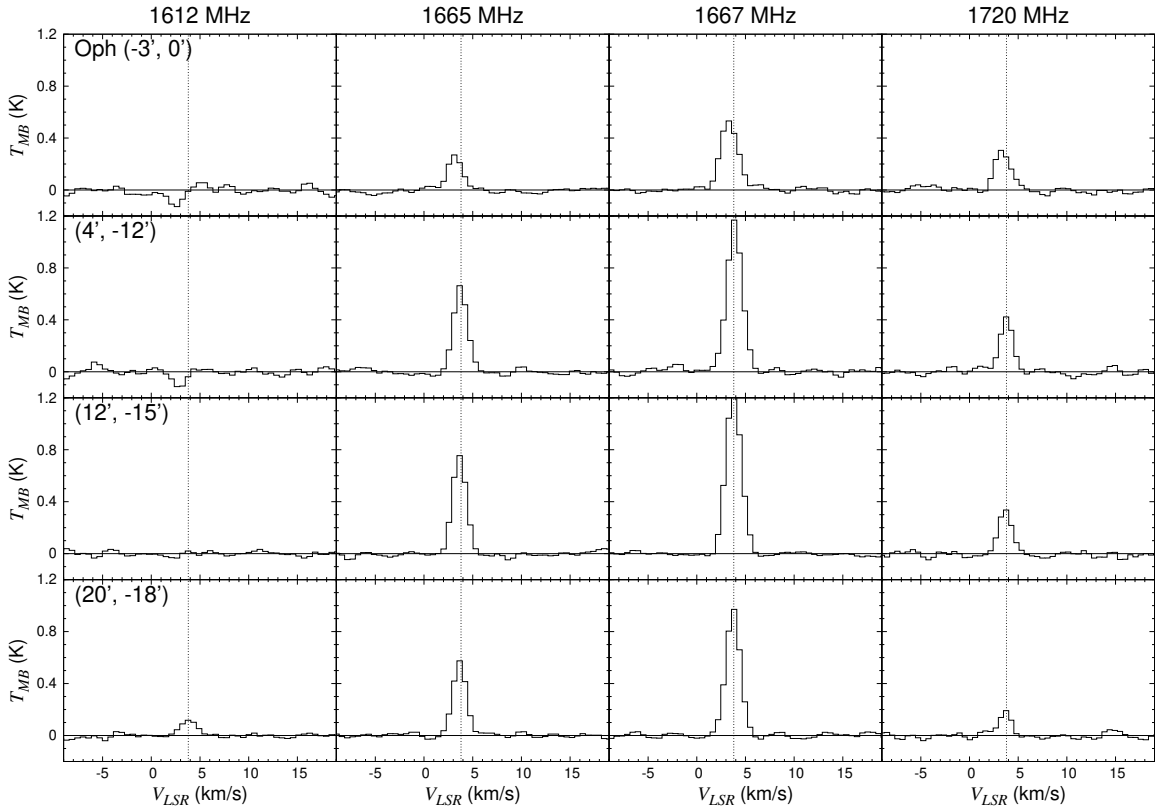

Figure 23. Observed spectra of the OH 18 cm transition toward ρ-Ophiuchi. Vertical dashed lines represent the typical LSR velocity of 3.8 km s^{-1}.

HD147889 with the intensity peak of the [C I] emission (Kamegai et al. 2003, Peak II in Figure 22). The other position is toward ρ-Oph A (Peak I in Figure 22). The 1612 MHz line appears in absorption toward the two positions nearest to HD147889 (Figure 23). The absorption feature is less significant for the more distant positions, and it eventually changes to emission behind the [C I] peak position. The observed line parameters are summarized in Table 12.

4.4.4 Lupus-1

The Lupus 1 molecular cloud is a nearby dark cloud, whose distance from the Sun is 155 pc (Lombardi et al. 2008) (Figure 24). This cloud involves Lupus-1A, which is known as a rich source of carbon-chain molecules (Sakai et al. 2010). The Lupus-1 cloud has a characteristic straight structure along the northwest to southeast direction, as revealed in the ^{13}CO (J=2–1) map by Tothill et al.

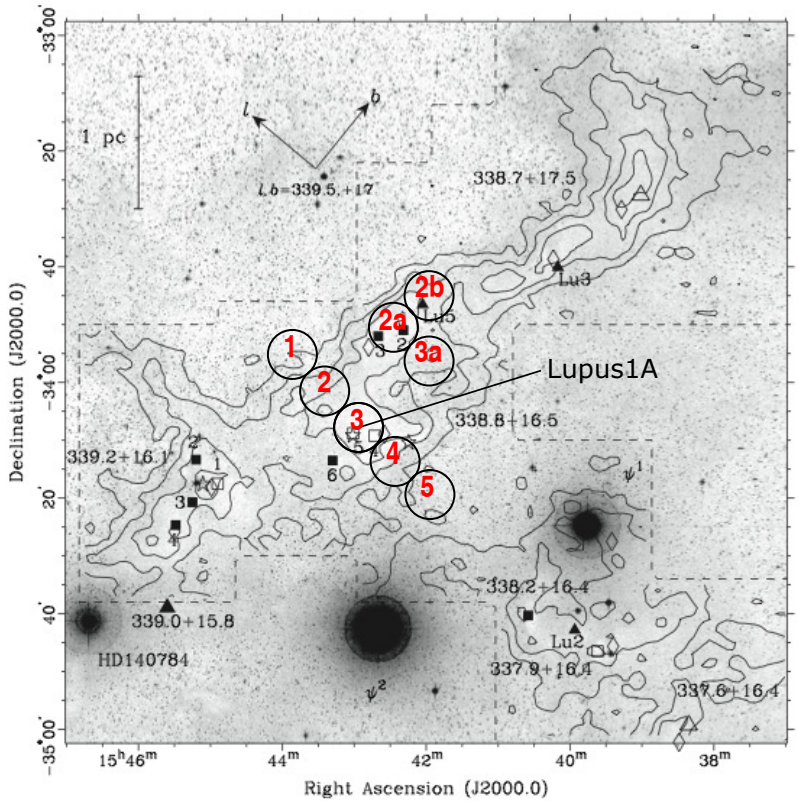

Figure 24. Contours show the integrated intensity map of the ^{13}CO (J=2–1) line overlaid on the optical (blue DSS2) image toward the Lupus-1 cloud (Tothill et al. 2009). We observed the OH 18 cm transition toward eight positions indicated by circles.

(2009) (contours in Figure 24). We conducted observations of the OH 18 cm transition toward five positions along the strip line centered on Lupus-1A, which is perpendicular to the straight structure (circles labeled #1–5 in Figure 24), using the GBT 100-m telescope in 2015. We also observed the three nearby positions labeled #2a, 2b and 3a in Figure 24. Figure 25 shows the observed spectra of the OH 18 cm transition. The OH hfs lines are the strongest at Lupus-1A (#3), where the two velocity components with narrow and broad linewidths are detected, as indicated by blue and red lines, respectively. The broad component is detected in all the observed positions, although it is very faint and only visible in the 1667 MHz line at cloud peripheries (#1 and #5). The narrow component is fainter than the broad component, and it is seen only toward a few positions in the central part of the filament (#2 (marginal), #3, #4 and #2a). In the broad component, the 1612 MHz line shows absorption or faint emission, while the 1720 MHz line is brighter than that expected under the LTE

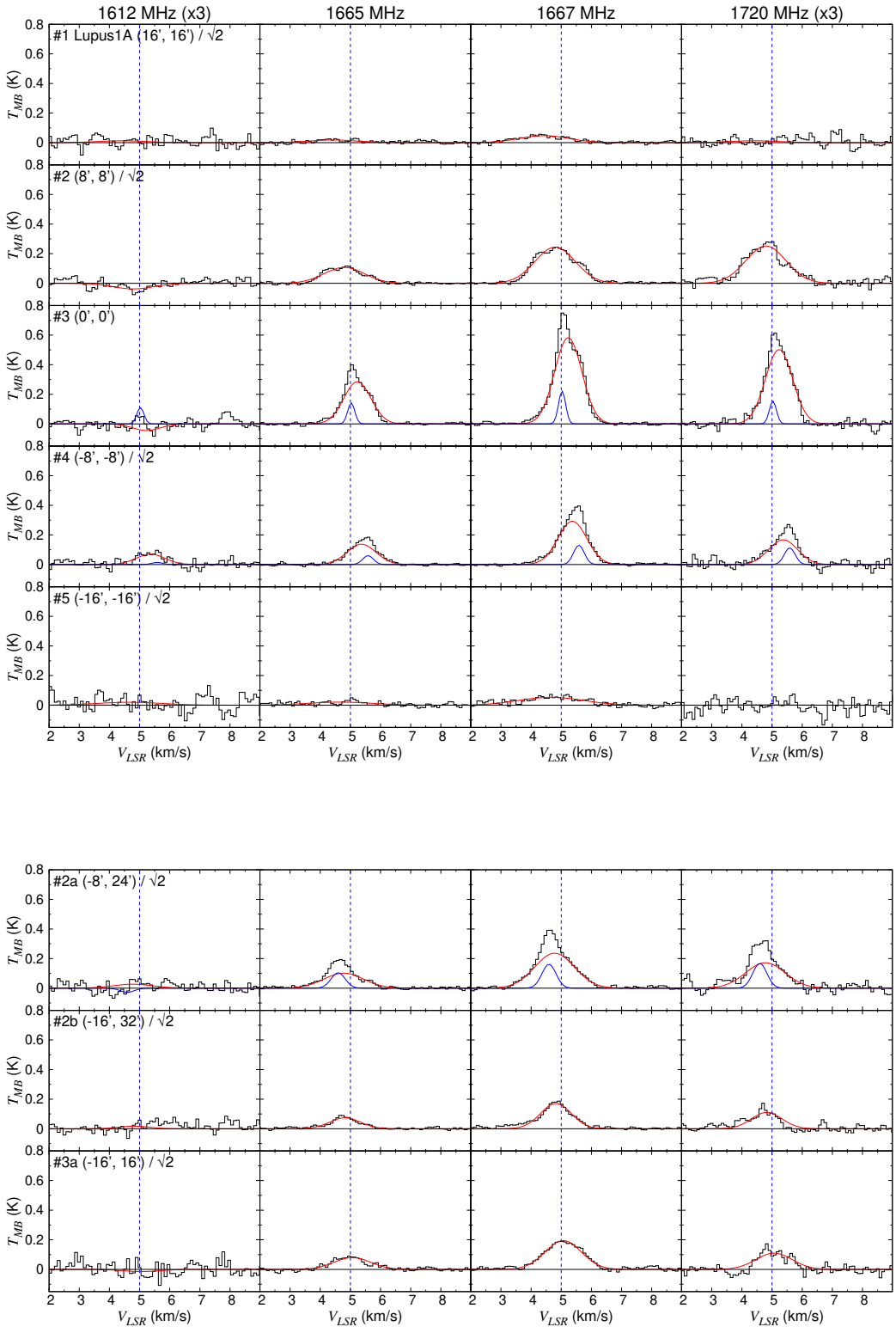

Figure 25. Observed spectra of the OH 18 cm transition toward the Lupus-1 cloud labeled as #1–5 (top) and as #2a, 2b and 3a (bottom) in Figure 24. Vertical blue dashed lines represent the typical LSR velocity of 5.0 km s^{-1}. The intensities of the 1612 and 1720 MHz lines are multiplied by a factor of 3.

condition. This anomaly is also seen in the narrow component except for Lupus-1A (#3 of Figure 24). Toward Lupus-1A, the relative intensities of the four OH hfs lines of the narrow component are close to the LTE values (1:5:9:1), indicating a high density at this position. The observed line parameters are summarized in Table 12.

4.5 Statistical Equilibrium Calculations

In order to constrain the physical conditions for absorption to occur in the 1612 MHz component, we conducted statistical equilibrium calculations by use of the Large Velocity Gradient (LVG) formalism (Goldreich & Kwan 1974). We employed the collisional cross sections calculated by Offer et al. (1994), where the state-to-state collisional cross sections with ortho and para H_2 considering the fine

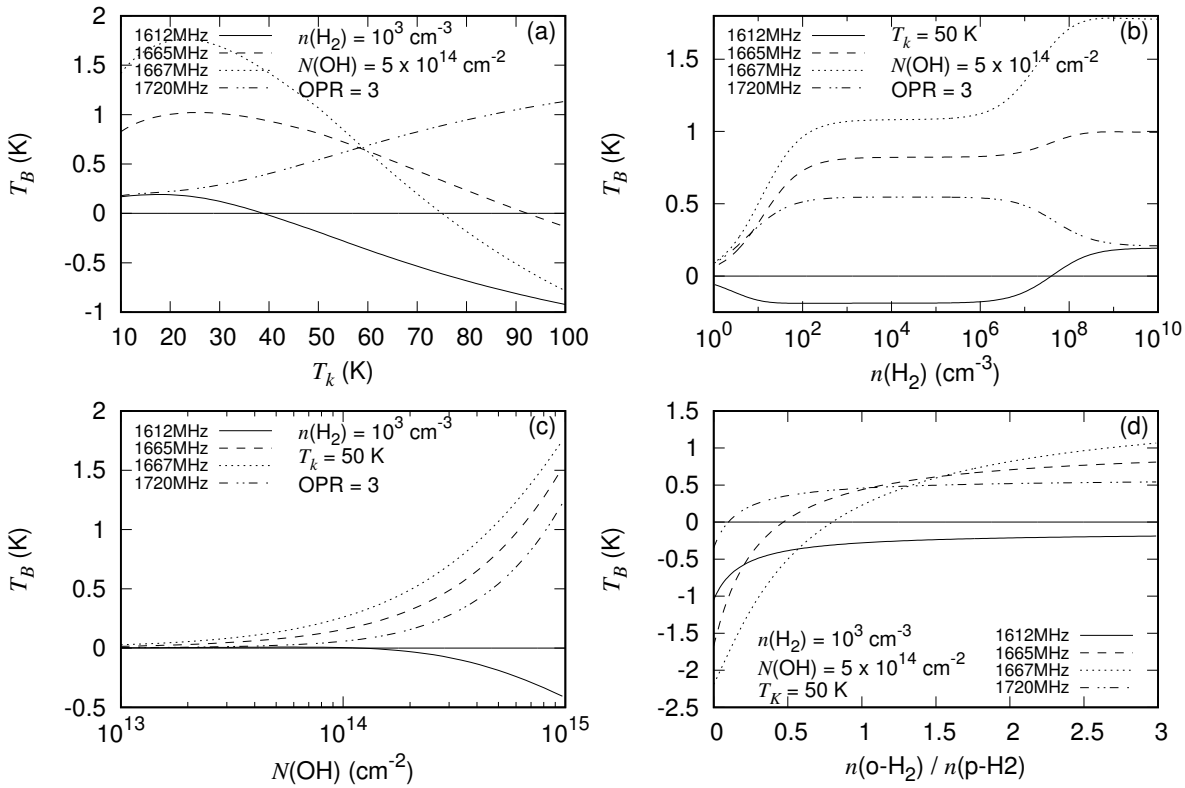

Figure 26. The expected intensities of the hfs lines of the OH 18 cm transition derived from our statistical equilibrium calculations as a function of (a) the gas kinetic temperature (T_k), (b) H_2 density ($n(H_2)$), (c) the OH column density (N(OH)), and (d) the H_2 ortho-to-para ratio.

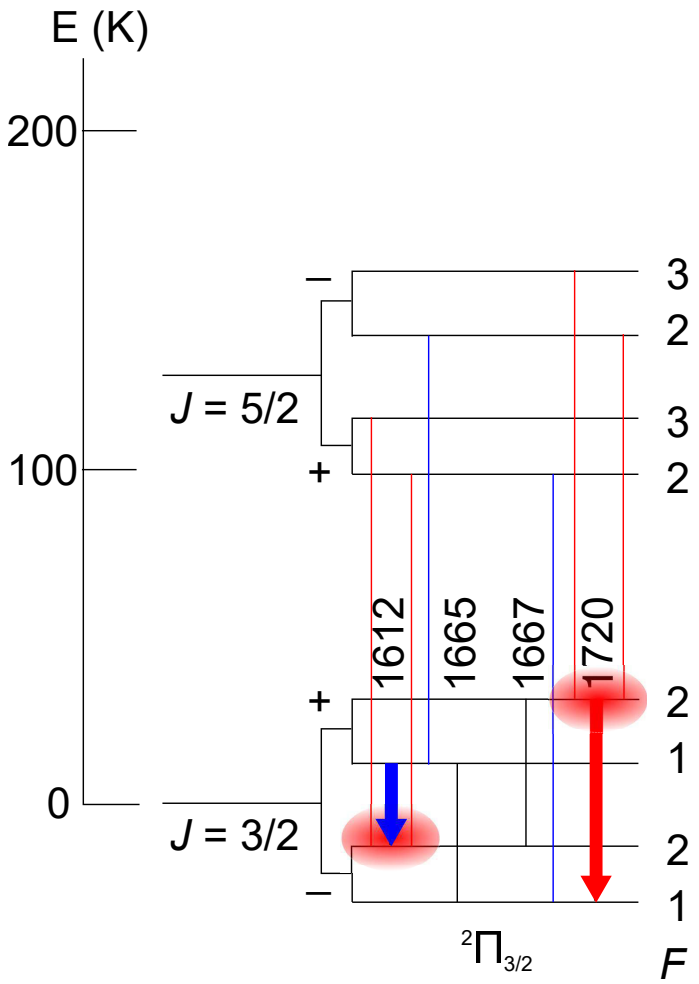

Figure 27. The rotational energy diagram for the ground rotational state ($^2\Pi_{3/2}$ $J = 3/2$) and the first rotationally excited state ($^2\Pi_{3/2}$ $J = 5/2$) of the OH molecule. The overpopulation in the F=2 levels in the ground rotational state is produced by the rotational transitions from the first rotationally excited state (red ellipses). In this situation, intensities of the 1612 and 1720 MHz lines become fainter and brighter, respectively, than those expected under the LTE.

and hyperfine structure levels are separately tabulated. We ignored the effects of line overlaps and the FIR pumping in this section, which will be discussed in detail later in Chapter 6.

The statistical equilibrium takes the form:

$$\begin{aligned}\frac{d(g_i n_i)}{dt} = &\sum_{j>i} \{g_j \beta_{ji} A_{ji} [n_j - R_{ji} (n_i - n_j)] \\ &+ g_j C_{ji} \left[n_j - n_i \exp\left(-\frac{h\nu_{ji}}{k_b T_k} \right) \right] \} \\ &- \sum_{i>j} \{g_i \beta_{ij} A_{ij} [n_i - R_{ij} (n_j - n_i)] \\ &+ g_i C_{ij} \left[n_i - n_j \exp\left(-\frac{h\nu_{ij}}{k_b T_k} \right) \right] \} \\ &= 0, \end{aligned} \tag{24}$$

where T_k, k_b, and h are the gas kinetic temperature, the Boltzmann constant, and the Planck constant, respectively. n_i and g_i represent the population and the degeneracy of energy level i of OH, respectively. A_{ij}, C_{ij}, and ν_{ij} are the Einstein A coefficient, the collisional rate, and the frequency of the transition, respectively, between the levels i and j; j in the first and third terms of Equation (24) represents summation over all levels. R_{ij} stands for the photon occupation number of the cosmic microwave background (CMB) radiation at the frequency of the transition between the levels i and j as:

$$R_{ij} = \frac{1}{\exp\left(h\nu_{ij}/k_b T_{CMB}\right) - 1}, \tag{25}$$

where T_{CMB} equals 2.73 K.

β_{ij} in the first and third terms of Equation (24) denote the photon escape probability of the transition between the levels i and j. We follow the standard large velocity gradient (LVG) model (Goldreich & Kwan 1974), in which a spherical cloud is assumed to have a large constant velocity gradient toward the center. A photon emitted at a center position of the cloud can be absorbed only near the emitting region due to a large doppler shift produced by the large velocity gradient. On that condition, the escape probability as well as the equation of the radiative transfer is constant throughout the cloud. Therefore, the statistical equilibrium calculation can be solved without considering the whole cloud structure. According to Goldreich & Kwan (1974), β_{ij} can be written as:

$$\beta_{ij} = \frac{1 - \exp\left(-\tau_{ij}\right)}{\tau_{ij}}. \tag{26}$$

τ_{ij} is the optical depth of the transition between the levels i and j:

$$\tau_{ij} = \frac{hc}{4\pi\Delta V} N(\mathrm{OH}) B_{ij} g_i (n_j - n_i), \tag{27}$$

where ΔV and $N(\mathrm{OH})$ are the linewidth and the OH column density, respectively. B_{ij} denotes the Einstein B coefficient of the transition between the levels i and j.

It should be noted that the rotational transition from the first rotationally excited state to the ground rotational state must be optically thick, in order to produce the 1612 MHz line absorption by the mechanism explained in Figure 27. Therefore, the geometry of the cloud, which is not considered in the LVG approximation, might affect the results of the statistical equilibrium calculations. However, such an exact treatment of the radiative transfer is very difficult, since it requires accurate information on the density and velocity structures of the cloud. Therefore, it is left for future works, although it is necessary for more quantitative analyses.

We confirmed that our program gives the same result as the statistical equilibrium calculation code RADEX (van der Tak et al. 2007), if we employ a static spherical cloud model (Osterbrock & Ferland 2006).

Figure 26 (a) shows the intensities of the four hyperfine components of the ground rotational state as a function of the gas kinetic temperature at the H_2 density of 10^3 cm^{-3}, the OH column density of 5×10^{14} cm^{-2}, and the H_2 ortho-to-para ratio (OPR) of 3. At low temperatures below 20 K, the relative intensities of the hyperfine components are close to the LTE values ($I_{1612} : I_{1665} : I_{1667} : I_{1720} = 1 : 5 : 9 : 1$). However, the intensities of the 1612 MHz and 1720 MHz components become different above 20 K, where the conjugate behavior of these two components develops. This is caused by more efficient collisional excitations from the ground rotational state to the first rotationally excited state with an increasing gas kinetic temperature. As schematically explained in Figure 27, the subsequent rotational transitions from the first rotationally excited state to the ground rotational state (blue and red lines) produce overpopulations in the F=2 levels in the ground rotational state (red ellipses). In this situation, the 1612 and 1720 MHz lines become fainter and brighter, respectively, than those expected in the LTE condition. This trend is similar to that pointed out by Elitzur (1976). As the

temperature is further raised, the 1612 MHz line appears in absorption above 40 K. Moreover, the 1665 MHz and 1667 MHz lines are also expected to be observed in absorption above ∼80 K and ∼90 K, respectively. Hence, the relative intensities of the hyperfine components are very sensitive to the gas kinetic temperature above 20 K. The lower temperature limit for the anomaly originates from the condition that the collisional excitation to the first rotationally excited state is possible to some extent to cause non-LTE populations among hyperfine structure levels. It should be noted that a deviation of the hyperfine intensities from the LTE values is also seen in the main line, which was pointed out by Crutcher (1979). This point is discussed later in Chapter 5.

On the other hand, the hyperfine intensity ratio is almost constant over a wide range of the H_2 density (10^2–10^7 cm^{-3}) (Figure 26 (b)). If the H_2 density is higher than the critical density for excitation to the first rotationally excited state (10^7 cm^{-3}), intensities of the hyperfine components tend to approach to the LTE values. As shown in Figure 26 (c), the 1612 MHz absorption feature requires the high OH column density, typically 10^{14} cm^{-2}, for the gas kinetic temperature of 40 K or higher. In addition, it is worth noting that the intensities of the four hfs lines are also sensitive to an H_2 ortho-to-para ratio, when the temperature is higher than 20 K (Figure 26 (d)). If the H_2 ortho-to-para ratio is close to 0 (the case for only para-H_2), not only the 1612 MHz line but also the other three lines appear in absorption at 50 K. Hence, we can determine the gas kinetic temperature, the OH column density, and the H_2 ortho-to-para ratio from the intensities of the four hfs component of the OH 18 cm transition.

4.6 Results and Discussions

4.6.1 Analysis methods and error estimation

We derive the gas kinetic temperature, the OH column density and the H_2 ortho-to-para ratio by the following two steps: (1) least-square fitting of gaussian profiles to the observed spectral lines and (2) another least-square fitting of the non-LTE model explained in Section 4.5 to the peak intensities determined by the step (1). First, we least-square fit gaussian profiles to the observed spectra of the four hfs lines of the OH 18 cm transition simultaneously, assuming that the LSR velocity and the linewidth are identical for the four hfs lines. Thus, the peak intensities of the four hfs lines ($I_{1612}^{\rm obs}$,

(1) least-square fitting of a gaussian profile to the spectrum

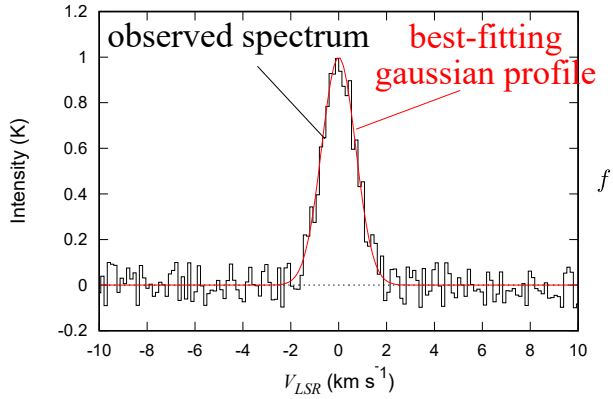

$$f(x) = I_0 \exp\left(-4\ln 2 \frac{(x - V_{LSR})^2}{\Delta V^2}\right)$$

(2) evaluation of a standard deviation from the residual

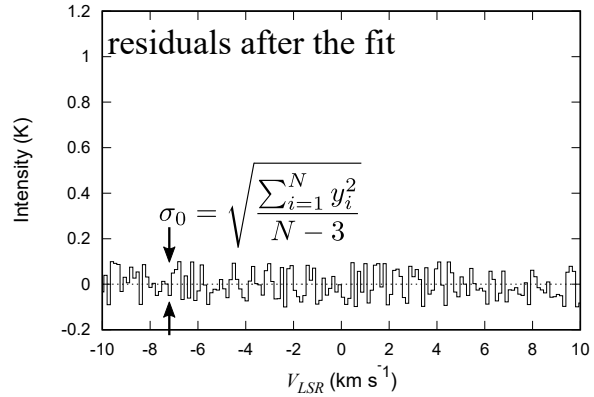

(3) evaluation of errors of line parameters (ε_i)

$$\boldsymbol{A} = \begin{pmatrix} \frac{\partial f_1}{\partial x_1} & \frac{\partial f_1}{\partial x_2} & \frac{\partial f_1}{\partial x_3} \\ \frac{\partial f_2}{\partial x_1} & \frac{\partial f_2}{\partial x_2} & \frac{\partial f_2}{\partial x_3} \\ \cdots & \cdots & \cdots \\ \frac{\partial f_N}{\partial x_1} & \frac{\partial f_N}{\partial x_2} & \frac{\partial f_N}{\partial x_3} \end{pmatrix}. \text{(Jacobian)} \qquad \boldsymbol{W} = \begin{pmatrix} w_1 & & \\ & \cdots & \\ & & w_N \end{pmatrix}. \text{(weight matrix)}$$

(Here, x_1, x_2, $x_3$represent I_0, V_{LSR}, ΔV, respectively.)

$$\boldsymbol{\epsilon} = \begin{pmatrix} {\epsilon_1}^2 & & \\ & {\epsilon_2}^2 & \\ & & {\epsilon_3}^2 \end{pmatrix} = \sigma_0^2 \boldsymbol{B^{-1}}, \text{ where } \boldsymbol{B} = \tilde{\boldsymbol{A}}\boldsymbol{W}\boldsymbol{A}.$$

Figure 28. A schematic illustration of our least-square analysis employed to determine the line parameters of the observed spectra. A Gaussian profile is employed for a model function. Parameters are the peak intensity (I_0), the LSR velocity (V_{LSR}) and the linewidth (ΔV) for a single line case. In the Gaussian fit of the spectral line profile, w_i is set to unity. Note that the four hfs lines of the OH 18 cm transition are fitted simultaneously in the actual analyses, assuming that the LSR velocity and the linewidth are identical for the four hfs lines, as described in the text.

$I_{1665}^{\rm obs}$, $I_{1667}^{\rm obs}$, $I_{1720}^{\rm obs}$), the LSR velocity (V_{LSR}), and the linewidth (ΔV) are determined by the fit. Errors of the obtained parameters are estimated from the residuals of the spectra by the error propagation, as schematically explained in Figure 28.

Then, these peak intensities of the four hfs lines are used to determine the gas kinetic temperature, the OH column density, and the H_2 ortho-to-para ratio by using our statistical equilibrium model by the least-square method. The H_2 density is fixed to be 10^3 cm^{-3}, since the hyperfine intensities are insensitive to the H_2 density within the range from 10^2 cm^{-3} to 10^7 cm^{-3}, as explained in Section 4.5. The H_2 densities of the observed sources are considered to fall within this range, as shown later in Section 4.6.2. In this calculation, the chi-square is actually minimized:

$$\chi^2 = \sum_{i=0,1,2,3} \left| \frac{I_i^{\rm model}(T_k, N({\rm OH}), {\rm OPR}) - I_i^{\rm obs}}{\sigma_{I_i}} \right|^2 , \tag{28}$$

where i=0, 1, 2, and 3 represent the 1612, 1665, 1667 and 1720 MHz lines, respectively. σ_{I_i} represents the error of the intensity of the line i, which is estimated from the residual of the gaussian fitting, as explained above. Errors of the obtained parameters are evaluated by finding the value of each parameter yielding $\Delta\chi^2 = \chi^2 - \chi^2_{min} = 1$. On the other hand, the errors are evaluated directly from the residuals of the fit by the error propagation, as in the case of Figure 28, when the H_2 ortho-to-para ratio is fixed in the fit. In this case, the gas kinetic temperature and the OH column density are taken as free parameters.

In order to verify that the error propagation method only considering the lowest order term (Figure 28) is appropriate for the error estimation in our model calculations, we carried out the above least-square fittings of the simulated data. First, the simulated data are prepared as follows. The intensities of the four hfs lines of the OH 18 cm transition are calculated by our statistical equilibrium calculations assuming the typical gas kinetic temperature of 50 K, the OH column density of 5 $\times$ 10^{14} cm^{-2}, and the H_2 ortho-to-para ratio of 3. These intensities are used for the 'real' spectrum of the OH 18 cm transition, where the LSR velocity and the linewidth are assumed to be 0 km s^{-1} and 1 km s^{-1}, respectively. Then, we add the artificial white noise to prepare the simulated spectrum. To this spectrum, we apply the least-square fittings in the first and second steps explained above. The

line parameters and physical parameters (T_k, N(OH), OPR) are thus determined by the fit. Errors of the parameters are evaluated by the error propagation method (Figure 28). Finally, we compare the 'real' value of each parameter and the value determined by the least-square fittings. If the deviation of the determined value from the 'real' value is smaller (larger) than the error of each parameter, the fitting is classified as 'correct' ('incorrect') for the parameter. The simulation is repeated 1000 times, and the number of 'correct' runs are counted for each parameter.

As a result, the intensities of the 1612, 1665, 1667 and 1720 MHz lines are 'correct' for 689, 676, 676, and 704 runs, respectively. They are close to 68 %, suggesting that the errors evaluated by the error propagation method in the first step of the least-square fittings (gaussian fitting) indeed correspond to the 68 % confidence level ($\Delta\chi^2 = 1$). Hence, the error propagation method is considered to be appropriate to evaluate the error of the line parameters.

As for the second step of the least-square fittings (non-LTE model), the T_k and N(OH) are 'correct' for 706 and 630 runs, respectively, when the H_2 ortho-to-para ratio is fixed in the fit. Although the counts for the OH column density of 630 is slightly small, they are almost comparable to 68%, considering the statistical error of the simulation ($\sqrt{1000} \sim 32$). On the other hand, when the H_2 ortho-to-para ratio (OPR) is taken as a free parameter, the T_k, N(OH) and OPR are 'correct' for 740, 738, and 769 runs, respectively. In this case, the obtained counts are apparently larger than 68%, suggesting that the errors are overestimated due to the break down of approximation using the lowest order term in the error propagation method employed here. Hence, the χ^2 method is employed to evaluate the error for this case, as explained above. However, this does not affect the contents and the conclusions of this thesis described in the forthcoming parts, because OPR is taken as a free parameter only for the spectra shown in Figure 29. We have indeed confirmed that the gas kinetic temperature and OH column density determined for the fixed and free OPR are almost comparable to each other for this spectrum.

χ^2 divided by the degree of freedom (dof) is employed to check the quality of the fit. The fittings to the spectra observed toward HCL2E, L183, ρ-Oph and Lupus yield the χ^2/dof of about 0.45–4.2, 10–15, 6.8–27, 3.0–130, respectively. The χ^2/dof value sometimes exceeds the unity, suggesting that our

model does not always reproduce the observed intensities well. Such a deviation might be caused by the imperfect treatment of the cloud geometry and its velocity structure. The far-infrared pumping effect and the effect of line overlaps might also contribute to this discrepancy, which is described later in detail in Chapter 6. On the other hand, the absorption feature of the 1612 MHz line and the enhanced emission of the 1720 MHz line are successfully reproduced by the fit even in the case of the large χ^2/dof. It should be noted that the errors of the determined physical parameters (T_k, N(OH), and OPR) do not include the systematic error due to imperfection of the model.

4.6.2 HCL2E

We first analyze the spectrum averaged for the 8 positions observed in HCL2E (Figure 29). The least-squares fit on the four hfs components yields the OH column density of $4.9^{+0.4}_{-0.4} \times 10^{14}$ cm^{-2}, the gas kinetic temperature of 55^{+4}_{-3} K, and the H_2 ortho-to-para ratio of $2.9^{+1.7}_{-0.8}$ with the χ^2/dof of 1.6. This result does not change within the error, if the H_2 density varies between 10^2 cm^{-3} and 10^4 cm^{-3}. The obtained parameters well reproduce the observed spectra (Figure 29). It should be noted that the quoted errors do not include the systematic uncertainty due to the collisional rates used, the radiative transfer effect, and the effect of neglecting infrared excitations to the excited rotational states. (e.g. Litvak 1969) As shown in Figure 29, the LSR velocity of the best-fitting profile of the 1612 MHz line (red line) slightly deviates from the observed spectra. It might be explained by multiple velocity

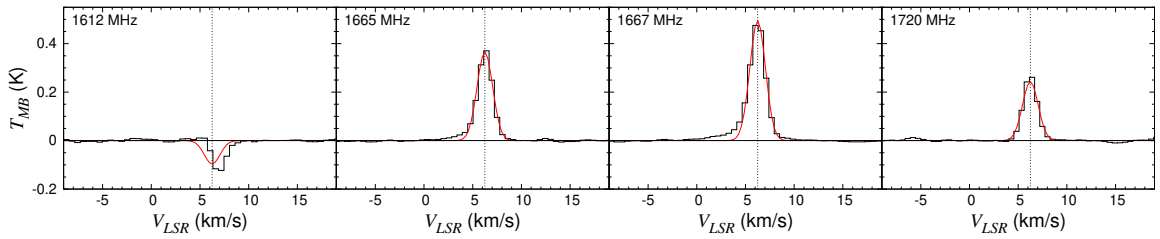

Figure 29. Spectra for the four hfs components of the OH 18 cm transition prepared by averaging the eight spectra (Figure 19) each observed toward the positions marked in Figure 18. Red lines show the Gaussian profiles with the best fit parameters, namely the OH column density of $4.9^{+0.4}_{-0.4} \times 10^{14}$ cm^{-2}, the gas kinetic temperature of 55^{+4}_{-3} K, and the H_2 ortho-to-para ratio of $2.9^{+1.7}_{-0.8}$.

components in the cloud, which are marginally seen as a wing component in the 1665 and 1667 MHz lines (V_{LSR} = 0–5 km s^{-1}). In this analysis, only a single velocity component is assumed due to the insufficient velocity resolution and signal-to-noise ratio. A more sensitive observation of the OH 18 cm transition, as well as a further analysis considering multi velocity components is necessary for more detailed analyses.

The gas kinetic temperature of 50 K corresponds to the FWHM linewidth produced by the thermal Doppler broadening of ∼0.5 km s^{-1}. This is smaller by a factor of 3–4 than the linewidths of the OH 18 cm transition observed toward HCL2E (Table 12). The linewidths observed toward L183, ρ-Oph and the Lupus-1 (broad component) (Table 12) are also broad ($>$ 1 km s^{-1}) compared to the thermal broadening. Such broad linewidths indicate the presence of supersonic turbulence or complex velocity structures in these clouds.

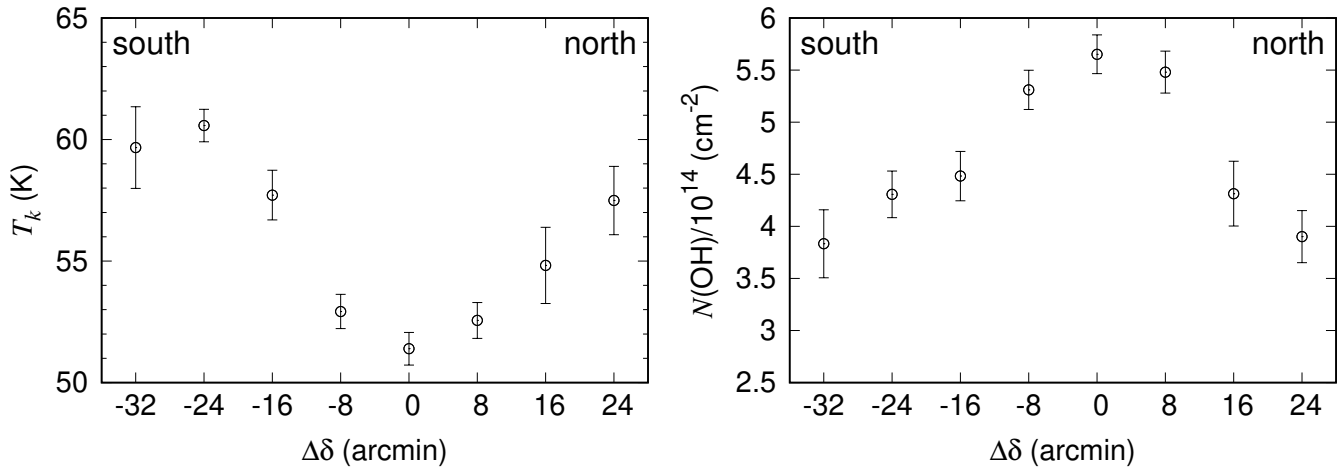

Figure 30. Gas kinetic temperatures (left) and OH column densities (right) for the eight positions observed in HCL2E derived from our statistical equilibrium calculations as a function of the angular offset along declination. Error bars show one standard deviation.

Further, we analyze individual positions to derive the OH column density and the gas kinetic temperature. The H_2 ortho-to-para ratio derived above is close to the statistical value of 3, and hence, we fix it to 3 in the fit. The results are shown in Table 7. For HCL2E, the derived gas kinetic temperature is 52 ± 1 K toward the central position (position A in Figure 18), and rises to 61 ± 1 K for positions located closer to the cloud boundary (Figure 30, left). Since HCL2E is a translucent cloud

whose visual extinction is about 4 magnitude (Maezawa 2000), this trend is naturally interpreted as photoelectric heating of the gas under irradiation of the interstellar UV radiation. In contrast, the OH column density is as high as (4–5) $\times$ 10^{14} cm^{-2} toward the central three positions, and decreases to 3.5 $\times$ 10^{14} cm^{-2} at the peripheries (Figure 30 right). Toward the central position, the fractional abundance of OH is estimated to be 1 $\times$ 10^{-7}. This is a typical fractional abundance of OH reported for diffuse and translucent clouds (Wiesemeyer et al. 2012; Weselak et al. 2010; Felenbok & Roueff 1996), and is consistent with chemical models (e.g. Le Petit et al. 2004, ; see also Chapter 2). In addition, the H_2 density is estimated to be $\sim$2 $\times$ 10^3 cm^{-3}, assuming the OH column density of 5 $\times$ 10^{14} cm^{-2}, the OH fractional abundance of 10^{-7}, and the cloud length along the line of sight of 1 pc. The H_2 density of 2$\times$ 10^3 cm^{-3} is indeed between the range from 10^2 to 10^7 cm^{-3}, where the intensities of the OH hfs lines are insensitive to the density (Section 4.5). Hence, the assumption for the H_2 density of 10^3 cm^{-3} in the fit (Table 7) is considered to be reasonable.

It should be noted that the gas kinetic temperature can be determined, even if the H_2 density is lower than 10^2 cm^{-3}. In this case, the intensities are sensitive to the H_2 density. In such a diffuse gas, the H_2 ortho-to-para ratio is considered to be close to the statistical value of 3. Therefore, the H_2 density, the gas kinetic temperature, and the OH column density can be determined by fitting the four hfs intensities of OH, assuming the H_2 ortho-to-para ratio of 3.

Table 7. Derived parameters for HCL2E, L183, ρ-Oph, and Lupus-1A[a] .

source	position	T_k [K]	N(OH) [cm^{-2}]	o/p ratio
HCL2E	(0′,24′)	58(1)	3.9(2)×10^{14}	3(fixed)
HCL2E	(0′,16′)	55(1)	4.3(3)×10^{14}	3(fixed)
HCL2E	(0′,8′)	53(1)	5.5(2)×10^{14}	3(fixed)
HCL2E	(0′,0′)	51(1)	5.7(2)×10^{14}	3(fixed)
HCL2E	(0′,-8′)	53(1)	5.3(2)×10^{14}	3(fixed)
HCL2E	(0′,-16′)	58(1)	4.5(2)×10^{14}	3(fixed)
HCL2E	(0′,-24′)	61(1)	4.3(2)×10^{14}	3(fixed)
HCL2E	(0′,-32′)	60(1)	3.8(3)×10^{14}	3(fixed)
L183	(0′,0′)	10(fixed)	2.7(1)×10^{14}	0(fixed)
L183	(0′,-8′)	31(8)	2.3(6)×10^{14}	3(fixed)
L183	(0′,-16′)	53(8)	2.0(13)×10^{14}	3(fixed)
ρ-Oph	(-3′,0′)	56(4)	5.3(20)×10^{14}	3(fixed)
ρ-Oph	(+4′,-12′)	44(3)	7.1(18)×10^{14}	3(fixed)
ρ-Oph	(+12′,-15′)	39(2)	7.1(8)×10^{14}	3(fixed)
ρ-Oph	(+20′,-18′)	28(7)	4.4(7)×10^{14}	3(fixed)
Lupus-1A	(8′, 8′) / $\sqrt{2}$	56(4)	1.7(3) ×10^{14}	3(fixed)
Lupus-1A	(0′, 0′) (broad)	47(4)	2.1(2) ×10^{14}	3(fixed)
Lupus-1A	(0′, 0′) (narrow)	24(1)	0.3(1) ×10^{14}	3(fixed)
Lupus-1A	(-8′, -8′)/$\sqrt{2}$ (broad)	42(7)	0.9(1) ×10^{14}	3(fixed)
Lupus-1A	(-8′, -8′)/$\sqrt{2}$ (narrow)	58(5)	0.2(5) ×10^{14}	3(fixed)
Lupus-1A	(-8′, 24′)/$\sqrt{2}$ (broad)	52(6)	1.3(2) ×10^{14}	3(fixed)
Lupus-1A	(-8′, 24′)/$\sqrt{2}$ (narrow)	60(1)	0.5(3) ×10^{14}	3(fixed)
Lupus-1A	(-16′, 32′)/$\sqrt{2}$	52(8)	0.7(2) ×10^{14}	3(fixed)
Lupus-1A	(-16′, 16′)/$\sqrt{2}$	52(9)	0.9(3) ×10^{14}	3(fixed)

NOTE—[a] The numbers in the parentheses represent the standard deviation of the fit in the units of the last significant digits.

4.6.3 L183

A similar least-squares analysis is also carried out toward the dark cloud L183. Since the absorption feature is not clearly seen in this source, the gas kinetic temperature of the source traced by the OH line must be lower than ∼50 K. Toward the dense core position, the intensity anomaly is almost absent. This means that the gas kinetic temperature is low and the excitation to the first rotationally excited state is inefficient. According to Figure 26, the gas kinetic temperature must be lower than 30 K for the intensities of the 1612 MHz line and the 1720 MHz line to be identical. We could reproduce the observed hyperfine pattern with a gas kinetic temperature below 25 K. Table 7 lists the result for a gas kinetic temperature of 10 K, which is the typical temperature for starless cores (e.g. Benson & Myers 1989). It should be noted that the 1720 MHz line may look slightly brighter than the 1612 MHz line. This is similar to what is reported for TMC-1 by Harju et al. (2000). However, it cannot be explained by our statistical equilibrium calculations described in this Chapter. This anomaly is revisited in Chapter 6 by considering FIR pumping effect. For the other two positions of L183, the gas kinetic temperature is determined from the hyperfine intensities. The temperature tends to increase toward the periphery (southern part), as shown in Table 7, indicating a contribution of the photoelectric heating by the interstellar UV radiation.

4.6.4 ρ-Ophiuchi

Since the intensity anomaly of the hyperfine components is clearly seen toward the four positions of the ρ-Ophiuchi molecular cloud, the gas kinetic temperature of each position is determined by least-squares analysis. This region is known as a photodissociation region illuminated by the exciting star HD147889. Weak radio continuum emission is extended over this region. However, its brightness temperature is mostly less than 100 mK at 2.3 GHz (Yui et al. 1993; Baart et al. 1980) which is much lower than the cosmic microwave background temperature. Hence, we ignore it in the analysis. Furthermore, we assume the H_2 ortho-to-para ratio to be the statistical value of 3. The gas kinetic temperatures and the OH column densities derived for the four positions are summarized in Table 7. The temperature is found to decrease with increasing distance, r, from the exciting star with the $r^{-1/2}$ law (Figure 31), which is expected from the balance between the heating by the exciting star

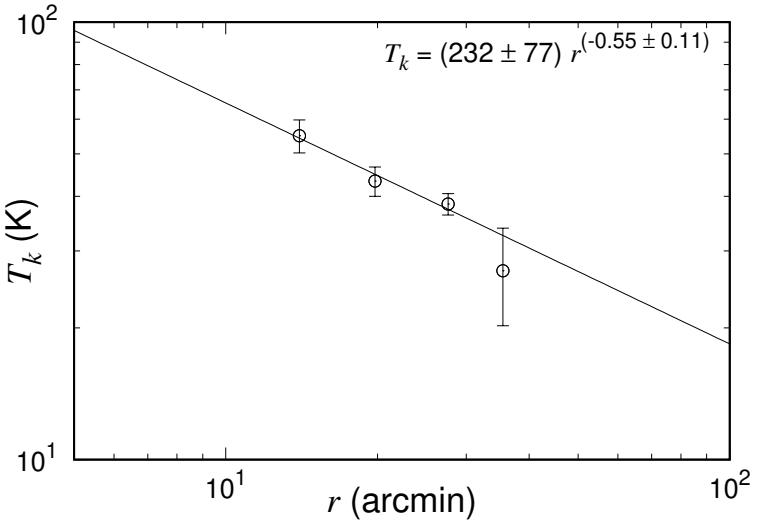

Figure 31. Gas kinetic temperatures for the four positions observed in ρ-Ophiuchi derived from our statistical equilibrium calculations as a function of the apparent distance (r) from the exciting star HD147889 (Figure 22). Error bars show one standard deviation. The temperature approximately follows the $r^{-1/2}$ law.

and thermal cooling. Kamegai et al. (2003) measured the excitation temperature of the fine structure levels of the neutral carbon atom to be 38 K and 29 K toward Peak I and the [C I] peak (Peak II) positions, respectively, by observing the $^3P_1 - {}^3P_0$ (492 GHz) and $^3P_2 - {}^3P_1$ (809 GHz) lines. These temperatures are lower than the present estimate from the OH hyperfine anomaly, probably because the [C I] lines trace denser regions in the PDR.

4.6.5 Lupus-1

We then apply the same statistical equilibrium analyses to the Lupus-1 data. The gas kinetic temperature and the OH column density of the broad and narrow components are determined (Table 7), except for the (+16′, +16′) and (-16′, -16′) positions due to the poor signal-to-noise ratio. As shown in the left panel of Figure 32, the gas kinetic temperature tends to rise toward the northeastern direction. Although the error of the derived temperatures are relatively large, this trend is apparent in the spectra (Figure 25). At the northeastern position (#2), the 1612 MHz line shows marginal absorption, indicating relatively high temperature, while it appears in weak emission at the south-western position (#4). Such a slight temperature gradient suggests the existence of a heating source

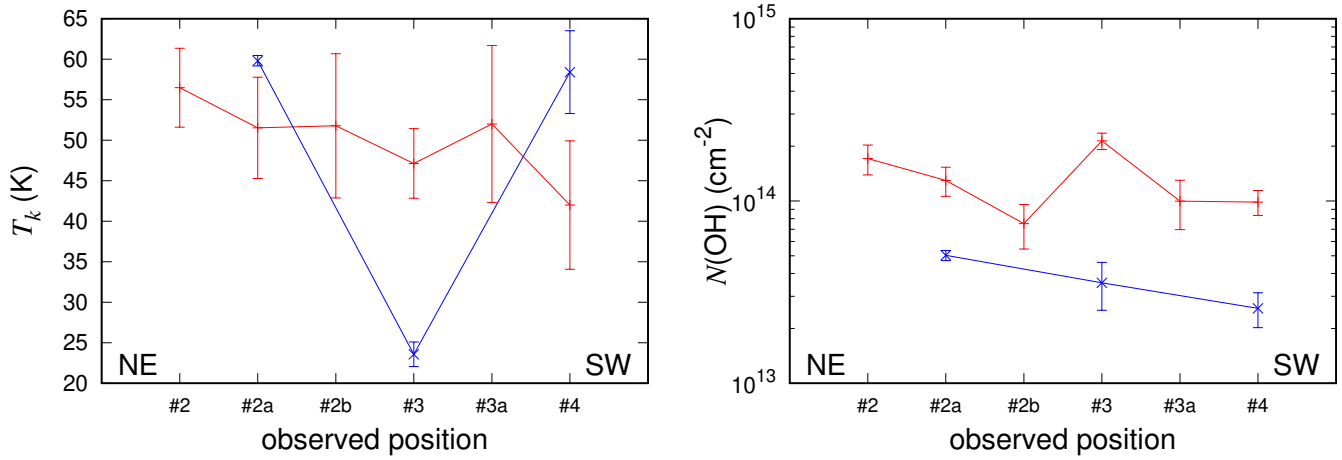

Figure 32. The gas kinetic temperatures (left) and the OH column densities (right) for the six positions observed in Lupus-1 derived from our statistical equilibrium calculations along the northeast to southwest direction. Derived parameters for the broad and narrow velocity components are indicated by red and blue colors, respectively. Error bars denote one standard deviation.

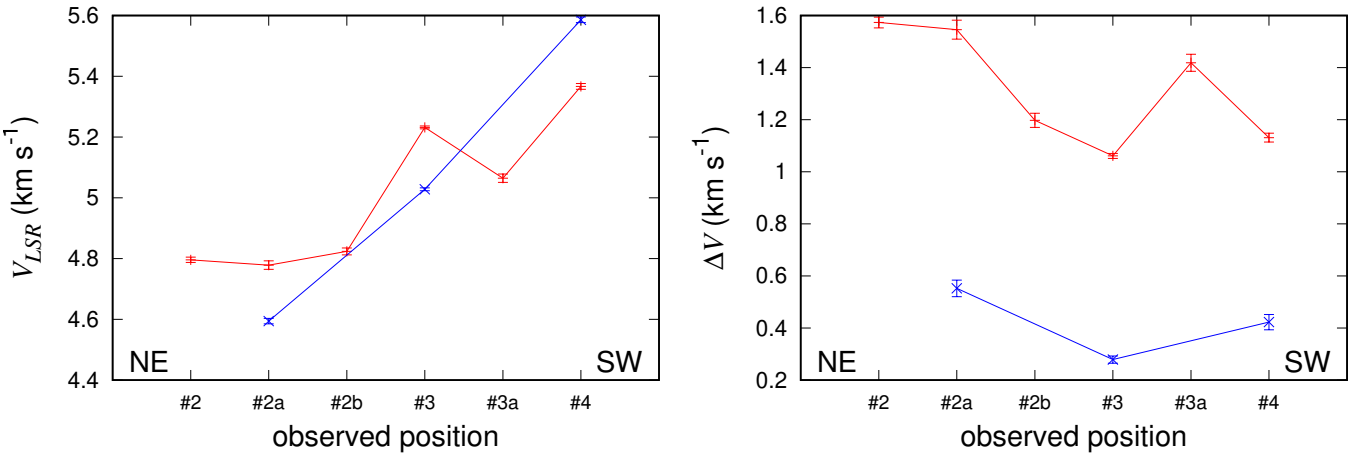

Figure 33. V_{LSR} (left) and FWHM linewidth (right) for the six positions observed in Lupus-1 derived by a Gaussian fit along the northeast to southwest direction. Derived parameters for broad and narrow velocity components are indicated by red and blue colors, respectively. Error bars denote one standard deviation.

toward the northeastern direction. In addition, the V_{LSR} velocities of the both velocity components tend to systematically increase from northeast to southwest (Figure 33 left), and the linewidth tends to be broader in the northeastern positions (Figure 33 right), suggesting the dynamical interaction

from the northeastern side. The velocity gradient along the northeast to southwest is also reported by Tothill et al. (2009); Benedettini et al. (2012) based on their CO and CS observations, respectively.

Figure 34 shows a large (∼100 pc) scale [H I] map (blue image) including the Lupus-1 molecular cloud within the yellow box (Tachihara et al. 2001). Since Lupus-1 is located between the Upper-Sco and Upper-Cen-Lup OB associations, UV radiation and dynamical interaction from them are considered to play an important role in the formation and shaping of the Lupus-1 molecular cloud (de Geus 1992; Tachihara et al. 1996, 2001). Since the gas kinetic temperature tends to be marginally higher in the north-eastern positions according to our OH observation, Lupus-1 seems to be more heated by the UV radiation from the Upper-Sco OB association. Moreover, the velocity gradient and the broader linewidth toward the north-eastern direction indicate a possible interaction between the [H I] shell surrounding the Upper-Sco OB association and the Lupus-1 molecular cloud.

4.7 Summary of this section

As demonstrated in this Chapter, the hyperfine intensity pattern of the OH 18 cm transition is an important probe for characterizing physical conditions of peripheries/envelopes of molecular clouds. In particular, it is a good thermometer over a wide range of the H_2 density. It is a good tracer of warm envelopes of molecular clouds which have not been studied extensively with the lines of CO and its isotopic species or the [H I] 21 cm line. These novel aspects of the OH 18 cm transition can be useful to trace transition zones between molecular cloud cores and diffuse clouds, which is important for an understanding of the formation processes of molecular clouds. However, the behavior of the hyperfine components of the OH 18 cm transition has not fully been understood. For example, a lower intensity of the 1720 MHz line than the 1612 MHz line cannot be explained by the statistical equilibrium calculations presented here. Such an anomaly is also seen in TMC-1 (Harju et al. 2000) and W40 (Crutcher 1977). We present more extensive observational exploration of this anomaly, together with further modeling, in Chapter 6.

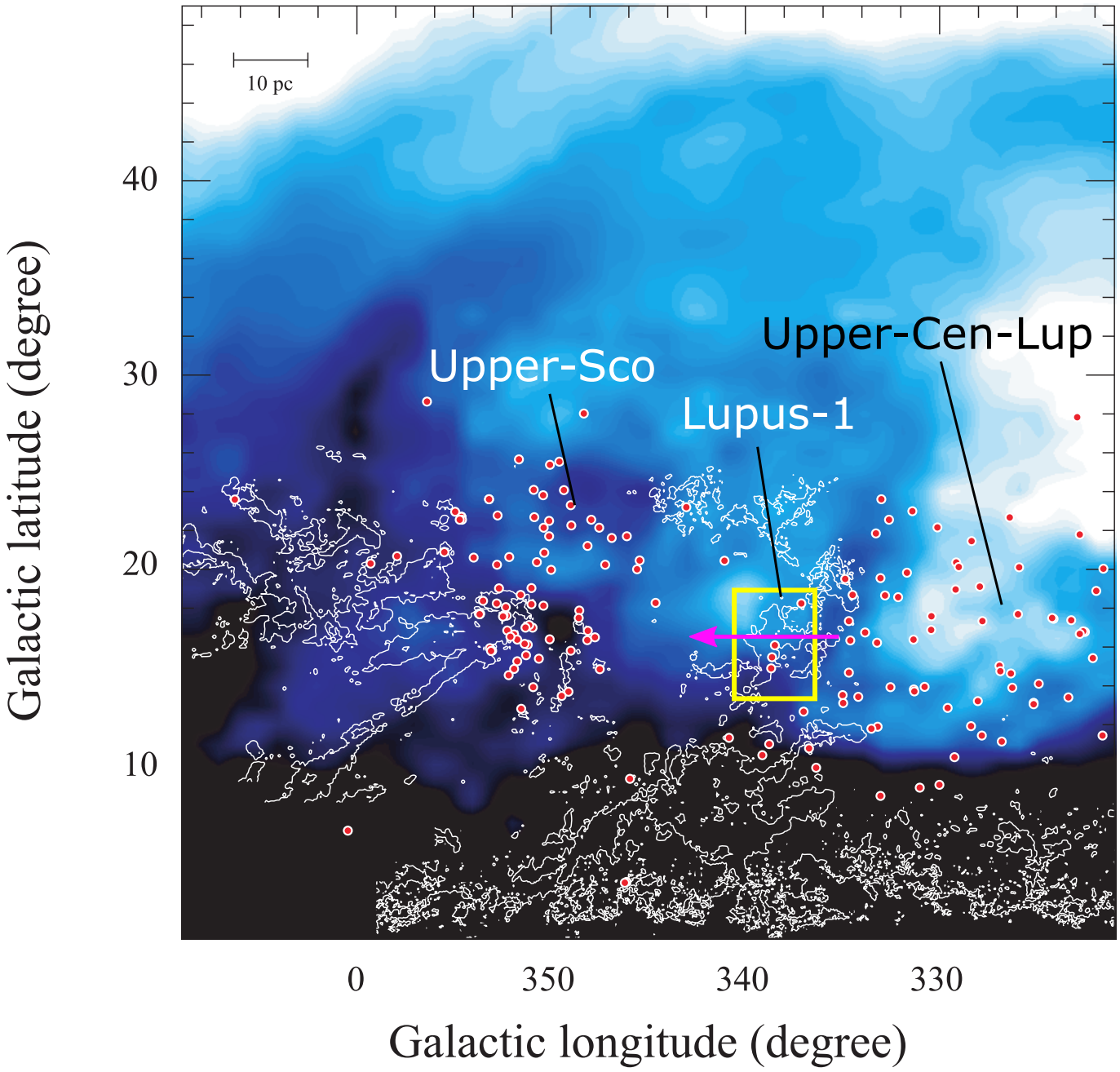

Figure 34. Integrated intensity map of the [H I] emission in blue image overlaid on the ^{12}CO in contours (Tachihara et al. 2001). The red dots represent positions of OB stars (Tachihara et al. 2001). Two large clusters in the Upper-Scorpius and Upper-Centaurus-Lupus OB associations can be seen. The Lupus-1 cloud is located in the area enclosed by the yellow rectangle. We observed the OH 18 cm transition along the strip line (#1–5 in Figure 24) parallel to the magenta arrow.

CHAPTER 5. Absorption feature in the main lines of OH

5.1 The Pipe nebula

In this Chapter, the new method using the hfs anomaly of the OH 18 cm transition to trace the warm region is applied to another molecular cloud, the Pipe nebula. The Pipe nebula is a filamentary ($\sim$ 3 pc $\times$ 18 pc) massive ($\sim 10^4$ $M_\odot$) dark molecular cloud complex (Frau et al. 2015), which was first observed in CO and its isotopologues by Onishi et al. (1999). Figure 35 shows a 2MASS visual extinction (A_K) map observed in the whole part of the Pipe nebula (Lombardi et al. 2006). As shown in Figure 35, the Pipe nebula roughly consists of three regions; B59 at the western end, the stem region which has a characteristic filamentary structure, and the bowl region exhibiting an extended structure in the eastern part. Since the Pipe nebula is a nearby ($\sim$ 145 pc) object (Alves & Franco 2007) with little star formation activity except for the B59 region (Onishi et al. 1999), it has been a good target to study molecular-cloud formation (Lada et al. 2008; Román-Zúñiga et al. 2010). It

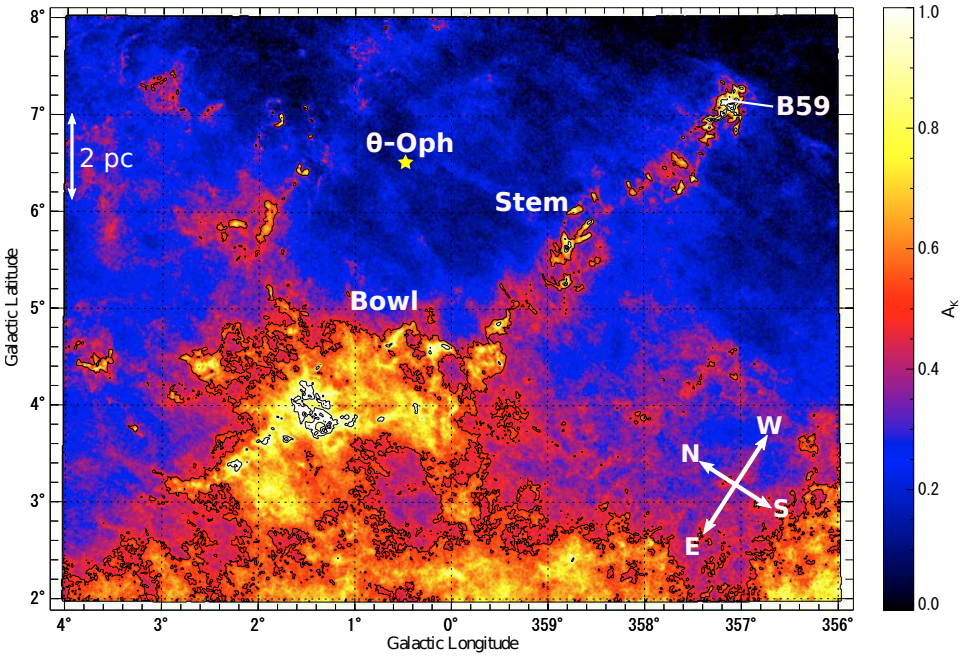

Figure 35. The visual extinction (A_k) map observed for the Pipe nebula (Lombardi et al. 2006). The position of the θ-Ophiuchi is represented by a yellow star mark.

has also been a good target for magnetic-field structure studies by polarimetry (Alves et al. 2008, 2014; Franco et al. 2010). A bright B2 IV star, θ Ophiuchi (HD 157056) is located at about 3 pc away from the Pipe nebula (Figure 35), and the heating effect of the UV radiation from the star has been proposed to understand the structure and the formation of the cloud (Onishi et al. 1999; Gritschneder & Lin 2012).

A velocity structure of the Pipe nebula was studied in the ^{12}CO and its isotopologue lines. Figure 36 shows the integrated intensity maps of the ^{13}CO ($J = 1-0$) (cyan contours) and ^{12}CO ($J = 1-0$)

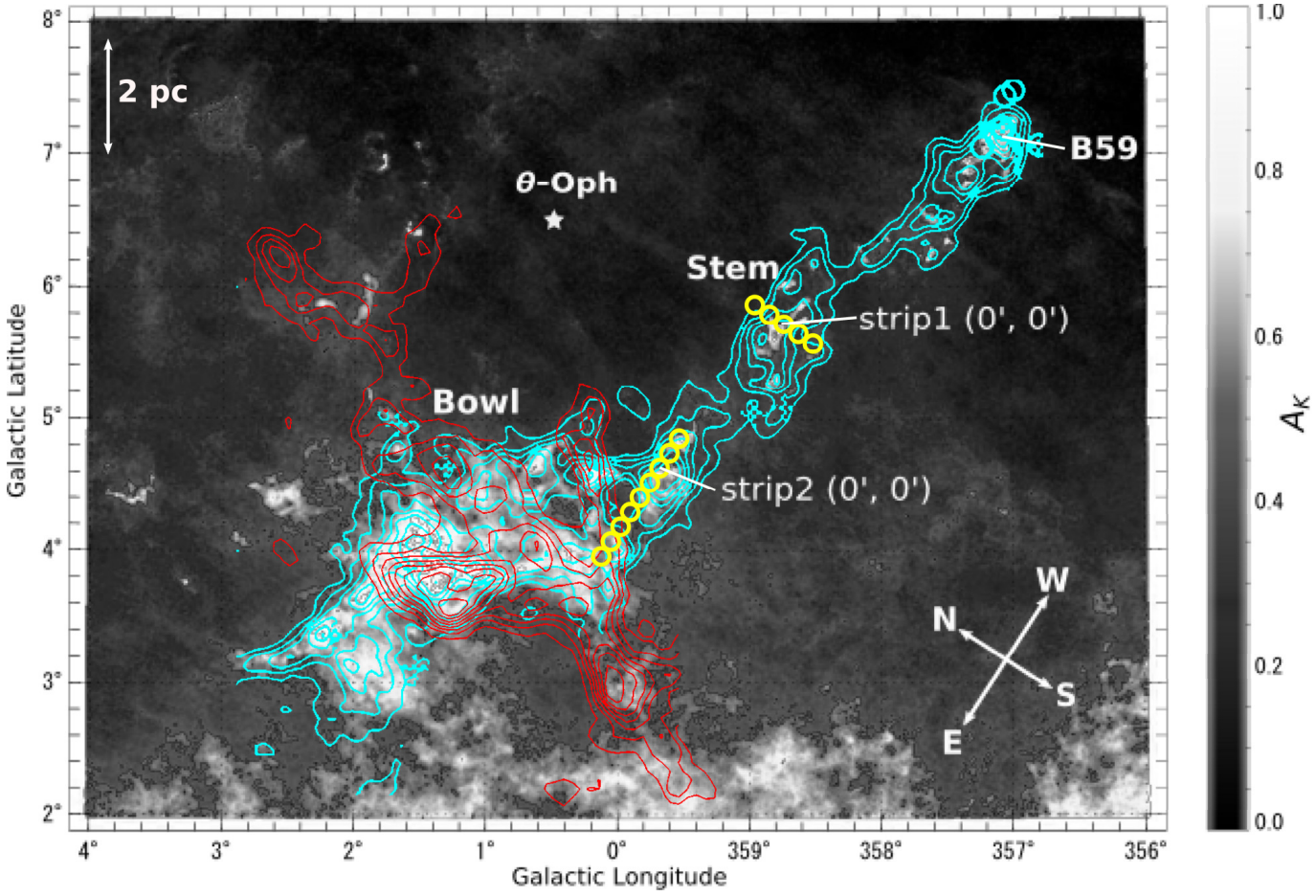

Figure 36. (Cyan) The integrated intensity map of the ^{13}CO (J=1–0) emission observed by Onishi et al. (1999). (Red) The integrated intensity map of the ^{12}CO (J=1–0) emission from 6 to 10 km s^{-1} observed by Onishi et al. (1999). (Gray) The visual extinction (A_k) map reported by Lombardi et al. (2006), which is the same as Figure 35. Yellow circles represent the observed positions in the OH 18 cm transition. A diameter of the circle corresponds to the HPBW beam size of the GBT 100-m telescope of 8 arcmin.

(red contours) lines by Onishi et al. (1999) overlaid on the visual extinction (A_K) map of Figure 35. The ^{12}CO map is prepared by integrating over the velocity range from 6 to 10 km s^{-1}. As shown in Figure 36, the ^{13}CO line traces a filamentary structure elongated along the west to east direction, which is seen in the visual extinction map. We hereafter call this structure as W-E filament. On the other hand, the ^{12}CO map exhibits another filamentary structure extended along the south to north direction (S-N filament) which is perpendicular to the W-E filament. According to Frau et al. (2015), the W-E filament has a blue-shifted velocity (V_{LSR} of 2–4 km s^{-1}), whereas the S-N filament has a red-shifted velocity (V_{LSR} of 6–7 km s^{-1}). These filamentary structures are overlapped on the bowl region, suggesting that they are colliding with each other there. This picture was predicted by Frau et al. (2015) on the basis of their combined analyses of the optical polarimetry, the visual extinction, and ^{13}CO data. They found that a gas in the bowl region tends to show a higher density and a broader linewidth, as well as a stronger polarization degree and a smaller dispersion of polarization angle in the optical observations, which is consistent with compressive motion caused by the filament-filament collisions.

In this Chapter, we investigate the origin of the Pipe nebula by examining the following two effects: (1) the UV heating from θ-Oph, and (2) the collisions between the W-E and S-N filaments. For this purpose, we explored a temperature structure of the Pipe nebula by observing the OH 18 cm transition. If the Pipe nebula is affected by the UV heating from θ-Oph, the gas kinetic temperature is likely to be increased with a decreasing distance from θ-Oph, as in the case of the ρ-Ophiuchi molecular cloud (Section 4.6.4). In addition, the temperature should be increased at the interface of the two filaments, if the filament collisions would occur.

5.2 Observation and data reduction

We observed the four hfs components of the OH 18 cm transition toward the Pipe nebula with the GBT 100-m telescope in 2018. The integration time was about 1.5 hours/position. Such a long integration time was necessary to obtain the rms noise temperature of 10 mK at a velocity resolution of 0.2 km s^{-1}. The data reduction was conducted in the similar way as that explained in Section 4.3.2. The observation was conducted along the two strip lines indicated by yellow circles in Figures

36. The reference (0′, 0′) positions of the strip-1 and strip-2 were (α_{2000}, δ_{2000}) = ($17^h20^m49^s.0$, -26°53′8.0″) and ($17^h27^m12^s.0$, -26°42′59.0″), respectively. On the strip-1, we assessed the UV heating effect from θ-Oph by determining the gas kinetic temperature as a function of the distance from the star. The strip-2 is parallel to the W-E filament seen in the visual extinction (A_K) map (Figure 35) and the ^{13}CO map (cyan contours in Figure 36). With the observation along the strip-2, we examine if the temperature is raised at the interface of the W-E and S-N filaments, in order to examine the possible collisions between them.

5.3 Result

Figure 37 shows the spectra of the OH 18 cm transition observed along the strip-1 (Figure 36). The 1612 MHz line shows a clear absorption feature for all the observed positions. In contrast, the 1720 MHz line shows a brighter emission than that expected under the LTE condition. This trend is the same as that presented in Chapter 4, indicating that we are looking at a warm ($>$ 40 K) gas component of the Pipe nebula in the OH 18 cm transition. The 1665 and 1667 MHz lines are the strongest at the central position, and they become weaker toward cloud peripheries. The typical V_{LSR} velocity of 3.3 km s^{-1} is represented by blue dotted lines in Figure 37.

Figure 38 shows the spectra of the OH 18 cm transition observed along the strip-2 (Figure 36). The top five spectra enclosed by a blue rectangle are observed in the stem region, whereas the bottom four spectra enclosed by a red rectangle are observed in the bowl region. Toward the stem region, the absorption feature of the 1612 MHz line and the enhanced emission of the 1720 MHz line are observed, as is the case of the strip-1 (Figure 37). The 1665 and 1667 MHz lines, which are called "main lines", are observed in emission at the V_{LSR} of $\sim$ 4 km s^{-1} in the stem region, as in ordinary cases. However, the main lines sharply turn from emission to absorption around the boundary between the stem region and the bowl region, which is apparent by comparing the spectra on the (+16′, 0′) and (+24′, 0′) positions. Namely, the main lines show emission at the (+16′, 0′) position, whereas clear absorption features of these lines are seen in the (+24′, 0′) position. Furthermore, the absorption feature in the main lines is the deepest at the (+32′, 0′) position, which is located at just the interface of the W-E and S-N filaments (Figure36). Therefore, the origin of the absorption feature

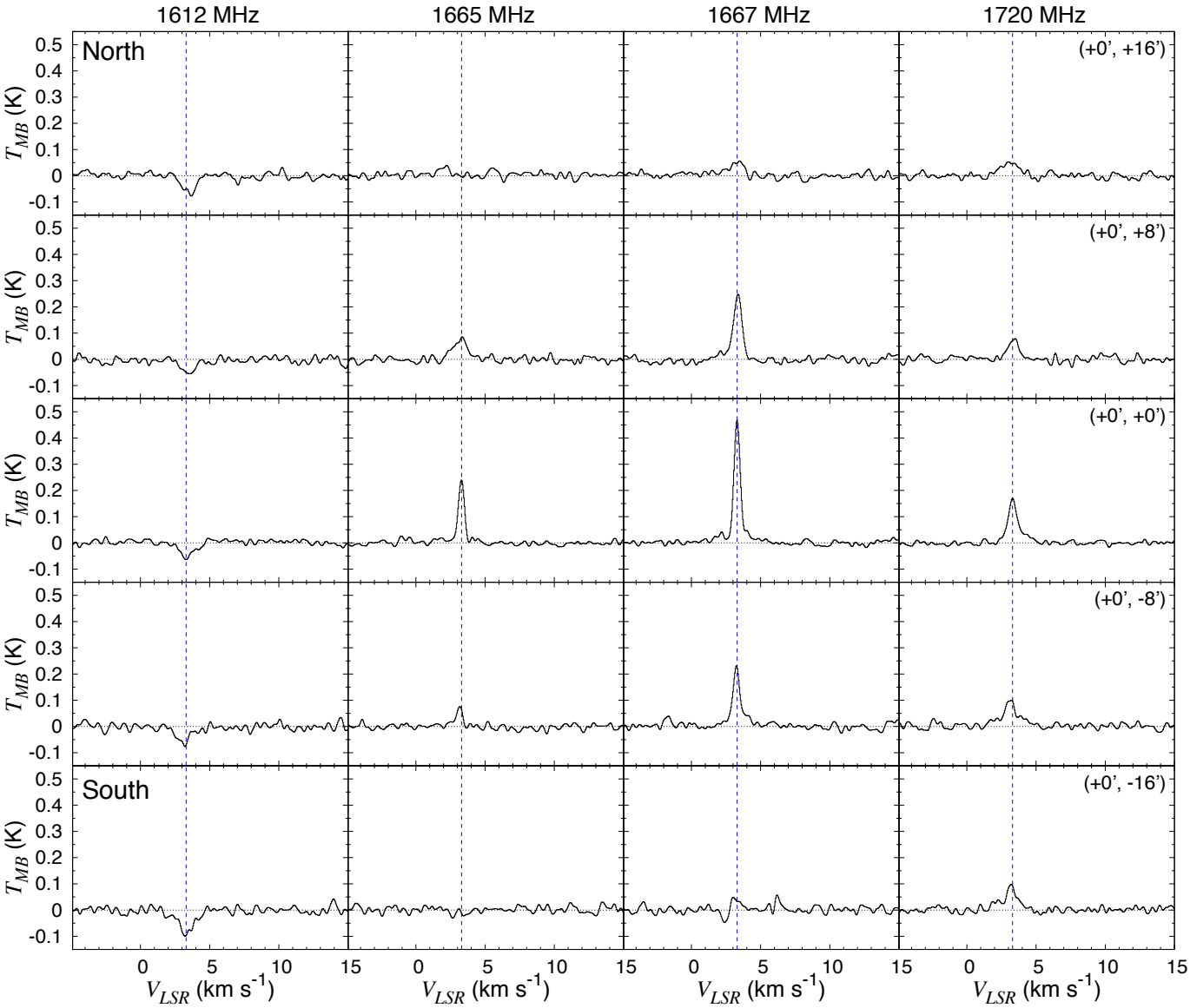

Figure 37. Spectra of the four hfs components of the OH 18 cm transitions observed toward the Pipe-nebula along the strip-1 in Figure 36. The blue dotted lines represent the V_{LSR} of 3.3 km s^{-1}.

in the main lines might be related to the collisions between these filamentary structures. It should be noted that this is the first detection of the absorption feature in the main lines in the course of our OH observations toward various molecular clouds without bright continuum sources. Detailed analyses of the main lines absorption and associated discussions in relation to the filament-filament collisions are discussed later in Section 5.5.

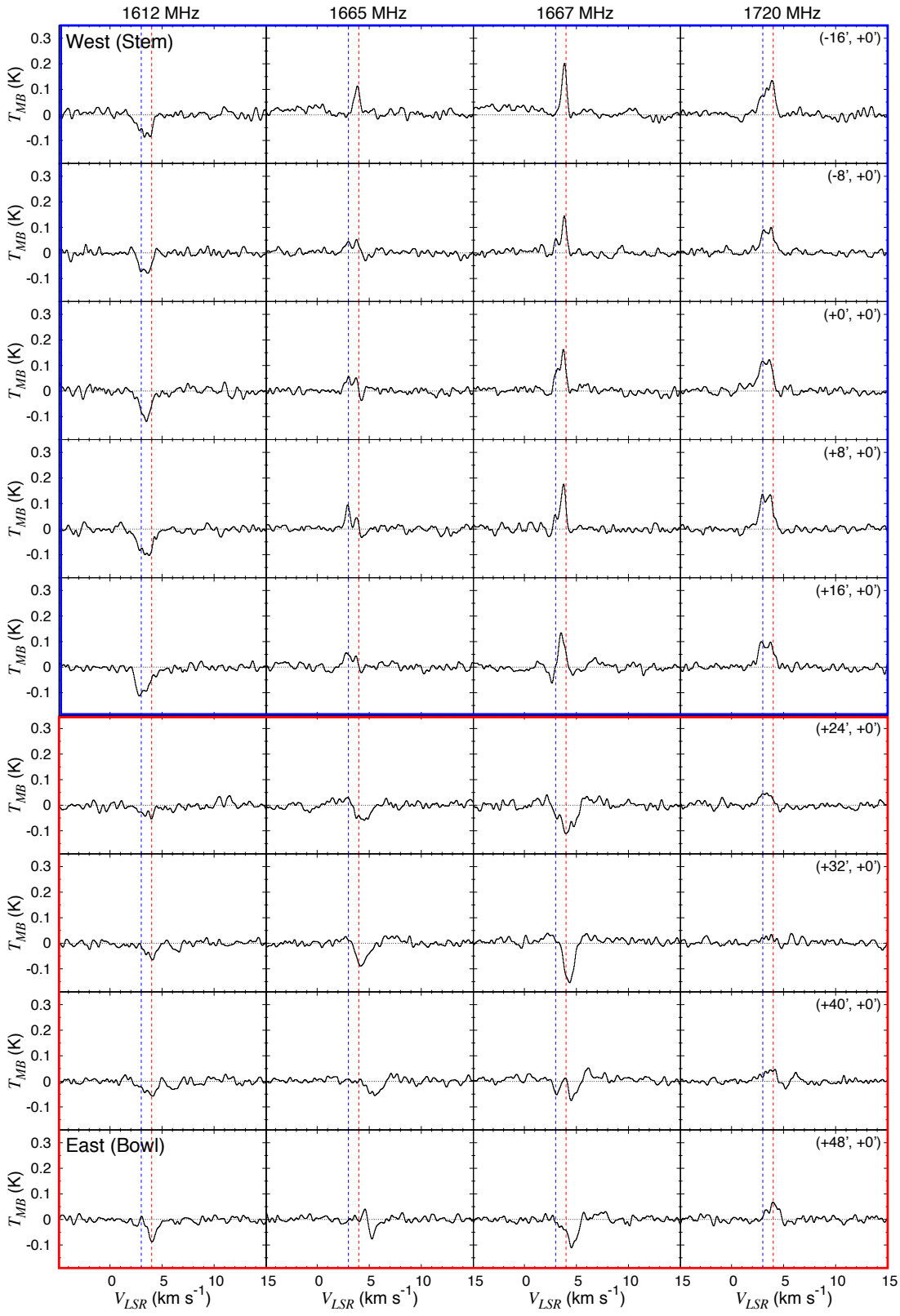

Figure 38. Spectra of the four hfs components of the OH 18 cm transitions observed toward the Pipe-nebula along the strip-2 in Figure 36. The blue and red dotted lines represent the V_{LSR} of 3.0 and 4.0 km s^{-1}, respectively. The spectra enclosed by the solid blue rectangle are for the stem region, while those enclosed by the solid red rectangle are for the bowl region.

Table 8. Observed line parameters toward the Pipe nebula along the strip-1. [a]

$\Delta\delta$ (arcmin)	V_{LSR} (km s^{-1})	FWHM (km s^{-1})	T_{MB}(1612) (K)	T_{MB}(1665) (K)	T_{MB}(1667) (K)	T_{MB}(1720) (K)
-16	3.27(1)	1.23(4)	-0.092(3)	-0.016(2)	0.026(2)	0.079(3)
-8	3.22(1)	0.82(1)	-0.073(3)	0.055(3)	0.191(4)	0.105(3)
0	3.23(1)	0.57(1)	-0.074(4)	0.226(4)	0.450(4)	0.188(4)
8	3.34(1)	0.82(1)	-0.063(3)	0.088(3)	0.229(3)	0.081(3)
16	3.32(2)	1.30(4)	-0.062(2)	0.005(2)	0.051(2)	0.053(2)

[a] $\Delta\delta$ in the first column denotes a DEC. offset from the (α_{2000}, δ_{2000}) = ($17^h20^m49^s.0$, -26°53′8.0″) position. The main beam temperatures (T_{MB}) of the four hfs lines of OH, the V_{LSR} value, and the linewidth (FWHM) are obtained by a Gaussian fit, assuming that the V_{LSR} values and the linewidths of the four hfs lines are identical for each observed position. The error in the parentheses represents one standard deviation, which applies to the last significant digits.

The four hfs components of the OH 18 cm transition consist of two velocity components in the stem region at V_{LSR} of ∼3.0 and ∼4.0 km s^{-1}, which are represented by blue and red dotted lines in Figure 38, respectively. Line parameters are summarized in Table 8. In contrast, the 3 km s^{-1} component is generally faint or almost absent in the bowl region, whereas the ∼4.0 and ∼5.0 km s^{-1} components are blended there. Hence, we could not determine the line parameters assuming two velocity components due to poor signal-to-noise ratio. The line parameters are then determined by fitting a single gaussian profile for the spectra in the bowl region (Table 9).

Table 9. Observed line parameters toward the Pipe nebula along the strip-2. [a]

	$\Delta\alpha$ (arcmin)	V_{LSR} (km s^{-1})	FWHM (km s^{-1})	T_{MB}(1612) (K)	T_{MB}(1665) (K)	T_{MB}(1667) (K)	T_{MB}(1720) (K)
Stem region	-16	3.26 (3)	1.45 (5)	-0.070 (3)	0.008 (3)	0.009 (3)	0.082 (3)
		3.84 (1)	0.54 (1)	-0.036 (6)	0.111 (5)	0.190 (5)	0.086 (7)
	-8	3.12 (1)	0.82 (4)	-0.078 (3)	0.039 (3)	0.038 (3)	0.088 (3)
		3.85 (1)	0.50 (1)	-0.063 (4)	0.041 (4)	0.135 (4)	0.089 (5)
	0	3.08 (3)	0.95 (5)	-0.084 (3)	0.044 (3)	0.055 (4)	0.118 (3)
		3.74 (1)	0.57 (2)	-0.083 (7)	0.022 (5)	0.138 (5)	0.082 (0)
	8	2.95 (1)	0.69 (2)	-0.092 (4)	0.076 (3)	0.028 (4)	0.129 (4)
		3.73 (1)	0.63 (1)	-0.114 (4)	0.023 (4)	0.160 (4)	0.132 (4)
	16	2.76 (1)	0.68 (2)	-0.105 (4)	0.051 (3)	-0.063 (4)	0.078 (4)
		3.57 (1)	0.90 (3)	-0.088 (3)	0.029 (3)	0.118 (3)	0.095 (3)
Bowl region	24	4.14 (2)	1.54 (5)	-0.036 (3)	-0.051 (3)	-0.102 (3)	0.019 (3)
	32	4.26 (1)	1.00 (2)	-0.055 (3)	-0.094 (4)	-0.155 (4)	0.014 (3)
	48	4.27 (2)	1.30 (5)	-0.066 (3)	0.0048 (3)	-0.090 (3)	0.051 (3)

[a] $\Delta\alpha$ in the first column denotes a R.A. offset from the (α_{2000}, δ_{2000}) = ($17^h27^m12^s.0$, -26°42′59.0″) position. The main beam temperatures (T_{MB}) of the four hfs line of OH, the V_{LSR} value, and the linewidth (FWHM) are obtained by a Gaussian fit, assuming that the V_{LSR} values and the linewidths of the four hfs lines are identical for each observed position. The error in the parentheses represents one standard deviation, which applies to the last significant digits.

5.4 Heating effect from θ-Ophiuchi

We determined the gas kinetic temperature and the OH column density for all the observed positions along the strip-1 (Figure 36) in the similar way as that explained in Section 4.6.1, assuming the H_2 column density of 10^3 cm^{-3} and the H_2 ortho-to-para ratio of 3 (Table 10). Since the hfs intensity anomaly of the OH 18 cm transition is insensitive to the H_2 density from 10^2 cm^{-3} to 10^6 cm^{-3}, the assumption of the H_2 density of 10^3 cm^{-3} is just arbitrary, and does not affect the results. Figure

Table 10. The derived parameters along the strip-1.[a]

$\Delta\delta$	T_k (K)	N(OH) (10^{14} cm^{-2})
-16′	78 (3)	1.3 (3)
-8′	66 (4)	1.0 (2)
0′	55 (3)	1.1 (1)
8′	61 (5)	0.99 (22)
+16′	75 (3)	1.1 (2)

[a]The numbers in the parentheses represent one standard deviation of the fit in units of the last significant digits.

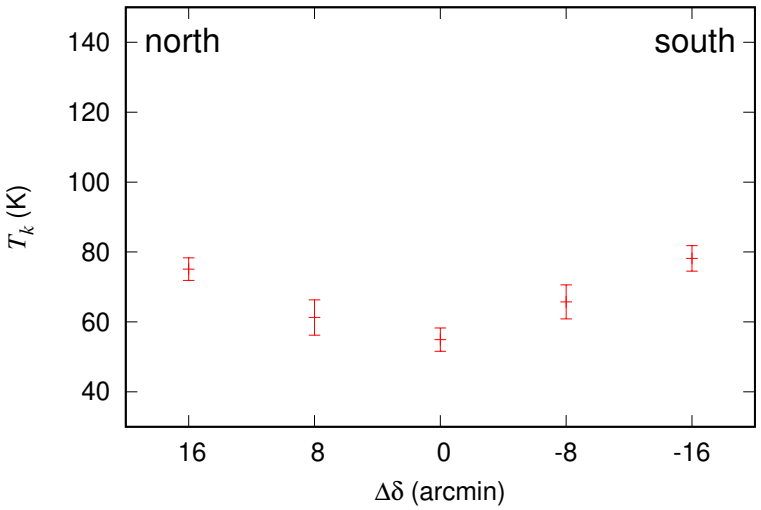

Figure 39. The gas kinetic temperatures along the strip-1 in Figure 36 determined by using our statistical equilibrium calculations. The abscissa is the angular offset from the center (Table 8). Error bars denote one standard deviation.

39 shows the derived gas kinetic temperatures as a function of the angular offset along the strip-1 (Figure 35). The θ-Ophiuchi star is closer to the northern positions on the left-hand side of Figure 39. The temperature is found to be higher in the cloud peripheries, indicating more efficient UV-shielding effect near the center of the W-E filament. However, we found no temperature gradient as a function of the distance from θ-Oph. Therefore, the heating effect from the star is not significant in the gas kinetic temperature, based on this observation. The temperature rise in the cloud peripheries would likely be caused by the interstellar UV radiation, as in the case of HCL2E (Figure 30 (left) in Section 4.6.2). This result seems consistent with a result by Onishi et al. (1999). They reported that the UV heating effect from θ-Oph on the cloud structure is negligible, since the total gravitational energy of the cloud estimated from ^{12}CO line is about two order of magnitude larger than the energy distributed by a stellar wind from θ-Oph over a period of 10 Myr. Our OH observation further confirms this picture in terms of the gas kinetic temperature.

5.5 The origin of the main lines absorption

In this section, we explore the origin of the absorption feature of the 1665 and 1667 MHz main lines of the OH 18 cm transition, which is observed in the bowl region of the Pipe nebula (Figure 38). This origin might be related to the interactions of the W-E and S-N filaments, since the absorption is exclusively observed in the bowl region where these filaments are overlapped, and the absorption is the deepest at just the interface of the filaments (i.e. $(+32', 0')$ position). Actually, the absorption feature in the main lines is already predicted by our statistical equilibrium calculations presented in Section 4.5. As shown in Figure 26 (a), the 1665 and 1667 MHz lines appear in absorption with a gas kinetic temperature higher than about 80 K and 90 K, respectively. The absorption becomes deeper as the increasing gas kinetic temperature. This prediction suggests that the main lines absorption observed in the bowl region traces a warm gas with a gas kinetic temperature higher than 90 K. A fact that the deepest absorption feature appears at the interface of the filaments means that the heating effect by the filament-filament collisions would be the most significant at the interface.

The absorption feature in the main lines of the OH 18 cm transition can qualitatively be explained in terms of the non-LTE effect. Most of the OH molecules excited to the rotationally excited states

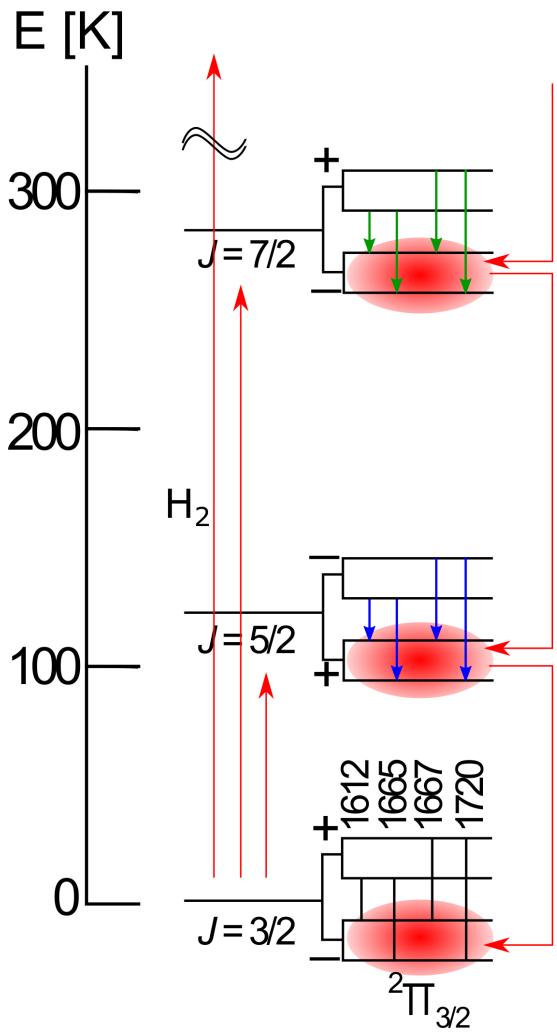

Figure 40. The rotational energy diagram for the $^2\Pi_{3/2}$ states of the OH molecule. The overpopulation in the lower Λ-type doubling levels of the rotationally excited states is produced by the Λ-type doubling transitions (green and blue arrows). The subsequent rotational transitions (red downward arrows) produce the overpopulations in the − levels of the J=3/2 states, respectively.

in the $^2\Pi_{3/2}$ ladder (J = 5/2, 7/2 or higher) by collisions with H_2 molecules are quickly de-excited to the ground rotational state ($^2\Pi_{3/2}$ J = 3/2) by the rotational transitions within the $^2\Pi_{3/2}$ ladder (red downward arrows in Figure 40). During the radiative decay, the Λ-type transitions within each rotational level can occur, as represented by the blue and green arrows in Figure 40. Thus the populations of the lower Λ-type doubling levels relative to the upper ones are slightly increased in the $^2\Pi_{3/2}$ J = 5/2, 7/2, or higher states, as represented by the red ellipses in Figure 40. These overpopulations in the lower Λ-type doubling levels subsequently produce a similar anomaly in the

ground rotational state via rotational transitions within the $^2\Pi_{3/2}$ ladder (red arrows in Figure 40). In this situation, the excitation temperatures of the 1665 and 1667 MHz lines are decreased, and these lines can appear in absorption against CMB, if they become lower than 2.73 K. It should be noted that the Λ-type transitions in the rotationally excited states rarely occur compared to the rotational transitions, since Einstein's A coefficients of these transitions are about 10^9–10^{10} times lower than those of the rotational transitions (Offer et al. 1994). This suggests that the Λ-type transitions in the rotationally excited states affect the population only slightly. Nevertheless, such a slight effect on the population can significantly change the excitation temperature of the OH 18 cm transition because of its small energy gap ($\Delta E \sim 0.08$ K). The energy gap of 0.08 K is so small that the populations of the upper and lower states of this transition are almost comparable even in the low temperature. For example, assuming the excitation temperature of 2 K, 10 K and 100 K, the population difference between the upper and lower states are about 2%, 0.4% and 0.04%, respectively. This implies that the excitation temperature can be lower than 2.73 K, just by raising the lower state population

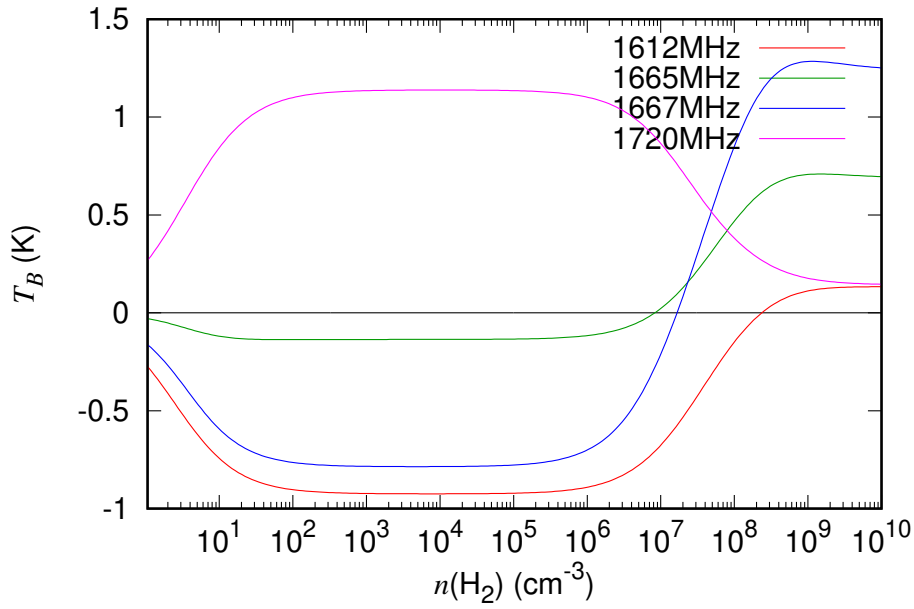

Figure 41. The derived intensities of the OH 18 cm transition hfs lines as a function of the H_2 density, where the OH column density, the gas kinetic temperature, and the H_2 ortho-to-para ratio are assumed to be 5×10^{14} cm^{-2}, 100 K and 3, respectively.

by only a few percent, which would be possible through the Λ-type transitions despite their slow radiation rate. The collisional excitations to the upper rotationally excited states are more efficient with increasing gas kinetic temperature, which leads to deeper absorption features of the main lines, as shown in Figure 26 (a). Note that the contributions from the $^2\Pi_{1/2}$ state have little contributions to the main lines absorption, since inter-ladder radiative transitions from $^2\Pi_{1/2}$ to $^2\Pi_{3/2}$ are much less frequent than those within the $^2\Pi_{1/2}$ or $^2\Pi_{3/2}$ ladders.

Figure 41 shows the expected intensities of the hfs lines of the OH 18 cm transition derived from our statistical equilibrium calculations. Here, the OH column density, the gas kinetic temperature and the H_2 ortho-to-para ratio are assumed to be 5×10^{14} cm^{-2}, 100 K and 3, respectively. The absorption features of the main lines as well as that of the 1612 MHz line are reproduced in the H_2 density range from 1 to 10^6 cm^{-3}. Moreover, intensities of all the four hfs lines are insensitive to the H_2 density from 10^2 to 10^6 cm^{-3}, as in the case of the result in Section 4.5 (Figure 26). This suggests that the radiative transitions is dominant over the collisional transitions at this H_2 density range at the gas kinetic temperature of 100 K. This is consistent with the above description on the origin of the main lines absorption, where the absorption is produced by Λ-type transitions through the rotational decay.

In order to examine if our statistical equilibrium analysis can quantitatively reproduce the absorption feature in the main lines as well as the intensities of the 1612 and 1720 MHz satellite lines, we first perform the least-squares fit on the OH spectra observed on (+32′, 0′) position (Figure

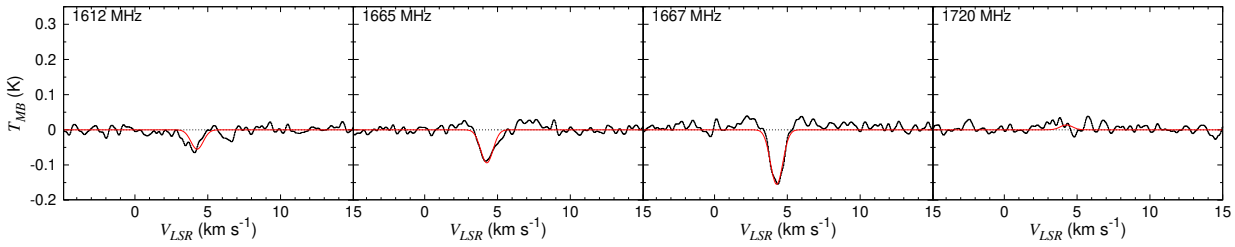

Figure 42. Spectra for the four hfs components of the OH 18 cm transition observed on the (+32′, 0′) position on the strip-2 (Figure 36). Red lines show the Gaussian profiles with the best-fit parameters derived from our statistical equilibrium calculations, namely the gas kinetic temperature of 108 K and the OH column density of 5.8×10^{13} cm^{-2}.

42), which shows the deepest absorption feature. In this analysis, we conduct the same statistical equilibrium calculation as that used in Chapter 4, assuming the H_2 density of 10^3 cm^{-3} and the H_2 ortho-to-para ratio of 3. As a result, the observed intensities of the four hfs lines are well reproduced by the simultaneous fit, as shown in the red lines in Figure 42. The gas kinetic temperature and the OH column density are determined to be 108 $\pm$ 6 K and (5.8 $\pm$ 1.1) $\times$ 10^{13} cm^{-2}, respectively. The gas kinetic temperature of 108 K is apparently higher than that derived in the stem region along the strip-1 (60–80 K) (Figure 39), suggesting the heating effect by the filament-filament collisions. From this analysis, we confirm the applicability of our statistical equilibrium calculation to a cloud with a gas kinetic temperature higher than 100 K by focusing on the main lines absorption.

It should be noted that radio continuum emission from background sources has only a limited effect on the above results. According to Jonas et al. (1998), intensity of the 2.3 GHz radio continuum emission in the Pipe nebula is 0.25–0.5 K. Assuming that the radio continuum emission at the frequency of $\sim$1–2 GHz mainly comes from the galactic H II regions toward the Pipe nebula, and thus thermal free-free emission dominates the continuum emission, the spectral index is estimated to be between -0.1 (optically thin) and 2 (optically thick) (Keto 2003). In this situation, the intensity of the continuum emission (T_{cont}) at the frequency of the OH 18 cm transition (1.612–1.720 GHz) is also lower than $\sim$0.5 K. Assuming the upper limit of T_{cont} of 2.73 + 0.5 = 3.23 K, the gas kinetic temperature is determined to be 97 $\pm$ 7 K by fitting the OH spectra in Figure 42. Hence, the gas kinetic temperature is overestimated by $\sim$10 % at most, if we ignore the contribution of the background free-free emission. However, the gas kinetic temperature of 97 K is still much higher than those determined for the strip-1 (60–80 K). In this work, we assume T_{cont} of 2.73 K, since it is difficult to estimate T_{cont} accurately for each observed positions due to the large beam size of the 2.3 GHz map by Jonas et al. (1998) (20′), and uncertainties in the spectral index. Although the gas kinetic temperature might be overestimated by 10 % at most, this does not change the results in the following sections. In particular, this assumption is negligible for the relative temperature structure of the Pipe nebula.

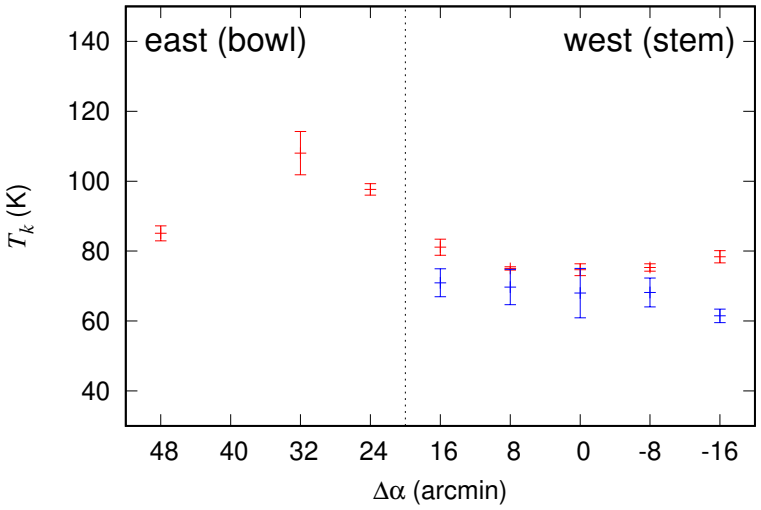

Figure 43. The gas kinetic temperatures along the strip-2 in Figure 36 determined by using our statistical equilibrium calculations. The abscissa is the angular offset from the center (Table 9). Error bars denote one standard deviation.

We then perform the same least-squares fit on all the spectra along the strip-2 (Figure 38) with our statistical equilibrium calculations assuming T_{cont} of 2.73 K, as explained above. The density and the ortho-to-para ratio of H_2 are assumed to be 10^3 cm^{-3} and 3, respectively during the fit. The derived gas kinetic temperatures and OH column densities are summarized in Table 11. Figure 43 shows the derived gas kinetic temperatures as a function of the angular offset from the center. As for the stem region (right five points in Figure 43), the temperatures of the 3 and 4–5 km s^{-1} components are determined to be about 60–70 K and 70–80 K, respectively, as represented by blue and red colors, respectively. Toward the bowl region (left four points in Figure 43), we assume only a single velocity component due to insufficient signal-to-noise ratio, as described in Section 5.3. The gas kinetic temperatures are determined to be 98 ± 1 K and 108 ± 6 K for the positions with $\Delta\alpha$ of 24′ and 32′, respectively. The gas kinetic temperature is determined to be 85 ± 2 K at a further eastern position ($\Delta\alpha = 48'$). As shown in Figure 43, the derived gas kinetic temperature is indeed higher at the positions exhibiting the deep main lines absorption ($\Delta\alpha = 24', 32'$) (Figure 38). Since these positions are located on the interface of the two filamentary structures (Figure 36), the rise

Table 11. The derived parameters along the strip-2.[a]

	$\Delta\alpha$	V_{LSR} (km s^{-1})	T_k (K)	N(OH) (10^{14} cm^{-2})
Stem region	-16′	3.26	78 (1)	1.6 (1)
		3.84	61 (1)	0.63 (6)
	-8′	3.12	75 (1)	0.97 (8)
		3.85	68 (4)	0.55 (14)
	0′	3.08	75 (1)	1.2 (1)
		3.74	68 (7)	0.58 (29)
	8′	2.95	75 (1)	1.00 (4)
		3.73	70 (5)	0.90 (24)
	16′	2.76	81 (2)	0.85 (10)
		3.57	71 (4)	1.1 (2)
Bowl region	24′	4.14	98 (1)	0.87 (7)
	32′	4.26	108 (6)	0.58 (11)
	48′	4.27	85 (2)	1.4 (1)

[a]The numbers in the parentheses represent one standard deviation of the fit in the units of the last significant digits.

of the gas kinetic temperature can be interpreted as the heating effect by the collisions between the filaments.

A warm gas, as high as 100 K, heated by the filament collisions is cooled down mainly by a rotational transition of CO for the H_2 density of 10^3 cm^{-3} (Inoue & Inutsuka 2012). The cooling time (t_{cool}) is estimated to be around 10^4 year according to Koyama & Inutsuka (2000) with a cooling rate of 10^{-26} erg cm^{-3} s^{-1} (Inoue & Inutsuka 2012). Assuming that a warm gas expands with a constant velocity of 1.5 km s^{-1}, which corresponds to a typical velocity difference between the blue-shifted and red-shifted components of the Pipe nebula of 3.0 km s^{-1} and 4–5 km s^{-1}, respectively, the gas can extend in space by about 0.015 pc within the cooling time. This length corresponds to a typical spatial scale of a shocked warm region, and hence we hereafter call it as $L_{warm} = 0.015$ pc. On the other hand, a cloud size along the line-of-sight direction (L_{LOS}) can be estimated from the H_2

density ($n(H_2)$), the OH column density (N(OH)) and the OH fractional abundance (X(OH)) with the following equation:

$$L_{LOS} = \frac{N(\mathrm{OH})}{X(\mathrm{OH})2n(\mathrm{H_2})}. \tag{29}$$

We employ the H_2 density of 10^3 cm^{-3} and the OH column density of 6×10^{13} cm^{-2}, whose values are determined for $\Delta\alpha$=32′ position (Table 11). Assuming the OH abundance of 10^{-7}, which is a typical value in diffuse clouds (Wiesemeyer et al. 2012), L_{LOS} is estimated to be 3×10^{17} cm ~ 0.1 pc. If the OH fractional abundance is one order of magnitude larger ($X(\mathrm{OH}) = 10^{-6}$), which is a possible value in a shocked gas according to Draine & Katz (1986), the L_{LOS} is could be 0.01 pc. The latter value ($L_{LOS} = 0.01$ pc) for the shocked gas case ($X(\mathrm{OH})$=10^{-6}) is comparable to the L_{warm} of 0.015 pc. This result suggests the presence of a shock compressive motion at the interface of the two filaments, and suggests the filament-filament collisions picture in the Pipe nebula.

5.6 Summary of this section

We observed the four hfs components of the OH 18 cm transitions toward the Pipe nebula along the two strip lines, and the gas kinetic temperatures are determined accurately. Along the strip-1, the gas kinetic temperature is found to have no relation to the distance from the nearby star, θ-Oph, suggesting that the heating effect from θ-Oph in the Pipe nebula is not significant. On the strip-2, the absorption feature of the 1665 and 1667 MHz main lines is observed in the bowl region, and the deepest absorption is observed just at the interface of the W-E and S-N filamentary structures. Our statistical equilibrium calculations successfully reproduce this absorption feature with a gas kinetic temperature higher than $\sim$ 90 K, and the absorption is found to be deeper with an increasing gas kinetic temperature. The derived temperature is indeed the highest at the interface of the filaments, indicating the heating effect by the collisions between these filaments. We confirm that the contribution of the radio continuum background emission along the line-of-sight direction have only a limited effect on the above results. This observation demonstrates a unique characteristic of the OH 18 cm transition as a new tool to study the molecular-cloud formation.

CHAPTER 6. Absorption feature in the 1720 MHz line of OH

6.1 Introduction

In the previous Chapters, we present the two types of hyperfine anomaly of the OH 18 cm transition; (1) the 1612 MHz absorption and enhanced 1720 MHz emission tracing a warm gas ($T_k > 40$ K), and (2) the main lines (1665 and 1667 MHz) absorption tracing a warmer gas ($T_k > 90$ K). In this Chapter, we represent another type of hyperfine anomaly, which was found in the course of our survey of the OH 18 cm transition toward various molecular clouds. Toward the cold dark cloud L183, the 1612 MHz line is brighter than the 1720 MHz line. This behavior is opposite to the above hyperfine anomalies described in Sections 4.6.3 and 4.7. The same trend was pointed out in the north part of TMC-1 ridge by Harju et al. (2000). Most notably, we have found an absorption feature in the 1720 MHz line and bright emission in the 1612 MHz line toward the north end of HCL2 (Figure 44). Recently, Xu et al. (2016) also reported the same anomaly in the northern part of HCL2 with the Arecibo 300-m telescope. Such an anomaly cannot be reproduced by our statistical equilibrium calculations mentioned in Chapters 4 and 5. It is predicted to be caused by far-infrared (FIR) pumping of the OH molecules to the second rotationally excited level, as discussed by Harju et al. (2000) and Elitzur et al. (1976). However, no quantitative analyses have been reported so far. For a full understanding of the hyperfine anomaly of the OH 18 cm transitions based on the non-LTE excitation calculation, we here investigate the anomaly by incorporating the effect of the far-infrared pumping.

6.2 Observation and data reduction

We observed four positions in Heiles Cloud 2 (HCL2) (Figure 44) and the cold dark cloud L183/L169 (Figure 45) in the OH 18 cm transition with the Effelsberg 100 m telescope in 2013 and 2016. The frontend and backend settings are the same as Chapter 4. The 18 cm/21 cm prime focus receiver was used, whose system noise temperature was about 20 K. The HPBW beam size is 8.2′. The FFTS

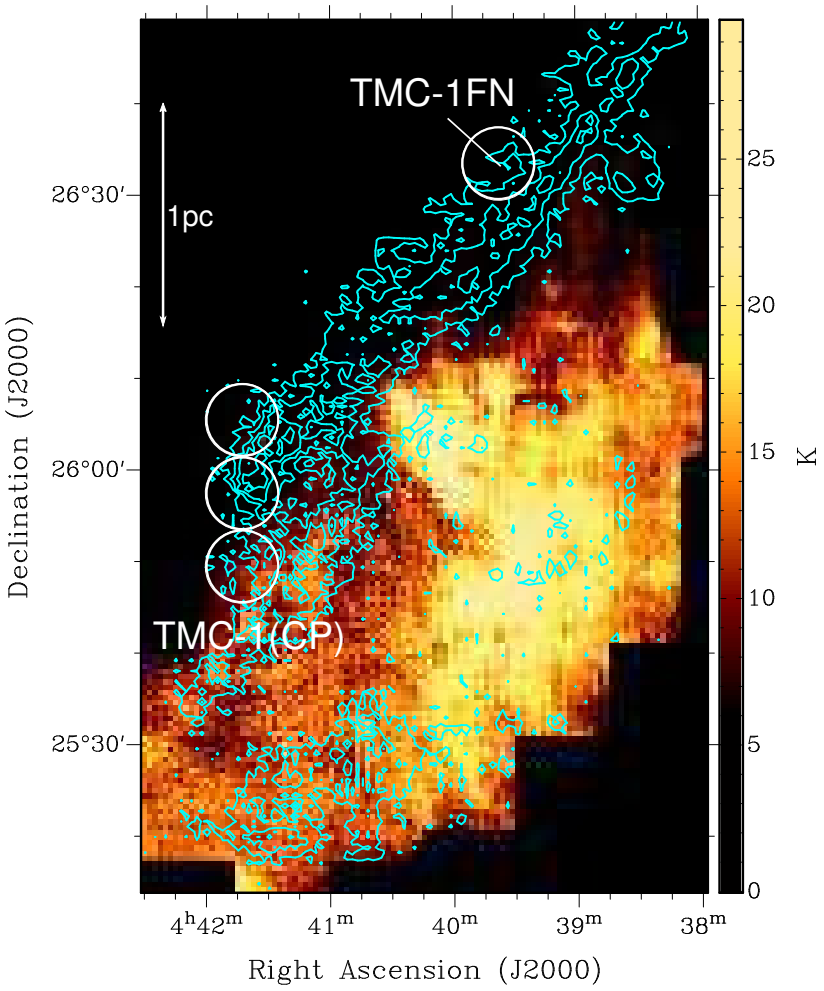

Figure 44. Integrated intensity map of $C^{18}O$ (J=1–0) (5.15 km s^{-1} < V_{LSR} < 5.45 km s^{-1}; contours) and ^{13}CO (J=1–0) (6.45 km s^{-1} < V_{LSR} < 6.95 km s^{-1}; color) observed toward HCL2 (Sunada & Kitamura 1999). Circles represent the positions observed in OH, and their diameter corresponds to the HPBW of the Effelsberg 100-m telescope.

spectrometer was employed as a backend, which has an instantaneous bandwidth of 100 MHz with a frequency resolution of 3.5 kHz. The resolution corresponds to a velocity resolution of 0.56 km s^{-1} at 1667 MHz.

We observed the four hfs components of the OH 18 cm transition with two frequency settings, where the 1612 MHz and 1720 MHz lines were separately observed. The 1665 MHz and 1667 MHz lines were observed in both frequency settings. The telescope pointing was maintained to be better than 20″, by observing nearby continuum sources. We used the frequency-switching mode with the

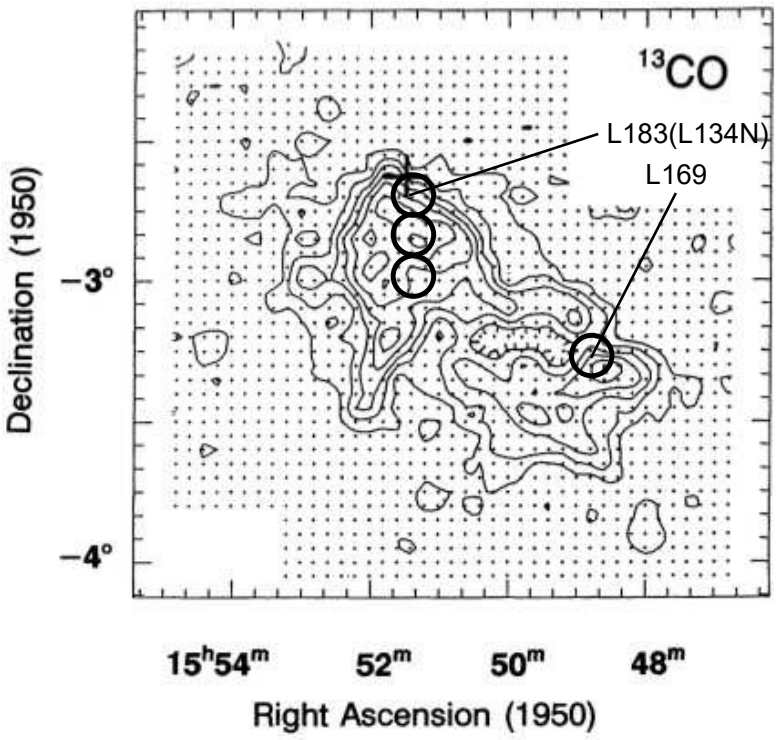

Figure 45. Contours show the integrated intensity map of ^{13}CO (J=1-0) toward L183 reported by Laureijs et al. (1995) (same as Figure 20). The cross marks the position of the NH_3 core of L183 (L134N) indicated by Laureijs et al. (1995). We observed the OH 18 cm transition toward L183 and L169. L169 is located in the southwest of L183.

frequency offset of 0.1 MHz. The rms (root-mean-square) noise levels of the observed spectra are about 8–16 mK. The data reduction was conducted in the same way as that explained in Section 4.3.1.

6.3 Results

Figure 46 shows the spectra of the OH 18 cm transition observed on the straight structure in the north part of HCL2 (Narayanan et al. 2008; Goldsmith et al. 2010), which we call TMC-1FN (Figure 44). These spectra are best explained by three Gaussian profiles centered on V_{LSR}=5.5 km s^{-1}, 6.5 km s^{-1}, and 8.2 km s^{-1}, respectively. The line parameters are summarized in Table 12. The 1612 MHz line appears in absorption in the red-shifted component (V_{LSR}=8.2 km s^{-1}), whereas it shows emission in the blue-shifted component (V_{LSR}=5.5 km s^{-1}). It is very faint in the

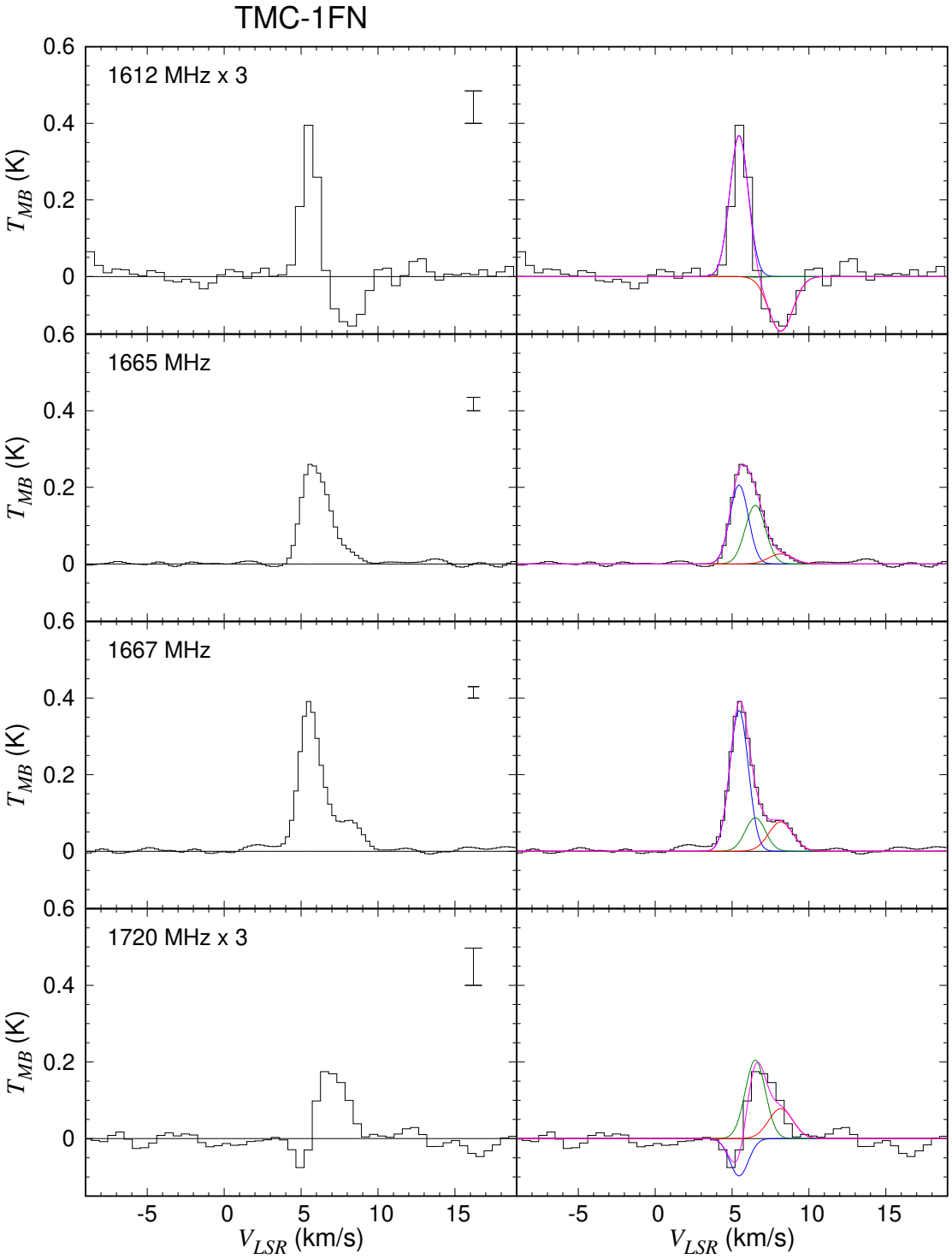

Figure 46. (Left) Observed spectra of the OH 18 cm transition toward TMC-1FN. Three times the rms noise of each spectrum is represented in the top right. (Right) The best-fit Gaussian profiles obtained by assuming three velocity components shown by blue, green, and red lines, whose central velocities are 5.5, 6.5, and 8.2 km s^{-1}, respectively. Magenta lines show the sum of these three velocity components.

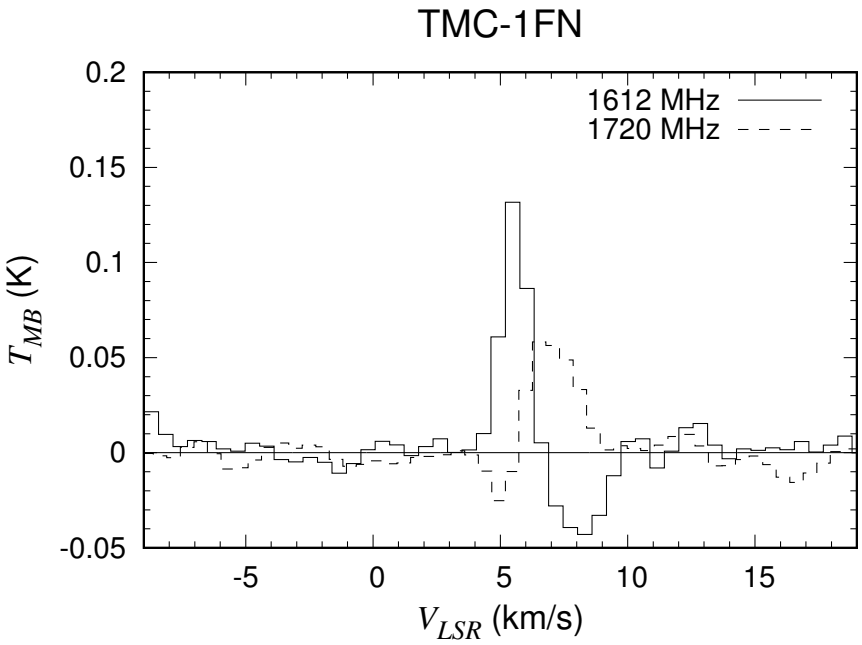

Figure 47. The 1612 MHz (solid) and the 1720 MHz (dashed) line spectra observed toward TMC-1FN.

central component (V_{LSR}=6.5 km s^{-1}). The absorption feature of the red-shifted component traces warm gas with a gas kinetic temperature higher than 40 K, according to our statistical equilibrium calculations mentioned in Chapter 4. On the other hand, *the absorption feature of the 1720 MHz line* is observed in the blue-shifted component. The conjugate behavior of these satellite lines in the two velocity components is clearly seen in Figure 47, in which the spectra of the 1612 MHz and the 1720 MHz lines are overlaid with each other. The 1612 MHz and 1720 MHz lines show absorption and bright emission, respectively, in the red-shifted component, whereas they show the opposite in the blue-shifted component. We performed additional statistical equilibrium calculations, but the 1720 MHz line absorption could not be reproduced in spite of an extensive parameter search. Although Xu et al. (2016) reported the absorption feature of the 1720 MHz line on the straight structure of HCL2 located in the northwest of TMC-1FN, they could not reproduce it with non-LTE radiative transfer model calculation, either.

A similar hfs intensity anomaly is also observed near the cold starless core TMC-1(CP) in HCL2 (Figure 44). Figures 48–50 show the observed spectra of the OH 18 cm transition toward three

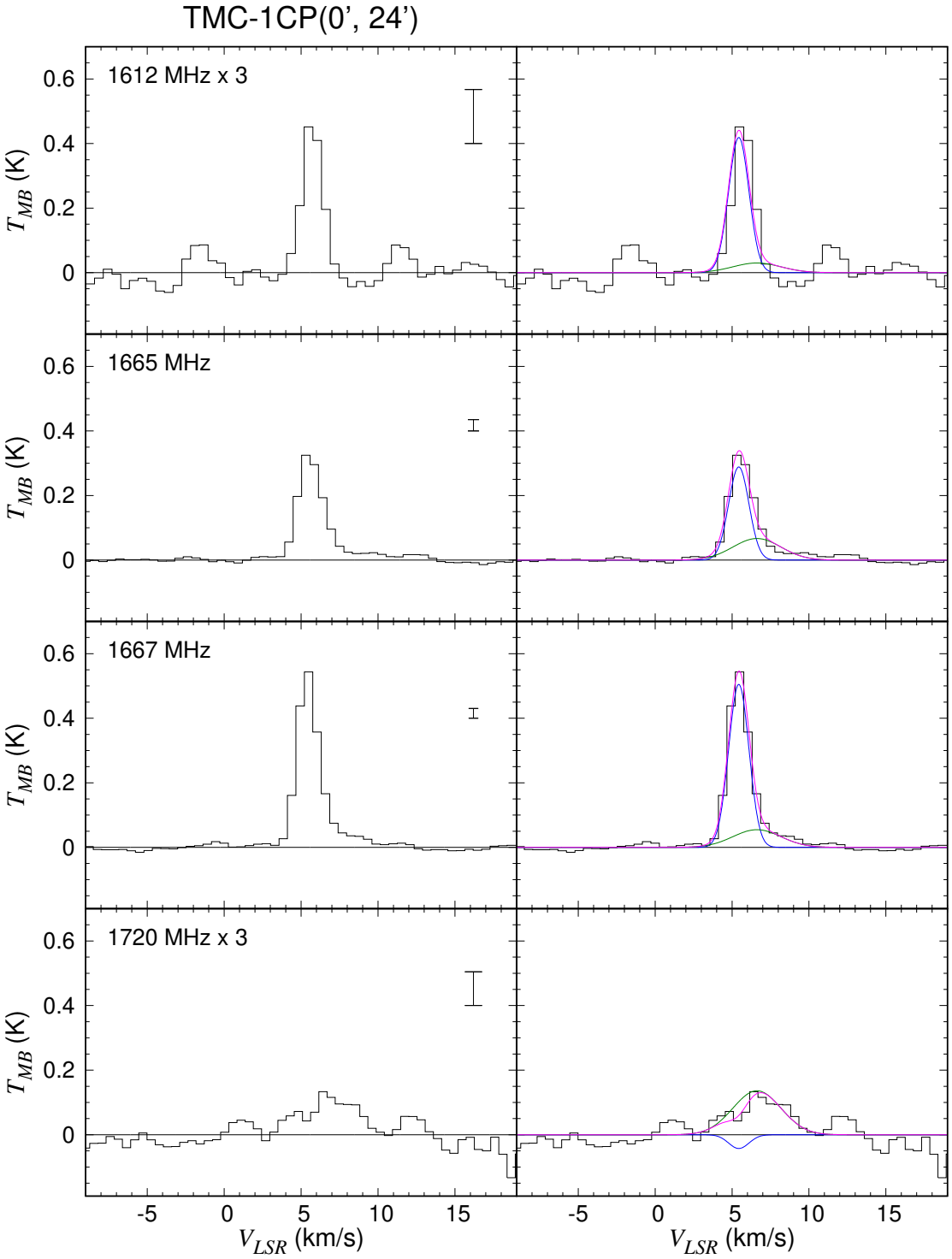

Figure 48. (Left) Observed spectra of the OH 18 cm transition toward 24′ north from TMC-1(CP). Three times the rms noise of each spectrum is represented in the top right. (Right) The best-fit Gaussian profiles obtained by assuming two velocity components are shown by blue, and red lines, whose central velocities are 5.4, and 6.6 km s^{-1}, respectively. Magenta line shows the sum of these three velocity components.

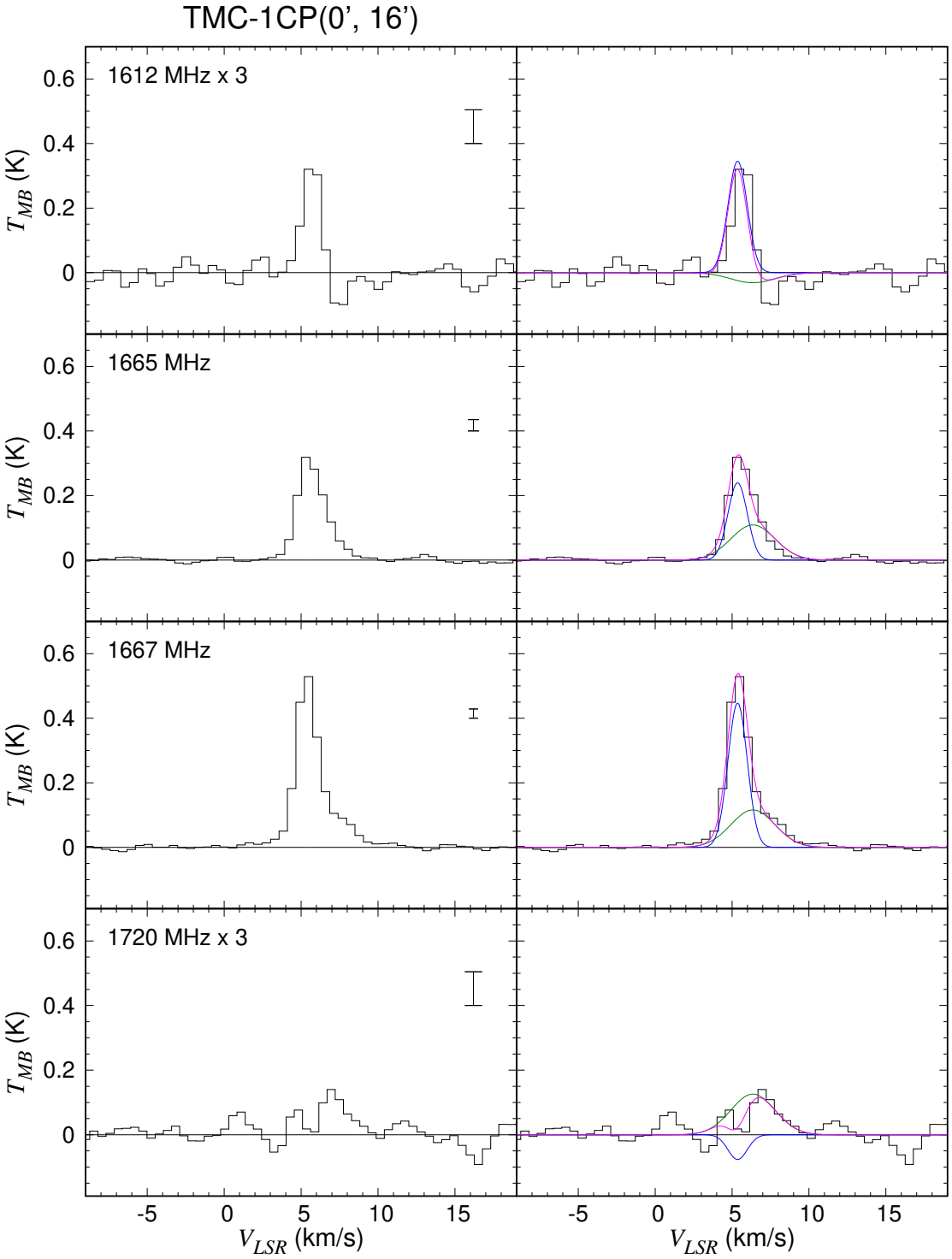

Figure 49. (Left) Observed spectra of the OH 18 cm transition toward 16′ north from TMC-1(CP). Three times the rms noise of each spectrum is represented in the top right. (Right) The best-fit Gaussian profiles obtained by assuming two velocity components are shown by blue, and red lines, whose central velocities are 5.4, and 6.4 km s^{-1}, respectively. Magenta lines show the sum of these three velocity components.

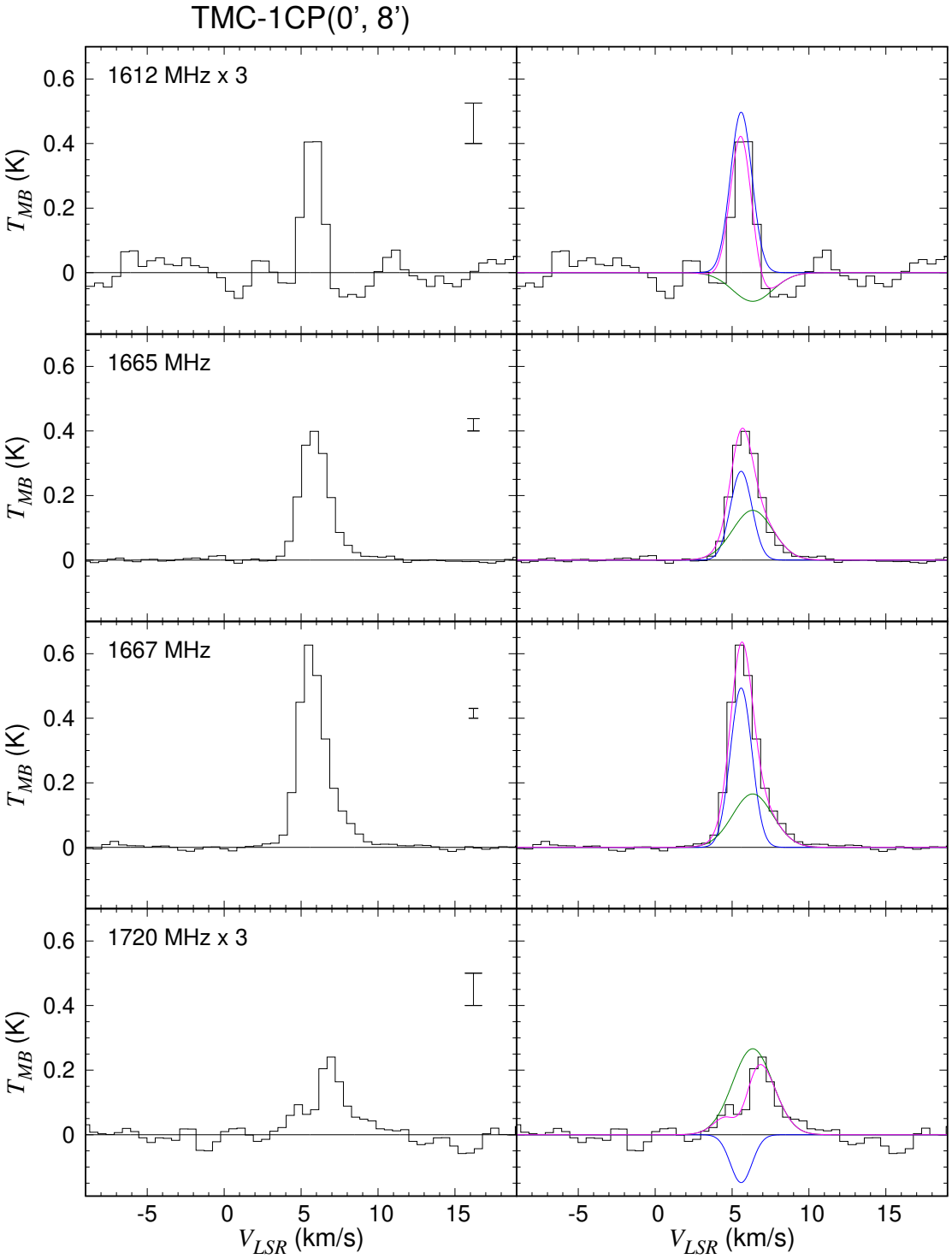

Figure 50. (Left) Observed spectra of the OH 18 cm transition toward 8′ north from TMC-1(CP). Three times the rms noise of each spectrum is represented in the top right. (Right) The best-fit Gaussian profiles obtained by assuming two velocity components are shown by blue, and red lines, whose central velocities are 5.6, and 6.3 km s^{-1}, respectively. Magenta lines show the sum of these three velocity components.

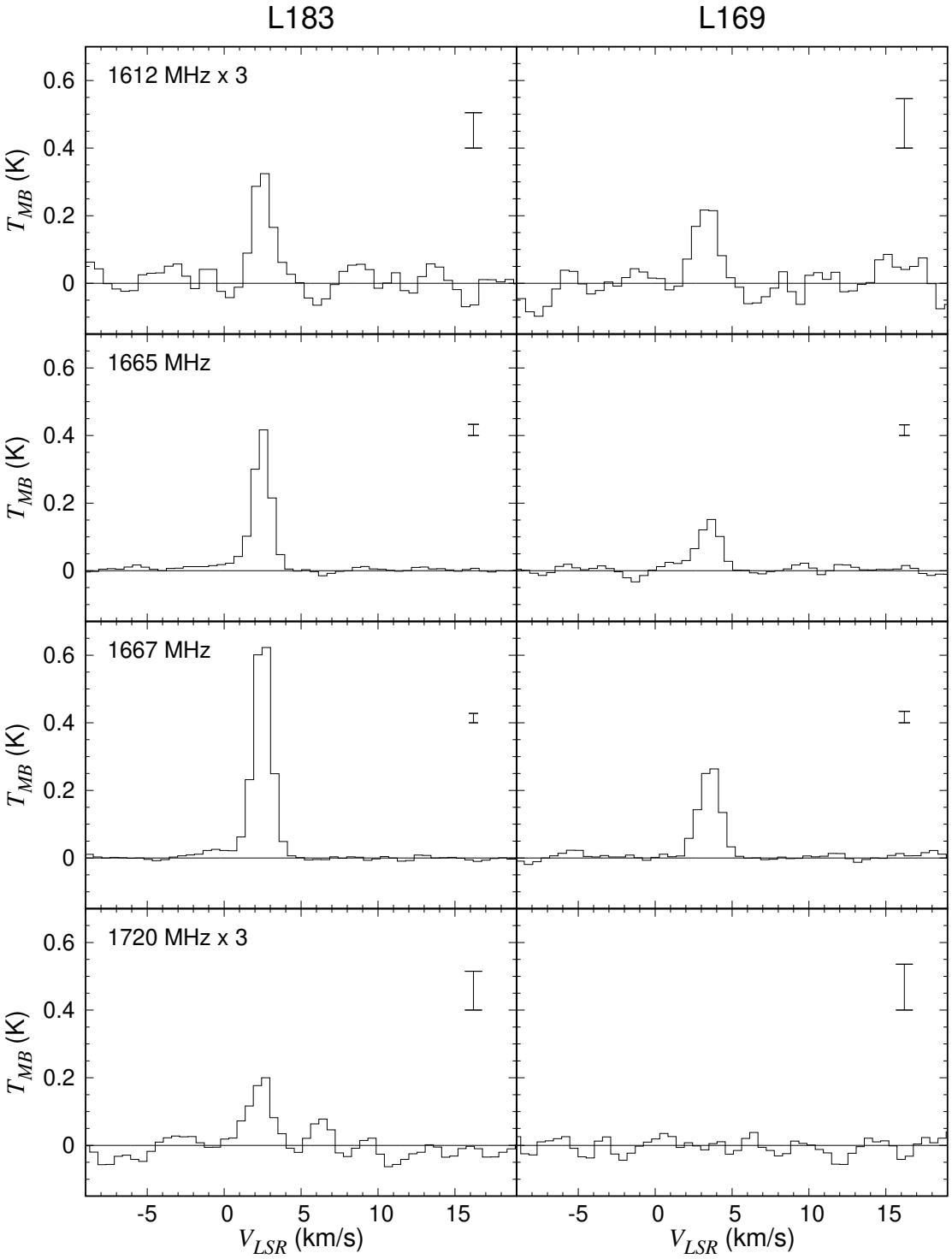

Figure 51. The observed spectra of the OH 18 cm transition toward L183 (left) and L169 (right). Three times the rms noise of each spectrum is represented in the top right of each panel.

positions located 24′, 16′, and 8′ north from TMC-1(CP), respectively, as indicated in Figure 44. The 1612 MHz line is observed in faint emission or slight absorption for the red-shifted component (V_{LSR}=6–10 km s^{-1}), suggesting that this velocity component traces warm gas. On the other hand, the 1720 MHz line is much fainter than the 1612 MHz line for the blue-shifted component (V_{LSR} $\sim$ 5 km s^{-1}), although these two lines should have the same intensity in LTE ($I_{1612} : I_{1665} : I_{1667} : I_{1720} = 1 : 5 : 9 : 1$). Harju et al. (2000) also reported that the 1720 MHz line is fainter than the 1612 MHz line toward the north part of TMC-1 ridge. Again, this anomalous feature could not be reproduced with our statistical equilibrium calculation described in Chapter 4. Figure 51 (left) shows the observed OH spectra toward L183 (Figure 45), which we already showed in Chapter 4 (Figure 21). The 1720 MHz line is slightly weaker than the 1612 MHz line toward L183. This feature is more evident in the dense core L169, which is adjacent to L183 (Figure 45). As shown in Figure 51 (right), the 1720 MHz line is totally absent toward L169, whereas the 1612 MHz line shows bright emission. An intensity ratio of the 1612 MHz line to the 1667 MHz line is about 1/3, which is three times higher than the expected value of 1/9 in LTE. The line parameters are summarized in Table 12.

As described above, the 1720 MHz line absorption (or its faint emission) and the enhanced 1612 MHz line emission are observed toward several sources. Thus, revealing the origin of this anomaly is important for a full understanding of the excitation mechanism of OH. For this purpose, we here investigate the effect of far-infrared pumping of OH.

Table 12. Observed Line Parameters

Source	R.A. (2000)	DEC (2000)	V_{LSR} (km s^{-1})	ΔV (km s^{-1})	T_{1612} (K)	T_{1665} (K)	T_{1667} (K)	T_{1720} (K)
TMC-1CP(0′, 24′)	$04^h41^m42^s.88$	+26°05′27″.0	5.44(2)	1.55(5)	0.14(1)	0.29(1)	0.50(1)	-0.01(1)
			6.62(30)	3.67(39)	0.009(8)	0.067(12)	0.054(13)	0.045(9)
TMC-1CP(0′, 16′)	$04^h41^m42^s.88$	+25°57′27″.0	5.36(2)	1.47(8)	0.12(1)	0.24(2)	0.44(2)	-0.025(16)
			6.35(21)	3.37(26)	-0.011(10)	0.11(1)	0.11(2)	0.042(10)
TMC-1CP(0′, 8′)	$04^h41^m42^s.88$	+25°49′27″.0	5.59(2)	1.65(8)	0.16(1)	0.27(3)	0.49(3)	-0.049(22)
			6.34(15)	3.07(18)	-0.029(13)	0.15(2)	0.16(3)	0.088 (15)
TMC-1FN	$04^h39^m37^s.66$	+26°33′27″.0	5.46(2)	1.41(3)	0.12(1)	0.20(1)	0.36(1)	-0.032(7)
(TMC-1CP(-28′, 52′))			6.51(5)	1.54(11)	0.000(7)	0.15(1)	0.087(13)	0.068(5)
			8.16(7)	1.85(15)	-0.047(4)	0.026(4)	0.076(4)	0.026(4)
L183	$15^h54^m00^s.54$	-02°51′48″.5	2.47(1)	1.37(2)	0.12(1)	0.41(1)	0.68(1)	0.073(8)
L169	$15^h51^m00^s.21$	-03°26′48″.5	3.53(2)	1.70(5)	0.079(6)	0.15(1)	0.27(1)	0.001(6)

NOTE—Intensities of the four hfs components of OH ($T_{1612}, T_{1665}, T_{1667}, T_{1720}$), linewidth ($\Delta V$) and V_{LSR} are obtained by a Gaussian fit, assuming that the ΔV and V_{LSR} values of the four hfs components are the same for each observed position. The error in the parentheses represents one standard deviation in the units of the last significant digits.

6.4 Effect of FIR pumping

The hyperfine intensity anomaly is caused by the excitation and de-excitation between the rotationally excited states and the ground state, as schematically illustrated in Figure 52. Emission from the first rotationally excited state ($J = 5/2$ of $^2\Pi_{3/2}$) to the ground state ($J = 3/2$ of $^2\Pi_{3/2}$) produces

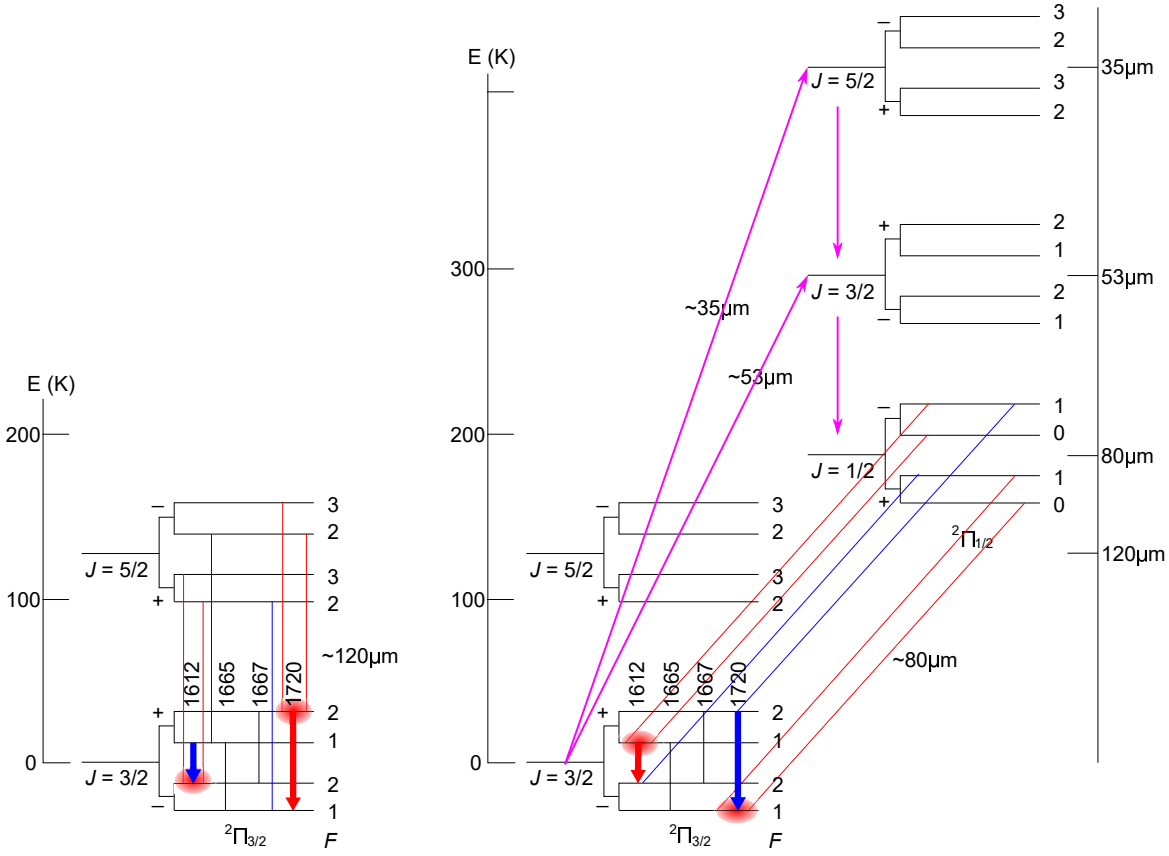

Figure 52. Schematic illustrations of the intensity anomaly of the OH 18 cm transition. (left) The transition from the first rotationally excited state to the ground state levels causes overpopulation in the $F = 2$ levels in the ground state, and the 1612 MHz line becomes weaker than expected under LTE. The 1720 MHz line becomes brighter at the same time. (right) The transition from the second rotationally excited state to the ground state levels works in the opposite way, and the $F = 1$ levels of the ground state become overpopulated. The 1720 MHz line and the 1612 MHz line become weaker and brighter, respectively, in this case. The populations in the second rotationally excited state levels can be enhanced by the FIR pumping from the ground state levels to the $^2\Pi_{1/2}$ $J = 3/2$ and $^2\Pi_{1/2}$ $J = 5/2$ state levels at wavelengths of 53 and 35 μm, respectively. The OH molecules are de-excited to the second rotationally excited state by the subsequent spontaneous emission, as represented by magenta arrows.

an overpopulation in the $F = 2$ levels in the ground state due to the selection rule, as described in Figure 52 (left). This anomalous population decreases the excitation temperature of the 1612 MHz line and increases that of the 1720 MHz line. This leads to the 1612 MHz line absorption against the CMB. On the other hand, emission from the second rotationally excited state ($J = 1/2$ of $^2\Pi_{1/2}$) to the ground state levels works in the opposite way (Figure 52, right). In this case, $F = 1$ levels in the ground state are overpopulated, increasing the excitation temperature of the 1612 MHz line and decreasing that of the 1720 MHz line. Thus the 1720 MHz line can appear in absorption if this trend is strong. In different parts of the ISM, both processes may occur with different contributions, but the collisional excitation with H_2 to the first rotationally excited state levels is more efficient than that to the second rotationally excited state. The first effect is therefore dominant, producing the absorption of the 1612 MHz line.

Nevertheless, the second effect can be dominant, if FIR pumping to the $^2\Pi_{1/2}$ $J = 3/2$ and $^2\Pi_{1/2}$ $J = 5/2$ states at wavelengths of 53 μm and 35 μm, respectively, are efficient. Most of the OH molecules excited to these states radiatively decay to the $^2\Pi_{1/2}$ $J = 1/2$ state by subsequent rotational transitions within the $^2\Pi_{1/2}$ ladder, as represented by magenta arrows in Figure 52. This is because the spontaneous emission rates of the transitions within the $^2\Pi_{1/2}$ ladder are typically one order of magnitude higher than those of the inter-ladder transitions between the $^2\Pi_{1/2}$ and $^2\Pi_{3/2}$ states. Then, rotational transitions from the $^2\Pi_{1/2}$ $J = 1/2$ state to the ground rotational state might produce the 1720 MHz line absorption, as described before. It should be noted that the direct FIR pumping from the $^2\Pi_{3/2}$ $J = 3/2$ ground state to the $^2\Pi_{1/2}$ $J = 1/2$ state at 80 μm does not contribute to the population anomaly, because the subsequent radiative de-excitation back to the ground state occurs under the same selection rules as the FIR pumping. These mechanisms are indeed confirmed by our simulations, as described in Section 6.4.1.4.

The effect of FIR pumping on the excitation of OH was studied by Elitzur et al. (1976). These authors showed that the 1612 MHz line becomes stronger and will display maser emission in extreme cases, particularly in the dusty envelopes of stars, so-called OH-IR stars. They reported that the 1612 MHz maser can be explained by the FIR pumping to the $^2\Pi_{1/2}$ $J = 5/2$ state by 35 μm photons

emitted from warm dust grains (T_d = 100–200 K). While no bright infrared source is associated with our observed sources, the FIR radiation from dust grains in surrounding warm clouds would contribute to the pumping to the $^2\Pi_{1/2}$ ladder. Therefore, we incorporate the effect of the FIR radiation into our statistical equilibrium calculations to examine whether we can explain the 1720 MHz line absorption, and to constrain the physical conditions in the OH bearing clouds.

In addition, we consider line overlaps by following the formulation of Guilloteau et al. (1981). They incorporated line overlaps of the far-infrared OH rotational transitions in their statistical equilibrium calculations assuming a uniform condition in a spherical cloud, and reported that the pumping effect due to the overlaps well explains the intensities of strong OH masers found in the dense envelopes of compact H_{II} regions.

6.4.1 Statistical equilibrium calculation considering the FIR pumping effect

6.4.1.1. Formulation

We incorporate the pumping effect by the FIR radiation from dust grains into our statistical equilibrium calculation (Section 4.5) in a similar way to that reported by Elitzur et al. (1976). We also consider the effect of line overlaps approximately, as described by Guilloteau et al. (1981). In this case, the statistical equilibrium takes the form:

$$
\begin{aligned}
\frac{d(g_i n_i)}{dt} = & \sum_{j>i} \left\{ g_j \beta_{ji} A_{ji} \left[n_j - \left(R_{ji} + R^d_{ji} \right) (n_i - n_j) \right] \right. \\
& + \sum_{k=(u_k,l_k)} \left(g_j A_{ji} P_{(ji),(u_k l_k)} n_j - g_{u_k} A_{u_k l_k} P_{(u_k l_k),(ji)} n_{u_k} \right) \\
& \left. + g_j C_{ji} \left[n_j - n_i \exp\left(-\frac{h\nu_{ji}}{k_b T_k} \right) \right] \right\} \\
& - \sum_{i>j} \left\{ g_i \beta_{ij} A_{ij} \left[n_i - \left(R_{ij} + R^d_{ij} \right) (n_j - n_i) \right] \right. \\
& + \sum_{k=(u_k,l_k)} \left(g_i A_{ij} P_{(ij),(u_k l_k)} n_i - g_{u_k} A_{u_k l_k} P_{(u_k l_k),(ij)} n_{u_k} \right) \\
& \left. + g_i C_{ij} \left[n_i - n_j \exp\left(-\frac{h\nu_{ij}}{k_b T_k} \right) \right] \right\} \\
= & \, 0. \qquad (30)
\end{aligned}
$$

$k = (u_k, l_k)$ in the second and fifth terms of Equation (30) denotes summation over all transitions of OH. R^d_{ij} is the photon occupation number of the dust FIR radiation at the frequency of the transition between the levels i and j. We examine two models for the derivation of R^d_{ij}. First, we assume that the dust grains emit gray-body radiation of dust temperature T_d and spectral index β_d. In this case, R^d_{ij} can be written as:

$$R^d_{ij} = \left(\frac{\nu}{\nu_{160}}\right)^{\beta_d} \frac{\eta}{\exp\left(h\nu_{ij}/k_b T_d\right) - 1}, \tag{31}$$

where η is a dilution factor of the dust thermal radiation. It is derived from the estimated intensity of the FIR radiation at 160 μm (I_{160}) divided by the intensity of the blackbody radiation (times ν^{β_d}) at this wavelength. We perform the calculation for β_d values from 0 to 3. Although a higher value of β_d gives a better fit to the observed spectra, there is no significant dependence on β_d as long as it is higher than 2. Therefore, β_d is assumed to be 2, which has been reported as a typical value for the diffuse ISM (e.g. Boulanger et al. 1996).

Second, we use DustEM to model the dust emission (Compiègne et al. 2011) (https://www.ias.u-psud.fr/DUSTEM/index.html) in order to derive R^d_{ij}. We employ the DustEM version calculated by Jones et al. (2013). As shown later, the FIR emission predicted by the DustEM model better reproduces the 1720 MHz line absorption of OH than the gray-body approximation, although it depends on the dust temperature.

β_{ij} in the first and fourth terms of Equation (30) denote the photon escape probability of the transition between the levels i and j, as explained in Section 4.5. $P_{(ij),(kl)}$ is the probability that a photon emitted in the transition between the levels i and j is absorbed by that between the levels k and l, which represents the effect of the line overlaps. We follow the formulation of β_{ij} and $P_{(ij),(kl)}$ introduced by Guilloteau et al. (1981), where a spherical homogeneous cloud with no velocity gradient is assumed. In this model, the analytical expressions of β_{ij} and $P_{(ij),(kl)}$ are determined by considering a photon emitted from the cloud center, and they are used throughout the cloud. Guilloteau et al. (1981) reported that this assumption have only a limited effect, according to the comparison of their results with those obtained from the exact treatment of the radiative transfer assuming a plane

parallel cloud. It should be noted that the effect of the FIR pumping and the line overlaps are not included in Chapters 4 and 5, which is equivalent to R^d_{ij}=0 and $P_{(ij),(kl)}$=0, respectively.

6.4.1.2. FIR model

The FIR pumping effect is incorporated by using the DustEM model by Jones et al. (2013) and the gray-body profile. In the DustEM model, the interstellar radiation field (ISRF) strength and the H column density are given as the parameters. We employ the ISRF strength of 0.4 G_0, since it best explains the shape of SED observed toward TMC-1FN (Flagey et al. 2009) among the ISRF values from 0.1 G_0 to 1.0 G_0 at a 0.1 G_0 interval (red solid line in Figure 53). Here G_0 stands for a scaling factor of the UV field with respect to the flux in the Habing field (Habing 1968). The H column density is also determined to be 1.5 $\times$ 10^{22} cm^{-2}. However, we use the H column density of 3 $\times$ 10^{23} cm^{-2} in the fiducial DustEM model for the statistical equilibrium calculations by scaling the FIR intensity by a factor of 20 (red dotted line in Figure 53) so as that the 1720 MHz absorption is reproduced. Apparently, this H column density is too large for the line-of-sight value by one order of magnitude. We will discuss this point later in Section 6.4.2.1. In the gray-body model, the dust temperature (T_d) and the dilution factor (η) are estimated to be 15 K and 0.003, respectively, by fitting the above DustEM model for the H column density of 1.5 $\times$ 10^{22} cm^{-2} (blue solid line in Figure 53). As in the case for the fiducial DustEM model, this gray-body profile is multiplied by a factor of 20 (blue dotted line), which is employed in our statistical equilibrium calculations.

It should be noted that the observed intensities at 25, 60 and 70 μm are slightly higher than those expected by the gray-body. Although the discrepancy is marginal in Figure 53, it is more evident in the mean SED of Taurus molecular cloud complex averaged over a 44 deg^2 area including TMC-1FN (Flagey et al. 2009). As shown in the solid red line in Figure 53, the DustEM model well reproduces the excess feature at shorter wavelengths compared to the gray-body. The FIR intensities at 35, 53 and 120 μm are predicted to be 2.2, 3.3 and 48 MJy sr^{-1}, respectively, by the DustEM model for the solid red line of Figure 53, while they are predicted to be 8.5 $\times$ 10^{-5}, 0.1 and 42 MJy sr^{-1}, respectively, with the gray-body for the solid blue line of Figure 53. Namely, the FIR intensities calculated by the DustEM model at 35 and 53 μm relative to the 120 μm intensity are 2 $\times$ 10^4

and 29 times larger, respectively, compared to those calculated by the gray-body model. Higher intensities in the 35 μm and 53 μm contribute to more efficient pumpings to the $^2\Pi_{1/2}$ $J = 5/2$ and $^2\Pi_{1/2}$ $J = 3/2$ states, respectively, which lead to the 1720 MHz line absorption, as described in Section 6.4.

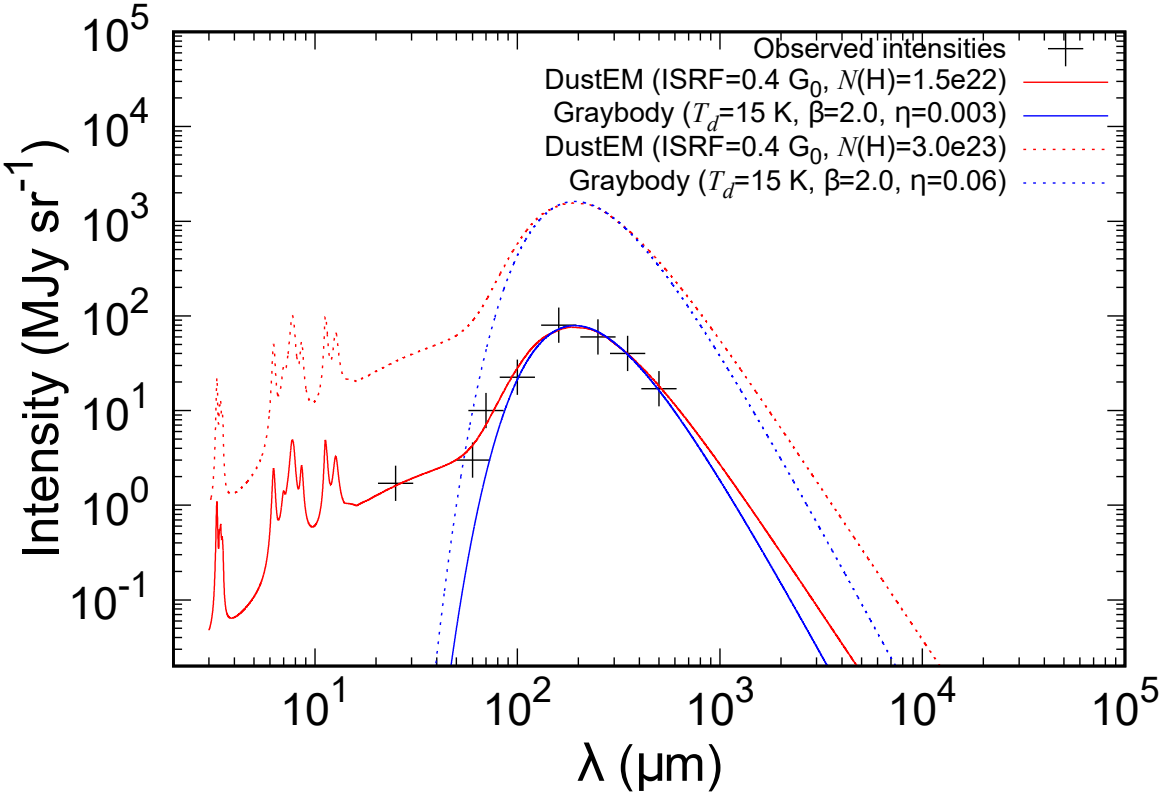

Figure 53. (Cross) Intensities of the mid- and far-infrared radiation observed toward TMC-1FN. The intensities are taken from Spitzer 70 and 160 μm maps by Flagey et al. (2009), IRAS 25, 60 and 100 μm maps by Flagey et al. (2009), and Herschel 250, 350 and 500 μm archival data with observation IDs of 1342202252 and 1342202253. (Solid red line) The best-fitting DustEM (Jones et al. 2013) profile assuming the ISRF of 0.4 G_0, which gives the best fitting result among the ISRF values from 0.1 G_0 to 1.0 G_0 at a 0.1 G_0 interval. (Solid blue line) The gray-body profile which best explains the above DustEM model assuming β of 2. The dust temperature (T_d) is determined to be 15 K. The observed intensities in 25, 60 and 70 μm are stronger than those estimated by the gray-body, whereas they are well reproduced by the DustEM model. The best-fitting DustEM and gray-body profiles are scaled by a factor of $\sim$20, and are employed in our statistical equilibrium calculations for the fiducial models, as shown by red and blue dotted lines, respectively. In Figures 57 and 59, this scaling is represented by the flux at 160 μm.

6.4.1.3. Condition for the 1720 MHz line absorption

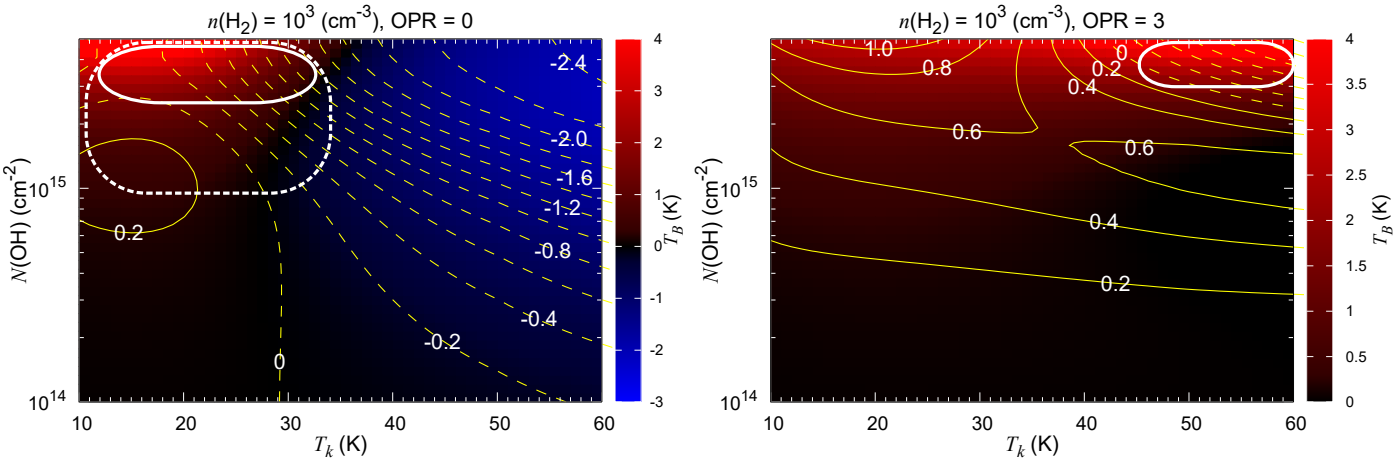

Figure 54. The intensity of the 1612 MHz line (color) and the 1720 MHz line (yellow contours) on the N(OH)–T_k plane derived from our statistical equilibrium calculation considering the effect of the FIR radiation. (Left) The H_2 ortho-to-para ratios is assumed to be 0. Contour levels are shown for the 1720 MHz line intensity from -2.4 K to 0.2 K with 0.2 K interval. Dashed contours correspond to negative brightness temperatures of the 1720 MHz line. The 1720 MHz line absorption and the bright emission of the 1612 MHz line can be reproduced for $N(\mathrm{OH}) > 3 \times 10^{15}$ cm^{-2} and $T_k < 30$ K (white solid circled area). The case when the 1720 MHz line is brighter than the 1612 MHz line can be reproduced for $N(\mathrm{OH}) > 10^{15}$ cm^{-2} and $T_k < 30$ K (white dotted circled area). (right) The H_2 ortho-to-para ratios is assumed to be 3. Contour levels are shown for the 1720 MHz line intensity from -0.8 K to 1.0 K with 0.2 K interval. The 1720 MHz line absorption and the bright emission of the 1612 MHz line can be reproduced for $N(\mathrm{OH}) > 2 \times 10^{15}$ cm^{-2} and $T_k > 40$ K (white circled area).

Figure 54 shows the intensities of the 1612 MHz line (color) and the 1720 MHz line (contours) derived from our statistical equilibrium calculation in the N(OH) – T_k plane. The FIR pumping effect is treated with the DustEM model by Jones et al. (2013) assuming an ISRF strength of 0.4 G_0 and the H column density of 3×10^{23} cm^{-2} (red dotted line of Figure 53). The H_2 density is assumed to be 10^3 cm^{-3} as a representative value. The H_2 ortho-to-para ratio is assumed to be 0 and 3 in the left and right panels, respectively. Dependences on these parameters are described later. The linewidth is assumed to be a typical observed value of 1.0 km s^{-1}.

Dashed contours in Figure 54 represent absorption of the 1720 MHz line, whereas the blue colored region corresponds to absorption of the 1612 MHz line. As shown in Figure 54 (left), the case for which the emission in the 1612 MHz line is stronger than that in the 1720 MHz line can be reproduced for parameters contained in the area approximately enclosed by the dotted lines. Namely, an OH column density higher than $\sim 10^{15}$ cm^{-2} and a gas kinetic temperature lower than $\sim$30 K are necessary, if the H_2 ortho-to-para ratio is 0. A higher OH column density ($N(\mathrm{OH}) > 3 \times 10^{15}$ cm^{-2}) is required to reproduce the 1720 MHz line absorption, as represented by the white solid lines. The reason why such a high column density is needed for the 1720 MHz line absorption is that the transitions from the second rotationally excited state to the ground state must be optically thick in order to produce the anomalous population by the mechanism described in Figure 52. Assuming the H_2 density of 10^3 cm^{-3} and the OH column density of 3×10^{15} cm^{-2}, the fractional abundance of OH is estimated to be 10^{-6}, which is an order of magnitude higher than the typical value of the fractional abundance in diffuse clouds (Wiesemeyer et al. 2012). However, the fractional abundance of OH is enhanced in the shocked gas, and it can reach value as high as $\sim 5 \times 10^{-5}$ according to Draine & Katz (1986). Hence the 1720 MHz line could appear in absorption in such an OH-rich gas which experienced the shock. It should be noted that the case in which the 1720 MHz line is weaker than the 1612 MHz line can be reproduced even with a typical OH fractional abundance of 10^{-7}.

Intensities of the 1612 MHz and the 1720 MHz lines are determined to be $\sim$1–4 K and $-$(0.1–0.4) K within the solid circle in Figure 54 (left), which are about one order of magnitude stronger than those observed toward TMC-1FN (Figure 46). It can be explained by the beam-dilution effect with a beam filling factor of $\sim$0.1, a plausible value since the 1720 MHz line absorption traces a relatively cold and dense structure, as shown in the following subsections.

For the H_2 ortho-to-para ratio of 3 (Figure 54, right), the 1720 MHz line absorption is reproduced for the OH column density of 10^{15} cm^{-2} or higher, and the gas kinetic temperature of 40 K or higher (white circle in Figure 54, right). This absorption feature is the result of line overlaps, as shown later in Section 6.4.1.4. In particular, line overlaps between the transitions from the first rotationally excited state to the ground rotational state play an important role, where the overlaps between the

Table 13. Velocity separation between the hyperfine structure components of the $J = 5/2$, $^2\Pi_{3/2}$ – $J = 3/2$, $^2\Pi_{3/2}$ transitions of OH (top), and that between hfs components of the $J = 1/2$, $^2\Pi_{1/2}$ – $J = 3/2$, $^2\Pi_{3/2}$ transitions (bottom)[a].

transition 1 (level1, level2)	transition 2 (level1, level2)	dV (km/s)
(6, 2)	(5, 2)	1.6
(6, 2)	(5, 1)	4.7
(5, 2)	(5, 1)	6.3
(8, 4)	(7, 4)	2.1
(8, 4)	(7, 3)	4.4
(7, 4)	(7, 3)	6.5
(10, 2)	(10, 1)	4.2
(10, 2)	(9, 1)	3.0
(10, 1)	(9, 1)	1.2
(12, 4)	(12, 3)	4.4
(12, 4)	(11, 3)	2.8
(12, 3)	(11, 3)	7.1

NOTE—[a] Levels in the first and second columns are represented in Figure 8.

two transitions from the first rotationally excited state to the $F = 2$ levels in the ground rotational state, i.e., transitions marked (6, 2) and (5, 2), and (8, 4) and (7, 4) in Table 13, are significant. Here, a typical observed linewidth of 1.0 km s^{-1} is considered. In this situation, the transitions to the $F = 2$ levels can be readily saturated, while those to the $F = 1$ levels are not. Hence, the $F = 1$ levels in the ground rotational state are relatively overpopulated, which makes the 1720 MHz line weaker. The 1720 MHz line can appear in absorption, if this trend is strong.

It should be noted that the line overlaps among the transitions from the second rotationally excited state to the ground state do not seriously contribute to the hfs anomaly. For instance, the overlap between transitions (10, 1) and (9, 1), which we hereafter term the (10, 1)–(9, 1) overlap, produces the overpopulation in the level 2 ($F = 2$) in the ground rotational state. It makes the 1720 MHz line brighter. However, this overpopulation is less effective than the overpopulation in the level 1 ($F = 1$) produced by the contribution of the first rotationally excited state, i.e., the (6, 2)–(5, 2) overlap. This is because the former overpopulation is suppressed by the (10, 2)–(10, 1) and (10, 2)–(9, 1) overlaps. Such a phenomenon also occurs in the other overlaps, and eventually the contribution of the line overlaps among the transitions from the second rotationally excited state to the anomaly is limited.

The collisional excitations to the first rotationally excited state occur more efficiently with a higher gas kinetic temperature and a higher H_2 ortho-to-para ratio. In addition, transitions from the first rotational excited states to the ground rotational state must be optically thick in order to produce the anomalous population by the above mechanism. Hence, a high OH column density ($> 10^{15}$ cm^{-2}) and a high gas kinetic temperature (> 40 K) are required to reproduce the absorption feature of the 1720 MHz line (Figure 54, right). However, the 1612 MHz line is much brighter than the 1665 MHz line when the 1720 MHz line appears in absorption for the H_2 ortho-to-para ratio of 3, as shown in Figure 72 of Appendix A, which is inconsistent with the observation. Therefore, we assume the H_2 ortho-to-para ratio of 0, the OH column density of 3×10^{15} cm^{-2}, and the gas kinetic temperature of 20 K (Figure 54, left) for our fiducial model in the following sections. Results for the H_2 ortho-to-para ratio of 3 and the OH column density of 3×10^{14} cm^{-2} are presented in Appendix A, for reference.

6.4.1.4. Dependence on FIR intensity and mechanism of the 1720 MHz absorption

Figure 55 shows the calculated intensities of the OH 18 cm transition as a function of the gas kinetic temperature for the three cases of the FIR intensity. As noted above, the OH column density and the H_2 ortho-to-para ratio are assumed to be $3{\times}10^{15}$ cm^{-2} and 0, respectively. The effect of the line overlaps is not considered in the left panels ((a)–(c)), whereas it is considered in the right panels ((d)–(f)). No FIR radiation is assumed to be present in the calculations illustrated in the top panels

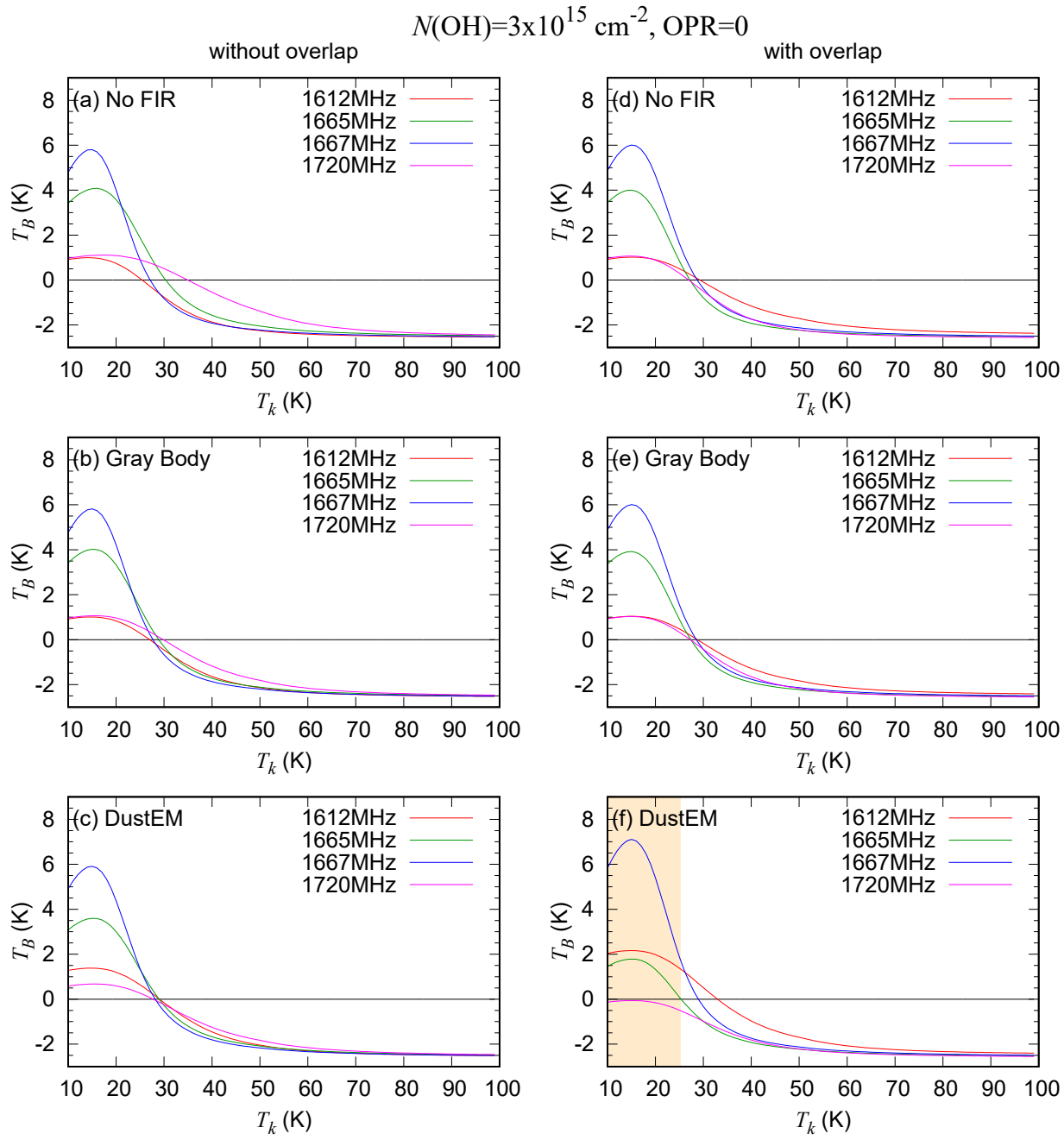

Figure 55. The derived intensities of the OH 18 cm transition hfs lines as a function of the gas kinetic temperature, where the H_2 density, the OH column density, and the ortho-to-para ratio of H_2 are assumed to be 10^3 cm^{-3}, 3×10^{15} cm^{-2}, and 0, respectively. The effect of line overlaps is not considered in the left panels ((a)–(c)), whereas it is considered in the right panels ((d)–(f)). The FIR radiation is not considered in the top panels ((a) and (d)), whereas the gray-body approximation with the dust temperature of 15 K is applied in the middle panels ((b) and (e)). The FIR radiation calculated by the fiducial DustEM model (Jones et al. 2013) is employed in the bottom panels ((c) and (f)). The orange area in the panel (f) represents the region where the 1720 MHz line appears in absorption and the other three lines show emission.

((a) and (d)), whereas the gray-body approximation with a dust temperature of 15 K applies for the middle panels ((b) and (e)). The FIR radiation calculated by the DustEM (Jones et al. 2013) is employed in the bottom panels ((c) and (f)). The ISRF strength of 0.4 G_0 and the H column density of 3×10^{23} cm^{-2} are assumed for the fiducial DustEM model, same as assumed for Figure 54.

As shown in Figure 55 (f), the 1720 MHz line absorption and the 1612 MHz line emission are reproduced by the fiducial DustEM model considering the effect of the line overlaps for gas kinetic temperatures lower than 30 K, which is consistent with the results in Section 6.4.1.3 (see the orange are of Figure 55 (f)). The effect of the line overlaps produces a weaker 1720 MHz line, which is clearly seen by comparing the left ((a), (b), (c)) and right ((d), (e), (f)) panels of Figure 55. All the four hfs lines of OH appear in absorption for gas kinetic temperatures higher than about 30 K. In contrast to the fiducial DustEM model, the absorption only in the 1720 MHz line is not reproduced by the model employing the gray-body approximation ((b) and (e)), although the 1720 MHz line becomes weaker than for the calculations assuming no FIR radiation ((a) and (d)). This is because the excitation to the $^2\Pi_{1/2}$ $J = 3/2$ and $^2\Pi_{1/2}$ $J = 5/2$ states via FIR radiation is more efficient in the DustEM model than in the gray-body model, due to an excess of the FIR radiation at shorter wavelengths in the DustEM model, as described in Section 6.4.1.2 (Figure 53).

In order to confirm this, we conduct the additional statistical equilibrium calculations assuming the same conditions of Figure 55 (f), but also applying an artificial wavelength threshold (λ_{th}) for the FIR radiation, where no FIR radiation is assumed for wavelengths shorter than λ_{th}. Figures 56 (a)–(d) show the results with λ_{th} values of 60, 50, 30 and 0 μm, respectively. The panel (d) of Figure 56 (λ_{th}=0 μm) is the same as the panel (f) of Figure 55. In the case of the λ_{th} of 60 μm (a), neither the 53 μm nor the 35 μm pumping effect is included, and hence, the 1720 MHz line absorption is not reproduced. On the other hand, the 1720 MHz line becomes very faint with a gas kinetic temperature lower than 30 K in the panel (b) (λ_{th}=50 μm). This is caused by the effect of 53 μm pumping, although the absorption feature is not reproduced. The intensity of the 1720 MHz line is further decreased by the contribution from the 35 μm pumping effect in the panel (c) (λ_{th}=30 μm), and the absorption feature is reproduced. The calculated OH hfs intensities in the panel (c)

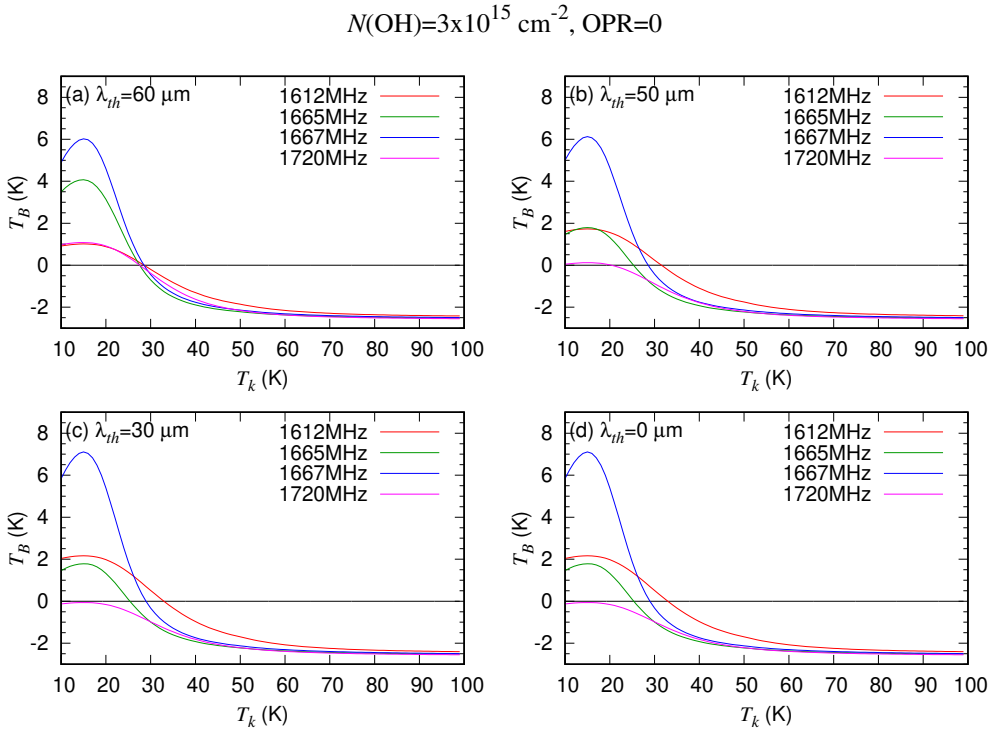

Figure 56. The hfs line intensities of the OH 18 cm transition as a function of the gas kinetic temperature, derived by introducing the artificial thresholds for the shortest wavelength in the fiducial DustEM model (Jones et al. 2013), where the H_2 density, the OH column density, and the ortho-to-para ratio of H_2 are assumed to be 10^3, 3×10^{15} cm^{-2}, and 0, respectively. Models assumed in each panel ((a)–(d)) are the same as those in Figure 55 (f) except for the FIR field. The threshold (λ_{th}) is (a) 60 μm, (b) 50 μm, (c) 30 μm. No FIR radiation is assumed at the wavelength shorter than the threshold. The panel (a) is the same as the panel (f) of Figure 55.

are almost comparable to those in the panel (d) (λ_{th}=0 μm), suggesting that the FIR pumping effect at a wavelength shorter than 30 μm is negligible. Therefore, the 1720 MHz line absorption can be explained by the FIR pumping effect in 53 μm and 35 μm, according to Figure 56.

Figure 57 summarizes the above results as a function of the intensity of the FIR radiation at 160 μm (I_{160}) for four combinations of an OH column density and a gas kinetic temperature. We employ the I_{160} as a representative value to scale the FIR intensity, since the observed SED is the strongest at this wavelength. It should be noted that the I_{160} is estimated to be 1.4×10^3 MJy sr^{-1} with the fiducial DustEM model assuming an ISRF of 0.4 G_0 and an H column density of 3×10^{23} cm^{-2} (red

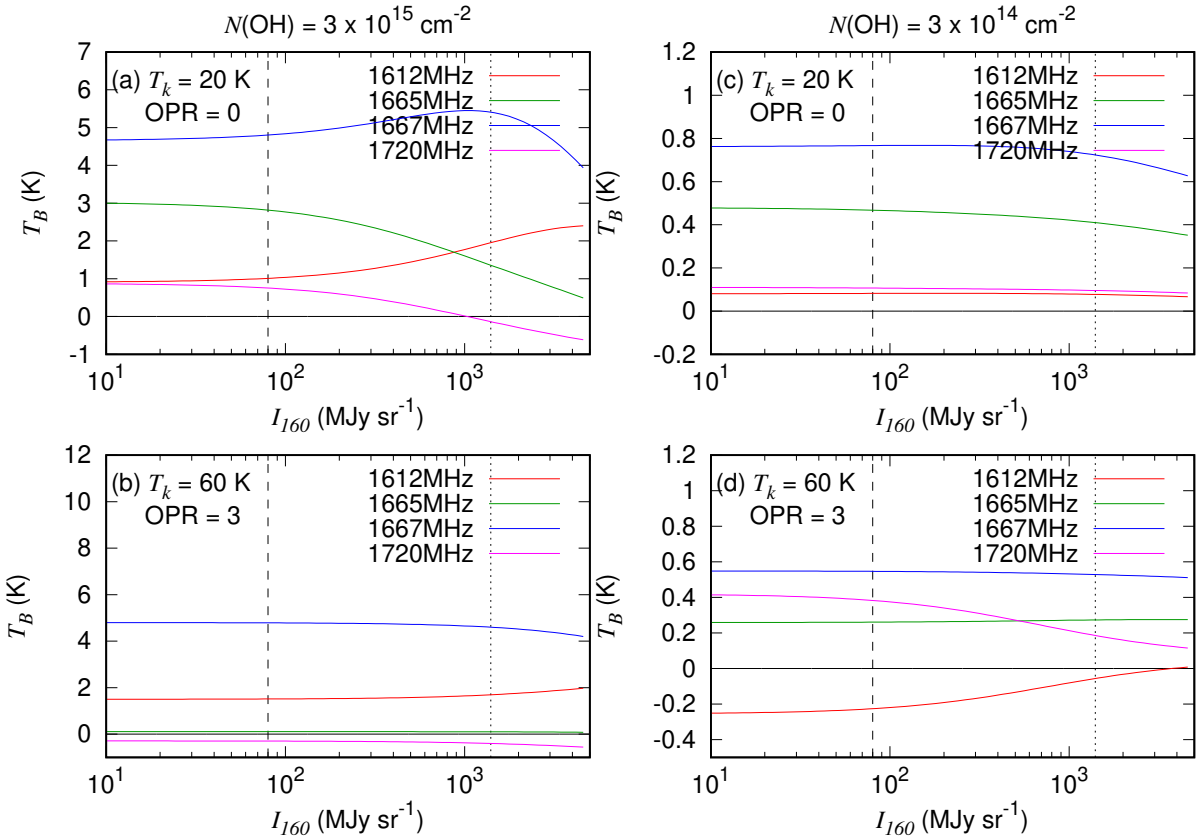

Figure 57. The intensities of the OH 18 cm transition hfs lines as a function of the intensity of the dust thermal emission at 160 μm (I_{160}) derived from our statistical equilibrium calculation. I_{160} is used as a parameter to scale the FIR intensity profile of the DustEM model (Figure 53). The dotted lines show I_{160} for the fiducial DustEM model, while the dashed lines show I_{160} observed toward TMC-1FN. The H_2 density is assumed to be 10^3 cm^{-3}. The column density of OH is assumed to be 3×10^{15} cm^{-2} (left) or 3×10^{14} cm^{-2} (right). The gas kinetic temperature and H_2 ortho-to-para ratio are assumed to be 20 K and 0, respectively, in the top panels, whereas they are assumed to be 60 K and 3, respectively, in the bottom panels.

dotted line in Figure 53). The H_2 ortho-to-para ratio is set to be 0 for the gas kinetic temperature of 20 K, while it is set to be 3 for the temperature of 60 K. The H_2 density is assumed to be 10^3 cm^{-3}. The DustEM model is applied for the FIR radiation, and the effect of the overlaps is considered. As shown in Figure 57, the effect of the FIR radiation is pronounced for two parameter combinations: high OH column density (3×10^{15} cm^{-2}) together with low gas kinetic temperature (20 K) (panel

(a)), and low OH column density (3×10^{14} cm^{-2}) and high gas kinetic temperature (60 K) (panel (d)). The 1720 MHz line becomes weaker and the 1612 MHz line becomes stronger for increasing FIR radiation intensity in both cases. In the former case, the 1720 MHz line appears in absorption for an FIR intensity larger than 10^3 MJy sr^{-1} (Figure 57 (a)). Note that the 1720 MHz line absorption is also reproduced for T_k=60 K and N(OH)=3×10^{15} cm^{-2} (panel (b)). This absorption is considered to be caused by the effect of the line overlaps through the mechanism explained in Section 6.4.1.3, since the intensities of the OH 18 cm transition are insensitive to the FIR intensity (Figure 57 (b)).

In Chapter 4, we presented that the OH 18 cm transition can be used as a thermometer for diffuse (N(OH)$\sim10^{14}$ cm^{-2}) and warm ($T_k\sim$50 K) molecular gas. As shown in Figure 57 (d), the effect of the FIR radiation is negligible for an 160 μm FIR intensity lower than about 10^2 MJy sr^{-1} under a diffuse warm gas conditions (T_k=60 K, N(OH)=3×10^{14} cm^{-2}). On the other hand, the absolute intensity of the 1612 MHz line absorption is decreased by $\sim$50% for I_{160} = 500 MJy sr^{-1}. This decrease of the 1612 MHz line intensity can cause a systematic error of $\sim$10 K in the gas kinetic temperature derived from our statistical equilibrium calculations assuming no FIR radiation. Hence, information on the accurate FIR intensity is necessary in order to determine the gas kinetic temperature precisely, if I_{160} is higher than 10^2 MJy sr^{-1}. Nevertheless, OH can still be used to explore a relative temperature structure of a cloud. The 1612 MHz line absorption disappears for I_{160} larger than 4×10^3 MJy sr^{-1}, suggesting that the OH 18 cm transition cannot be used as a thermometer for clouds with such strong FIR radiation fields.

6.4.1.5. Dependence on H_2 density

Figure 58 shows the calculated intensities of the OH 18 cm transition as a function of the H_2 density, where contributions of the FIR radiation in panels ((a)–(f)) are the same as those in Figure 55. Here, the OH column density, the gas kinetic temperature, and the H_2 ortho-to-para ratio are assumed to be 3×10^{15} cm^{-2}, 20 K, and 0, respectively. According to Figures 58 (e) and (f), the absorption of the 1720 MHz line is reproduced for an H_2 density lower than 10 and 10^3 cm^{-3}, respectively. The H_2 density is required to be sufficiently low for FIR pumping to be effective, because collisional excitations with H_2 becomes dominant over the FIR pumping as the H_2 density increases. When

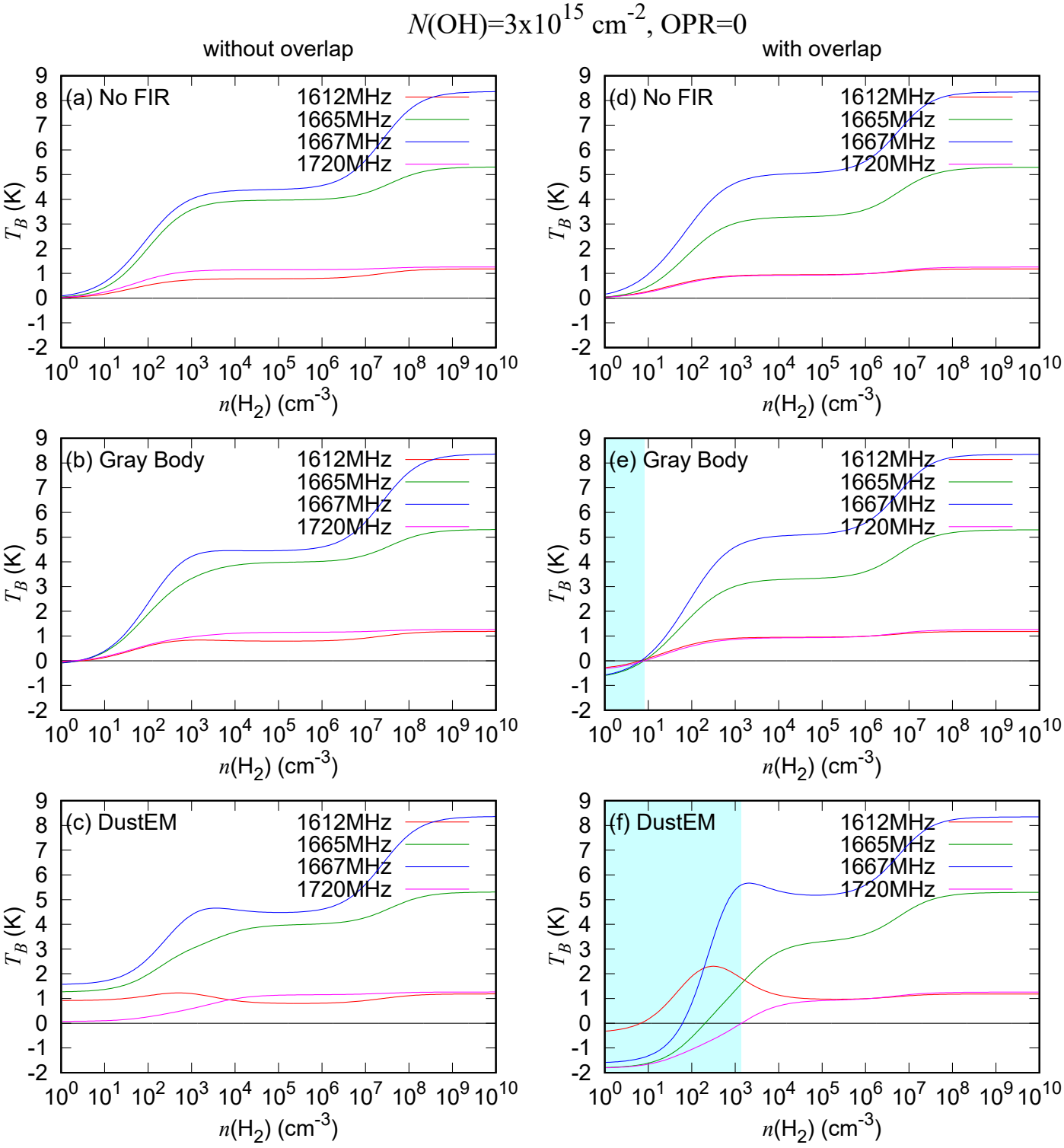

Figure 58. The derived intensities of the OH 18 cm transition hfs lines as a function of the H_2 density, where the OH column density, the gas kinetic temperature, and the ortho-to-para ratio of H_2 are assumed to be 3×10^{15} cm^{-2}, 20 K, and 0, respectively. Models assumed in each panel ((a)–(f)) are the same as those in Figure 55. The cyan areas in the panels (e) and (f) represent the region where the 1720 MHz line appears in absorption.

the effect of the line overlaps is not considered (Figure 58, (c)), the 1720 MHz line is actually much weaker than the 1612 MHz line, but it shows a faint emission. When the effect of line overlaps and the FIR radiation assuming the gray-body are considered (Figure 58, (e)), the 1612, 1665 and 1667 MHz line also show absorption for the H_2 density lower than 10 cm^{-3}. On the other hand, the absorption only for the 1720 MHz line is reproduced, for H_2 densities between 10^2 and 10^3 cm^{-3}, by the DustEM FIR model assuming the line overlaps (Figure 58, (f)).

Figure 59 shows the intensity of the 1720 MHz line in the $n(H_2)$–I_{160} plane. Here, the OH column density, the gas kinetic temperature, and the H_2 ortho-to-para ratio are assumed to be 3×10^{15} cm^{-2}, 20 K, and 0, respectively (fiducial model). The DustEM model is employed for including the

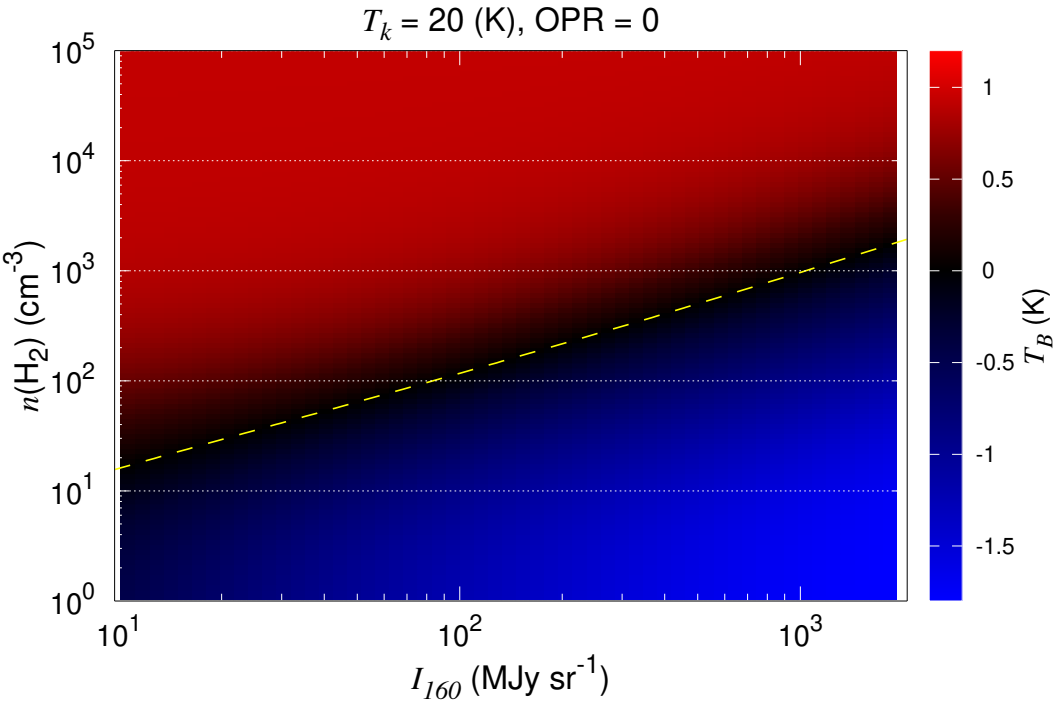

Figure 59. The intensity of the 1720 MHz line on the I_{160}–$n(H_2)$ plane derived from our statistical equilibrium calculation considering the effect of the FIR radiation and line overlaps. I_{160} is used as a parameter to scale the FIR intensity profile of the DustEM model (Figure 53). A blue colored area corresponds to negative brightness temperatures of the 1720 MHz line. The yellow dashed line represents a 1720 MHz line intensity of 0 K. The FIR intensity at 160 μm (I_{160}) stronger than $\sim 10^2$ MJy sr^{-1} is necessary to reproduce the 1720 MHz line absorption with the H_2 density of 10^2 cm^{-3}. I_{160} stronger than 10^3 MJy sr^{-1} is needed with the H_2 density of 10^3 cm^{-3}.

FIR radiation. The yellow dotted line represents the boundary between emission (red color) and absorption (blue color) of the 1720 MHz line, revealing that the threshold value of the H_2 density increases with stronger FIR radiation (Figure 59). This trend is reasonable, since the FIR pumping effect must be dominant over the collisional excitations with H_2 in order to produce the 1720 MHz line absorption. According to Figure 59, the absorption feature of the 1720 MHz line requires an H_2 density of $\sim 10^3$ cm^{-3} or lower for I_{160} of 10^3 MJy sr^{-1}, whereas it requires an H_2 density of $\sim 10^2$ cm^{-3} or lower for I_{160} of 10^2 MJy sr^{-1}.

6.4.1.6. Dependence on H_2 ortho-to-para ratio

Figure 60 shows the calculated intensities of the OH 18 cm hfs lines as a function of the H_2 ortho-to-para ratio for the gas kinetic temperature of 20 K. The H_2 density and the column density of OH are assumed to be 10^3 cm^{-3} and 3×10^{15} cm^{-2}, respectively. The ISRF strength and the H column

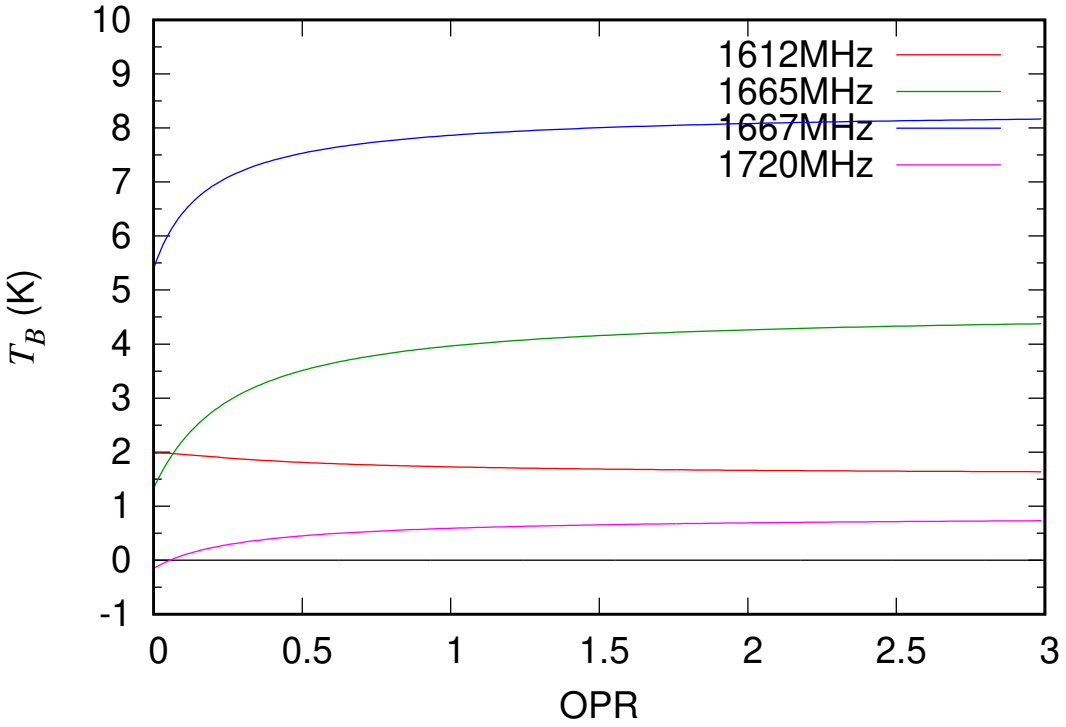

Figure 60. The derived intensities of the four hfs lines of the OH 18 cm transition as a function of the H_2 ortho-to-para ratio, where the H_2 density, the gas kinetic temperature and the column density of OH are assumed to be 10^3 cm^{-3}, 20 K, and 3×10^{15} cm^{-2}, respectively.

density for the DustEM model are assumed to be 0.4 G_0 and 3 $\times$ 10^{23} cm^{-2}, respectively. The effect of line overlaps is considered. According to Figure 60, the 1720 MHz line gradually becomes weaker as the H_2 ortho-to-para ratio becomes lower. The H_2 ortho-to-para ratio of $\sim$ 0 is necessary to reproduce the 1720 MHz line absorption, if the H_2 density is 10^3 cm^{-3}.

6.4.1.7. Summary of this section

According to our new statistical equilibrium calculations that include effects of the FIR pumping and the line overlaps, the absorption feature of the 1720 MHz line can be reproduced, when the OH column density is high ($>$ 10^{15} cm^{-2}) , the gas kinetic temperature is low ($<$ 30 K) and the H_2 ortho-to-para ratio is low ($\sim$0) (Figure 54, left). The H_2 density is also required to be lower than 10^3 cm^{-3}, when the ISRF strength and the H column density are assumed to be 0.4 G_0 and 3 $\times$ 10^{23} cm^{-2}, respectively, in the DustEM model (Jones et al. 2013). The upper limit of the H_2 density becomes higher for stronger FIR radiation. On the other hand, effects of the FIR pumping and the line overlaps are negligible for an OH column density lower than $\sim$ 10^{15} cm^{-2} and FIR intensity at 160 μm lower than $\sim$ 10^2 MJy sr^{-1}. The absorption feature of the 1612 MHz line disappears with the FIR intensity at 160 μm higher than 4 $\times$ 10^3 MJy sr^{-1}. Nevertheless, the OH 18 cm transition can still be used as a thermometer of a diffuse warm gas, as explained in Chapter 4, unless such a strong FIR field (I_{160} $>$ 5 $\times$ 10^3 MJy sr^{-1}) is present.

The absorption feature of the 1720 MHz line is also reproduced with a high column density ($>$ 10^{15} cm^{-2}), a high gas kinetic temperature ($>$ 40 K), and the H_2 ortho-to-para ratio of 3 (Figure 54, right). However, the 1612 MHz line emission is too strong compared to the observed intensities in this case.

We have employed the collisional rate coefficients of OH reported by Offer et al. (1994) in our statistical equilibrium calculations. Recently, Kłos et al. (2017) reported new collisional rate coefficients, although the hyperfine structure of OH was not considered. We obtained hfs-resolved rate coefficients by private communication (from Dr. François Lique), which are approximately calculated from these fine structure rate coefficients by using the M-J random method (Kłos et al. 2017). In order to examine the robustness of our statistical equilibrium calculations described in the previous

subsections, we also conducted the calculations by using these collisional rate coefficients. The results are presented in Appendix B. Even with these collisional rate coefficients, the essential features of our results on the hfs intensity anomaly do not change significantly. Thus, uncertainties of the collisional rate coefficients are considered to have a limited effect on the results of the hfs intensity anomalies of the OH 18 cm transition.

6.4.2 Fitting the observed spectra

We compare our new model with the spectra of the OH 18 cm transition observed toward TMC-1FN, TMC-1(CP), L183, and L169. Since the 8.2 km s^{-1} and 6.5 km s^{-1} components of TMC-1FN and the $\sim$ 6.4 km s^{-1} component of TMC-1 (CP) show absorption or faint emission in the 1612 MHz line, they are expected to trace warm molecular gas (Chapter 4). Hence, we determined the gas kinetic temperature and the OH column density for these components (Table 14) assuming an H_2 density of 10^3 cm^{-3}. On the other hand, the 5.5 km s^{-1} component of TMC-1FN, the $\sim$ 5.4 km s^{-1} component of TMC-1 (CP), L183, and L169 show absorption or faint emission of the 1720 MHz line, and hence, they likely trace cold dense regions.

6.4.2.1. TMC-1FN

The 1720 MHz line absorption is detected with $\sim$3 σ confidence level toward TMC-1FN. To explain this feature, the FIR intensity of $\sim 10^3$ MJy sr^{-1} at 160 μm is necessary according to our new statistical equilibrium calculations. This is stronger by one order of magnitude than the value observed with *Spitzer* (80–120 MJy sr^{-1}) according to Flagey et al. (2009). In order to explain this, we assess the geometrical effect of a filamentary structure, for which the FIR intensity inside might be enhanced. Assuming that the filament is a cylinder with a Plummer-like density profile (Malinen et al. 2012), the FIR intensity inside the filament can be 3–4 times stronger than the observed value. Details of the calculation are described in Appendix C. A further factor of 2–3 necessary to explain the 1720 MHz absorption might be explained by contributions from a filamentary structure in the northwest of TMC-1FN (Xu et al. 2016), another filament near TMC-1 (CP) (Figure 44), or by diffuse gas extended in the southwestern part of HCL2 (Figure 44). However, contributions from other filamentary structures might be small compared to the contribution from the nearest filament, since they

Table 14. Best fit parameters determined by our statistical equilibrium calculation.

Source	V_{LSR} (km/s)	$n(H_2)$ (cm^{-3})	T_k (K)	N(OH) (cm^{-2})	o/p
TMC-1CP(0′, 24′)	6.62	10^3(fixed)	31(1)	5.1(14) × 10^{14}	0.1(fixed)
TMC-1CP(0′, 16′)	6.35	10^3(fixed)	35(1)	5.0(4) × 10^{14}	0.3(fixed)
TMC-1CP(0′, 8′)	6.34	10^3(fixed)	43(1)	5.6(3) × 10^{14}	0.7(fixed)
TMC-1FN	6.51	10^3(fixed)	30(3)	3.6(3) × 10^{14}	0.1(fixed)
	8.16	10^3(fixed)	70(3)	1.4(4) × 10^{14}	3.0(fixed)

NOTE—We derived the OH column density and the gas kinetic temperature for the 6.5 km s^{-1} and the 8.2 km s^{-1} components of TMC-1FN, and the ∼ 6.4 km s^{-1} component of TMC-1 (CP), where the H_2 ortho-to-para ratio has been changed from 0 to 3 with a 0.05 interval, and is fixed to the value that gives the best-fit result. The error in the parentheses represents one standard deviation. The V_{LSR} corresponds to those in Table 12.

occupy smaller solid angle than the nearest filament. In addition, contributions from the extended gas component is limited, considering that the observed FIR intensity of this component is comparable to that observed in TMC-1FN. Approximations employed in the calculations, in particular, neglect of the velocity gradient in the treatment of the line overlap (Guilloteau et al. 1981), may also contribute to this discrepancy. Contributions from non-local line overlaps (Cesaroni & Walmsley 1991; Elitzur et al. 1976) caused by the velocity gradient within the cloud might explain more efficient FIR pumping, although quantitative analysis on this effect is rather difficult.

For the 8.2 km s^{-1} component, the gas kinetic temperature and the OH column density are determined to be 70 ± 3 K and (1.4 ± 0.4) × 10^{14} cm^{-2}, respectively, where the H_2 density and the ortho-to-para ratio are assumed to be 10^3 cm^{-3} and 3, respectively. For the 6.5 km s^{-1} component, the gas kinetic temperature and the OH column density are determined to be 30 ± 3 K and (3.6 ± 0.3) × 10^{14} cm^{-2}, respectively. An H_2 ortho-to-para ratio of 0.1 provides the best fit, although

it cannot be constrained by the fitting procedure. For the 5.5 km s^{-1} component, the gas kinetic temperature and the OH column density are estimated to be lower than 30 K, and higher than 10^{15} cm^{-2}, respectively, in order to reproduce the 1720 MHz line absorption according to our statistical equilibrium analysis.

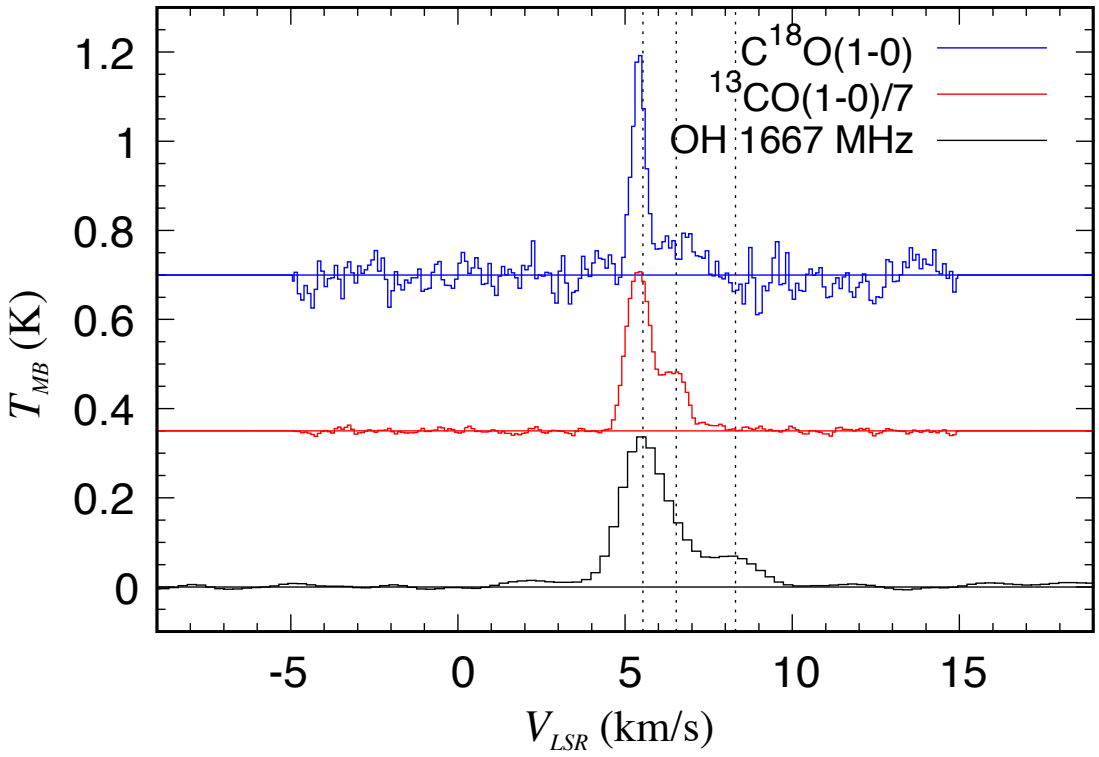

Figure 61. Spectra for the 1667 MHz (black) hfs line of the OH 18 cm transition, the ^{13}CO ($J = 1 - 0$) line (red) and the C^{18}O ($J = 1 - 0$) line (blue) observed toward TMC-1FN (Figure 44). The ^{13}CO and C^{18}O lines are averaged over the beam size of the OH 18 cm transition, as revealed by the white circle in Figure 44. Dashed lines show the velocities of the three components (5.5 km s^{-1}, 6.5 km s^{-1}, and 8.2 km s^{-1}).

Figure 61 shows the spectrum of the 1667 MHz line of OH observed toward TMC-1FN with the ^{13}CO ($J = 1 - 0$) and C^{18}O ($J = 1 - 0$) line spectra observed toward the same position with NRO 45-m telescope (Sunada & Kitamura 1999). The ^{13}CO and C^{18}O line profiles are prepared by averaging these lines' spectra over the beam size of the OH 18 cm transition. As shown in Figure 61, the 8.2 km s^{-1} component, which is clearly seen in OH, is not detected in both ^{13}CO and C^{18}O. On the other hand, the 6.5 km s^{-1} component is clearly seen in ^{13}CO and C^{18}O, while the C^{18}O emission

is prominent for the 5.5 km s^{-1} component. These results suggest that the 8.2 km s^{-1} component traces diffuse warm gas that cannot readily be traced by ^{13}CO, whereas the 5.5 km s^{-1} component traces relatively cold and dense gas also traced by C^{18}O. The 6.5 km s^{-1} component appears to trace gas at intermediate temperature and density between these two structures. This picture is consistent with the derived gas kinetic temperatures and the H_2 ortho-to-para ratio (Table 14). In fact, the gas kinetic temperature should be higher in the outer part of the cloud, which produces a deeper absorption feature of the 1612 MHz line and brighter 1720 MHz emission. Since the higher V_{LSR} components tend to trace a warmer part of the cloud in TMC-1FN (Table 14), the observed spectra of OH seem to reflect the cloud structure with the increasing gas kinetic temperature toward cloud peripheries as does the increasing V_{LSR}.

Figure 44 shows the integrated intensity maps of C^{18}O (J=1–0) (cyan contours) and ^{13}CO (J=1–0) (color) observed with the NRO 45-m telescope for the entire region of HCL2 (Sunada & Kitamura 1999). A prominent straight structure is seen in the northern part of HCL2 in the C^{18}O map, which also has been pointed out by Narayanan et al. (2008) and Goldsmith et al. (2010). Interestingly, the velocity of the blue-shifted component detected in the OH 18 cm transition ($V_{LSR} \sim 5.5$ km s^{-1}) corresponds to that of C^{18}O exhibiting the straight structure, whereas the velocity of the red-shifted component seen in OH ($V_{LSR} \sim$ 6–10 km s^{-1}) corresponds to that of the southwestern extended gas in the ^{13}CO map. These two structures are interfacing with each other, suggesting a compressive motion as the origin of the straight structure (Figure 62). Such a compressive motion is consistent with the decreasing velocity from southwest to northeast across the straight structure observed in ^{13}CO and C^{18}O. In addition, the existence of an [H I] cloud in the northeast of TMC-1FN is suggested by the archival data of The Galactic Arecibo L-band Feed Array HI (GALFA-HI) Survey maps (Peek et al. 2011). Furthermore, the 6–10 km s^{-1} component traces a diffuse warm gas, whereas the 5.5 km s^{-1} component traces a cold and dense core illuminated by the FIR radiation from dust grains, according to our statistical equilibrium calculation. It is likely that the 5.5 km s^{-1} component traces cold cores surrounded by the warm envelope gas in HCL2.

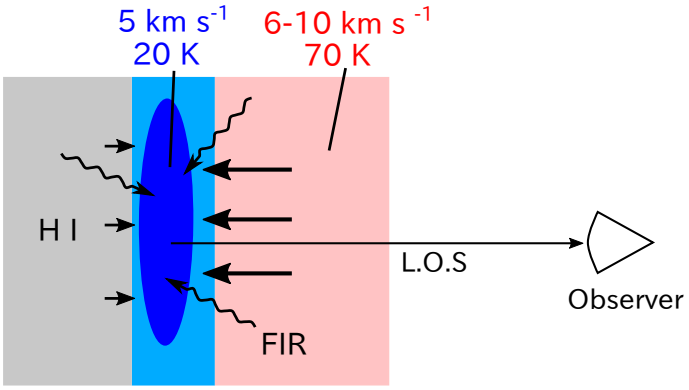

Figure 62. Schematic illustration of the cross section of TMC-1FN along the line-of-sight. The cold (∼ 20 K) and a dense core (5 km s^{-1}) is formed by compressive motion of the extended warm gas (6–10 km s^{-1}). We observe the source from the right hand side.

The 6.5 and 8.2 km s^{-1} components show the 1612 MHz line absorption, in spite of the FIR pumping effect seen in the 5.5 km s^{-1} component. This can be explained by the above picture of TMC-1FN (Figure 62). A warm envelope gas traced by the 6.5 and 8.2 km s^{-1} components is likely to be illuminated by fainter FIR radiation than the gas traced by the 5.5 km s^{-1} component. The OH column density for the 6.5 and 8.2 km s^{-1} components is also lower. According to the results in Appendix C, the FIR intensity at 160 μm is estimated to be ∼400 and 100 MJy sr^{-1} at positions 0.5 pc and 1.0 pc distant from the center of the TMC-1FN filament, respectively. The OH column densities are determined to be 3.6 $\times$ 10^{14} cm^{-2} and 1.4 $\times$ 10^{14} cm^{-2} for the 6.5 and 8.2 km s^{-1} components, respectively (Table 14). As described in Section 6.4.1.7, our calculation shows that the FIR pumping effect is negligible, for an OH column density lower than 10^{15} cm^{-2} and I_{160} lower than 100 MJy sr^{-1}. On the other hand, the 1612 MHz line indeed appears in absorption for I_{160} lower than 4 $\times$ 10^{3} MJy sr^{-1}, if the OH column density is 3 $\times$ 10^{14} cm^{-2} (Figure 57 (d)). Hence, even though there might be a moderate FIR field (4 $\times$ 10^{3} MJy sr^{-1}), the 1612 MHz line absorption in the 6.5 and 8.2 km s^{-1} components can be reproduced as long as the OH column density is lower than $\sim$ 10^{15} cm^{-2}. Note that the intensities of the 1612 and 1720 MHz lines are slightly affected by the FIR pumping effect in this case (Figure 57).

6.4.2.2. TMC-1 (CP)

The OH spectra toward TMC-1 (CP) consists of the two components (5.36–5.59 km s^{-1} and 6.34–6.62 km s^{-1}), as mentioned in Section 6.3. The gas kinetic temperature is determined to be about 40 K for the red-shifted component (6.34–6.62 km s^{-1} component), which shows weak emission or absorption of the 1612 MHz line. On the other hand, the gas kinetic temperature is considered to be lower than 30 K for the blue-shifted component (5.36–5.59 km s^{-1}), according to the DustEM model considering the effect of the line overlaps. The FIR intensity is assumed to be 1.4×10^3 MJy sr^{-1} at 160 μm. However, only an upper limit to the gas kinetic temperature can be determined, because of the limited signal-to-noise ratio. The derived parameters for the red-shifted components are summarized in Table 14.

6.4.2.3. L183 and L169

As shown in Figure 51, the 1720 MHz line shows weak emission in L183, and it is totally absent in L169. From these results, the gas kinetic temperature is estimated to be lower than 30 K according to our statistical equilibrium calculations that include FIR pumping (Figure 54). The gas kinetic temperature of 30 K is lower than values determined for positions 8′ and 16′ south from L183 in Section 4.6.3 (31 K and 53 K, respectively). Previous studies have shown that there is a dense core in the northern part of L183, which is traced in the NH_3 line (cross position in Figure 45) (Swade 1989; Dickens et al. 2000). A rather diffuse molecular cloud seen in ^{13}CO emission is extended toward its southern part (Laureijs et al. 1995; Lehtinen et al. 2003). Thus the increase of the gas kinetic temperature toward the southern peripheries in L183 indicates that photoelectric heating by interstellar UV radiation is less effective in the core position.

6.5 Interferometric observation of TMC-1FN with VLA

For the full understanding of the origin of the 1720 MHz line absorption, we conducted the high-resolution observation of the OH 18 cm transition with the Very Large Array (VLA) in 2017. We examine the spatial distribution of the OH 18 cm transition with better angular resolution (46″) than that of the Effelsberg telescope (8.2′). Assuming the above picture of TMC-1FN (Figure 62), the 5.5 km s^{-1} component, which shows the 1720 MHz absorption, would be better traced by VLA than the

Effelsberg telescope, since the extended components (V_{LSR} of 6.5 and 8.2 km s^{-1}) are considered to be resolved out in the interferometric observation. As shown later, the 6.5 and 8.2 km s^{-1} components are indeed almost resolved out. On the other hand, the 1720 MHz line shows *emission* at V_{LSR} of 5.3 km s^{-1} with VLA, although its absorption is marginally seen at V_{LSR} of $\sim$5.0 km s^{-1}. In Sections 6.5.2 and 6.5.3, we show that the 1720 MHz line emission ($V_{LSR} \sim$ 5.3 km s^{-1}) comes from a cold dense core embedded in TMC-1FN, which was not resolved by the Effelsberg.

6.5.1 Observation and data reduction

The observation was conducted with VLA in 2017 February and March. We employed the D-configuration of the array whose synthesized beam size was $\sim$46″, which is more than 10 times better than the beam size of the Effelsberg (8.2′). An instantaneous bandwidth and resolution of the backend were 500 kHz and 0.244 kHz, respectively. The resolution corresponds to the velocity resolution of 0.0439 km s^{-1} at 1667 MHz. 3C147 was employed for the bandpass and the absolute flux calibrations. We observed the J0431+2037 every an hour for the phase calibration. Total integration time on source was 8.6 hours.

We used the CASA (the Common Astronomy Software Applications) package for the data reduction. We used CLEAN algorithm to obtain images from visibility data, where the natural weighting was employed. Continuum images were prepared by averaging over line-free channels. Then, we obtained line images by subtracting the continuum image from the original ones. The field center of the observation was TMC-1FN (-4′, -4′) = ($4^h39^m28^s.7$, $26^d31'27''.0$) (Figure 63), which is located on the center of the straight structure seen in the C^{18}O map.

6.5.2 Spatial distribution of the 1667 MHz line

Figure 63 shows the integrated intensity map of the 1667 MHz line (V_{LSR} = 4.9–6.9 km s^{-1}) observed with VLA (color), overlaid on the C^{18}O integrated intensity map (white contours) which is the same as the cyan contours in Figure 44. Positions of TMC-1FN (0′, 0′) and (-4′, -4′) are indicated by white and red circles, respectively, whose diameters correspond to the beam size of the Effelsberg (8.2′). The latter position is the field center of the observation. As shown in Figure 63, the 1667

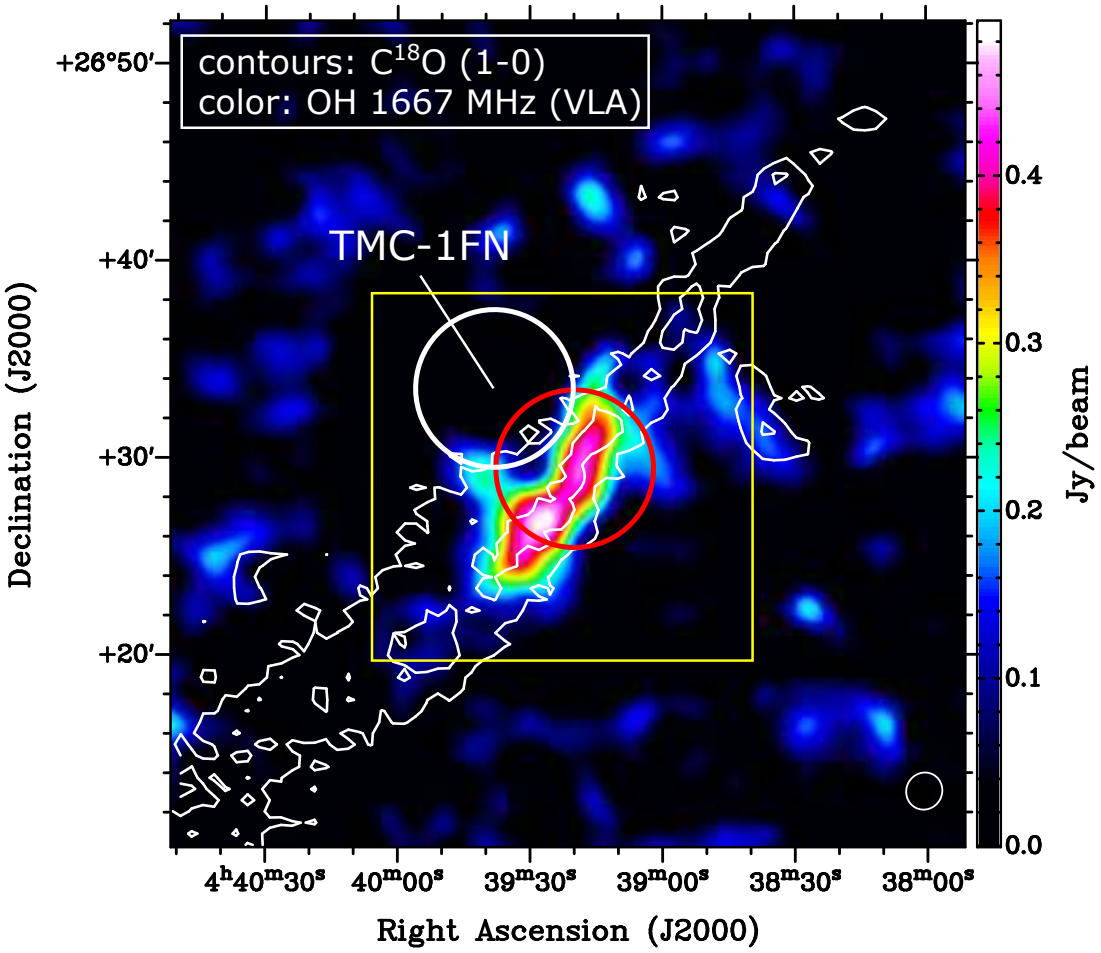

Figure 63. (Color) The integrated intensity map of the 1667 MHz line (V_{LSR} = 4.9–6.9 km s^{-1}) observed with VLA. (Contours) The C^{18}O integrated intensity map (V_{LSR}=6.45–6.95 km s^{-1}), which is the same as the cyan contours in Figure 44. White and red circles represent the position of TMC-1FN and TMC-1FN (-4′, -4′), with their diameters corresponding to the HPBW beam size of the Effelsberg 100-m telescope of 8.2′. A yellow rectangle represents the zoomed region for Figure 64.

MHz line is concentrated on the center of the straight structure near the field center, and well traces the C^{18}O distribution, which is more evident in the zoomed image within the area enclosed by the yellow rectangle (Figure 64). This region is known to have higher H_2 column density ((1–2) $\times$ 10^{22} cm^{-2}) than its surroundings, according to the WFCAM extinction map and the Herschel SPIRE 250, 350 and 500 μm maps (Malinen et al. 2012). On the other hand, the 1667 MHz line is almost absent in the southwest of the straight structure, which is contrary to the ^{13}CO emission extended there (Figure 44). Furthermore, the 1667 MHz line is even absent toward TMC-1FN within the beam size

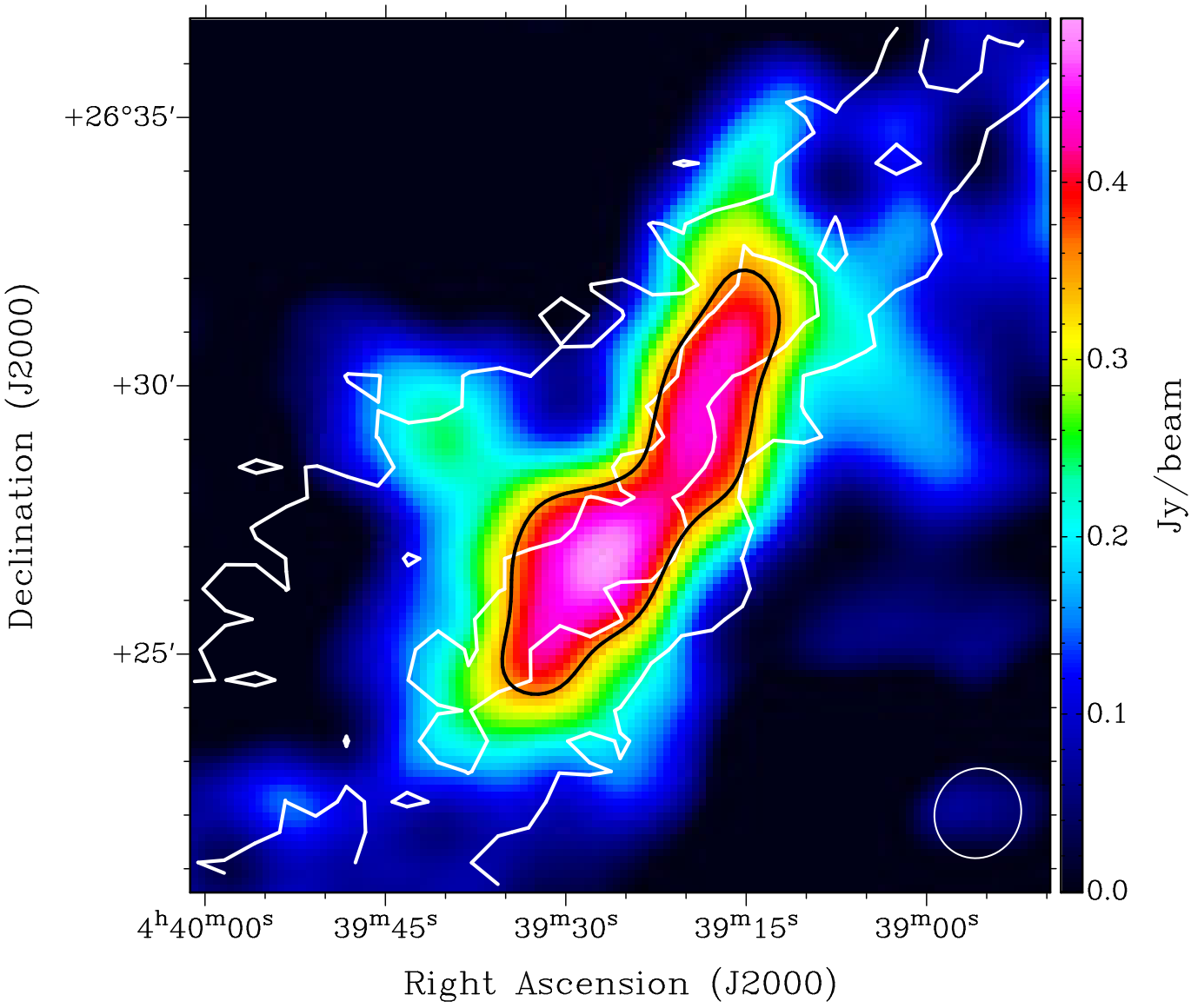

Figure 64. The zoomed image of Figure 63 within the area enclosed by the yellow rectangle in Figure 63.

of the Effelsberg (white circle in Figure 63). These results suggest that extended components are resolved out in the VLA observation, whereas dense and compact components of the cloud traced by $C^{18}O$ are more sensitively observed with VLA than the Effelsberg telescope.

6.5.3 Spectra exhibiting the LTE intensity ratio

Spectra of the OH 18 cm transition observed with VLA obtained by averaging over the area within the red circle in Figure 63 is shown in the left panel of Figure 65 (blue line), overlaid on the spectra observed toward TMC1-FN with the Effelsberg telescope (red line). The vertical dotted lines repre-

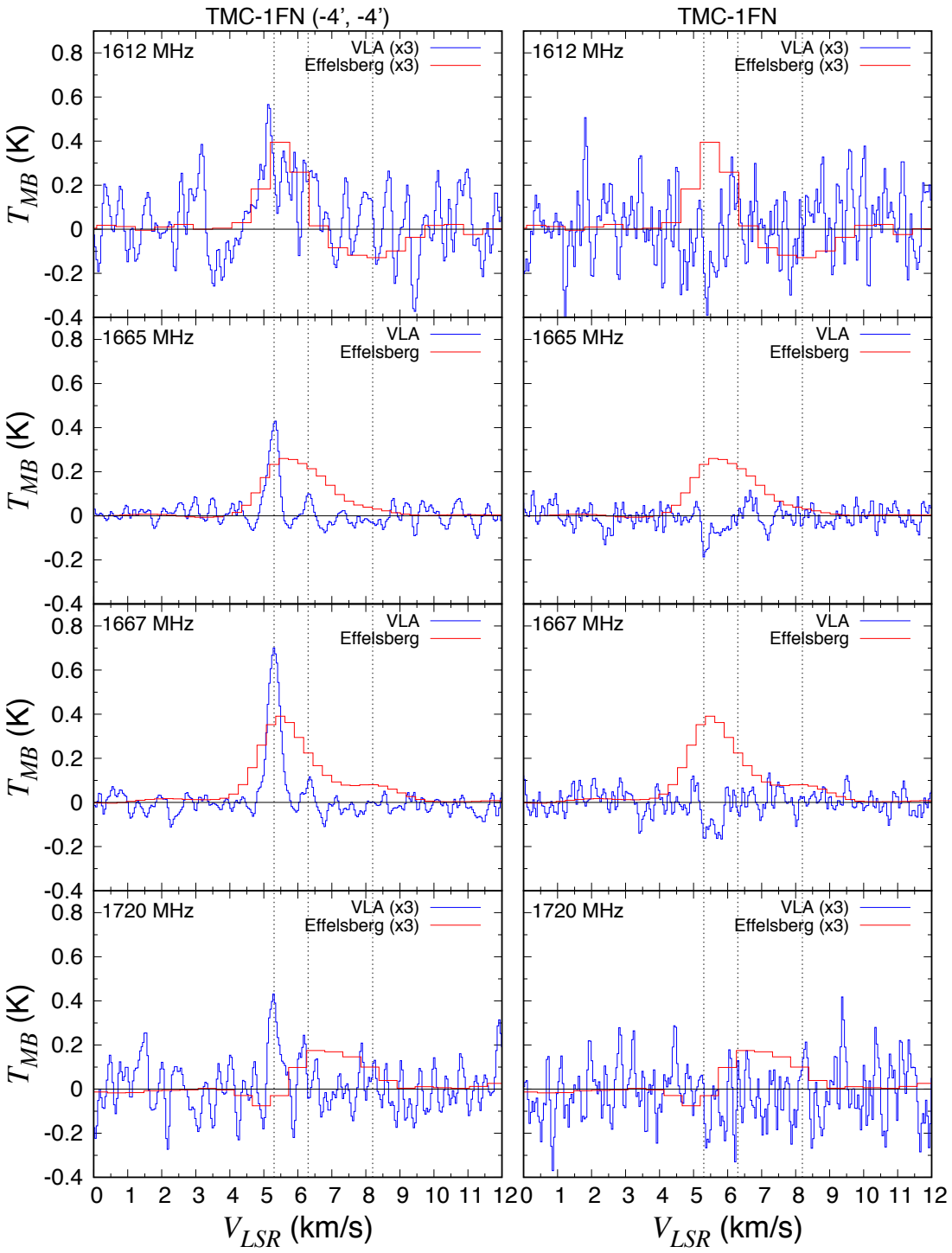

Figure 65. (Blue) Spectra of the OH 18 cm transition observed with VLA prepared by averaging over the area enclosed by the red and white circles in Figure 63 are shown in the left and right panels, respectively. (Red) Spectra of the OH 18 cm transition observed with the Effelsberg toward TMC-1FN (white circle in Figure 63). The vertical dotted lines represent V_{LSR} of 5.3, 6.3, and 8.2 km s^{-1}. The intensities of the 1612 and 1720 MHz lines are multiplied by a factor of three.

sent the V_{LSR} of 5.3, 6.3 and 8.2 km s^{-1}. As shown in the left panel of Figure 65, all the four hfs lines of the OH 18 cm transition are observed in emission at V_{LSR} of ∼5.3 km s^{-1} with VLA. This is apparently different from the 5.5 km s^{-1} component observed with the Effelsberg (red line), where the 1720 MHz line appears in absorption. In addition, linewidth of the 5.3 km s^{-1} component observed with VLA (0.3–0.4 km s^{-1}) is narrower than that of the 5.5 km s^{-1} component observed with the Effelsberg (1.0 km s^{-1}) by a factor of ∼2. According to our statistical equilibrium calculations including the FIR pumping effect, an H_2 density higher than 10^4 cm^{-3} and a gas kinetic temperature lower than 20 K are necessary to reproduce the emission of all the four hfs lines (Figures 55 (f) and 58 (f)). Moreover, H_2 density higher than 10^5 cm^{-3} is required to reproduce the comparable intensities of the 1612 MHz and 1720 MHz lines (Figure 58 (f)). Therefore, the 5.3 km s^{-1} component is considered to trace a cold and dense core inside the 5.5 km s^{-1} component.

At the V_{LSR} of ∼6.3 km s^{-1}, the 1665 and 1667 MHz lines show faint emission in the VLA spectra, while the signal-to-noise ratio is insufficient to detect this component in the 1612 and 1720 MHz lines. Intensity ratio between the 6.3 and 5.3 km s^{-1} components of the 1667 MHz line is determined to be ∼ 0.14 from the VLA data. This is lower by a factor of ∼2 than the ratio between the 6.5 and 5.5 km s^{-1} components derived from the Effelsberg data (∼ 0.25), suggesting that the 6.3 km s^{-1} component is resolved out to some extent in the VLA observation. Such a resolving out effect is more clearly seen in the 8.2 km s^{-1} component, which is totally absent in the VLA spectra (Figure 65). This is reasonable, since the 8.2 km s^{-1} component traces a more extended gas than the 6.3 km s^{-1} component, according to the results in Section 6.4.2.1. The OH spectra obtained with VLA toward TMC-1FN prepared by averaging over the white circle in Figure 63 is shown in the right panel of Figure 65 for reference. All the four hfs lines of the OH 18 cm transition are indeed absent, which is apparent in the 1667 MHz line map (Figure 63). Note that the absorption features of the 1665 and 1667 MHz lines at V_{LSR} of 5–6 km s^{-1} are artificial signals produced by sidelobes of strong emissions around TMC-1FN (-4′, -4′).

In order to explore the origin of the 1720 MHz line emission observed with VLA (V_{LSR} ∼5.3 km s^{-1}) more precisely, we obtain the spectra of the OH 18 cm transition with a better signal-to-noise

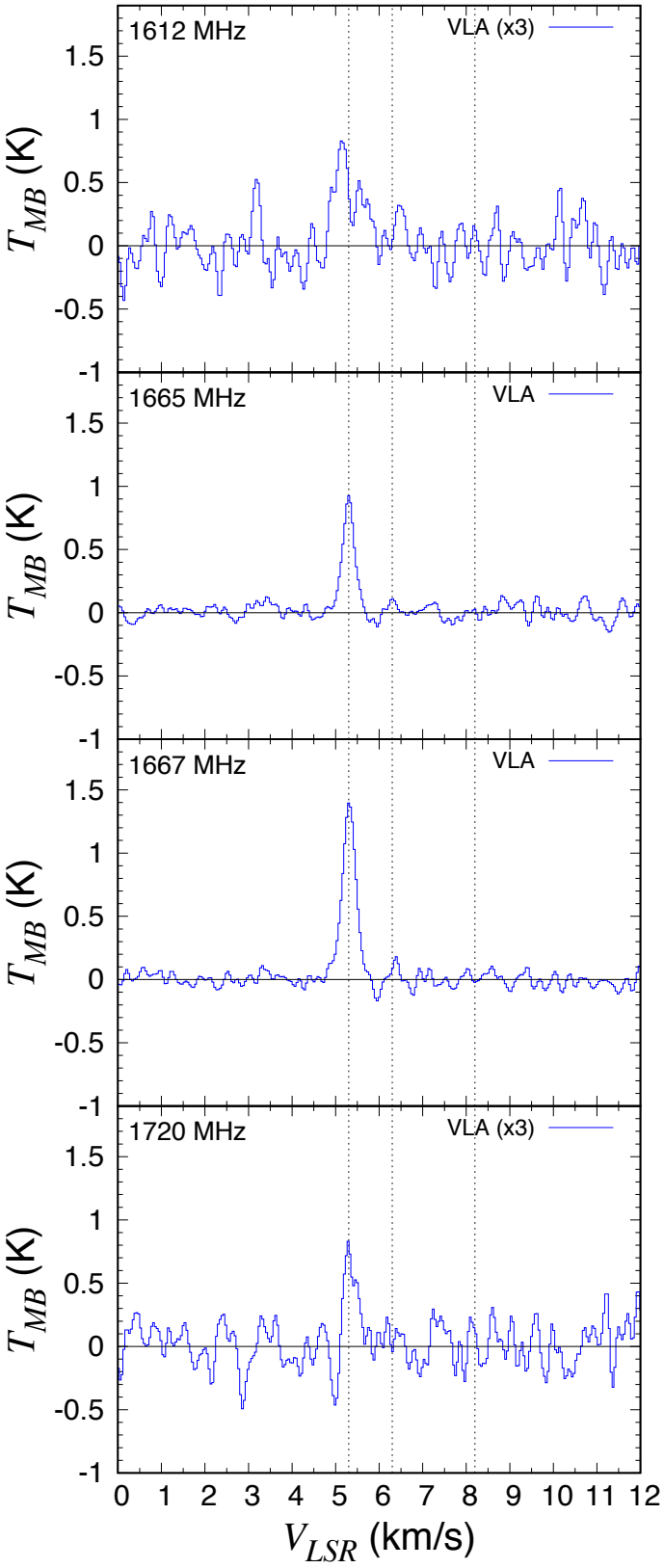

Figure 66. Spectra of the OH 18 cm transition observed with VLA prepared by averaging over the area enclosed by the black contour in Figure 64. A marginal absorption feature of the 1720 MHz line is seen in the V_{LSR} of 5.0 km s^{-1}. The intensities of the 1612 and 1720 MHz lines are multiplied by a factor of three.

ratio than the left panel of Figure 65, by averaging over the area enclosed by the black contour in Figure 64. This black contour corresponds to the 5σ level ($\sim$0.35 Jy/beam) of the image. The obtained spectra is shown in Figure 66. Again, the 5.3 km s^{-1} component shows emission for all the hfs components, whereas a hint of the absorption feature of the 1720 MHz line is seen in V_{LSR} of 5.0 km s^{-1}. Although this absorption feature is marginal, the 1612 MHz line also shows a peak in the same velocity, and the 1665 and 1667 MHz lines exhibit a wing component there. The strong 1720 MHz emission ($V_{LSR} \sim 5.3$ km s^{-1}) and its marginal absorption ($V_{LSR} \sim 5.0$ km s^{-1}) suggest that the gas traced by 1720 MHz absorption is also resolved out, and more compact component, which shows the 1720 MHz emission, is revealed by VLA. This picture is confirmed by the fact that the intensities of the 1665, 1667 and 1720 MHz lines relative to the 1612 MHz line for the 5.3 km s^{-1} component, which are determined to be 5.3$\pm$1.0, 8.6$\pm$1.6, 1.7$\pm$0.4, respectively, are close to those expected under the LTE condition (5, 9 and 1, respectively).

Above all, TMC-1FN is considered to consist of four components; (1) a warm extended gas traced by the 1612 MHz absorption ($V_{LSR} \sim 8.2$ km s^{-1}, $T_k > 40$ K, N(OH) $< 10^{15}$ cm^{-2}, OPR $\sim$ 3), (2) an intermediate gas traced by the faint 1612 MHz emission which connects the 8.2 and 5.5 km s^{-1} components ($V_{LSR} \sim 6.5$ km s^{-1}, $T_k \sim$ 30–40 K, N(OH) $< 10^{15}$ cm^{-2}), (3) a relatively cold and dense gas traced by the 1720 MHz absorption ($V_{LSR} \sim 5.5$ km s^{-1}, $T_k < 30$ K, N(OH) $> 10^{15}$ cm^{-2}, $n(\mathrm{H_2}) < 10^3$ cm^{-3}, OPR $\sim$ 0), and (4) a cold dense core deep inside the cloud revealed by VLA, which shows the LTE ratio ($V_{LSR} \sim 5.3$ km s^{-1}, $T_k \sim 10$ K, $n(\mathrm{H_2}) > 10^4$ cm^{-3}, OPR $\sim$ 0). Physical conditions of these components can be estimated by different hfs anomalies of the OH 18 cm transition. This result demonstrates the unique characteristic of the OH 18 cm transition as a tracer of molecular-cloud formation over a wide range of $\mathrm{H_2}$ density from diffuse clouds to dense cores.

6.6 Summary

We have shown that the absorption feature of the 1720 MHz line of the OH 18 cm transition can be reproduced by taking account of the effect of pumping of FIR radiation from dust grains. We have developed a statistical equilibrium calculation code considering the effects of the FIR radiation and line overlaps, and have investigated the origin of the 1720 MHz line absorption. As a result, the 1720

MHz absorption is found to trace a dense ($N(\mathrm{OH}) > 10^{15}$ cm^{-2}) and cold ($T_k < 30$ K) core illuminated by relatively strong FIR radiation from dust grains in surrounding clouds. On the other hand, we have confirmed that the absorption feature of the 1612 MHz line can be used to determine the gas kinetic temperature of the diffuse warm gas for a wide range of an H_2 density, even in the presence of the FIR radiation. Toward TMC-1FN and TMC-1(CP), the gas kinetic temperature is determined to be 30–70 K for the red-shifted component, whereas it is lower than $\sim$ 30 K for the blue-shifted component in which the 1720 MHz line is seen in absorption. Combined analyses of OH, ^{13}CO, and C^{18}O suggest that the peculiar straight structure in HCL2 is likely formed by the compression of the warm envelope gas in southwestern direction. Hence, its unique characteristics, combined with the excitation calculations, make the quartet of the hfs lines of the OH 18 cm transition a powerful probe to study molecular cloud formation and a tracer of CO-dark molecular gas.

Nevertheless, we still have the shortage of the FIR intensity by a factor of 2–3 in order to fully reproduce the 1720 MHz absorption, even if we consider the filamentary structure of the cloud. This contradiction might be explained by contributions from extended gas and other filaments, and effect of non-local line overlaps. Since quantitative analyses on these effects are rather difficult, they have to be left for future works. However, this study has clarified the mechanism of the observed 1720 MHz absorption in molecular clouds and its physical meaning, and it will be a stiff base for such future studies. The full understanding of the hyperfine anomalies of the OH 18 cm transition is essentially important for future observational studies of OH using the Five-hundred-meter Aperture Spherical radio Telescope (FAST) (http://fast.bao.ac.cn/en/) and Square Kilometre Array (SKA) (https://www.skatelescope.org/).

CHAPTER 7. Conclusions and Future Prospects

We conducted sensitive observations of the four hfs components of the OH 18 cm transition toward various molecular clouds with the Effelsberg 100-m telescope and the GBT 100-m telescopes. As a result, we find three types of hfs anomaly of the OH 18 cm transition;

1. The 1612 MHz absorption in a diffuse warm gas ($T_k > 40$ K, 10^{14} cm$^{-2} < N(\mathrm{OH}) < 10^{15}$ cm^{-2}).

2. The 1665 MHz and 1667 MHz absorption in a warmer gas than that for 1 ($T_k > 90$ K).

3. The 1720 MHz absorption in a relatively cold and dense gas ($T_k < 30$ K, $N(\mathrm{OH}) > 10^{15}$ cm^{-2}, $n(\mathrm{H_2}) < 10^3$ cm^{-3}) illuminated by the strong FIR radiation from surrounding gas.

We developed the statistical equilibrium calculation code, which successfully reproduces these hfs anomalies. From these calculations, the fundamental pumping mechanisms producing each hfs anomaly as well as the physical conditions required to reproduce the anomalies are revealed.

As for the 1612 MHz line absorption, the gas kinetic temperature can be determined accurately by fitting our statistical equilibrium calculation to the observation. The absorption feature of the main lines (1665 and 1667 MHz) is observed only toward the Pipe nebula, where the two filamentary structures are interfacing with each other. The gas kinetic temperature is required to be high ($T_k >$ 90 K), suggesting the substantial heating by filament-filament collisions. From these analyses of the 1612 MHz absorption and the main lines' absorption, we demonstrate that the OH 18 cm transition can be used as a good thermometer of diffuse warm gas ($T_k > 40$ K), which is a key to understanding the transition from an atomic gas to a molecular cloud (Chapters 1 and 2).

The 1720 MHz line absorption is observed on the straight structure of HCL2, TMC-1FN. Its weak emission or faint absorption with the enhanced 1612 MHz emission is observed toward L169, L183 and TMC-1(CP). We conducted statistical equilibrium calculations that include the effects of the line overlaps and FIR pumping. As a result, we find that the FIR pumping to $^2\Pi_{1/2}$ $J = 3/2$ and $^2\Pi_{1/2}$ $J = 5/2$ states from the ground rotational state at 53 μm and 35 μm, respectively, plays an

Table 15. Derived parameters (three sources).

source	#	V_{LSR} (km/s)	FWHM (km/s)	T_k (K)	N(OH) (cm^{-2})
W49N	1	40.0	1.1	37±25	$(2.3\pm1.9)\times10^{14}$
	2	59.6	4.0	> 35	$< 6\times10^{14}$
	3	60.6	1.4	–	–
	4	63.0	1.5	66±15	$(1.5\pm0.6)\times10^{14}$
W31C	1	28.3	2.9	69±2	$(2.9\pm1.3)\times10^{14}$
	2	40.0	4.0	68±2	$(3.3\pm1.7)\times10^{14}$
SgrB2(M)	1	-80.8	36.5	–	–
	2	-41.1	2.8	> 40	$< 2.5\times10^{15}$
	3	-23.3	40.6	100±13	$(4.4\pm0.7)\times10^{15}$
	4	1.0	11.8	116±18	$(1.8\pm0.2)\times10^{15}$
	5	13.5	18.3	10(fixed)	$(3.1\pm0.2)\times10^{16}$

NOTE—Gas kinetic temperature and OH column density of each velocity component toward W49N, W31C and Sgr B2(M) derived with our statistical equilibrium calculation. Colored numbers in the second column correspond to those described in the 1667 MHz line spectra in Figure 67.

important role, although further study is necessary to fully explain the shortage of the observed FIR intensity.

We also conducted the interferometric observation of the OH 18 cm transition toward TMC-1FN with VLA. The extended component traced by the 1612 MHz absorption is resolved out in the integrated intensity map. Furthermore, the 1720 MHz line appears in emission with VLA at the velocity where it shows absorption with the Effelsberg. The hfs intensity ratio is close to that expected under LTE, suggesting that the VLA reveals a dense core deep inside the cloud.

All these results show that the OH 18 cm transition is a new and powerful tool to study molecular-cloud formation, because it traces a variety of physical conditions over the wide range of an H_2 density and the gas kinetic temperature.

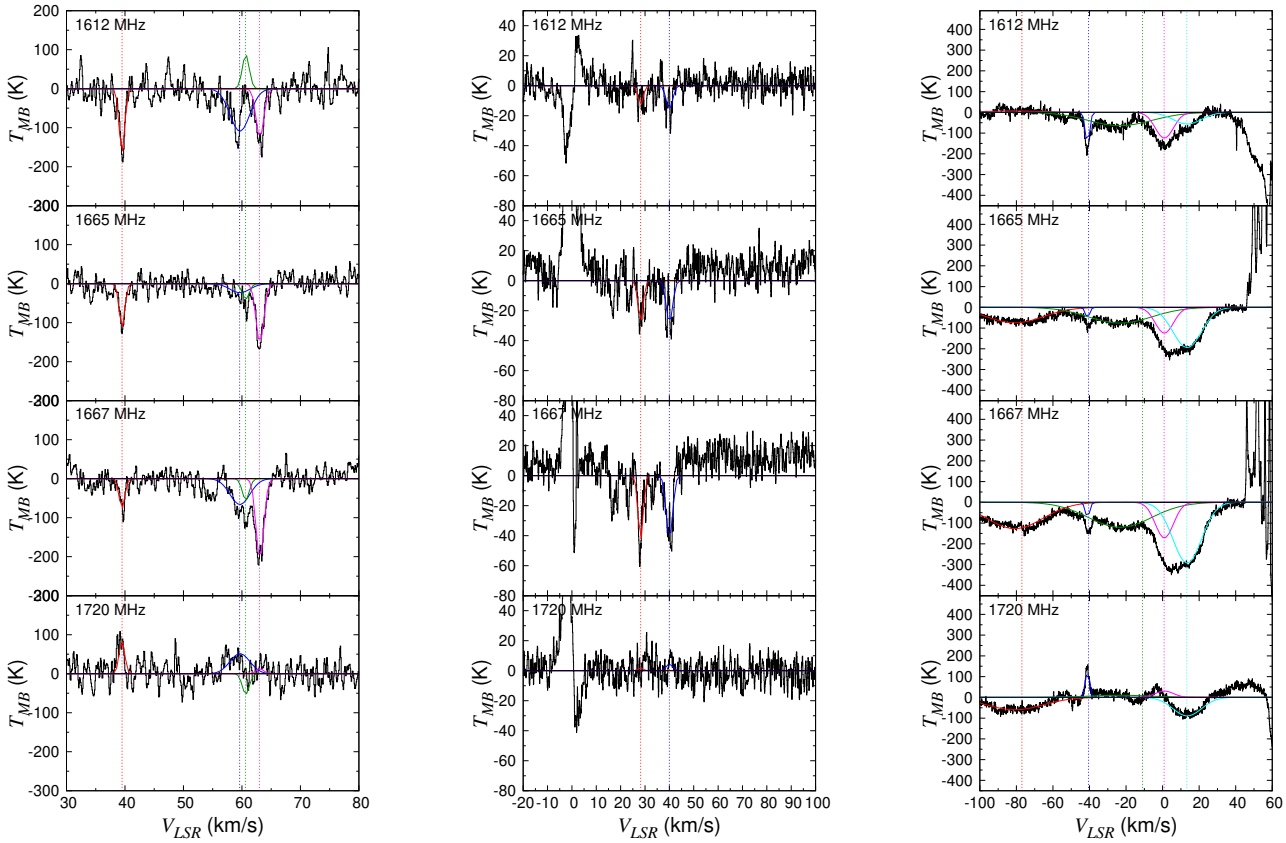

Figure 67. The OH 18 cm line spectra observed toward (left) W49N, (middle) W31C and (right) Sgr B2M with VLA. The continuum emission is subtracted. Color lines show the result of Gaussian fit, where the systemic velocity and the linewidth are assumed to be the same for the four hyperfine components. The emission features are produced by maser emission at the systemic velocity of the star-forming regions.

This method can be used to diagnose the Galactic spiral arm clouds. Their chemical compositions have been studied by observing molecular lines in the submillimeter-wave and THz regions. They are observed in absorption against the strong continuum sources (Godard et al. 2010; Gerin et al. 2011). Many submillimeter-wave absorption lines of interstellar hydrides such as CH, CH^+, SH^+, OH^+, NH and HCl^+ have been detected in the Galactic spiral arms with Herschel (Gerin et al. 2010; Godard et al. 2012; De Luca et al. 2012; Persson et al. 2012; Indriolo et al. 2015; Liszt & Gerin 2016), revealing rich chemistry in diffuse ISM. On the other hand, it is difficult to determine the physi-

cal condition of such clouds from the submillimeter-wave absorption lines, because the above hydrides are mostly populated in the ground rovibrational state, and the excitation analysis is almost impossible. However, physical characterization of these clouds is really awaited for detailed understandings of their chemistry. In particular, information on the temperature is essential to evaluate the effect of UV penetration. The OH 18 cm transition will solve this problem. To examine this possibility, we analyzed VLA archival data of OH observed toward strong radio continuum sources, most of which are well-known high-mass star-forming regions. Figure 67 shows the spectra of OH toward W31C, W49N and Sgr B2(M), where the absorption features of foreground spiral arm clouds are seen in several velocity components. The conjugate feature of the satellite lines similar to that observed in HCL2E (Figure 19) is seen toward these three sources. The 1612 MHz line shows deep absorption compared with the 1665 and 1667 MHz line absorption, whereas the 1720 MHz line shows emission. To analyze these observational results, we incorporate the effect of the background continuum radiation into our statistical equilibrium calculation, and conduct the least-square analysis to each velocity component. The derived gas kinetic temperatures and OH column densities are summarized in Table 15, where the density and the ortho-to-para ratio of H_2 are assumed to be 10^3 cm^{-3} and 3, respectively. Note that the results do not strongly depend on the H_2 density, as demonstrated in Figure 26. The clouds are indeed found to be warm (35–120 K) except for the three clouds (V_{LSR}=60.6 km/s component in W49N and V_{LSR}=36.5 km/s and 13.5 km/s components in Sgr B2(M)) where the above anomaly is not observed.

As shown above, the OH 18 cm transition is also a good tracer of the physical conditions of the Galactic spiral arm. Such a study to determine the gas kinetic temperature provides us with basic information in exploring the molecular-cloud formation in the Galaxy. Unfortunately, a long observation time (30–60 minutes per position) is required to obtain a sufficient signal-to-noise ratio for the satellite lines, and hence, a large-scale mapping observation has not been feasible with the currently available radio telescopes. However, this situation will be changed relatively soon. Mapping observations of the OH 18 cm transition with the FAST 500-m telescope, which is the largest radio single-dish telescope in China, toward various molecular clouds will reveal their temperature structures with a

better spatial resolution and sensitivity. Such studies will give us with important information on the origin of the straight structure, which is ubiquitous in molecular clouds (Section 2.1) and indeed seen in HCL2 (Figure 44), Lupus-1 (Figure 24) and the Pipe nebula (Figure 35). Moreover, observations of the OH 18 cm transition toward external galaxies using the SKA, which will be the largest radio interferometer available in the mid-2020s, will reveal the temperature structure of spiral arms of external galaxies. All these studies would improve our understandings of molecular-cloud formation. The work presented here will be a sound base for these future studies.

Acknowledgements

Special thanks are due to my thesis supervisor Professor Satoshi Yamamoto for all his kind and invaluable support during my PhD course. I would like to thank Dr. Yoshimasa Watanabe for his support in the observations of the OH 18 cm transition and the analyses of the observed data, Dr. Nami Sakai for her fruitful discussions on the interpretations of the observed results, Prof. Shuichiro Inutsuka and Prof. Tsuyoshi Inoue for their discussion on the molecular-cloud formation by a possible filament-filament collisions in the Pipe nebula, and Mr. Hiroshi Inokuma for his assistance in the early stage of this work.

I am very grateful to Prof. Karl, M. Menten for his lots of discussion on the OH hyperfine anomalies as well as his kind support during the stay in the Effelsberg 100-m telescope and Max-Planck-Institut für Radioastronomie in Bonn, Germany. I am also very grateful to Dr. Claire Chandler for her advice in the analyses of the VLA data and kind support during my stay in the National Radio Astronomy Observatory (NRAO) in Soccoro, USA.

I am grateful to the members of my dissertation committee: Prof. Masami Ouchi, Prof. Yasushi Suto, Prof. Tadayuki Takahashi, Prof. Kazuhisa Mitsuda, and Prof. Nobuaki Imai for their valuable comments and suggestions.

I thank the members of Yamamoto group: Dr. Ana López Sepluclre, Dr. Daiki Shibata, Dr. Tatsuya Soma, Dr. Yuri Nishimura, Dr. Yoko Oya, Mr. Kento Yoshida, Mr. Muneaki Imai, Mr. Yutaro Chiba, Mr. Masaki Takegahara, Ms. Yuki Okoda, Mr. Takanori Fujita, Mr. Osamu Oguchi, and Ms. Miki Ueda.

This study is financially supported by the Advance Leading Graduate Course for Photon Science (ALPS) and Grants-in-Aid from Ministry of Education, Sports, Science, and Technologies of Japan (25400223, 25108005, 18H05222, and 17J02168).

APPENDIX

A. Results of the new statistical equilibrium calculations with various parameters

Here, we present results of our statistical equilibrium calculations with different OH column densities and H_2 ortho-to-para ratios (Figures 68–73). Assumptions in the calculations for panels ((a)–(f)) are the same as those in Figures 55 and 58.

Figures 68 and 69 show the calculated intensities of the OH 18 cm transition as a function of the gas kinetic temperature, where the H_2 ortho-to-para ratio is assumed to be 0 and 3, respectively. The OH column density is assumed to be 3×10^{14} cm^{-2}. The 1720 MHz line absorption is not reproduced with such a low OH column density, as described in Section 6.4.1.3. On the other hand, the effect of the FIR radiation is seen for the gas kinetic temperature higher than 30 K, since the intensity of the 1612 MHz line in panels (b), (c), (e), and (f) is slightly higher than that in panels (a) and (d). The 1720 MHz line is also slightly fainter. The effect of the line overlaps is negligible for the H_2 ortho-to-para ratio of 0 (Figure 68), whereas the 1667 MHz line is slightly brighter by considering the effect of the overlaps for the H_2 ortho-to-para ratio of 3 (Figure 69).

Figures 70 and 71 show the derived intensities of the OH 18 cm transition as a function of the H_2 density, where the H_2 ortho-to-para ratio is assumed to be 0 and 3, respectively. Again, the 1720 MHz line absorption is not reproduced with the OH column density of 3×10^{14} cm^{-2}, whereas the effect of the FIR is seen for the H_2 density lower than $\sim 10^2$ cm^{-3}.

Figure 72 shows the calculated intensities of the OH 18 cm transition as a function of the gas kinetic temperature, where the H_2 density, OH column density, and H_2 ortho-to-para ratio are assumed to be 10^3 cm^{-3}, 3×10^{15} cm^{-2}, and 3, respectively. The absorption feature of the 1720 MHz line is reproduced for the gas kinetic temperature higher than about 50 K by considering the effect of the line overlaps (Figures 72 (d)–(f)), as shown in Section 6.4.1.3. However, the 1665 MHz line appears in absorption for the gas kinetic temperature higher than about 60 K, and the 1612 MHz line is too strong compared to the 1665 MHz line for the gas kinetic temperature between 50 K and 60 K.

Figure 73 shows the calculated intensities of the OH 18 cm transition as a function of the H_2 density, where the OH column density, the gas kinetic temperature, and the H_2 ortho-to-para ratio are assumed to be 3×10^{15} cm^{-2}, 20 K, and 3, respectively. Qualitative features of the four hyperfine structure lines are similar to those derived for the H_2 ortho-to-para ratio of 0 (Figure 55). On the other hand, the effects of the FIR radiation and line overlaps are smaller for the H_2 ortho-to-para ratio of 3, and the H_2 density required to show the 1720 MHz line absorption is lower by a factor of $\sim$2–3. It can be explained by more efficient collisional excitations to the first rotationally excited state levels by collisions with ortho-H_2 than para-H_2, which might compensate the FIR pumping effect and the effect of the line overlaps.

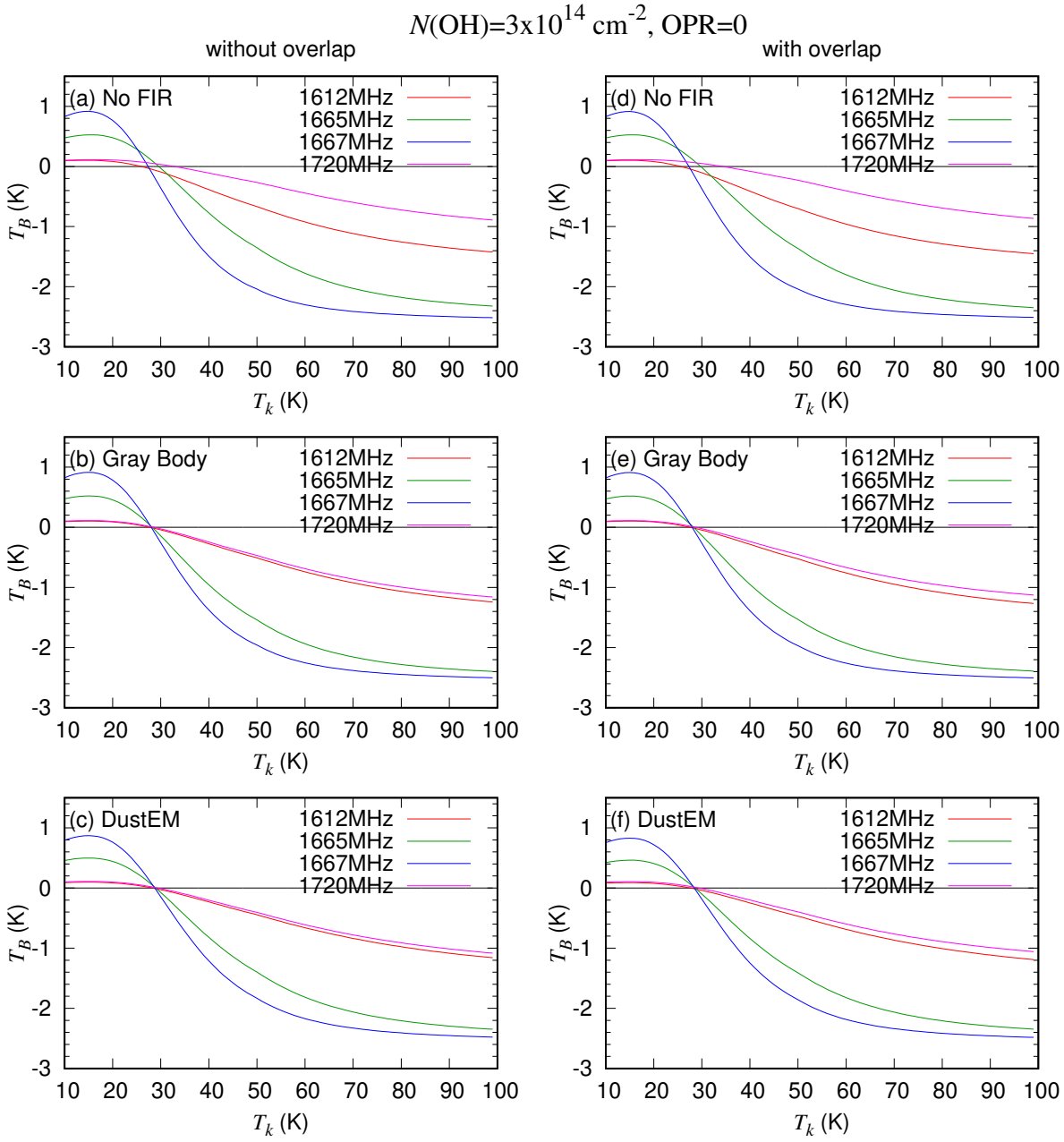

Figure 68. The derived intensities of the OH 18 cm transition hfs lines as a function of the gas kinetic temperature, where the H_2 density, the OH column density, and the ortho-to-para ratio of H_2 are assumed to be 10^3 cm^{-3}, 3×10^{14} cm^{-2}, and 0, respectively. Models assumed in each panel ((a)–(f)) are the same as those in Figure 55.

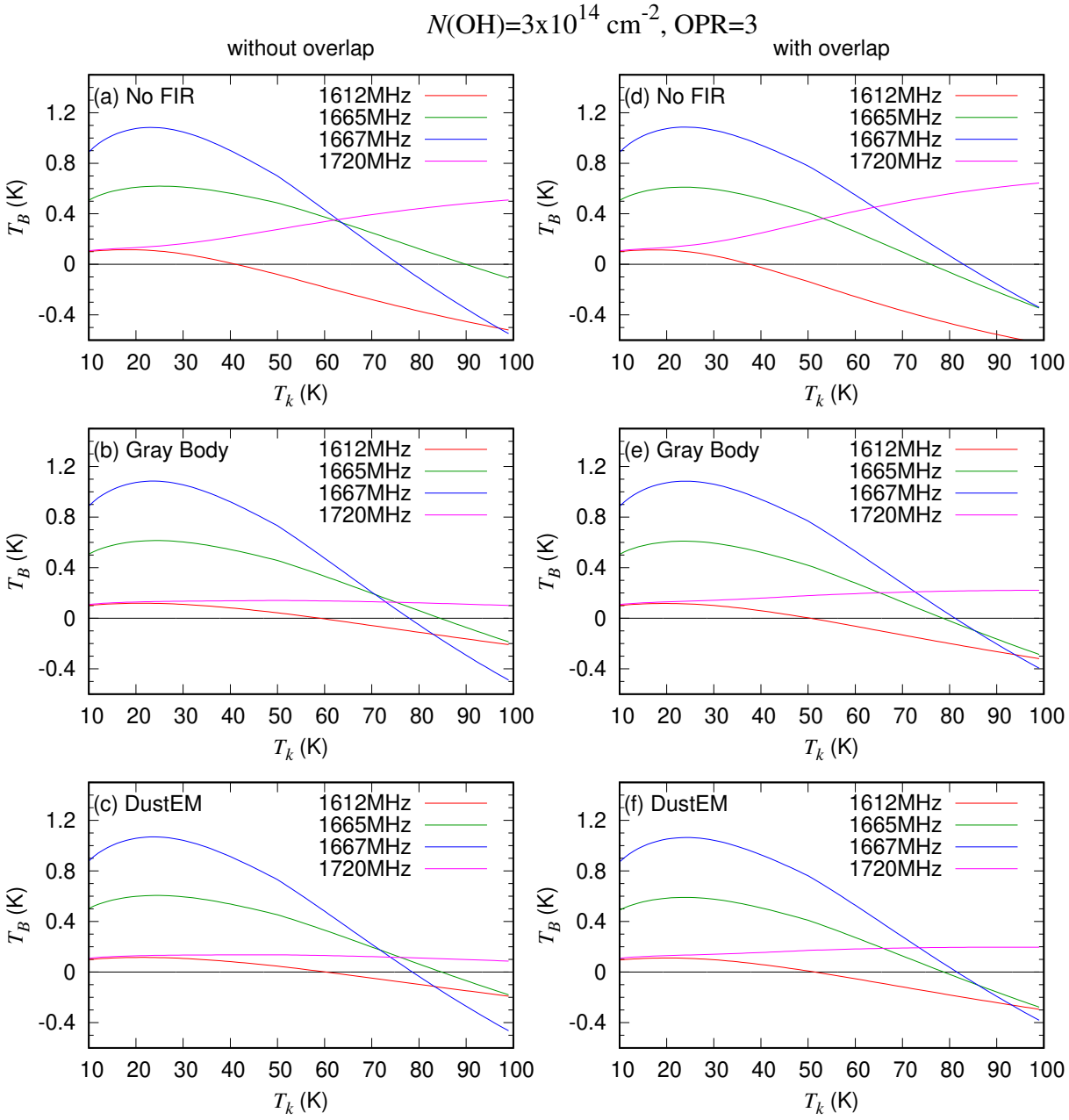

Figure 69. The derived intensities of the OH 18 cm transition hfs lines as a function of the gas kinetic temperature, where the H_2 density, the OH column density, and the ortho-to-para ratio of H_2 are assumed to be 10^3 cm^{-3}, 3×10^{14} cm^{-2}, and 3, respectively. Models assumed in each panel ((a)–(f)) are the same as those in Figure 55.

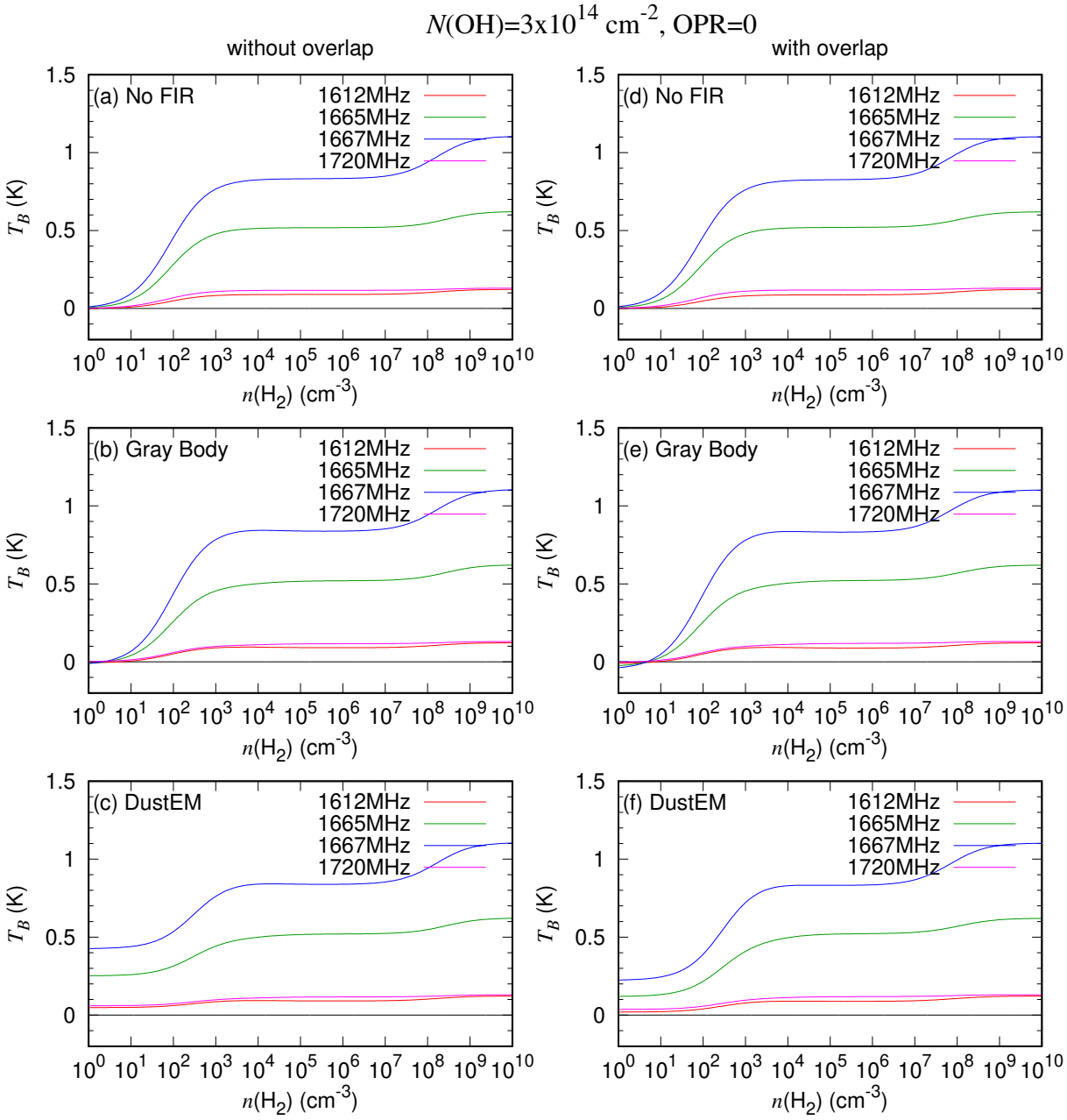

Figure 70. The derived intensities of the OH 18 cm transition hfs lines as a function of the H_2 density, where the OH column density, the gas kinetic temperature, and the ortho-to-para ratio of H_2 are assumed to be 3×10^{14} cm^{-2}, 20 K, and 0, respectively. Models assumed in each panel ((a)–(f)) are the same as those in Figure 55.

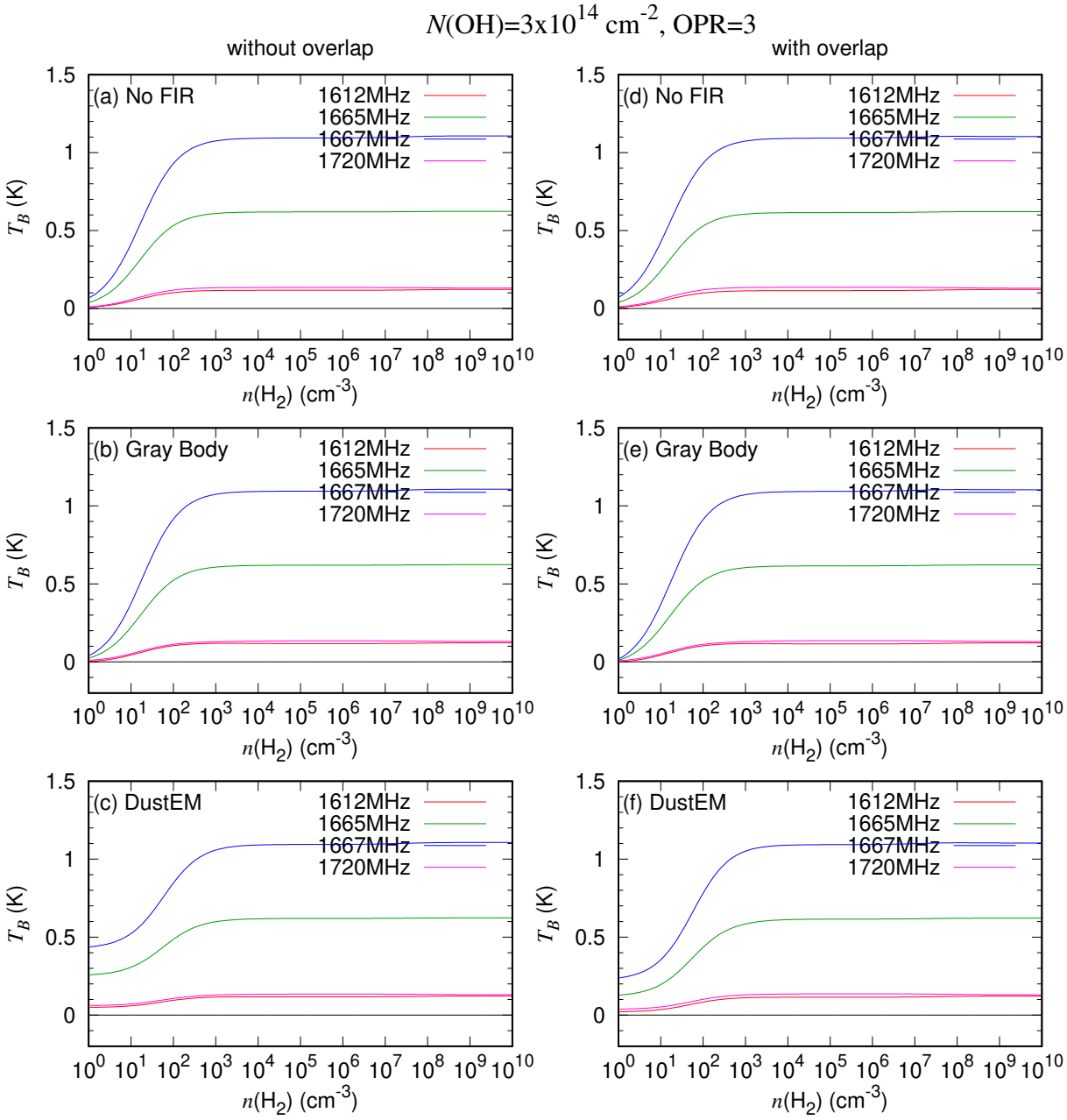

Figure 71. The derived intensities of the OH 18 cm transition hfs lines as a function of the H_2 density, where the OH column density, the gas kinetic temperature, and the ortho-to-para ratio of H_2 are assumed to be 3×10^{14} cm^{-2}, 20 K, and 3, respectively. Models assumed in each panel ((a)–(f)) are the same as those in Figure 55.

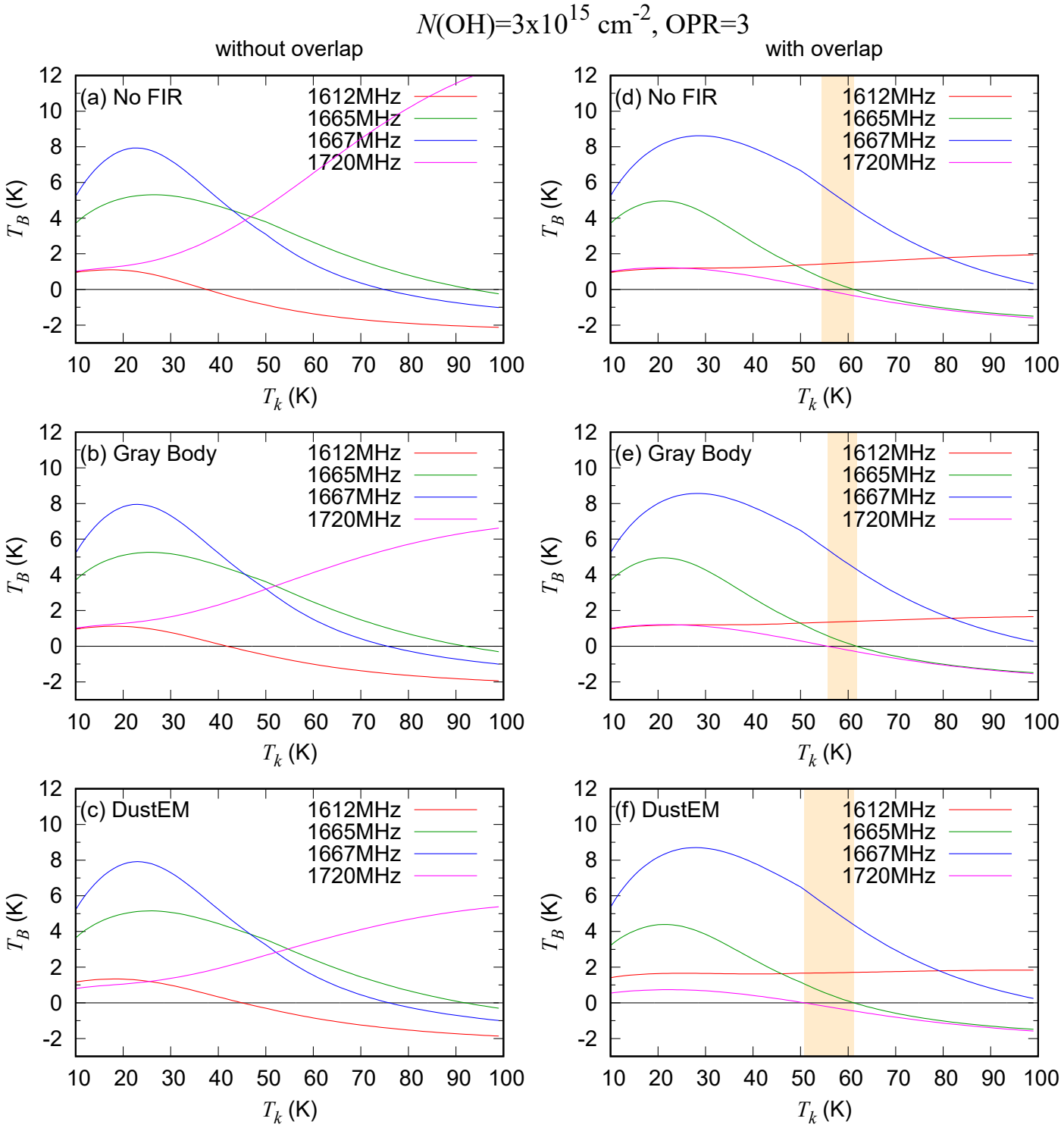

Figure 72. The derived intensities of the OH 18 cm transition hfs lines as a function of the gas kinetic temperature, where the H_2 density, the OH column density, and the ortho-to-para ratio of H_2 are assumed to be 10^3 cm^{-3}, 3×10^{15} cm^{-2}, and 3, respectively. Models assumed in each panel ((a)–(f)) are the same as those in Figure 55. The orange areas in the panels (d)–(f) represent the region where the 1720 MHz line appears in absorption and the other three lines show emission.

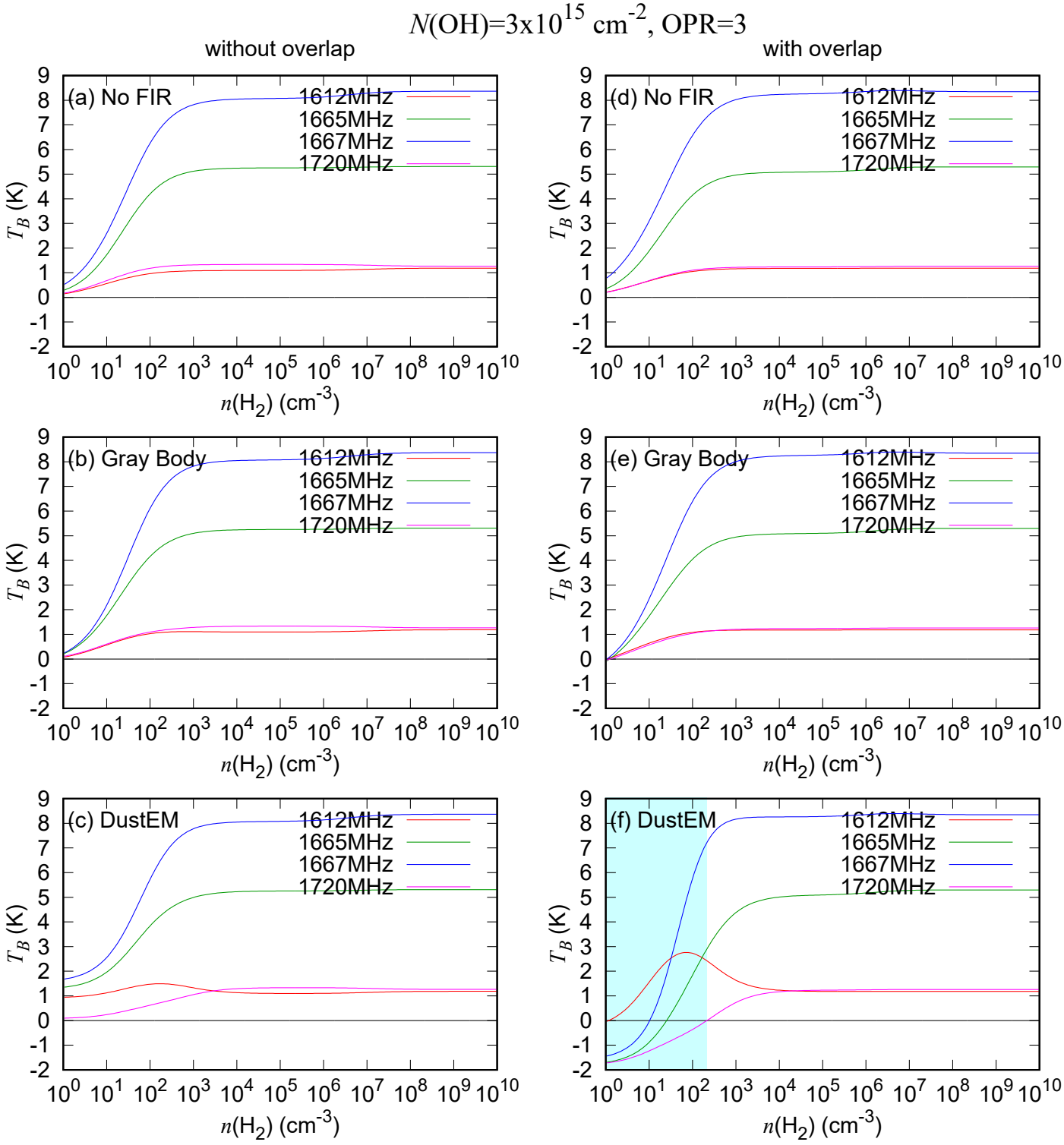

Figure 73. The derived intensities of the OH 18 cm transition hfs lines as a function of the H_2 density, where the OH column density, the gas kinetic temperature, and the ortho-to-para ratio of H_2 are assumed to be 3×10^{15} cm^{-2}, 20 K, and 3, respectively. Models assumed in each panel ((a)–(f)) are the same as those in Figure 55. The cyan area in the panel (f) represents the region where the 1720 MHz line appears in absorption.

B. Effects of uncertainties in the collisional rate coefficients of OH

We employ the collisional rate coefficients of OH calculated by Offer et al. (1994) in our statistical equilibrium calculations. Here, we assess the robustness of our calculations by conducting our calculations with the hfs-resolved collisional rate coefficients, which are evaluated by applying the M-J random method to the new hfs-unresolved rates reported by Kłos et al. (2017). These rate coefficients have been provided by Dr. François Lique. Although they are based on the new interaction potential, the hfs-resolved collisional rate coefficients are not considered rigorously in the M-J random method (Kłos et al. 2017). Hence, we have just used these rates to confirm our results in the main text.

Figure 74 shows derived intensities of the OH 18 cm transition as a function of the H_2 density with the collisional rate coefficients by Offer et al. (1994) (dotted lines) and the new rate coefficients (solid lines). It can be seen that all the four solid lines slightly shift to the left in comparison with the dotted lines shown in the same color. This suggests that the FIR pumping effect is slightly less

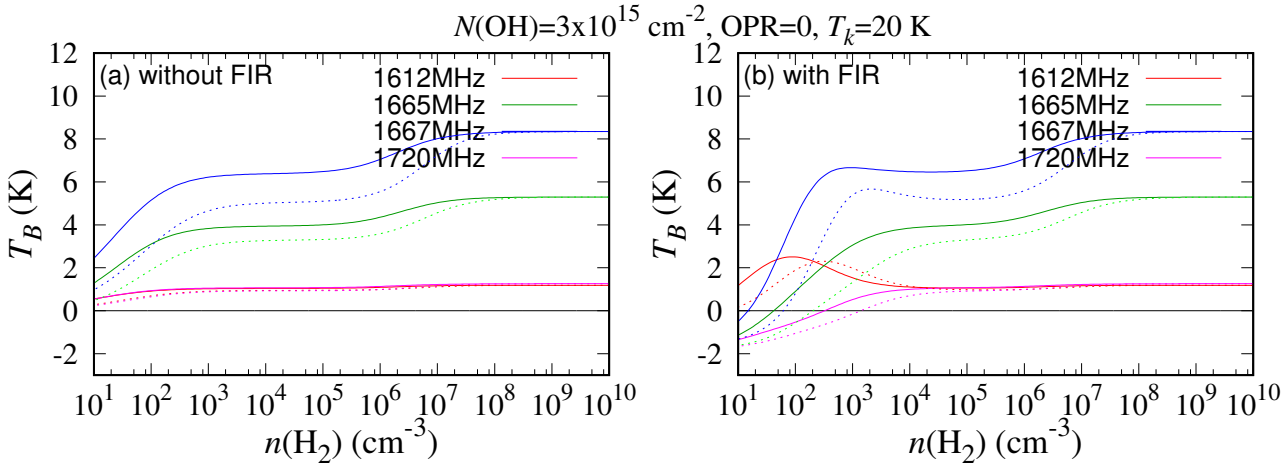

Figure 74. The derived intensities of the OH 18 cm transition hfs lines as a function of the H_2 density. Dotted lines represent results with the collisional rate coefficients of OH calculated by Offer et al. (1994), whereas solid lines show those with the new rate coefficients calculated by applying M-J random method to hfs-unresolved rates by Kłos et al. (2017) (solid line). Effect of the FIR radiation is not included in the left panel, whereas FIR radiation calculated with the fiducial DustEM model (N(H)=3 $\times$ 10^{23} cm^{-2}, ISRF=0.4 G_0) is included in the right panel.

efficient with the new rate coefficients. The H_2 density required to show the 1720 MHz line absorption becomes lower by a factor of about 2 with the new rate coefficients (Figure 74, right). Hence, the FIR intensity must be 2 times stronger in order to reproduce the 1720 MHz line absorption with the new rate coefficients, assuming the same H_2 density. Nevertheless, the new rate coefficients does not change the qualitative features of the four hfs lines' behavior. Furthermore, the absorption in the 1720 MHz line can be reproduced even with the new rate coefficients. Therefore, uncertainties in the collisional rate coefficients of OH are considered to only have a limited effect, a factor of 2 at most, on the results discussed in the Section 6.4. Nevertheless, we have to add a caveat that accurate collisional rate coefficients considering the hyperfine structure are awaited for more quantitative analysis of the hyperfine anomaly of the OH 18 cm transition.

C. A geometrical effect of a filamentary structure

In this section, we considered the geometrical effect on the intensity of the FIR radiation in TMC-1FN by taking into account the density profile and the geometry of a filamentary structure. We assume that the filament has a cylinder shape with a radius of W and a length of $2L$, as shown in Figure 75. Its density profile is assumed to be the Plummer-like profile, which can be written as a function of the radial distance from the central axis of the cylinder (s) (Plummer 1911):

$$\rho(s) = \frac{\rho_c}{\left(1 + \frac{s^2}{r_p^2}\right)^{\frac{p}{2}}}. \tag{C1}$$

By considering a position P inside the filament in Figure 75, where the distance from the center of the cylinder O is r_0, the FIR intensity averaged over all directions (θ and ϕ) can be written as:

$$I_{inner}(\nu) = u(\nu)\frac{2}{\pi}\int_0^{\frac{\pi}{2}} d\phi \frac{2}{\pi}\int_0^{\frac{\pi}{2}} d\theta \int_{-R(\theta,\phi)}^{R(\theta,\phi)} dr \rho(s(r,\theta,\phi)), \tag{C2}$$

where $u(\nu)$ denotes the FIR intensity per hydrogen at a given frequency ν. $R(\theta,\phi)$ and $s(r,\theta,\phi)$ are defined as:

$$R(\theta,\phi) = \begin{cases} R_1(\theta,\phi) = \frac{\sqrt{W^2 - r_0^2\cos^2\phi}}{\cos\theta} & (0 < \theta < \theta_c(\phi)) \\ R_2(\theta,\phi) = \frac{L}{\sin\theta} & (\theta_c(\phi) < \theta < \frac{\pi}{2}) \end{cases} \tag{C3}$$

$$s^2(r,\theta,\phi) = \begin{cases} s_1^2(r,\theta,\phi) = s_0^2(r\cos\theta + r_0\sin\phi) & (0 < \theta < \theta_c(\phi)) \\ s_2^2(r,\theta,\phi) = s_0^2(r\cos\theta) & (\theta_c(\phi) < \theta < \frac{\pi}{2}). \end{cases} \tag{C4}$$

Here, $\theta_c(\phi)$ and $s_0^2(x)$ are represented as:

$$\theta_c(\phi) = \tan^{-1}\frac{L}{\sqrt{W^2 - r_0^2\cos^2\phi}} \tag{C5}$$

$$s_0^2(x) = \left| \begin{pmatrix} 0 \\ -r_0 \end{pmatrix} + x \begin{pmatrix} \cos\phi \\ \sin\phi \end{pmatrix} \right|^2 \tag{C6}$$

$$= x^2 - 2xr_0\sin\phi + r_0^2. \tag{C7}$$

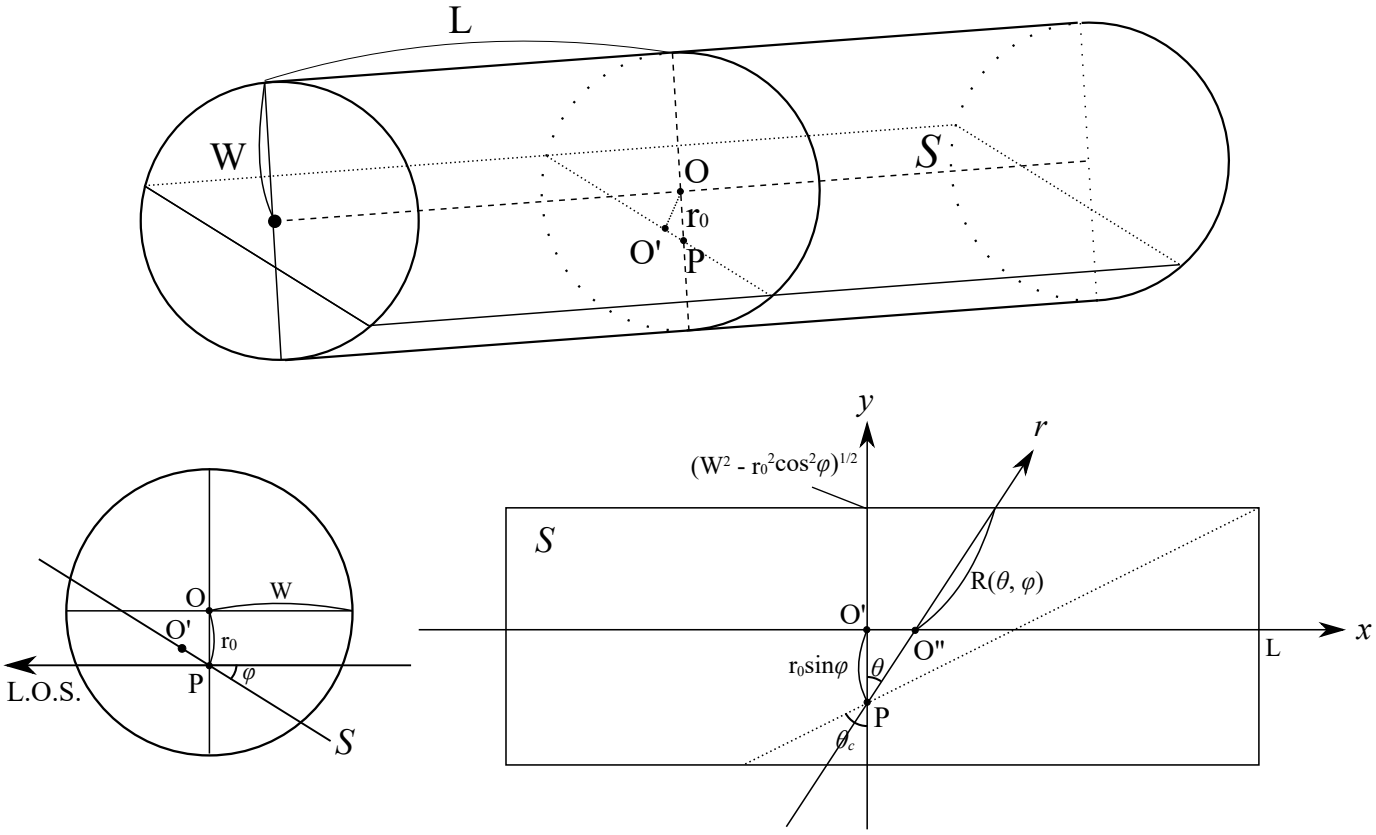

Figure 75. Schematic illustration of a cylindrical model to estimate the geometrical effect of a filament on the intensity of FIR radiation. The FIR intensity at the position P inside the filament is determined by averaging over all direction (θ and ϕ). We also derived the FIR intensity along the line-of-sight perpendicular to the cylinder crossing the position P, as an estimate of the observed intensity.

We define the following functions by substituting the relations $\tilde{r_0} = r_0/r_p$, $\tilde{W} = W/r_p$, and $\tilde{L} = L/r_p$ for Equations (C3)–(C7):

$$\tilde{R}(\theta,\phi) = \begin{cases} \tilde{R}_1(\theta,\phi) = \frac{\sqrt{\tilde{W}^2 - \tilde{r}_0^2\cos^2\phi}}{\cos\theta} & (0 < \theta < \theta_c(\phi)) \\ \tilde{R}_2(\theta,\phi) = \frac{\tilde{L}}{\sin\theta} & (\theta_c(\phi) < \theta < \frac{\pi}{2}) \end{cases} \tag{C8}$$

$$\tilde{s}_0^2(x) = x^2 - 2x\tilde{r}_0\sin\phi + \tilde{r}_0^2 \tag{C9}$$

$$\tilde{s}^2(r,\theta,\phi) = \begin{cases} \tilde{s}_1^2(r,\theta,\phi) = \tilde{s}_0^2(r\cos\theta + \tilde{r}_0\sin\phi) & (0 < \theta < \theta_c(\phi)) \\ \tilde{s}_2^2(r,\theta,\phi) = \tilde{s}_0^2(r\cos\theta) & (\theta_c(\phi) < \theta < \frac{\pi}{2}). \end{cases} \tag{C10}$$

Then, Equation (C2) becomes

$$I_{inner}(\nu, r_0) = u(\nu)\frac{4r_p\rho_c}{\pi^2}\int_0^{\frac{\pi}{2}} d\phi \left[\int_0^{\theta_c} d\theta \int_{-\tilde{R}_1(\theta,\phi)}^{\tilde{R}_1(\theta,\phi)} d\tilde{r}\left(1+\tilde{s}_1^2(\tilde{r},\theta,\phi)\right)^{-\frac{p}{2}}\right. \tag{C11}$$

$$\left. + \int_{\theta_c}^{\frac{\pi}{2}} d\theta \int_{-\tilde{R}_2(\theta,\phi)}^{\tilde{R}_2(\theta,\phi)} d\tilde{r}\left(1+s_2^2(\tilde{r},\theta,\phi)\right)^{-\frac{p}{2}}\right]. \tag{C12}$$

On the other hand, the FIR intensity along the line-of-sight perpendicular to the cylindrical axis at the position with the distance of r_0 from the center of the cylinder is:

$$I_{LOS}(\nu, r_0) = u(\nu)\int_{-\sqrt{W^2-r_0^2}}^{\sqrt{W^2-r_0^2}} \rho\left(\sqrt{r^2+r_0^2}\right) dr. \tag{C13}$$

Figure 76 shows the intensity ratio of $I_{inner}(\nu,\ r_0)$ relative to $I_{LOS}(\nu,\ r_0)$ as a function of the distance from the center of the cylinder r_0. Dependence on the FIR frequency (ν) is canceled by the division. Here we assume the Plummer-like profile reported by Malinen et al. (2012) (ρ_c=9.02×10^4

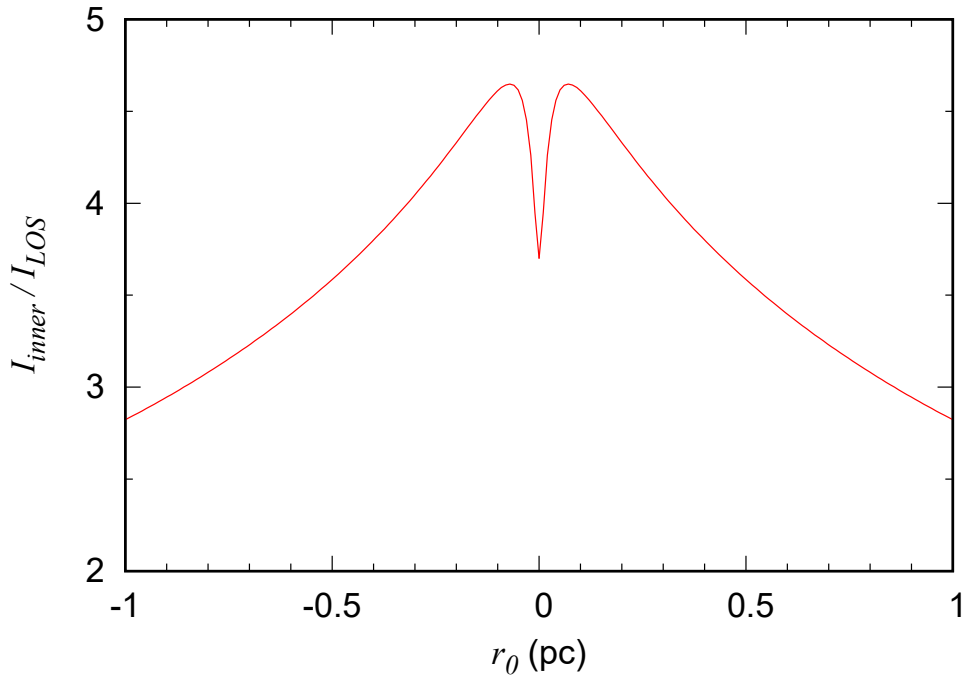

Figure 76. The ratio of the FIR intensity inside the filament ($I_{inner}(\nu,\ r_0)$ in Equation (C12)) to that along the line-of-sight perpendicular to the filament ($I_{LOS}(\nu,\ r_0)$ in Equation (C13)) as a function of r_0. Here the Plummer-like density profile (Equation (C1)) with ρ_c=9.02×10^4 cm^{-3}, r_p=0.012 pc, and p=1.84, and the cylindrical length of 2.5 pc are assumed. The FIR radiation inside the filament within 1 pc can be stronger by a factor of 3–4 compared to the observed value along the line-of-sight.

cm^{-3}, r_p=0.012 pc, p=1.84), which is derived from WFCAM extinction map toward the filamentary structure harboring TMC-1FN. The length of the cylinder is assumed to be 2.5 pc, which is estimated from the Herschel 250 μm map (Figure 77) observed toward HCL2 region. According to Figure 76, the FIR intensity at TMC-1FN, which is located at $\sim$0.25 pc distant from the center of the filament, is estimated to be about 4 times stronger than the observed intensity, assuming that the filament is perpendicular to the line-of-sight direction. Therefore, the FIR intensity at 160μm toward TMC-1FN is estimated to be 300-400 MJy sr^{-1} according to the observed value with *Spitzer* (Flagey et al. 2009).

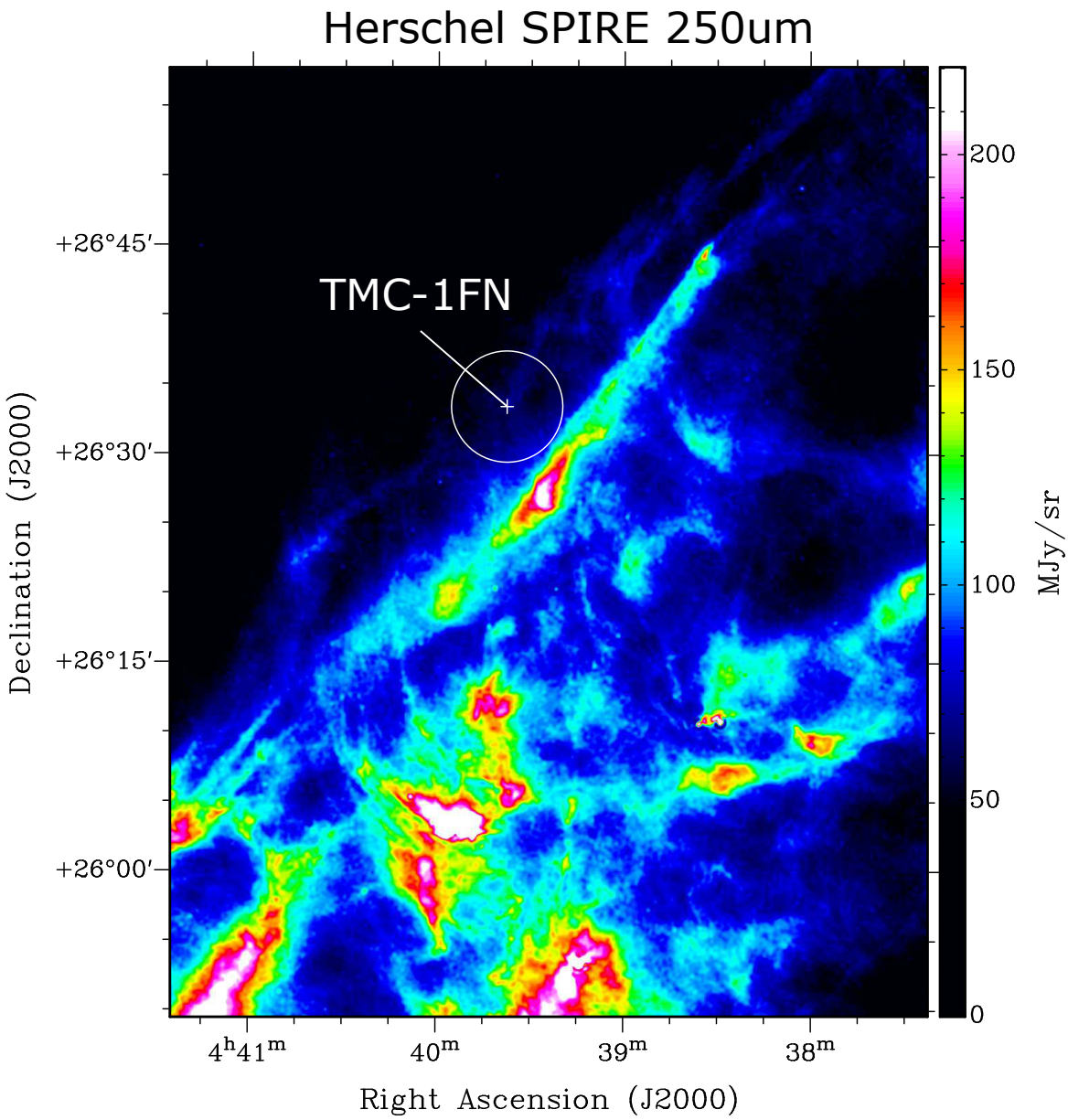

Figure 77. The Herschel SPIRE 250μm map on the HCL2 region obtained from archival data with the observation IDs of 1342202252 and 1342202253. White circle represents the observed position of TMC-1FN in the OH 18 cm transition and its beam size. A filamentary structure observed in $C^{18}O$ (Figure 44) is clearly seen in the southwestern part of TMC-1FN.

REFERENCES

Allen, R. J., Hogg, D. E., & Engelke, P. D. 2015, AJ, 149, 123, doi: 10.1088/0004-6256/149/4/123

Alves, F. O., & Franco, G. A. P. 2007, A&A, 470, 597, doi: 10.1051/0004-6361:20066759

Alves, F. O., Franco, G. A. P., & Girart, J. M. 2008, A&A, 486, L13, doi: 10.1051/0004-6361:200810091

Alves, F. O., Frau, P., Girart, J. M., et al. 2014, A&A, 569, L1, doi: 10.1051/0004-6361/201424678

André, P., Men'shchikov, A., Bontemps, S., et al. 2010, A&A, 518, L102, doi: 10.1051/0004-6361/201014666

Arzoumanian, D., Shimajiri, Y., Inutsuka, S.-i., Inoue, T., & Tachihara, K. 2018, PASJ, 70, 96, doi: 10.1093/pasj/psy095

Baart, E. E., de Jager, G., & Mountfort, P. I. 1980, A&A, 92, 156

Benedettini, M., Pezzuto, S., Burton, M. G., et al. 2012, MNRAS, 419, 238, doi: 10.1111/j.1365-2966.2011.19687.x

Benson, P. J., & Myers, P. C. 1989, ApJS, 71, 89, doi: 10.1086/191365

Biermann, P., & Tinsley, B. M. 1974, A&A, 30, 1

Boulanger, F., Abergel, A., Bernard, J.-P., et al. 1996, A&A, 312, 256

Castets, A., Duvert, G., Dutrey, A., et al. 1990, A&A, 234, 469

Caswell, J. L. 2004, MNRAS, 349, 99, doi: 10.1111/j.1365-2966.2004.07472.x

Cesaroni, R., & Walmsley, C. M. 1991, A&A, 241, 537

Cohen, R. J. 1995, Ap&SS, 224, 55, doi: 10.1007/BF00667821

Compiègne, M., Verstraete, L., Jones, A., et al. 2011, A&A, 525, A103, doi: 10.1051/0004-6361/201015292

Crutcher, R. M. 1973, ApJ, 185, 857, doi: 10.1086/152460

—. 1977, ApJ, 216, 308, doi: 10.1086/155472

—. 1979, ApJ, 234, 881, doi: 10.1086/157570

Crutcher, R. M., Troland, T. H., Goodman, A. A., et al. 1993, ApJ, 407, 175, doi: 10.1086/172503

Cudaback, D. D., & Heiles, C. 1969, ApJ, 155, L21, doi: 10.1086/180296

Dame, T. M., Hartmann, D., & Thaddeus, P. 2001, ApJ, 547, 792, doi: 10.1086/318388

Dame, T. M., Ungerechts, H., Cohen, R. S., et al. 1987, ApJ, 322, 706, doi: 10.1086/165766

Darling, J. 2003, Physical Review Letters, 91, 011301, doi: 10.1103/PhysRevLett.91.011301

Darling, J., & Giovanelli, R. 2002, AJ, 124, 100, doi: 10.1086/341166

de Geus, E. J. 1992, A&A, 262, 258

De Luca, M., Gupta, H., Neufeld, D., et al. 2012, ApJ, 751, L37, doi: 10.1088/2041-8205/751/2/L37

Dickens, J. E., Irvine, W. M., Snell, R. L., et al. 2000, ApJ, 542, 870, doi: 10.1086/317040

Draine, B. T., & Katz, N. 1986, ApJ, 306, 655, doi: 10.1086/164375

Duarte-Cabral, A., Acreman, D. M., Dobbs, C. L., et al. 2015, MNRAS, 447, 2144, doi: 10.1093/mnras/stu2586

Ebisawa, Y., Inokuma, H., Sakai, N., et al. 2015, ApJ, 815, 13, doi: 10.1088/0004-637X/815/1/13

Elitzur, M. 1976, ApJ, 203, 124, doi: 10.1086/154054

Elitzur, M., Goldreich, P., & Scoville, N. 1976, ApJ, 205, 384, doi: 10.1086/154289

Felenbok, P., & Roueff, E. 1996, ApJ, 465, L57, doi: 10.1086/310129

Flagey, N., Noriega-Crespo, A., Boulanger, F., et al. 2009, ApJ, 701, 1450, doi: 10.1088/0004-637X/701/2/1450

Franco, G. A. P. 1989, A&A, 223, 313

Franco, G. A. P., Alves, F. O., & Girart, J. M. 2010, ApJ, 723, 146, doi: 10.1088/0004-637X/723/1/146

Frau, P., Girart, J. M., Alves, F. O., et al. 2015, A&A, 574, L6, doi: 10.1051/0004-6361/201425234

Fukui, Y., Kawamura, A., Minamidani, T., et al. 2008, ApJS, 178, 56, doi: 10.1086/589833

Gerin, M., Kaźmierczak, M., Jastrzebska, M., et al. 2011, A&A, 525, A116, doi: 10.1051/0004-6361/201015050

Gerin, M., de Luca, M., Goicoechea, J. R., et al. 2010, A&A, 521, L16, doi: 10.1051/0004-6361/201015115

Glover, S. C. O., & Smith, R. J. 2016, MNRAS, 462, 3011, doi: 10.1093/mnras/stw1879

Godard, B., Falgarone, E., Gerin, M., Hily-Blant, P., & de Luca, M. 2010, A&A, 520, A20, doi: 10.1051/0004-6361/201014283

Godard, B., Falgarone, E., Gerin, M., et al. 2012, A&A, 540, A87, doi: 10.1051/0004-6361/201117664

Goicoechea, J. R., Chavarría, L., Cernicharo, J., et al. 2015, ApJ, 799, 102, doi: 10.1088/0004-637X/799/1/102

Goldreich, P., & Kwan, J. 1974, ApJ, 189, 441, doi: 10.1086/152821

Goldsmith, P. F., Heyer, M., Narayanan, G., et al. 2008, ApJ, 680, 428, doi: 10.1086/587166

Goldsmith, P. F., Velusamy, T., Li, D., & Langer, W. D. 2010, ApJ, 715, 1370, doi: 10.1088/0004-637X/715/2/1370

Gritschneder, M., & Lin, D. N. C. 2012, ApJ, 754, L13, doi: 10.1088/2041-8205/754/1/L13

Guilloteau, S., Lucas, R., & Omont, A. 1981, A&A, 97, 347

Gundermann, E. J., Goldstein, Jr., S. J., & Lilley, A. E. 1965, AJ, 70, 321, doi: 10.1086/109734

Gusdorf, A., Güsten, R., Menten, K. M., et al. 2016, A&A, 585, A45, doi: 10.1051/0004-6361/201425325

Habing, H. J. 1968, Bull. Astron. Inst. Netherlands, 19, 421

Hacar, A., Tafalla, M., Kauffmann, J., & Kovács, A. 2013, A&A, 554, A55, doi: 10.1051/0004-6361/201220090

Harju, J., Winnberg, A., & Wouterloot, J. G. A. 2000, A&A, 353, 1065

Heiles, C. E. 1968, ApJ, 151, 919, doi: 10.1086/149493

Heiner, J. S., & Vázquez-Semadeni, E. 2013, MNRAS, 429, 3584, doi: 10.1093/mnras/sts645

Heyer, M. H., Morgan, J., Schloerb, F. P., Snell, R. L., & Goldsmith, P. F. 1992, ApJ, 395, L99, doi: 10.1086/186497

Hirahara, Y., Suzuki, H., Yamamoto, S., et al. 1992, ApJ, 394, 539, doi: 10.1086/171605

Hoffman, I. M., Goss, W. M., Brogan, C. L., & Claussen, M. J. 2005, ApJ, 620, 257, doi: 10.1086/427018

Hollenbach, D., Kaufman, M. J., Bergin, E. A., & Melnick, G. J. 2009, ApJ, 690, 1497, doi: 10.1088/0004-637X/690/2/1497

Hollenbach, D., Kaufman, M. J., Neufeld, D., Wolfire, M., & Goicoechea, J. R. 2012, ApJ, 754, 105, doi: 10.1088/0004-637X/754/2/105

Indriolo, N., Neufeld, D. A., Gerin, M., et al. 2015, ApJ, 800, 40, doi: 10.1088/0004-637X/800/1/40

Inoue, T., & Inutsuka, S.-i. 2012, ApJ, 759, 35, doi: 10.1088/0004-637X/759/1/35

Inutsuka, S.-i., Inoue, T., Iwasaki, K., & Hosokawa, T. 2015, A&A, 580, A49, doi: 10.1051/0004-6361/201425584

Jonas, J. L., Baart, E. E., & Nicolson, G. D. 1998, MNRAS, 297, 977, doi: 10.1046/j.1365-8711.1998.01367.x

Jones, A. P., Fanciullo, L., Köhler, M., et al. 2013, A&A, 558, A62, doi: 10.1051/0004-6361/201321686

Kalberla, P. M. W., Burton, W. B., Hartmann, D., et al. 2005, A&A, 440, 775, doi: 10.1051/0004-6361:20041864

Kamegai, K., Ikeda, M., Maezawa, H., et al. 2003, ApJ, 589, 378, doi: 10.1086/374352

Kanekar, N., Chengalur, J. N., & Ghosh, T. 2004, Physical Review Letters, 93, 051302, doi: 10.1103/PhysRevLett.93.051302

Keto, E. 2003, ApJ, 599, 1196, doi: 10.1086/379545

Kłos, J., Ma, Q., Dagdigian, P. J., et al. 2017, Monthly Notices of the Royal Astronomical Society, 471, 4249, doi: 10.1093/mnras/stx1968

Koyama, H., & Inutsuka, S.-I. 2000, ApJ, 532, 980, doi: 10.1086/308594

Lada, C. J., Muench, A. A., Rathborne, J., Alves, J. F., & Lombardi, M. 2008, ApJ, 672, 410, doi: 10.1086/523837

Laureijs, R. J., Fukui, Y., Helou, G., et al. 1995, ApJS, 101, 87, doi: 10.1086/192234

Le Petit, F., Roueff, E., & Herbst, E. 2004, A&A, 417, 993, doi: 10.1051/0004-6361:20035629

Lehtinen, K., Mattila, K., Lemke, D., et al. 2003, A&A, 398, 571, doi: 10.1051/0004-6361:20021411

Liseau, R., White, G. J., Larsson, B., et al. 1999, A&A, 344, 342

Liszt, H. S., & Gerin, M. 2016, A&A, 585, A80, doi: 10.1051/0004-6361/201527273

Little, L. T., MacDonald, G. H., Riley, P. W., & Matheson, D. N. 1979, MNRAS, 189, 539, doi: 10.1093/mnras/189.3.539

Litvak, M. M. 1969, ApJ, 156, 471, doi: 10.1086/149982

Lombardi, M., Alves, J., & Lada, C. J. 2006, A&A, 454, 781, doi: 10.1051/0004-6361:20042474

Lombardi, M., Lada, C. J., & Alves, J. 2008, A&A, 480, 785, doi: 10.1051/0004-6361:20079110

Loren, R. B. 1989a, ApJ, 338, 902, doi: 10.1086/167244

—. 1989b, ApJ, 338, 925, doi: 10.1086/167245

Maezawa, H. 2000, PhD thesis, Univ. Tokyo

Malinen, J., Juvela, M., Rawlings, M. G., et al. 2012, A&A, 544, A50, doi: 10.1051/0004-6361/201219573

Mattila, K., Winnberg, A., & Grasshoff, M. 1979, A&A, 78, 275

Mizuno, A., Onishi, T., Yonekura, Y., et al. 1995, ApJ, 445, L161, doi: 10.1086/187914

Mookerjea, B., Israel, F., Kramer, C., et al. 2016, A&A, 586, A37, doi: 10.1051/0004-6361/201527366

Myers, P. C., Ho, P. T. P., Schneps, M. H., et al. 1978, ApJ, 220, 864, doi: 10.1086/155976

Narayanan, G., Heyer, M. H., Brunt, C., et al. 2008, ApJS, 177, 341, doi: 10.1086/587786

Offer, A. R., van Hemert, M. C., & van Dishoeck, E. F. 1994, J. Chem. Phys., 100, 362, doi: 10.1063/1.466950

Onishi, T., Kawamura, A., Abe, R., et al. 1999, PASJ, 51, 871, doi: 10.1093/pasj/51.6.871

Osterbrock, D. E., & Ferland, G. J. 2006, Astrophysics of Gaseous Nebulae and Actice Galactic Nuclei (Mill Valley, CA: Univ. Science Books)

Oya, Y., Sakai, N., López-Sepulcre, A., et al. 2016, ApJ, 824, 88, doi: 10.3847/0004-637X/824/2/88

Peek, J. E. G., Heiles, C., Douglas, K. A., et al. 2011, ApJS, 194, 20, doi: 10.1088/0067-0049/194/2/20

Penzias, A. A., & Burrus, C. A. 1973, ARA&A, 11, 51, doi: 10.1146/annurev.aa.11.090173.000411

Persson, C. M., De Luca, M., Mookerjea, B., et al. 2012, A&A, 543, A145, doi: 10.1051/0004-6361/201118686

Pineda, J. L., Langer, W. D., Velusamy, T., & Goldsmith, P. F. 2013, A&A, 554, A103, doi: 10.1051/0004-6361/201321188

Pineda, J. L., Langer, W. D., Goldsmith, P. F., et al. 2017, ApJ, 839, 107, doi: 10.3847/1538-4357/aa683a

Plume, R., Bensch, F., Howe, J. E., et al. 2000, ApJ, 539, L133, doi: 10.1086/312847

Plummer, H. C. 1911, MNRAS, 71, 460, doi: 10.1093/mnras/71.5.460

Román-Zúñiga, C. G., Alves, J. F., Lada, C. J., & Lombardi, M. 2010, ApJ, 725, 2232, doi: 10.1088/0004-637X/725/2/2232

Sakai, N., Maezawa, H., Sakai, T., Menten, K. M., & Yamamoto, S. 2012, A&A, 546, A103, doi: 10.1051/0004-6361/201219106

Sakai, N., Shiino, T., Hirota, T., Sakai, T., & Yamamoto, S. 2010, ApJ, 718, L49, doi: 10.1088/2041-8205/718/2/L49

Sakai, N., Oya, Y., Sakai, T., et al. 2014, ApJ, 791, L38, doi: 10.1088/2041-8205/791/2/L38

Schöier, F. L., van der Tak, F. F. S., van Dishoeck, E. F., & Black, J. H. 2005, A&A, 432, 369, doi: 10.1051/0004-6361:20041729

Smith, R. J., Glover, S. C. O., Clark, P. C., Klessen, R. S., & Springel, V. 2014, MNRAS, 441, 1628, doi: 10.1093/mnras/stu616

Sunada, K., & Kitamura, Y. 1999, in Interstellar Turbulence, ed. J. Franco & A. Carraminana, 208

Suzuki, H., Yamamoto, S., Ohishi, M., et al. 1992, ApJ, 392, 551, doi: 10.1086/171456

Swade, D. A. 1989, ApJ, 345, 828, doi: 10.1086/167954

Tachihara, K., Dobashi, K., Mizuno, A., Ogawa, H., & Fukui, Y. 1996, PASJ, 48, 489, doi: 10.1093/pasj/48.3.489

Tachihara, K., Toyoda, S., Onishi, T., et al. 2001, PASJ, 53, 1081, doi: 10.1093/pasj/53.6.1081

Tang, N., Li, D., Heiles, C., et al. 2016, A&A, 593, A42, doi: 10.1051/0004-6361/201528055

—. 2017, ApJ, 839, 8, doi: 10.3847/1538-4357/aa67e9

Torres, R. M., Loinard, L., Mioduszewski, A. J., & Rodríguez, L. F. 2007, ApJ, 671, 1813, doi: 10.1086/522924

Tothill, N. F. H., Löhr, A., Parshley, S. C., et al. 2009, ApJS, 185, 98, doi: 10.1088/0067-0049/185/1/98

Troland, T. H., & Crutcher, R. M. 2008, ApJ, 680, 457, doi: 10.1086/587546

Turner, B. E., & Heiles, C. E. 1974, ApJ, 194, 525, doi: 10.1086/153271

van der Tak, F. F. S., Black, J. H., Schöier, F. L., Jansen, D. J., & van Dishoeck, E. F. 2007, A&A, 468, 627, doi: 10.1051/0004-6361:20066820

van Dishoeck, E. F., & Black, J. H. 1988, ApJ, 334, 771, doi: 10.1086/166877

van Langevelde, H. J., van Dishoeck, E. F., Sevenster, M. N., & Israel, F. P. 1995, ApJ, 448, L123, doi: 10.1086/309613

Weaver, H., Williams, D. R. W., Dieter, N. H., & Lum, W. T. 1965, Nature, 208, 29, doi: 10.1038/208029a0

Weinreb, S., Barrett, A. H., Meeks, M. L., & Henry, J. C. 1963, Nature, 200, 829, doi: 10.1038/200829a0

Weisberg, J. M., Johnston, S., Koribalski, B., & Stanimirović, S. 2005, Science, 309, 106, doi: 10.1126/science.1112494

Weselak, T., Galazutdinov, G. A., Beletsky, Y., & Krełowski, J. 2010, MNRAS, 402, 1991, doi: 10.1111/j.1365-2966.2009.16028.x

Wiesemeyer, H., Güsten, R., Heyminck, S., et al. 2012, A&A, 542, L7, doi: 10.1051/0004-6361/201218915

—. 2016, A&A, 585, A76, doi: 10.1051/0004-6361/201526473

Winkel, B., Kerp, J., Flöer, L., et al. 2016, A&A, 585, A41, doi: 10.1051/0004-6361/201527007

Wolak, P., Szymczak, M., & Gérard, E. 2012, A&A, 537, A5, doi: 10.1051/0004-6361/201117263

Xu, D., & Li, D. 2016, ApJ, 833, 90, doi: 10.3847/1538-4357/833/1/90

Xu, D., Li, D., Yue, N., & Goldsmith, P. F. 2016, ApJ, 819, 22, doi: 10.3847/0004-637X/819/1/22

Yui, Y. Y., Nakagawa, T., Doi, Y., et al. 1993, ApJ, 419, L37, doi: 10.1086/187131

Zuckerman, B., & Palmer, P. 1974, ARA&A, 12, 279, doi: 10.1146/annurev.aa.12.090174.001431